Nano Studies

9

2014

Nano Studies

9

2014

Nano Studies, 2014, 9

UDG [53 + 54 + 620.22] (051.2)
N – 21

Nano Studies is a biannual scientific journal published in Georgia.

Nano Studies' topics of interest include Nanoscience and Nanotechnology, and related problems of Physics, Chemistry and Materials Science.

Nano Studies publish following categories of scientific articles: research papers, communications, reviews and discussions.

Nano Studies publish scientific articles in English and also in Georgian and in Russian.

Summaries of all the articles of **Nano Studies** are referred in **Georgian Abstracts Journal** and are accessible in **Tech Inform** (Georgia's Central Institute for Scientific and Technical Information) database: **http://www.tech.caucasus.net**

Full-texts of articles published in **Nano Studies** are free-accessible in **Nano Archive** database: **http://www.nanoarchive.org** and journal's web-site: **www.NanoStudies.org**

Editor & Publisher: **Levan Chkhartishvili**
Editorial Assistant: **Tamar Berberashvili**

Address of Editorial Office: **Department of Engineering Physics**
Georgian Technical University
Campus 4, Room 307
77 Merab Kostava Avenue
Tbilisi, 0175, Georgia
www.NanoStudies.org

E-mail: **chkharti2003@yahoo.com**
Phone: **995 322 37 19 42**
Mobile: **995 599 34 07 36**

Publishing House **Nekeri**

ISSN 1987 – 8826

CONTENTS

Proceedings of the 3rd International Conference
"Nanotechnologies" (October 20 – 24, 2014, Tbilisi, Georgia)

Regular Papers

Science History Pages

Chronicle

THE INNOVATIVE CONCRETE NANOTECHNOLOGY IN GEORGIA

R. Skhvitaridze [1], B. Keshelava [1], I. Giorgadze [1],
G. Tsintskaladze [2], Sh. Verulava [1]

[1] Scientific Center "Nanodughabi'
Georgian Technical University
Tbilisi, Georgia
rajden.skhvitaridze@gmail.com
[2] P. Melikishvili Institute of Physical and Organic Chemistry
I. Javakjishvili Tbilisi State University
Tbilisi, Georgia

Accepted May 2, 2014

It has already been reported about the possibility of enlarging of cement production with active mineral additives. It was shown that joint thermal treatment of active mineral additives increases strength of the cement [1].

As is known, the properties of the concrete, besides other factors, depend on the activity of the mineral additives that are inserted into the cement [2].

The practice has shown, that in some cases high class high performance concretes are very brittle and are sensitive to variable thermal and mechanic influences. Therefore more frequent reinforcement of structures made of this concrete becomes necessary. Thus deficit and expensive steel reinforcement charges increase and construction prime price goes up.

In 21st c., concrete remains as main and most important building material. Therefore it is necessary the studying its disatvanges and to searching for their elimination methods.

From the concrete anisotropy arises its is almost brittleness, what is a global problem.

Concrete compressive strength is about 10-times higher than its bending strength and 20-times higher than tensile strength. Concrete is the artificial stone, which with its structure and genesis is similar to natural stones of the sedimentation origin.

Anisotrophy affects mechanical strength of rocks of sedimenation origin too. But in the structure of a natural stone practically there are no open pores and hollows, therefore its mechanical strength is higher than that of concrete.

Concrete mechanical strength anisotropy decreases the buildings durability and seismic resistance.

To eliminate concrete stone anisotropy, it must be reinforced. Practically the most widespread reinforcement methods are ordinary- and pre-stressing using concrete reinforcement by periodically profiled steel or wire net.

In the 50s of the 20th c., in different countries began so-called "dispersed reinforcing" of concrete using fibers of different origin. Generally, the "dispersed reinforcing" means reinforcing by bars prepared from any material uniformly distributed in the concrete volume

with length less than 55 mm. Sometimes, such method is called as 3D-reinforcing or reinforcing of the whole volume. However, it does not give provide full guarantee to eliminate concrete anisotropy and reinforcing of the whole volume of the concrete. Because of this, we tried to realize the following.

- Modification of concrete structure using innovation methods of dispersed reinforcing, which means independent 3D dispersed and nano-reinforcing using as a fiber 3 – 200 nm zeolite thread and needle like crystals, for example clinoptilolite and natrolite (**Figure 1**).

Figure 1. Natrolite.

- According to Ref. [3], during the hydration of cement entered in AFt phase with the size of 40 – 90 nm using new formations as crystal rudiment, when for example newly formed thread and ettringite needle like crystals (**Figure 2**) and zeolite's or natrolite's crystal hydrate, independent nano or zeonano reinforcings take place. After this, there are formed for example clusters of natrolite and ettringite – zeoettringite, probably, with the chemical formula $Na_2O \cdot 2Al_2O_3 \cdot 3SiO_2 \cdot 6CaO \cdot 3SO_3 \cdot 34H_2O$.

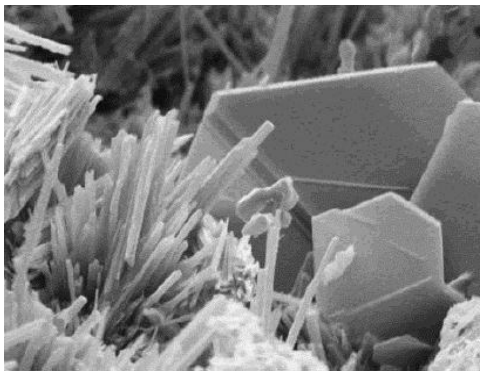

Figure 2. Ettringite.

In the presented work, cements were obtained with the clinker produced by Heidelberg Cement's Kaspi Cement Plant and Tedzami's zeolite tuff. Before inserting into the cement mixture additives subjected to thermal treatment at the temperature 100 – 700 °C. Data, testifying active mineral additives thermal treatment positive influence on the strength of the cement and concrete see in **Table 1**.

Table 1. Properties of Portland cement with the zeolite tuff.

Cement composition	Water demand, %	Ssetting times, min		Compressive strength (2 days), MPa	Compressive strength (7 days), MPa	Compressive strength, (28 days), MPa
Comparable Clinker 95 % + Gypsum 5 %	95	1:35	2:40	30.7	39.8	50.8
Clinker 90 % + Zeolite Tuff 5 % + Gypsum 5 %	105	1:35	2:25	26.5	37.1	52.3
Clinker 90 % + Zeolite Tuff (thermally treated at 700 °C) 5 % + Gypsum 5 %	96	1:20	2:10	32.3	42.4	55.5

Figure 3 shows results of the XRD analysis of the active mineral additive – zeolite tuff, thermally treated at 100 – 700 °C.

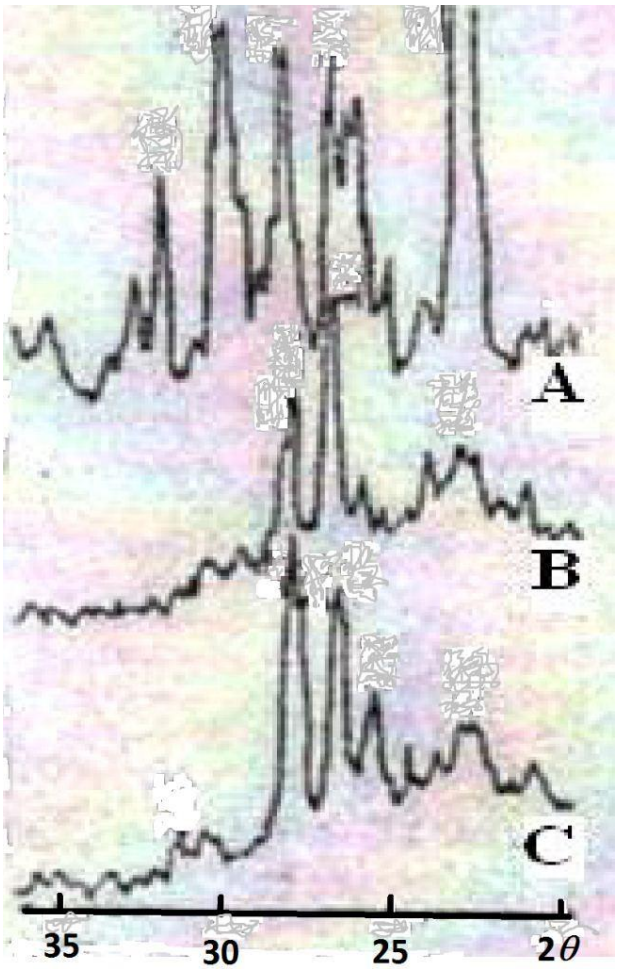

Figure 3. XRD analysis of zeolite tuff.

Interesting results were obtained by studying the physical-mechanical properties of cement based on Portland cement with thermally treated mineral additives (**Figure 4**). Inserting of zeolite tuff in cement–concrete mixture decreases concrete anisotropy because compressive strength increases by 43 %, bending strength by 35 % and strength on split by 44 %.

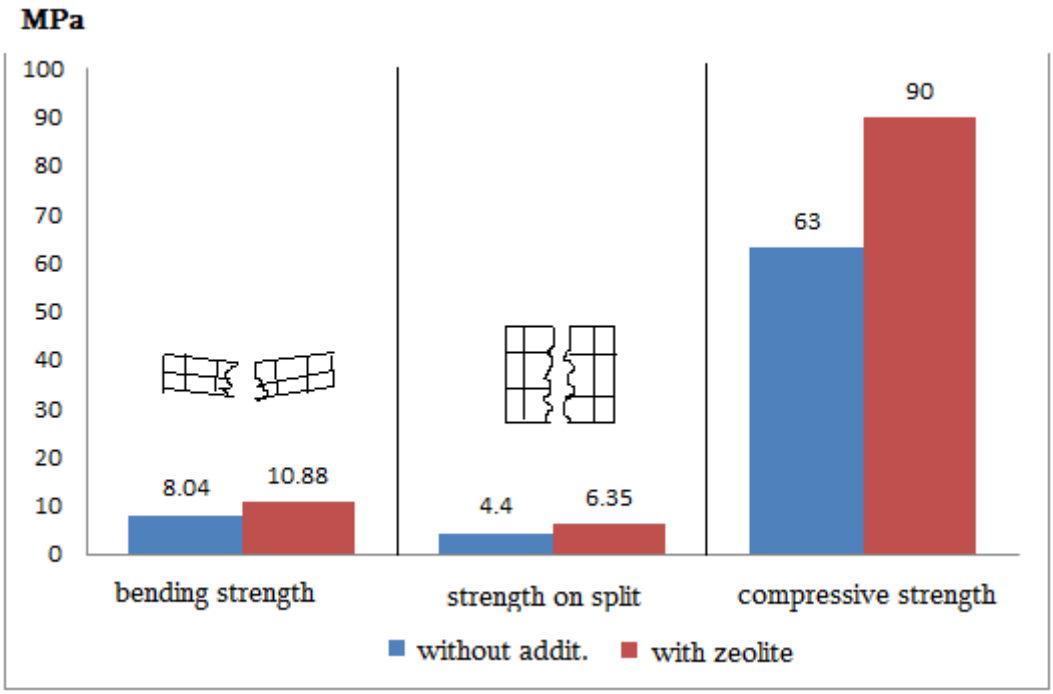

Figure 4. Cement's physical-mechanical properties.

The main factor of the active mineral additive is mineralogical composition thermally treated before crystallization or till full dehydration, which increases activity of mineral additives.

Inserting of thermal treated mineral additive – zeolite tuff ($Al_2O_3 \cdot 2SiO_2$ in the cement mixture and clinker minerals react at the nano level and product is ettringite, probably, with the chemical formula $3CaO \cdot Al_2O_3 \cdot 3CaSO_4 \cdot 32H_2O$) increases activity, compressive and flexural strength of concrete.

Our opinion is that, increasing of concrete compressive strength with the thermal treatment of mineral additive caused by the presence of active silica SiO_2 and alumina Al_2O_3 in mineral additives, which help in formation of additional crystal-hydrates containiong AFt phases together with fresh ettringite on the nano-level.

References

1. R. Skhvitaridze. Chemical and technological foundations of development of clay shale containing cements production in Georgia. Ceramics, 2003, 2 (10), 17-23.
2. R. Skhvitaridze, B. Keshelava, I. Giorgadze, G. Tatarashvili. Using of cements modified at the nanolevel by mineral additives. In: Proc. 12th Int. Conf. Mech. Technol. Composite Mater. 2009, Varna, 126-129.
3. W. Jia. Investigation of structure and properties of the interacial zone between lime aggregate and cement paste. J .Chin. Silic. Soc., 1987, 2, 114-121.

Посвящается светлой памяти
члена-корресподента АН Грузии, профессора
Арсена Ерастовича Швелашвили

СТРУКТУРНЫЕ ОСОБЕННОСТИ КООРДИНАЦИОННЫХ СОЕДИНЕНИЙ НЕКОТОРЫХ МЕТАЛЛОВ С СУЛЬФАНИЛАМИДНЫМИ ПРЕПАРАТАМИ

Э. Б. Миминошвили [1], Л. А. Беридзе [2]

[1] Грузинский технический университет
Тбилиси, Грузия
mimino@gtu.ge
[2] Тбилисский государственный медицинский университет
Тбилиси, Грузия
beridze_lali@mail.ru

Принята 27 мая 2014 года

В работе представлены результаты исследований биологически активных сульфаниламидсодержащих координационных соединений, начатых под руководством члена-корреспондента академии наук Грузии Арсена Швелашвили. Для выводов использованы как ранние работы с соавторством Арсена Швелашвили, так и оставленные им материалы в виде рукописей [1 – 8].

Введение

Из известных сегодня лекарственных веществ для многих не до конца и не в совершенстве изучены механизмы их действия и превращений в организме. Для установления на молекулярном уровне возможных изменений, необходима информация не только об элементном составе химических соединений, но и об их структуре, т.е. знание пространственного расположения атомов в молекулах (ионах), из которых построены кристаллы лекарственных препаратов. Без последней информации невозможно выявление механизма их превращений. Знание точной пространственной структуры лекарственных веществ важно, прежде всего, для понимания механизма взаимодействия лекарственных средств с макромолекулами ферментов, белковых гормонов, рецепторов и т.д. Это, в свою очередь, может служить основой для создания лекарственных препаратов нового поколения, молекулы (ионы) которых будут определенным образом, более активно воздействовать на функцию некоторых ферментов или рецепторов.

Целью настоящей работы является осуществление сравнительной характеристики структур, изученных нами сульфаниламидсодержащих соединений, выявление различий в составе их структурных элементов и значительных изменений в характеризующих строение геометрических параметрах.

Сульфаниламиды как составом и свойствами, так и значениями геометрических параметров структур близки друг к другу. Одновременно, в стереохимическом отношении, сульфаниламид – анионы, имеющие донорные атомы N, O, S, могут выступать в роли как мостикового, так и бидентатно-циклического лиганда. Они всегда содержат сульфамидную (сульфонамидную) группу $–SO_2–NHR$ и R-радикал имеет гетероциклическую природу (R = пиродиновый, пиридазиновый и другие гетероциклы). При их замене карбоксамидной или нитрильной группами теряют антибиотические свойства. Установлено, что находящаяся в *пара*-положении аминогруппа должна быть незамещенной, а в бензольном кольце нельзя внести дополнительных заместителей, так как они уменьшают антибактериальную активность. В зависимости от природы радикала получаются соответствующие препараты: этазол (Aet), сульфадиметоксин (F), сульфадимезин (S), сульфапиридазин (R), норсульфазол (L) и др. Антибактериальное действие сульфаниламидов связано с тем, что они являются антиметаболитами *пара*-аминобензойной кислоты (**Рисунок 1а**), из-за структурного сходства последней с амидом сульфаниловой кислоты (**Рисунок 1б**); *пара*-аминобензойная кислота участвует в образовании микробами необходимой для их развития фолиевой кислоты [9 – 10].

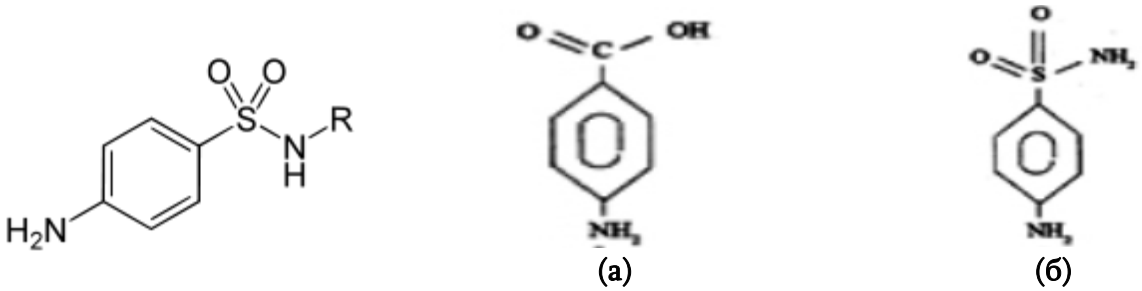

(а) (б)

Рисунок 1.

Из оставленных работ Арсена Ерастовича Швелашвили следует, что в структурноисследованных соединениях действием объемных внешнесферных анионов происходит дестабилизация энергии связи координированных атомов с комплексообразователем на 20 – 25 %. Установлен следующий ряд влияния гетероциклов на σ -донорные свойства атомов: норсульфазол (R = тиазол) < сульфадиметоксин (R = 2,6-диметоксипиримидин) < сульфадимезин (R = 4,6-диметоксипиримидин) ~ сульфапиридазин (R =3-метоксипиридазин). На основе изучения прямым методом (рентгеноструктурным аннализом) строения этазолсодержащих координационных соединений (R = 5-этил-1,3,4-тиадиазол) отвергнуто соображение о координации этазола третичным атомом азота; вместе с этим экспериментальные данные дали основу для предположения, что этазолсодержащее координационное соединение магния является эффективным противовоспалительным средством. В эксперименте, во время модельного стафилококового сепсиса сульфаниламидсодержащие координационные соединения биометаллов (II) проявляли бактериостатические свойства.

В изученных нами и описанных в литературе кристаллических соединениях сульфаниламиды в депротонированном виде являются внешнесферными ацидо-анионами (протон отщепляется от N–H и получается соответствующий анион) и исключительно редко участвуют в образовании координационной связи. Объяснение полученных результатов стерическим эффектом (объемом предполагаемого лиганда), дает право

ожидать, что при их участии в комлексообразовании должны образоваться только *транс*-формы полиэдров.

Некоторые кристаллографические данные соединений

Экспериментальные данные получены в одинаковых условиях на автоматическом дифрактометре. Структуры определены прямым методом и уточнены МНК в изотропном приближении для атомов водорода и анизотропном для остальных атомов. В расчетах использован комплекс программ SHELXTL [11].

I. $F = C_{12}H_{14}N_4O_4S$

Формульный вес M_r = 310.334; симметрия триклинная; a = 7.961(2), b = 9.322(2); c = 10.425(2) Å; α = 93.48(3), β = 95.39(3), γ = 114,09(3) °; T = 293 K, пр. гр. P-1, Z = 2; $\rho_{выч}$ = 1.475 г / см^3; μ (Cu Kα) = 2.979 см$^{-1}$; окончательное значение R-фактора 0.050. Съемку кристаллов проводили на автоматическом дифрактометре Nicolet P3 по стандартной методике (λ Cu Kα 1.54180 Å, метод съемки $\theta/2\theta$-сканирование) [12].

II. $MgF_2 \cdot 11H_2O$

Валовый состав $C_{24}H_{48}N_8O_{19}S_2Mg$; формульный вес M_r = 841.125; симметрия моноклинная; a = 19.753(4), b = 34.031(7), c = 13.859(3) Å; β = 125.37(3) °, V = 7597(3) Å^3; T = 293 K, пр. гр. $C2/c$, Z = 8; $\rho_{выч.}$ = 1.48 г / см^3; μ (Cu Kα) = 2.169 мм$^{-1}$, окончательное значение R-фактора 0.042. Набор экспериментальных данных получен на автоматическом дифрактометре Nicolet P3 (λ Cu Kα, метод съемки $\theta/2\theta$-сканирование) [13, 14].

III. $Mn(Aet)_2 \cdot 11H_2O$

Валовый состав $C_{20}H_{44}N_8O_{15}S_4Mn$; формульный вес M_r = 819.809; симметрия моноклинная; a = 17.160(2), b = 14.115(1), c = 15.130(2) Å; β = 98.23(3) °; V = 3626.9(7) Å^3; T = 293 K, пр. гр. $P2_1/n$, Z = 4; $\rho_{выч.}$ = 1.51 г / см^3; μ (Cu Kα) = 6.01 см$^{-1}$; окончательное значение R-фактора 0.045. Набор экспериментальных данных получен на автоматическом дифрактометре SYNTEX P–1 (λ Mo Kα 0/71069 Å, графитовый монохроматор, метод съемки $\theta/2\theta$ - сканирование) [15].

IV. $Cuen_2(Aet)_2 \cdot 2H_2O$

Валовый состав $C_{24}H_{42}N_{12}O_6S_4Cu$; формульный вес M_r = 786.485; симметрия моноклинная; a = 17.065(4), b = 9.875(3), c = 10,580(2) Å; β = 108,37(2) °; V = 1692.1(5) Å^3; T = 293 K, пр. гр. $P2_1/a$, Z = 2; $\rho_{выч.}$ = 1.55 г / см^3; окончательное значение R-фактора 0.060; набор экспериментальных данных получен на автоматическом дифрактометре SYNTEX P–1 (λ Mo Kα, графитовый монохроматор, метод съемки $\theta/2\theta$-сканирование) [16, 17].

V. $Cuen_2S_2 \cdot 2H_2O$

Валовый состав $C_{26}H_{46}N_{12}O_6S_4Cu$; формульный вес M_r = 814.539; симметрия ромбическая; a = 26.992(5), b = 6.669(1), c = 20.331(4) Å; V = 3659.2(8) Å^3; T = 293 K; пр. гр. $Pca2_1$, Z = 4; $\rho_{выч.}$ = 1.48 г / см^3; окончательное значение R-фактора 0.052; набор экспериментальных данных получен на автоматическом дифрактометре SYNTEX P–1 (λ Mo Kα, графитовый монохроматор, метод съемки $\theta/2\theta$-сканирование) [18].

VI. $Nien_3F_2$

Валовый состав $C_{30}H_{50}N_{14}O_8S_2Ni$; формульный вес M_r = 857.642; симметрия триклинная; a = 13.562(4), b = 13.462(5), c = 13.19(5) Å; α = 80.77(3), β = 115.02(2), γ = 110.78(3) °; V = 2040(1) Å^3; T = 293 K; пр. гр. P-1; Z = 2; $\rho_{выч}$ = 1.40 г / см^3, μ (Cu Kα) = 6.25 см$^{-1}$; окончательное значение R-фактора 0.043. Съемку кристаллов

проводили на автоматическом дифрактометре Nicolet P3 по стандартной методике (λ Cu Kα, метод съемки $\theta/2\theta$-сканирование) [19].

VII. $Sr(Aet)_2 \cdot 8H_2O$

Валовый состав $C_{20}H_{38}N_8O_{12}S_4Sr$; формульный вес M_r = 798.4; симметрия моноклинная; a = 10.390(2), b = 14.609(3), c = 21.931(5) Å; β = 92,42(2) °; V = 3326(1) Å^3; T = 293 K, пр. гр. $P2_1/c$; Z = 4; $\rho_{выч.}$ = 1.59 г / см^3, μ(Mo Kα) = 19.69 см$^{-1}$; окончательное значение R-фактора 0.041; набор экспериментальных данных получен на автоматическом дифрактометре SYNTEX P–1 (λ Mo Kα, графитовый монохроматор, метод съемки $\theta/2\theta$ -сканирование) [20, 21].

VIII. $Ba(Aet)_2 \cdot 7H_2O$

Валовый состав $C_{40}H_{72}Ba_2N_{16}O_{22}S_8$; формульный вес M_r = 1660.3; симметрия моноклинная; a = 9.793(2), b = 15.408(3), c = 22.553(6) Å; β = 94.98(2) °; V = 3390(1) Å^3; T = 293 K, пр. гр. $P2_1/c$; Z = 2, $\rho_{выч.}$ = 1.63 г / см^3, μ(Mo Kα) = 1.48 мм$^{-1}$; окончательное значение R-фактора 0.047; набор экспериментальных данных получен при комнатной температуре на автоматическом дифрактометре SYNTEX P–1 (λ Mo Kα, графитовый монохроматор, метод съемки $\theta/2\theta$-сканирование) [22].

IX. $NiR_2 \cdot 2H_2O$

Валовый состав $C_{22}H_{26}N_8O_8S_2Ni$; формульный вес M_r = 653.323; симметрия моноклинная; a = 20.116(3), b = 8,221(2), c = 16.923(4) Å; β = 75.19(5) °; V = 2705.6(7) Å^3; T = 293 K; пр. гр. $C2/c$; Z = 4; $\rho_{выч.}$ = 1.61 г / см^3; μ(Cu Kα) = 36.80 см$^{-1}$. Набор экспериментальных данных получен на автоматическом дифрактометре SYNTEX P–1 (λ Cu Kα – 1.54180 Å, графитовый монохроматор, метод съемки $\theta/2\theta$-сканирование) [23].

Структурные типы и единицы

Все изученные соединения кроме первого и девятого ионные и относятся к структурам ионно-островного, а первый и девятый – молекулярно-островного типа. Несмотря на это они различаются составом структурных единиц (кристаллографически независимых) и по этому признаку их можно распределить в группы:

1. F = $C_{12}H_{14}N_4O_4S$

В соединении структурной единицей является молекула сульфодиметоксина (4-аминобензолсульфамидо-2,6- иметоксипиримидин).

2. $M(A)_2 \cdot 11H_2O$

Структурная формула $[M(OH_2)_6](A)_2 \cdot 5H_2O$, где M(II) = Mg и Mn. A = F ($(F)^-$ – анион сульфодиметоксина) и Aet ($(Aet)^-$ – анион этазола, 2-(пара-аминобензолсульфамидо-5-этил-1,3,4-тиадиазола). Структурная единица состоит из гекса-аквакомплексного катиона $[M(OH_2)_6]^{2+}$, двух анионов $(F)^-$ и $(Aet)^-$ и пяти молекул воды. В соединении $Mn_{0,5}Mg_{0,5}(Aet)_2 \cdot 11H_2O$ металлы Mg(II) и Mn(II) статистически замещают друг друга, образуя непрерывный ряд твердых растворов.

3. $Cuen_2(Aet)_2 \cdot 2H_2O$

Структурная формула $[Cuen_2(OH_2)_2](Aet)_2$ (где en – молекула этилендиамина $H_2N–CH_2–CH_2–NH_2$, $(Aet)^-$ – анион этазола). Структурная единица состоит из катиона $[Cuen_2(OH_2)_2]^{2+}$ и двух анионов $(Aet)^-$.

4. $Cuen_2S_2 \cdot 2H_2O$

Структурная формула $[Cuen_2(OH_2)]S_2{\cdot}H_2O$ (где en – молекула этилендиамина $H_2N–CH_2–CH_2–NH_2$, $S^-C_{12}H_{13}N_4O_2S$ – анион сульфадимезина, 4-амино–N-(4,6-диметил-2-пиримидинил)бензолсульфонамид). Структурная единица состоит из катиона $[Cuen_2(OH_2)]^{2+}$, двух анионов $(S)^-$ и одной молекулы воды.

5. $Nien_3F_2^-$

Структурная формула $[Nien_3]F_2$ (где en – молекула этилендиамина, $(F)^-$ – анион сульфодиметоксина). Структурная единица состоит из катиона $[Nien_3]^{2+}$, двух анионов $(F)^-$.

6. $M(Aet)_2{\cdot}nH_2O$

Структурная формула $[M(Aet)(OH_2)_5](Aet){\cdot}kH_2O$ (где M(II) = Sr и Ba, k = 3 и 2 (соответственно, $(Aet)^-$ – анион этазола). Структурная единица состоит из катиона $[M(Aet)(OH_2)_5]^+$, аниона $(Aet)^-$ и 3 или 2 молекул воды.

7. $NiR_2{\cdot}2H_2O$

В соединении структурной единицей является комплексная молекула $[Ni(R)_2(OH_2)_2]$ ($(R)^-–C_{11}H_{11}N_4O_3S$, анион сульфапиридазина, 6-(п-аминобензолсульфамидо)-3-метоксипиридазин).

Строение некоторых исходных компонентов: молекул этилендиамина и сульфадимезина, а также анионов этазола и сульфапиридазина

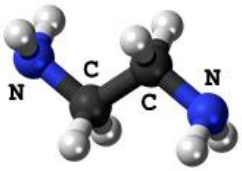

en – молекула этилендиамина ($H_2N–CH_2–CH_2–NH_2$)

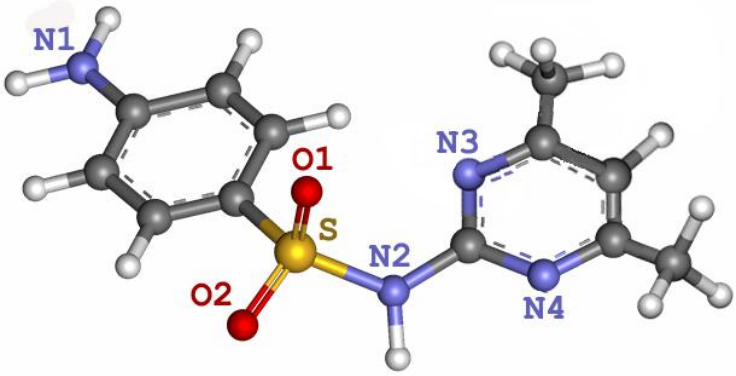

S – молекула сульфадимезина.

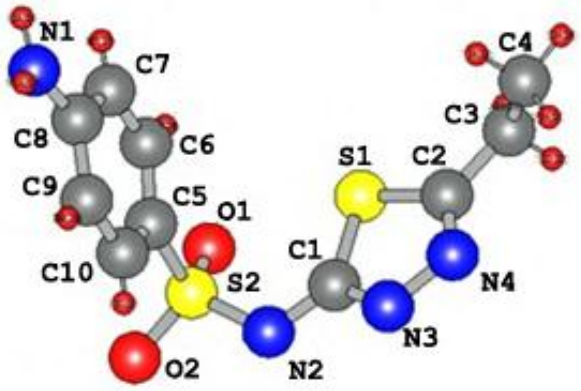

Aet – анион этазола.

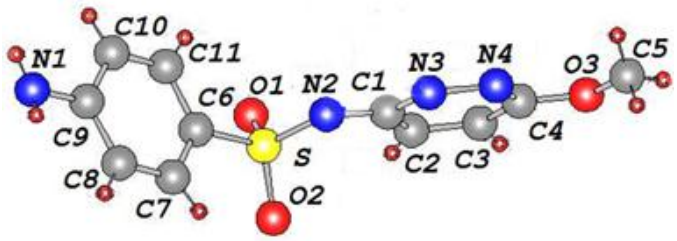

R – анион сульфапиридазина.

Строение и состав структурных единиц

1. В соединении структурной единицей является молекула сульфодиметоксина (4-аминобензолсульфонамидо-2,6-диметоксипиримидина). Структура расшифрована с удовлетворительной точностью и локализованы все – как средней тяжести, так и легкие атомы. Строение молекулы представлено на **Рисунке 2**.

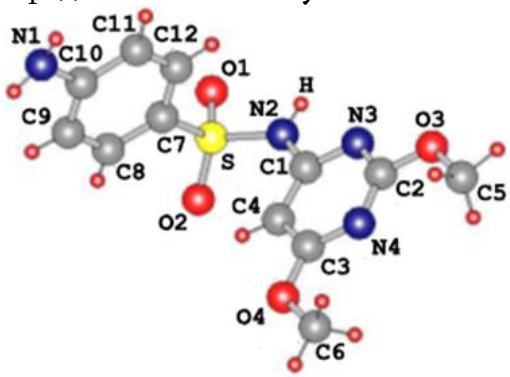

Рисунок 2. F – молекула сульфодиметоксина

2. Структуры с общей формулой $[M(OH_2)_6](A)_2{\cdot}5H_2O$ (где M(II) = Mg и Mn. A = F – сульфодиметоксин и Aet – этазол) являются ионными. В $[M(OH_2)_6]^{2+}$ – гексааквакомплексах длины M–O связей, а также соответствующие углы находятся в пределах, принятых для октаэдрических конфигурации этих металлов. Изучено также этазолсодержащее соединение $[M(OH_2)_6](Aet)_2{\cdot}5H_2O$ ($M = Mn_{0.5}Mg_{0.5}$) и установлено, что в нем ионы Mg(II) и Mn(II) статистически замещают друг друга, образуя непрерывный ряд твердых растворов. Анионы сульфодиметоксина и этазола получены депротонированием иминогруппы (на **рисунке 2** N(2)H в любом анионе) и расположены вне координационной сферы. Гексааквакомплексный катион $[M(OH_2)_6]^{2+}$ проедставлен на **Рисунке 3а**.

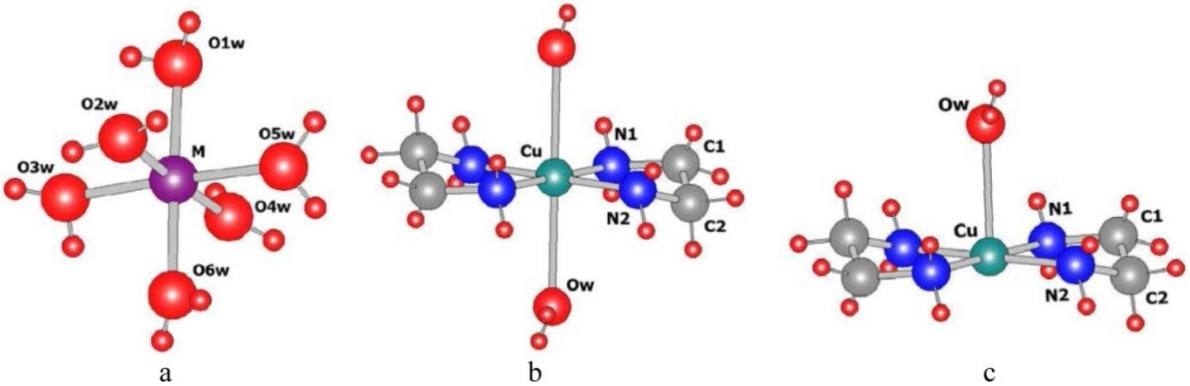

a b c

Рисунок 3. (a) гекса-аквакомплексный катион $[M(OH_2)_6]^{2+}$, комплексные катионы (b) $[Cuen_2(OH_2)_2]^{2+}$ и (c) $[Cuen_2OH_2]^{2+}$.

3. Соединение $Cuen_2(Aet)_2{\cdot}2H_2O$ построен из $[Cuen_2(OH_2)_2]^{2+}$ центросимметричных катионов с конфигурацией тетрагональной бипирамиды. В комплексном катионе две молекулы этилендиамина (en = $H_2N–CH_2–CH_2–NH_2$) координированы обоими атомами азота, выполняют роль бидентатного лиганда, образующего пятичленный цикл и расположены в экваториальной плоскости, с *транс*-позицией (**Рисунок 3б**). Заполнение полиэдра меди до шести осуществляется двумя молекулами воды, соединенными центром симметрии. Анионы этазола получены депротонированием иминогруппы и расположены вне координационной сферы.

4. У соединения $Cuen_2S_2{\cdot}2H_2O$, несмотря на сходство его состава с предыдущим соединением, структура совершенно иная. Координационный полиэдр меди является тетрагональной пирамидой. В комплексном катионе $[Cuen_2OH_2]^{2+}$ две молекулы этилендиамина, аналогично предыдущего соединения, координируются обоими атомами азота и являются бидентатными, образующими пятичленные циклы, лигандами. Они расположены в основе пирамиды. Заполнение координационного числа до пяти осуществляется одной молекулой воды (**Рисунок 3с**). Анионы сульфодимезина получены депротонированием иминогруппы и расположены вне координационной сферы.

5. В отличие от двух предыдущих соединений, в $Nien_3F_2$ молекулы воды замещены третьей молекулой этилендиамина и образован комплексный катион $[Nien_3]^{2+}$ (**Рисунок 4**). Анионы сульфодиметоксина получены депротонированием иминогруппы и расположены вне координационной сферы.

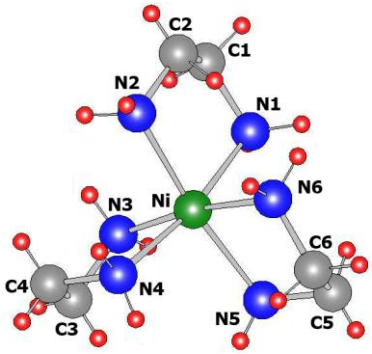

Рисунок 4. Комплексный катион $[Nien_3]^{2+}$ю

6. В группе соединений с структурной формулой $[M(Aet)(OH_2)_5](Aet){\cdot}kH_2O$ (где M(II) = Sr и Ba, k = 3 и 2 соответственно) анионы этазола образованы депротонированием –NH– группы. Один из них (I) – внешнесферный анион, другой (II) координирован к иону металла (Sr^{2+} и Ba^{2+}) N(21) и O(21) атомами, выполняя роль мостикового бидентатно циклического лиганда (**Рисунок 5**, в нумерациях атомов 1 указывает на порядковый номер атома в ионе, 2 – порядковый номер иона этазола).

Координационное число Sr(II) равно восьми: пять мест занимают молекулы воды, два – атомы N(21) и O(21) аниона этазола, а дополнение координационного числа до восьми осуществляется атомом $O(21)^i$, связанным центром симметрии с O(21) атомом лиганда соседнего комплекса. Атомы O(21) и $O(21)^i$ выполняют роль мостиков между двумя атомами стронция, связанными тем же центром симметрии, т.е. получается центросимметричный димерный катион $[(H_2O)_5Sr(Aet)_2Sr(OH_2)_5]^{2+}$.

Наряду с увеличением ионного радиуса по сравнению Sr(II) координационное число Ba(II) увеличивается до девяти. В координационной сфере четыре позиции, с

монодентатной функцией, занимают атомы кислорода молекул воды. Следующие четыре места, с бидентатно-мостиковой функцией, заняты атомами кислорода SO_2 группировок координированного иона этазола и молекул воды. O(1), O(1)^{i} – атомы кислорода ионов этазола. Атомы кислорода молекул воды O(2w) и O(2w)^{i} (**Рисунок 6**, атомы O(2w) и O(2w)^{i} указаны курсорами) в отличие от соединения Sr(II), в соединении Ba(II) выполняют бидентатно-мостиковой функцию (они также связаны между собой центром симметрии). Заполнение координационного числа до девяти осуществляется атомом азота N(2) того же иона этазола. Мост, образованный кислородными атомами между связанными тем же центром симметрии Ba(II)–Ba(II)^{i} ионами, способствует получению центросимметричного димерного катиона, структурная формула которого $[(H_2O)_4Ba(OH_2)(Aet)_2(H_2O)Ba(OH_2)_4]^{2+}$ (следовательно, несмотря на одинаковый состав, структурная формула комплексного катиона Ba(II) отличается от формулы комплексного катиона Sr(II) $[(H_2O)_5Sr(Aet)_2Sr(OH_2)_5]^{2+}$).

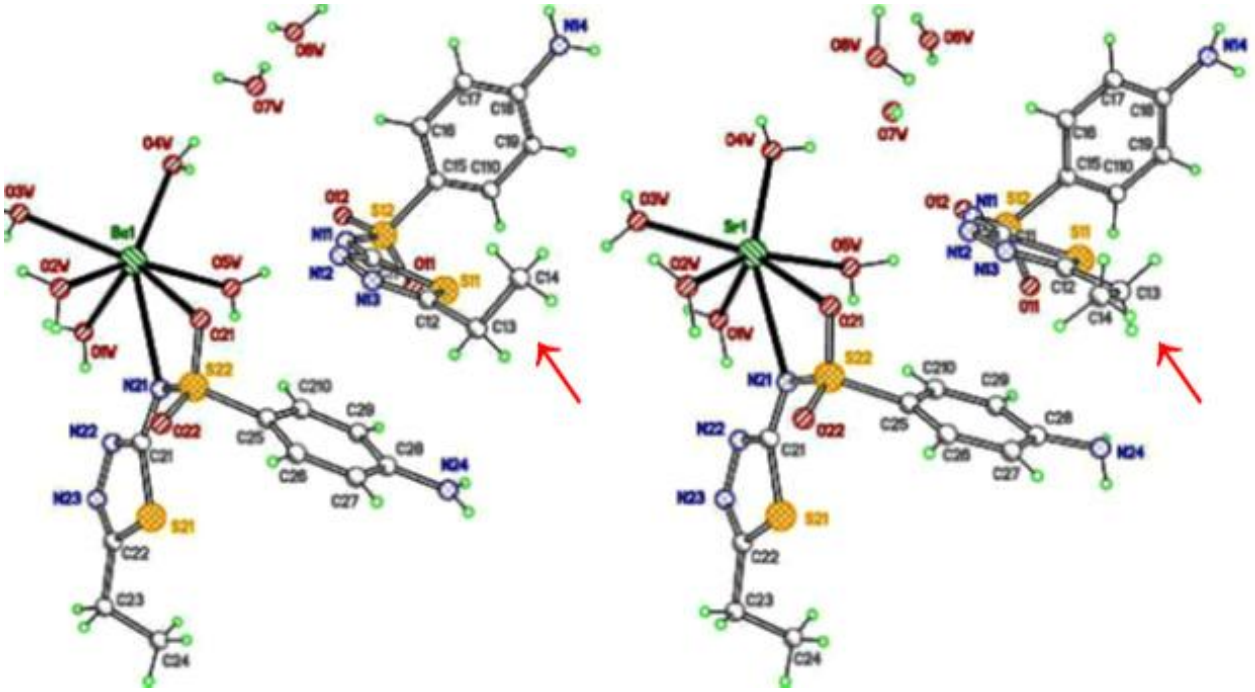

Рисунок 5. Проекция фрагментов структур Sr и Ba на кристаллографической плоскости (100).

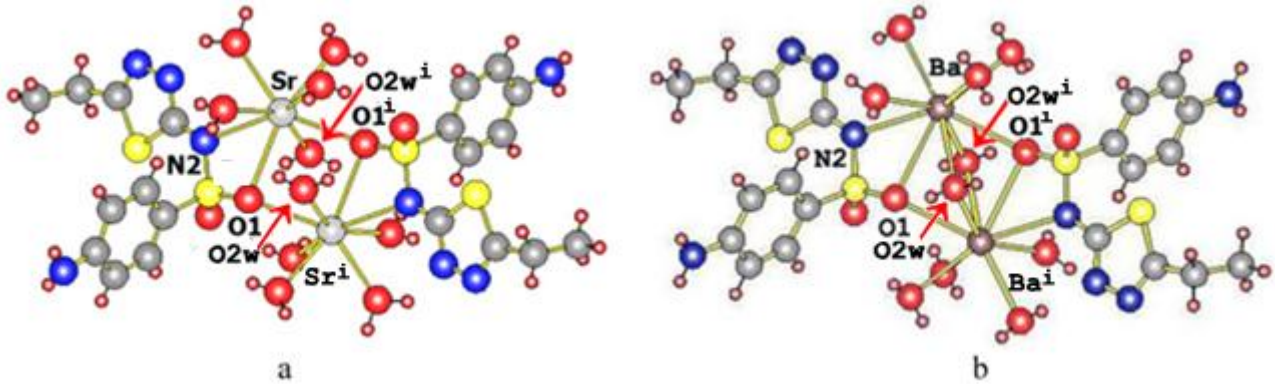

Рисунок 6. Катионы (a) $[(H_2O)_5Sr(Aet)_2Sr(OH_2)_5]^{2+}$ и (b) $[(H_2O)_4Ba(OH_2)(Aet)_2(H_2O)Ba(OH_2)_4]^{2+}$.

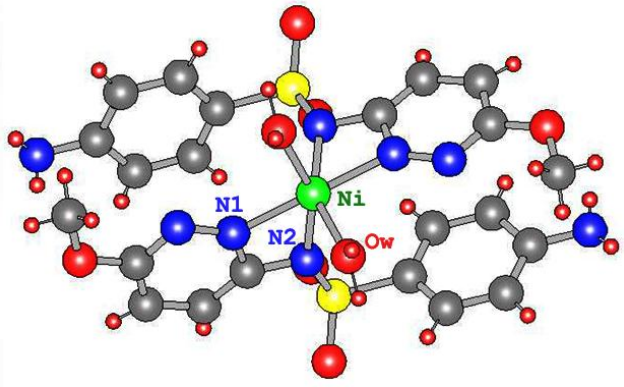

Рисунок 7. Комплексная молекула $[Ni(R)_2(OH_2)_2]$.

7. $NiR_2{\cdot}2H_2O$ – в исследуемом соединении структурной единицей является комплексная молекула $[Ni(R)_2(OH_2)_2]$ (**Рисунок 7**). Координационное число Ni(II) равно шести. Так как атом никеля находится на оси симметрии второго порядка, полиэдр получается с помощью трех независимых атомов. Две из них, атомы азота (N(1) и N(2)), принадлежат аниону сульфапиридазина (в соединении $[Sr(Aet)(OH_2)_5](Aet){\cdot}3H_2O$ координация с атомом металла осуществляется атомами N(1) и O(1) аниона этазола) и одним атомом кислорода молекулы воды (O(w)).

Краткое описание и характеристика структур

На основе литературных источников установлено, что для сульфаниламидов допустимы, в зависимости от условий, как протонирование, так и депротонирование. Однако в работах, рассмотренных в статье, ни в одном случае не замечено протонирование сульфаниламидов. Как в изученных нами, так и в литературе описанных кристаллических соединениях с металлами малых ионных радиусов (M(II) = Mg, Mn, Co, Ni, Cu, Zn) сульфаниламиды выполняют функцию внешнесферного ацидо-аниона и несмотря на наличие донорных N, O, S атомов, не участвуют в образовании координационной связи. Действительно, в описанных соединениях II–VI сульфаниламиды являются внешнесферными ацидо-анионами, а комплексные катионы получаются молекулами воды или этилендиамина. Во всех случаях этилендиамин координируется обоими атомами азота и является бидентатным, образующим пятичленный цикл, лигандом с характерным для него *гош*-конформацией. Известно, что из-за ярко выраженного эффекта Яна–Теллера стереохимия Cu(II) по сравнении со стереохимией других элементов более сложная и для полиэдров соединений IV и V получаются, соответственно, тетрагонально-бипирамидальная (4 + 2) и тетрагонально-пирамидальная (4 + 1) кофигураций.

Результаты анализа строения комплексного катиона $[Nien_3]^{2+}$ указывают на реализацию высокоэнергетической конформационной формы λλλ, что можно объяснить образованием водородных связей между катионами и анионами. Анализ строения комплексного катиона не указывает на какую-нибудь обращающее внимание особенность в его геометрии.

Таблица 1. Некоторые геометрические параметры сульфаниламидов: длины (Å) и углы (°).

№	S–O	S–N	S–C	C–S–N	O–S–O	O–S–N	C–S–O	Φ	Θ
I	1.419(3) 1.436(3)	1.638(3)	1.746(3)	106.7(2)	117.8(1)	109.1(2) 103.3(2)	108.4(2) 110.9(1)	58.8	77.6
II	1.457(3) 1.441(3) 1.448(4) 1.462(4)	1.571(3) 1.577(4)	1.760(4) 1.770(5)	107.0(2) 108.7(2)	114.4(2) 114.7(2)	114.9(2) 115.2(2) 105.5(2) 104.9(2)	107.5(2) 107.0(2) 106.3(2) 106.7(2)	62.7 68.5	102.1 91.7
III	1.444(3) 1.447(3) 1.457(2) 1.457(3)	1.586(3) 1.578(3)	1.752(3) 1.745(3)	108.0(3) 108.0(2)	114.7(4) 114.3(3)	113.5(3) 105.6(2) 112.6(3) 105.5(3)	106.4(3) 108.3(3) 109.1(3) 107.2(3)	66.5 61.8	91.3 91.7
IV	1.452 1.445	1.590	1.775	105.56	116.46	105.68 113.44	109.04 106.12	67.2	99.8
V	1.445 1.438 1.466 1.421	1.587 1.573	1.772 1.770	108.6 107.7	117.7 113.6	112.9 103.7 116.3 105.3	107.7 106.9 105.7 107.9	60.0 68.0	90.9 96.8
VI	1.461(3) 1.444(4) 1.440(4) 1.453(3)	1.570(3) 1.581(4)	1.766(5) 1.757(4)	108.7(2) 108.2(2)	113.7(2) 113.6(2)	105.4(2) 115.9(2) 104.8(2) 115.0(2)	105.7(2) 106.7(2) 108.0(2) 106.8(2)	65.3 68.0	84.8 89.9
VII	1.443(3) 1.440(4) 1.452(4) 1.457(3)	1.586(4) 1.588(4)	1.760(5) 1.752(4)	108.2(2) 110.4(2)	114.8(2) 114.7(2)	113.7(2) 113.4(2) 104.9(2) 103.1(2)	106.7(2) 108.0(2) 106.0(2) 108.9(2)	69.5 71.6	83.5 89.4
VIII	1.439(13) 1.449(14) 1.460(11) 1.450(9)	1.587(7) 1.580(6)	1,751(12) 1,706(9)	109.3(4) 109.0(4)	115.1(6) 115.7(6)	112.6(6) 103.2(8) 105.5(8) 113.9(6)	106.8(9) 107.3(6) 108.5(9) 106.2(7)	63.1 71.3	85.7 92.5
IX	1.465(4) 1.463(5)	1.658(4)	1,735(5)	101.3(2)	114.2(2)	107.1(2) 116.9(2)	108.7(3) 109.0(3)	**7.2**	89.1

В соединениях VII и VIII, где M(II) = Sr и Ba, комплексообразователи являются ионами металлов с большим радиусом. Наше соображение о возможности координации в таких системах оправдалось и из двух анионов этазола один оказался координированным. В обоих случаях (соединениях) координация осуществляется атомами кислорода и азота SO_2 и NH групп. Несмотря на данные рентгеноструктурного анализа, по которым они должны быть изоструктурный, эти соединения отличаются друг от друга как составом, так и строением. Их структурные формулы: $[Sr(Aet)(OH_2)_5](Aet)\cdot 3H_2O$ и $[Ba(Aet)(OH_2)_5](Aet)\cdot 2H_2O$. С первого взгляда они отличаются только количеством воды во внешней сфере (3 и 2 соответственно); причиной является различие в строении

находящегося во внешней сфере анионов этазола. Из проекций фрагментов структур Sr(II) и Ba(II) на кристаллографической плоскости (100) (**Рисунок 5**, курсоры) ясно показывают, что связь C13–C14 по разному ориентирована к пятичленному циклу S11C11N12N13C12. Если в соединении катионе Sr(II) связь C13–C14 находится в плоскости цикла, в соединении Ba(II) она перпендикулярна к плоскости; поэтому, число молекул растворителя в структуре с атомом Ba(II) соответствует доступной для растворителя пустоте – 54 $Å^3$, а в структуре с атомом Sr(II) – 58 $Å^3$. Разность составляет 4 кубических ангстрема. Различие в ионных радиусах Sr(II) и Ba(II) отражается в составе и строении катионов: $[(H_2O)_5Sr(Aet)_2Sr(OH_2)_5]^{2+}$ и $[(H_2O)_4Ba(OH_2)(Aet)_2(H_2O)Ba(OH_2)_4]^{2+}$, соответственно.

При координации с атомами металлов (II) – Mg, Mn, Co, Ni, Cu, Zn, в исключительных случаях, из-за стереофактора, логично получение *транс*-форм, однако для соединения IX получено противоположное; осевая симметрия второго порядка молекулы $[Ni(R)_2(OH_2)_2]$ (анионы сульфапиридазина и молекулы воды) указывает *цис*-октаэдрическую форму комплекса. Ясно, что в *цис*-позиций компоненты молекулярного комплекса из-за «объемной тесноты» более напряжены, чем находясь в *транс*-позиций. У нас нет обяснения факта образования данной структуры, но безусловно, что напряжение, возникнутое из-за *цис*-позиций анионов сульфапиридазина, деформация молекулы, отразится в изменений его геометрических параметров. В молекуле $[Ni(R)_2(OH_2)_2]$ два аниона сульфапиридазина координированы с ионом Ni^{2+} атомами азота имино группы и гетероцикла пиридазина (N(1) и N(2) на **Рисунке 7**), тогда как этазол с ионами Sr^{2+} и Ba^{2+} координирован атомами азота и кислорода NH и SO_2 групп (N(2) и O(1) на **Рисунке 6**).

В литературе притнято охарактеризовать геометрию сульфаниламидов не только длинами и углами валентных связей, но и CSNC торсионными (угол *гош*-конформации – Ф) и межциклическими (угол ванны – Θ) двухгранными углами. Некоторые параметры, характеризующие геометрию сульфаниламидов, приведены в **Таблице 1**.

Полученные данные свидетельствуют, что в сульфаниламидсодержащих структурах угол ванны Θ меняется в широком интервале 55 – 100 °, а угол *гош*-конформации Ф – 55 – 70 °. Исключением из этой закономерности оказалось соединение $[Ni(R)_2(OH_2)_2]$, для которого Ф = 7.2 °. Из-за наличия структурных аномалии в координационном соединении никеля(II), по нашему мнению, представляет интерес синтез никеля(II) с разными сульфаниламидами и исследование их физико-химических и биологических активностей.

Ссылки

1. А. Е. Швелашвили, К. Д. Амирханашвили, А. П. Богданов, В. В. Зеленцов. Сообщ. АН ГССР, 1984, 114, 2, 75-79.
2. А. Е. Швелашвили, К. Д. Амирханашвили, А. Н. Соболев, Э. Б. Миминошвили. Сообщ. АН ГССР, 1986, 121, 1, 85-86.
3. А. Е. Швелашвили, Э. Б. Миминошвили, Т. О. Вардосанидзе. В сб.: VI Всесоюзное совещание по кристаллохимии неорганических координационных соединений. 1992, Львов.
4. А. Е. Швелашвили, Э. Б. Миминошвили, В. К. Бельский. В сб.: Тезисы докладов Национальной кристаллохимической конференции. 1998, Черноголовка, 228-228.

5. М. Г. Цкитишвили, П. В. Гогоришвили, М. В. Чрелашвили, А. Е. Швелашвили. Изв. АН ГССР (Сер. хим.), 1979, 5, 1, 13-19.
6. М. Г. Цкитишвили, А. Е. Швелашвили, И. И. Микадзе, М. В. Чрелашвили, Н. Б. Жоржолиани. Изв. АН ГССР (Сер. хим.). 1981, 7, 3, 204-212.
7. М. Г. Цкитишвили, А. Е. Швелашвили, И. И. Микадзе, Н. Б. Жоржолиани, М. В. Чрелашвили. Изв. АН ГССР (Сер. хим.), 1981, 7, 4, 300-305.
8. А. Е. Швелашвили, М. Г. Цкитишвили, И. И. Микадзе, М. В. Чрелашвили, К. Д. Амирханашвили, Д. З. Каландаришвили. Изв. АН ГССР (Сер. хим.), 1986, 12, 1, 17-24.
9. М. Д. Машковский. Лекарственные средства, Том 2. 1988, Ташкент: Медицина, 273-297.
10. http://en.wikipedia.org/wiki/Sulfonamide_(medicine)
11. G. M. Sheldrik. SHELXTL. User Manual (Revision 4). 1983, Nicolet XRD Corporation.
12. Э. Б. Миминошвили, Д. А. Эдиберидзе, К. Э. Миминошвили, С. Р. Зазашвили. Georg. Eng. News, 2007, 1, 51-54.
13. A. Shvelashvili, M. Tskitishvili, M. Kvitsiani, E. B. Miminoshvili. Bull. Georg. Acad. Sci., 2001, 163, 1, 74-77.
14. E. B. Miminoshvili, K. E. Miminoshvili, L. A. Beridze. J. Struct. Chem., 2008, 49, 4, 762-765.
15. E. B. Miminoshvili, K. E. Miminoshvili, L. A. Beridze. J. Struct. Chem.,2009, 50, 1, 170-175.
16. К. Д. Амирханашвили, А. П. Богданов, В. В. Зеленцов, А. Е. Швелашвили, М. Г. Цкитишвили. Сообщ. АН ГССР, 1984, 114, 3, 533-536.
17. К. Д. Амирханашвили, А. П. Богданов, В. В. Зеленцов, А. Е. Швелашвили, М. Г. Цкитишвили. Сообщ. АН ГССР, 1984, 114, 3, 533-536.
18. А. Е. Швелашвили, К. Д. Амирханашвили, А. Н. Соболев, М. Г. Цкитишвили, Т. О. Вардосанидзе. Сообщ. АН ГССР, 1984, 115, 2, 289-292.
19. А. Е. Швелашвили, К. Д. Амирханашвили, А. Н. Соболев, Э. Б. Миминошвили, М. Г. Цкитишвили. Сообщ. АН ГССР, 1986, 121, 1, 85-86.
20. Э. Б. Миминошвили, Л. А. Беридзе, С. Р. Зазашвили, К. Э. Миминошвили. Georg. Eng. News, 2008, 4, 27-28.
21. E. B. Miminoshvili, K. E. Miminoshvili, L. A. Beridze, S. R. Zazashvili. J. Struct. Chem., 2010, 51, 1, 181-186.
22. E. B. Miminoshvili, K. E. Miminoshvili, L. A. Beridze, S. R. Zazishvili. J. Struct. Chem., 2013, 54, 4, 820-823.
23. É. B. Miminoshvili, L. A. Beridze, S. R. Zazashvili. J. Struct. Chem., 2011, 52, 4, 820-823.

SENSITIVITY AND LOW-FREQUENCY NOISES OF GAS SENSORS MADE ON NANOSCALE COMPOSITE MATERIAL

R. V. Hovhannisyan, H. D. Khondkaryan, M. S. Aleksanyan,
F. V. Gasparyan, V. M. Arakelyan, V. M. Aroutiounian

Yerevan State University
Yerevan, Armenia
fgaspar@ysu.am

Accepted May 29, 2014

1. Introduction

High interest towards portable gas sensors is caused by the possibility of their wide use in different devices. For example, alcohol sensors can be used in medical equipment, for control of chemical processes and food quality, for determination of alcohol level in wines, and human intoxication degree. Since ethanol is one of most widespread kinds of alcohol and has many useful and harmful properties, an important problem is detecting ethanol in atmosphere and measuring its concentrations in different media [1 – 4]. Acetone is one of most widespread volatile compounds in human breathing and can play an important role for monitoring patients with pancreatic diabetes [5]. Acetone also plays an important role in chemical industry for monitoring technological processes.

Almost all of most important parameters of resistive semiconductor sensors depend on the correct choice of sensing material. Metal oxides are known to be very sensitive to the environmental composition; therefore, these oxides and their composites are widely used as sensing materials for such sensors. Right choice of oxides constituting the composite may lead not only to exhibiting sensitivity to target gases or its increase, but also to improving the number of such important parameters of the sensor as long-term stability, high speed of operation, selectivity, and so on. It is known that admixture of Ga-and Sn-containing particles in a composite raises the sensor sensitivity to reduction gases and structure porosity, removing thus the possibility of long-term drift.

Noise spectroscopy and diagnostics are among the powerful and sensitive tools for studies of properties of semiconductors and different-purpose devices, in particular, gas sensors [6 – 9]. Phenomenon of low frequency (LF) fluctuations of electric current in semiconductors and semiconductor devices is an object of investigations of many researchers and engineers [10 – 16]. Studies have shown that behavior and magnitude of LF-noise in devices based on nanosize porous silicon differs essentially from the noise in devices based on crystalline silicon [11 – 13]. Since the sensors based on porous silicon, are very sensitive to different gases present in environment, the level and frequency dependence of LF-noises in these sensors also depends on the type and concentration of these gases. At present, there is no full understanding of the sensitivity mechanism and LF-noise character in the sensors for different gases. In formation of internal noises, besides surface effects, also the bulk properties of the material are important.

Present work studies static (sensitivity and so on) and dynamic (LF-noises) characteristics of gas sensors based on nanosize porous structures of silicon. Action of different gases is examined.

We fabricated and studied thin-film resistive gas sensor based on $In_2O_3 \cdot Ga_2O_3 \cdot SnO_2$ (70 : 20 : 10) nanocomposite. We study sensitivity of this sensor to action of ethanol and acetone vapors. Also the noise spectrum is examined in the absence and in the presence of different concentrations of these vapors.

2. Techniques of experiment

In_2O_3·Ga_2O_3·SnO_2 ceramic target used in the process of magnetron sputtering, was fabricated on the basis of mixture of In_2O_3, Ga_2O_3, and SnO_2 (70 : 20 : 10) powders and annealed 5 h thermally at temperature 900 °C. Then, the mixture was carefully stirred in an agate mortar, for full homogenization. To the mechanical mixture of In_2O_3·Ga_2O_3·SnO_2, we added 3 mass % of polypropylene powder serving as binding material. Then, from obtained powder, pellets were moulded at temperature 160 °C with diameter 40 mm and height 3 mm. Subsequent thermal sintering of moulded pellets was performed in the order presented in **Table 1**.

Table 1.

Regime	Duration
Rise 20–950°C	6 hours
Exposure at 950°C	2 hours
Rise 950–1360°C	6 hours
Exposure at 1360°C	15 hours
Drop 1360–40°C	11 hours

Obtained pellets were used as targets for HF magnetron sputtering of thin films on the polycor substrate. Parameters of the sputtering process were chosen as follows: generator power 60 W, process duration 2 min, target–substrate distance 7 cm, substrate temperature 200 °C. After that, catalytic particles of palladium were deposited by the technique of ion–plasma sputtering onto the obtained polycor In_2O_3·Ga_2O_3·SnO_2 structure during 2 s and gold comb ohmic contacts during 1 h. The fabricated samples underwent thermal treatment in air at 350 °C during 2 h in order to remove possible mechanical stresses and to stabilize sensor parameters.

We studied, by means of special measuring system, the sensitivity (ratio R_{air}/R_{gas}, where R_{air} is the structure resistance in air and R_{gas} the structure resistance in the presence of gas in air) of fabricated sensor to ethanol (C_2H_5OH) and acetone (C_3H_6O) vapors. The sample was placed into a hermetic chamber where a certain concentration of gas can be supplied (from

100 to 10 000 ppm). For obtaining the needed concentration of ethanol or acetone vapors, we insert into the chamber corresponding amount of liquid alcohol or acetone. A heater placed inside the chamber, allows raising the working body (WB) temperature up to 350 °C. Variation of sensor resistivity depending on the WB temperature and acting gas concentration was measured by means of the special software created by A. Adamyan in Borland Delphi 6.0 [15]. All measurements were performed under 1 V dc-voltage applied to the sensor.

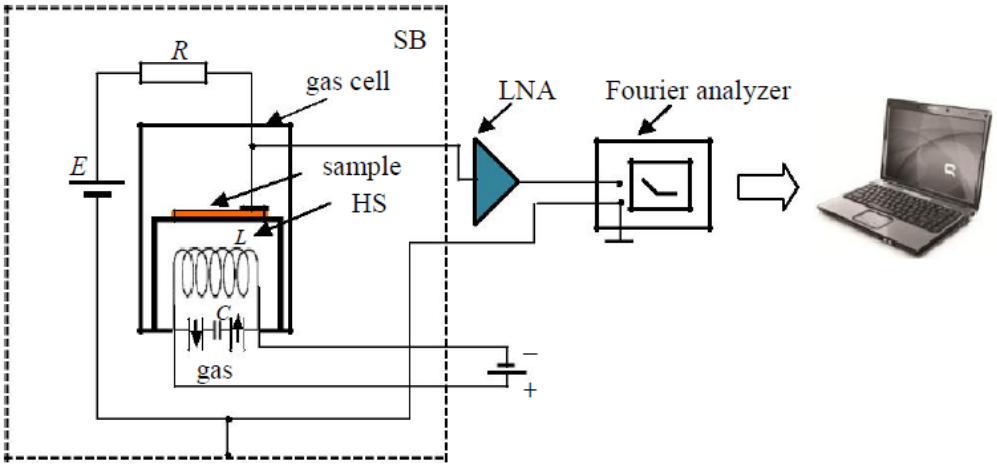

Figure 1. Experimental setup for noise measurement: SB – shielded box, LNA – low-noise amplifier, E – dc-source, and HS – heating system.

Measurement of noises was carried out by the method of direct filtration in the frequency range from 1 to 300 Hz at WB temperature 250 °C. LF noises were measured in the dc regime, i.e., the fluctuations of voltage were measured. Values of current were taken from linear region of sample CVC. Measuring setup is shown in **Figure 1**. It consists of current source with low level of own noises (9 V dc-voltage source) providing dc in the sample and the gas chamber fabricated of special thermoglass inside which the heater is mounted. The heater is fed by a dc source placed outside the measuring setup. The sample was attached to the heater by pressing. The system was placed in a permalloy box shielded from the external electromagnetic influence. The measuring part consists of an amplifier (Model–5184 Preamplifier) and spectral Fourier analyzer (Handyscope 3, TiePieEngineering) operating in Windows 7. Data obtained from spectral analyzer, are transferred to a computer and processed by means of LabView software.

3. Results and discussion

It is known that the sensitivity of resistive sensors to influence of gases is caused by chemical reactions running between molecules of studied gas and oxygen ions adsorbed on the surface of sensing material. Mechanism of sensitivity of a thin layer of In_2O_3·Ga_2O_3·SnO_2 nanocomposite to acetone vapors may be described as follows: first the oxygen from air adsorbs on the surface of oxide (physisorption), then stronger bond forms between the absorber and absorbed substance via overlapping of electronic shells of adsorbent and adsorbate atoms (chemisorption). At low temperatures the surface reactions are running too slow to be useful. With increase in film temperature, the amount of chemisorbed substance increases and

chemisorption of oxygen produces ionic kinds, such as O^{2-}, O_2^- и O^- , which capture electrons from the conduction band of the semiconductor. These ions desorb from the surface at temperatures, respectively, 80 130 and 500 °C. Thus, in the range of used temperatures, only the most stable oxygen ions will react with acetone. When the sensor undergoes influence of reduction gases, e.g., ethanol, gas molecules react with adsorbed O^- and, by forming CO_2 и H_2O, release captured electrons back into the conduction band of the semiconductor. This leads to the increase in the concentration of charge carriers in the sample and decrease in sample resistance.

Results of measurements of sensor sensitivity to ethanol vapors at different WB temperatures are presented in **Figure 2**.

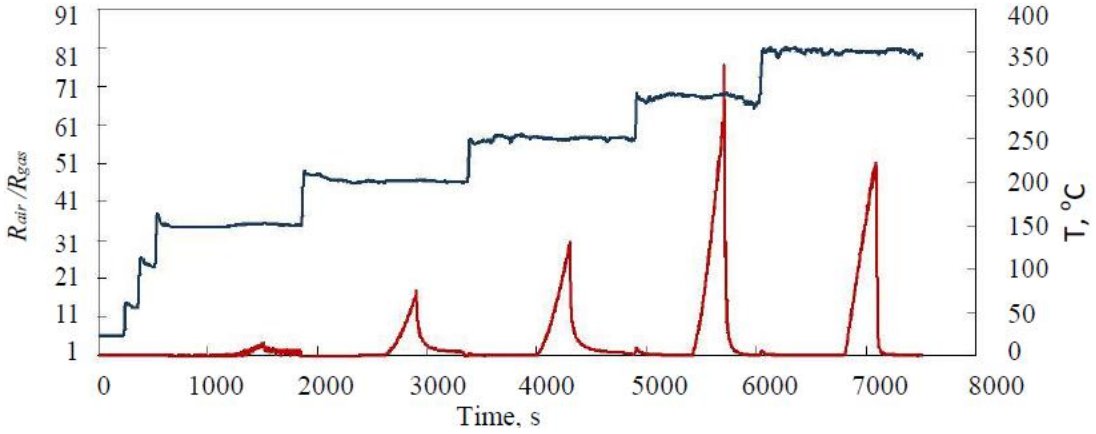

Figure 2. Sensitivity to alcohol vapor versus temperature of working body; acting gas concentration 5000 ppm.

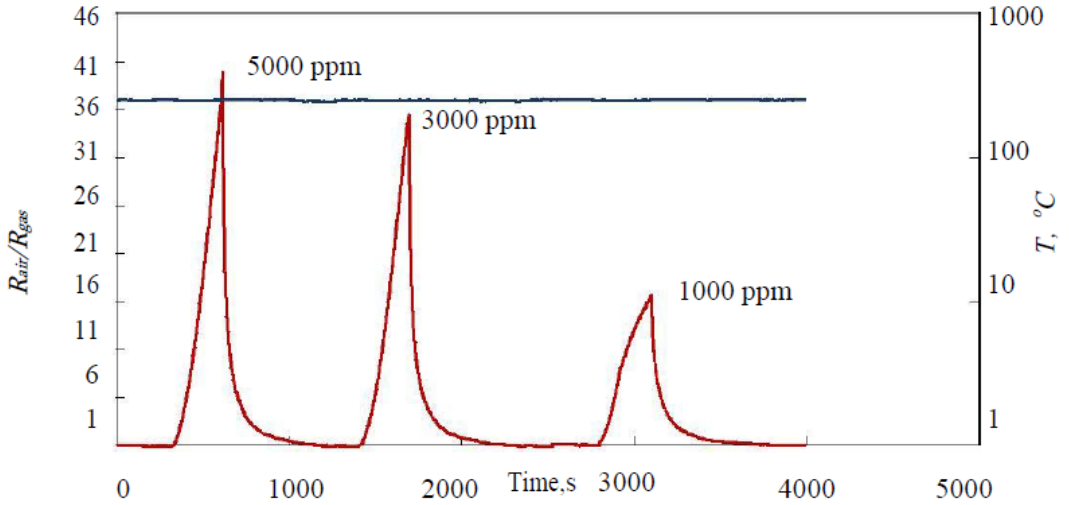

Figure 3. Sensitivity of the sensor with polycor / In_2O_3·Ga_2O_3·SnO_2 (70 : 20 : 10) structure versus the concentration of alcohol vapors in air atmosphere. Temperature of working body 250 °C.

During measurements, the concentration of acting gas (ethanol vapor) was 5000 ppm. It is seen in the figure that changes in resistance under action of ethanol vapor are observed beginning from the WB temperature 150 °C (4-times). The highest sensitivity, 76, was recorded at WB temperature 300 °C. Decrease in the sensor sensitivity at WB temperatures above 300 °C can be explained by the fact that, probably, the rate of desorption of acting gas is at these

temperatures higher than the rate of adsorption. Despite that the highest sensitivity is observed at 300 °C, subsequent studies of low-concentration influence were performed at WB temperature 250 °C, because the power consumed by sensor is lower and the long-term stability of its parameters is higher than at relatively lower temperatures. Response observed at 250 °C is well sufficient for its detection. Note also that our fabricated sensor has good selectivity properties: sensitivity to influence of isobutane and propane was negligibly low. Results of measurements of sensitivity of our sensors at different concentrations of ethanol and acetone vapors in air atmosphere is shown in **Figures 3** and **4**, respectively. WB temperature is in these figures is 250 °C.

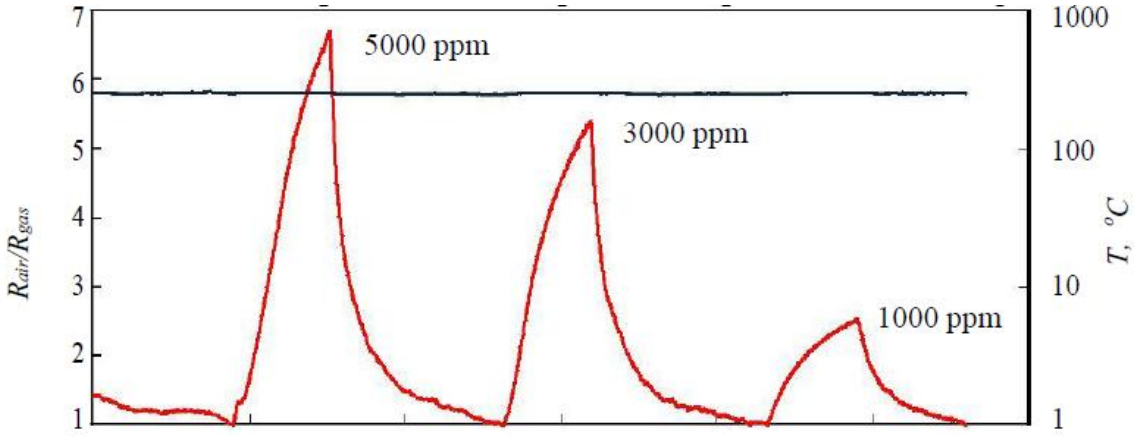

Figure 4. Sensitivity of the sensor with polycor / In_2O_3·Ga_2O_3·SnO_2 (70 : 20 : 10) structure versus the concentration of acetone vapors in air atmosphere. Temperature of working body 250 °C.

Table 2. Numerical values of response and restoration times of sensors under action of different concentrations of ethanol and acetone vapors in air atmosphere.

Acting gas	Concentration, ppm	Response time, min	Restoring time, min
Ethanol vapor	5000	4.4	2.3
	3000	4.2	2.6
	1000	4	5.41
Acetone vapor	5000	4.1	5.6
	3000	3.5	3.95
	1000	3.2	4.53

Monotonic increase in the sensor sensitivity with the increase in concentration of ethanol and acetone vapors allows determining to high accuracy the concentration of acting gas. **Table 2** lists numerical values of response and restoration times of sensors under action of different concentrations of ethanol and acetone vapors in air atmosphere.

Long times of response in case of ethanol and acetone vapors are due to the fact that, as indicated above, for obtaining corresponding concentrations, a strictly definite amount of liquid alcohol or acetone is placed into chamber and a certain time is required for full evaporation of this amount. The time of response of the sensor reckoned from the moment of reaching 90 % of maximal sensitivity, includes the time needed for full evaporation of ethanol and acetone. **Figure 5** demonstrates the measured frequency dependences of spectral density (SD) of noise voltage. Measurements were performed in the frequency range from 1 to 300 Hz at temperature 250 °C. Noises in a sample were measured during passage through it of forward dc (current generator regime). Spectra are drawn in the log–log scale. We see in **Figure 5** that the noise spectra differ quantitatively for different gas media in LF range and have differing slopes.

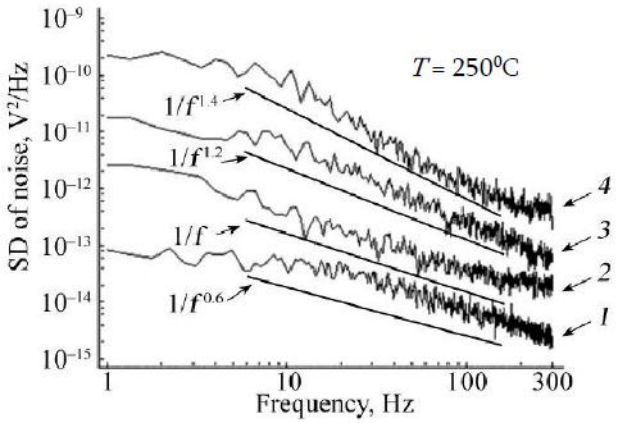

Figure 5. Noise spectrum of fluctuations of signal from tested sample at different concentrations of alcohol vapors in atmosphere: (1) – air, (2) – air + 0.1 % ethanol, (3) – air + 0.3 % ethanol, (4) – air + 0.5 % ethanol.

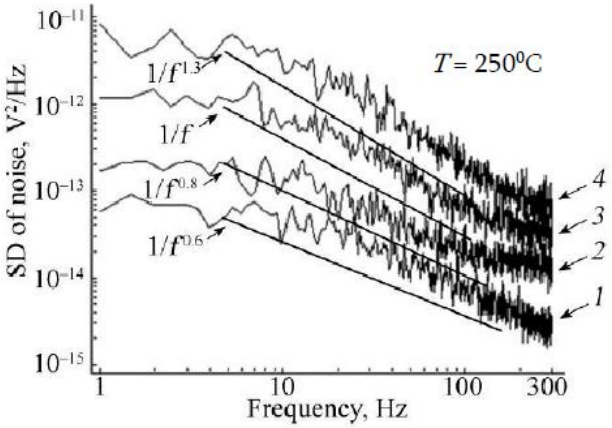

Figure 6. Noise spectrum of fluctuations of signal from tested sample at different concentrations of acetone vapors: (1) – air, (2) – air + 0.1 % acetone, (3) – air + 0.3 % acetone, (4) – air + 0.5 % acetone.

The measured noise, as distinct from [9], has not purely $1/f$ spectrum and is probably associated with random fluctuations of potential barriers at semiconductor–gas interface. Measured SD of LF noises may be described by a sum of Lorentzians having distributed multiple relaxation times $\tau^{-\alpha}$ where $0 < \alpha < 2$ ($\alpha \neq 1$) [16]. Corresponding SD has the form $S_V \propto f^{-\gamma}$, where $\gamma \equiv -2 + \alpha$ and f is frequency. As we can observe in **Figures 5** and **6**, when gas vapors with higher concentration, enter the atmosphere of gas chamber, SD of noises increases and simultaneously increases the curve slope. Exponent γ equals 0.6 in air. With adding alcohol vapors, it increases and takes the values $\gamma = 1$ (air + 0.1% ethanol), $\gamma = 1.2$ (air + 0.3 % ethanol), and $\gamma = 1.4$ (air + 0.5 % ethanol). As indicated in Fig. 6, behavior of noises in the medium of acetone vapors is, in principle, the same, although the rate of change in the level of noises is slower and the values of exponent γ are $\gamma = 1.2$ (air + 0.1 % acetone), $\gamma = 1$ (air + 0.3 % acetone), and $\gamma = 1.3$ (air + 0.5 % acetone).

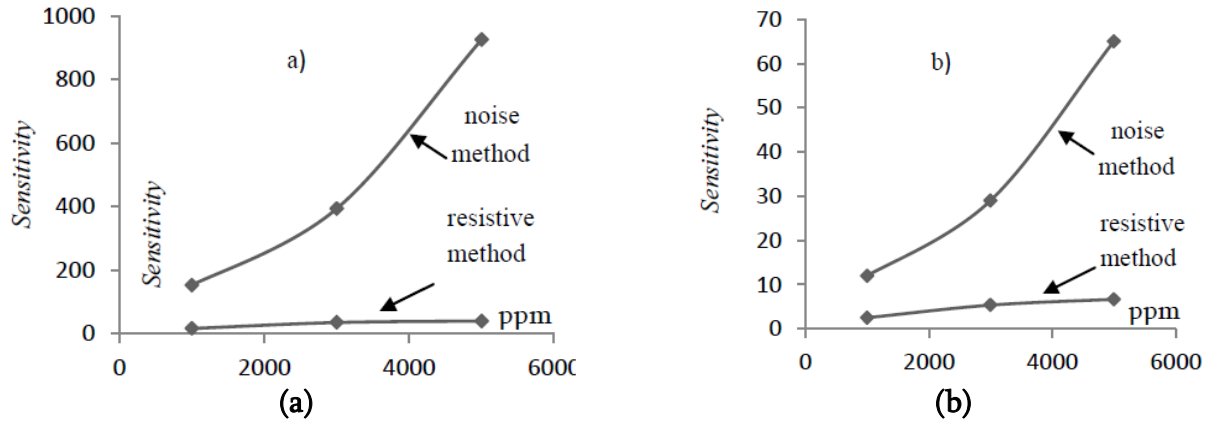

Figure 7. Concentration dependence of gas sensitivity recorded by noise and resistive methods for (a) ethanol and (b) acetone vapors.

We performed an experiment on measurements of the gas sensitivity of sensor, using the resistive and noise techniques. Calculation in noise method is made from change in SD of noises, when the sample is placed from air medium into the medium of air with tested gas. In noise method, the sensor sensitivity G_N was estimated as [14] $G_N = S_V(f)_{tg}/S_V(f)_{air}$, where $S_V(f)_{air}$ and $S_V(f)_{tg}$ are SD of noise voltage of sensor in respective media. Comparison of recorded gas sensitivities showed that the noise method is by an order of magnitude better than the resistive method. Note also that at low frequencies (10 Hz), the sensitivity of sensor is, although inconsiderably, but higher than at higher frequencies. Advantage of the noise technique is clearly displayed at high concentrations of vapors of the tested gas (see **Figures 6** and **7**).

4. Conclusion

We fabricated, by magnetron sputtering technique, thin-film resistive sensor based on nanocomposite In_2O_3·Ga_2O_3·SnO_2 (70 : 20 : 10) structure. Gas sensitivity of fabricated sensors has been measured at different WB temperatures and different concentrations of acting gases (ethanol and acetone). It was established that our elaborated sensor exhibits noticeable sensitivity to ethanol vapors at already WB temperature of 150 °C.

Comparative analysis of sensor sensitivity to different concentrations of ethyl alcohol and acetone showed that the sensor has much higher sensitivity to ethanol vapor. It was established that the gas sensitivity of our developed sensors to influence of such gases as isobutane and methane is negligibly low; this means that our sensor is selective. Since the sensor sensitivity depends linearly on concentration of ethanol and acetone vapor (in case of resistive method), it may also be used for determination of concentrations of these gases. We have shown that the noise diagnostics not only allows determining most sensitively the concentrations of gas vapors, but can also characterize changes in energy distribution of surface states.

Acknowledgments

Work was performed within the frames of Project 13–1C075 supported by SCS RA.

References

1. J. Xu, J. Han, Y. Zhang, Y. Sun, B. Xie. Sensors and Actuators B, 2008, **132**, 334.
2. Y. Zhang, X. He, J. Li, Z. Miao, F. Huang. Sensors and Actuators B, 2008, **132**, 67.
3. N. Beckers, M. Taschuk, M. Brett. Sensors and Actuators B, 2013, **176**, 1096.
4. C. Wang, Y. Weng, T. Chou, Z. Naturforsch, 2006, **61b**, 560.
5. V. Aroutiounian, Semiconductor Gas Sensors. 2013, WP, 408.
6. V. Aroutiounian, Z. Mkhitaryan, A. Shatveryan, F. Gasparyan, M. Ghulinyan, L. Pavesi, L. Kish, C. Granqvist. IEEE Sens. J., 2008, **8**, 786.
7. Z. Mkhitaryan, A. Shatveryan, V. Aroutiounian, F. Gasparyan. J. Contemp. Phys. (Arm. Acad. Sci.), 2008, **43**, 131.
8. M. Kotarski, J. Smulko. Metrol. Meas. Syst., 2009, **16**, 457.
9. V. Aroutiounian, Z. Mkhitaryan, A. Adamian, C. Granqvist, L. Kish. Procedia Chem., 2009, 1, 216.
10. Z. Mkhitaryan, F. Gasparyan, A. Surmalyan. Sensors and Transducers, 2009, **104**, 58.
11. Z. Mkhitaryan, F. Gasparyan, A. Surmalyan. In: Proc. 20th Int. Conf. Noise & Fluctuations. 2009, Pisa, 137.
12. J. Ederth, J. Smulko, L. Kish, P. Heszler, C. Granqvist. Sensors and Actuators, 2006, **113**, 310.
13. Z. Mkhitaryan, A. Shatveryan, V. Aroutiounian, F. Gasparyan. J. Contemp. Phys. (Armenian Acad. Sci.), 2008, **43**, 72.
14. J. Ederth, J. Smulko, L. Kish, P. Heszler, C. Granqvist. Sensors and Actuators B, 2006, **113**, 310.
15. A. Adamyan, Z. Adamyan, V. Aroutiounian, A. Arakelyan, K. Touryan, J. Turner. Int. J. Hydrogen Energy, 2007, **32**, 4101.
16. S. Watanabe. J. Korean Phys. Soc., 2005, 46, 646.

NANO LUMBER, INNOVATIVE CONSTRUCTION MATERIAL OF THE 21st CENTURY

T. Khmelidze, D. Nikabadze, M. Nikoladze

Georgian Technical University
Tbilisi, Georgia
xmeltam@gmail.com
datonikaba@gmail.com
malkhaz.nikoladze@yahoo.com

Accepted June 2, 2014

1. Introduction

Since the ancient ages the humanity was using lumber for construction of livings and for heating as firewood, manufactures working tools, and battle equipment. According to the nowadays forecast of European scientists, lumber will stay in 21st century as one of the most demanded environmental friendly material for construction of residential houses and manufacturing of decorative or utilities items.

During the whole period of its existing, human improve the timber treatment methods and ways, but only in middle of 20th century they were able to develop industrial technology of glued structures that gives us opportunity to use different quality materials to create large-span and curvilinear shape elements. The glued timber structures differ by ecological compatibility, manufacturability, strength, reliability and beautiful appearance.

Despite the lot of positive properties, these structures have some disadvantages, as burning, rotting, water absorption that creates possibility of cracks origination and accordingly decreases load bearing capability. Mainly these problems are decisive, while instead of timber for construction of residential building other traditional construction materials were selected.

In constructions mainly are applied wood of coniferous trees (pine, white spruce, larch), while application of wood of deciduous trees is rather limited because their quality is lower in comparison with coniferous trees, as well as their physical-technical indicators. Also would be mentioned that is limiting the application of 3rd and 4th quality lumber in construction that represents the most share in felled limber output. The 1st and 2nd quality lumber is very scarce.

For solution of this problem in worldwide scale recently are carried out researches for transition of low quality lumber into a high quality, to reach this is applied so-called nanotechnology that gives us opportunity by application of the wood deeply industrial nanotechnology to obtain a new material with totally different properties – glued wooden constructions by nano-composites that gives to lumber the unique properties and is a new for nature.

2. Results and discussion

Technology of obtaining nano-lumber provides introduction in lesser quality lumber of nano-composites that fill free spaces in lumber and considerably improves its properties.

There are many ways to synthesize nanoparticles: chemical recovery, photolysis, radiation chemistry, processing under high pressure, etc. To stabilize the synthesis process,

there are applied various nano-stabilizer materials of synthetic origin, as are: hard matrixes, water-organic emulsions, macromolecular solutions, etc.

Natural polysaccharide has an important role in nano-composites (polyposis) – arabinogalactan (E – 409) that is contained in the lumber of Siberian larch (dauria). It shares 15 % of lumber's volume, which means that it is easily obtainable polymer with possibility to create complex compounds with metals and oxides.

The arabinogalactan (E – 409) represents a branched structure water-soluble polysaccharide with high molecular weight and the size of molecule up to 2 nm. Its solution has low viscosity, easily penetrate in capillary system of plants and zoo tissues. It has a fire-retardant property. Arabinogalactan (E – 409) creates unique nanocomposite complexes with different types of insoluble molecules, in particular, dihydroquercetine and is able to transfer these molecules into the deep of biological tissues. The arabinogalactan (E – 409) gluing properties are widely used in manufacturing technology of high quality paper (for strength improvement).

The dihydroquercetine represents a strong antioxidant with a property to attract free radicals in the biological tissues and in the same time eliminates oxidation, burning and rotting processes. The developed on its basis preparations in USA and Europe are known as "taxopholines". It is successfully used to protect pipes from corrosion, in the agriculture- as stimulator for the growth of plants, in medicine for strengthening blood vessels walls, etc.

The application of nanotechnology in manufacturing at drying of Siberian larch makes possible to remove water extract from the lumber, which contains molecules of dihydroquercetine that are in turn placed in the arabinogalactan micro-molecular shell. After the modification of particles of these unique material with the size of 20 nm, there are applied the low cost lumber (pine, cedars) for deep treatment that gives to this material totally new properties: increases quality, strength, fire and bio-resistance.

The weight of coniferous trees after such kind of treatment increases up to 10 – 15 %, sometimes even up to 35 %. From this result, we can use a new name – porous nanocomposite that consists of porous material of polymer matrixes of natural or artificial origin, in which micro- and macroporous surfaces are equally covered by the nanofilm that gives to lumber additional properties. In the lumber materials of different types, number of microporous is changing in the range 25 – 35 %, total amount of micro- and macroporous makes up to 60 %. These porous surface areas multiple times are greater than the outer surface area of the material. The coniferous plants have more homogenous micro- and macrostructures then deciduous plants. Accordingly the coniferous plants are more easily subjected to nanotreatment.

The depth of the lumber treatment with nano-composites depends on the preliminary given options of treatment and freely would reach 20 – 25 mm from the surface that is good enough to manufacture of glued structures. Such structures do not change their geometrical sizes, because nanofilm originated in natural wood is porous and do not let to moisture percolate into the bulk structure and the lumber becomes totally hydrophobic. In turn these exclude the saturation and accordingly changing in sizes and origination of new cracks. Besides, the nanotreatment provides the decrease in drying ratio (decrease in geometrical sizes in process of drying) and at the last stages the removal of cohesive moisture.

On our planet there are big weather changes for last 10 years related to the global warming. These changes are resulting in the serious outcomes – floods, droughts, forest fires became frequent accidents, accompanying with human victims and large material losses.

Due to this, to create new technologies, materials and structures we will be set new requirements that will give the possibility to avoid or at least decrease devastating results of the climate change. Earth is under the influence of active seismic actions that mostly makes losses for Japan, Asia and Pacific Ocean area. Devastating storms happen in the North America, there are many floods in the Europe and etc.

To solve these problems in buildings, including wooden structures, it is necessary to improve many properties, as are: seismic resistance, strength, ecological compatibility, durability, fire resistance, bio resistance, etc. The nano-lumber, used completely or incompletely, partly solves building tasks. It has great future in seismically active and north regions with cold climate.

The **Figure 1 – 6** illustrate the practicality of the wood structures made from nanocomposites (photos shown are provided by the German company "Weining Group"), which shows bridges made from glued nano-lumber in Germany and Switzerland.

Figure 1.

Figure 2.

Figure 3.

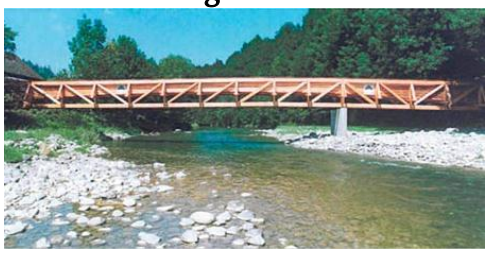

Figure 4.

Figure 5.

Figure 6.

Figure 7.

Figure 8.

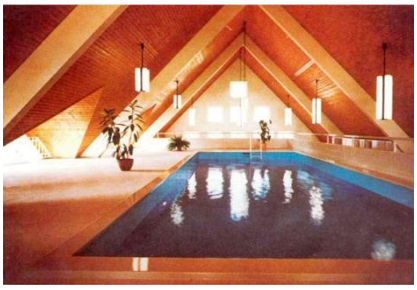

Figure 9.

Figure 10.

Figure 11.

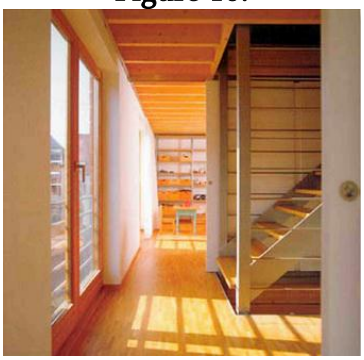

Figure 12.

In **Figures 7 – 12**, there are presented gymnasium and aqua parks placed in Netherlands.

3. Conclusion

The existing literature and analysis of the survey on innovative construction material – nano-lumber – gives us a possibility to formulate opinions about results of using this material and related nanotechnology in construction: (1) expands the range of the products made from natural wood; (2) reduces the cost of construction and operating costs; (3) improves the seismic resistance of structures and stability of geometric sizes, hydro- and fire-resistance; (4) contributes to the creation of a new individual architectural forms; (5) accelerates construction-installation throughout the building cycle; (6) makes it possible the creation of buildings and structures with elevated antiseptic protection; (7) creation of environmentally friendly housing; (8) provides improved period of using of building in the mostly difficult climates, mining-geological, and seismic conditions.

In order to increase the potential of industrial wood processing in Georgia with local raw materials to work on, it will be set up a large production base, which will meet requirements of market with sawn wood, cardboard, paper and modern bearing wooden construction, including stick on constructions using nanotechnology.

References

1. R. R. Safin, E. Y. Razumov, M. K. Gerasimov, D. A. Achmetova. Studying of vacuum-conductive process of timber modifying. Lumber Treat. Ind., 2009, 3, 9-11.
2. E. Y. Razumov. Physical picture of processes occurring during pre-drying and heat-treatment of lumber. In: Proc. 4th Int. Sci. Conf. Lumber. 2011, Prague, 233-238.
3. B. Yu. Voronin. Manufacturing of glued timber structures from timber composite. e-Journal, 2011: www.nanonewsnet.ru, nanomarket.ru.
4. T. Khmelidze. Wood and Plastic Construction. 2008, Tbilisi: Georg. Tech. Univ.

LESS-COMMON, ULTRASMALL, AND RADIOACTIVE NANOPARTICLES

B. I. Kharisov, O. V. Kharissova

Universidad Autónoma de Nuevo León
Monterrey, Mexico
The University of Texas
Arlington, USA
bkhariss@mail.ru

Accepted July 1, 2014

Introduction

When the nanotechnology area began to develop intensively as an independent field in the frontiers of physics, chemistry, materials chemistry and physics, medicine, biology, and other disciplines two decades ago, such terms as “nanoparticle”, “nanopowder”, “nanotube”, “nanoplate”, and other related shape-like terms had rapidly become very common. For instance, a simple search using *SciFinder* results hundreds thousands of articles with keywords “nanoparticle” or “nanotube”. At the same time, during the last years, efforts of researchers have led to reports of enormous number of the nanostructure types above and the discovery of more rare species, such as “nanodumbbells”, “nanoflowers”, “nanorices”, “nanolines”, “nanotowers”, “nanoshuttles”, “nanobowlings”, “nanowheels”, “nanofans”, “nanopencils”, “nanotrees”, “nanoarrows”, “nanonails”, “nanobottles”, or “nanovolcanoes”, among many others.

The problem how to name a discovered rare nanoform is commonly resolved according to imagination of researchers. Since any novel nanoform / nanostructure could theoretically get useful, unexpected and unpredictable applications (as, for example famous graphene, discovered not long ago [1]), each new achievement, reproducible or not, is welcome due to an extreme importance of nanotechnology at this moment and in future. Without a good understanding of the reasons for shape formation, approaches to the synthesis of nanostructures can be hard to carry out. According to the available literature, no any universal generalization of rare and common nanostructures is observed in available literature. Several existing classifications are related with dimensionality of the nanostructure itself and their components [2, 3] (for instance, 0D clusters and particles, 1D nanotubes and nanowires, 2D nanoplates and layers, 3D core / shell nanoparticles or self-assembled massives, intermediate dimensional nanostructures as fractals or dendrimers) or the classification based on the triad symmetry group-shell composition-structural formula of the shell (here nanostructures are divided in branches, classes, and subclasses determined by the symmetry group of a shell and the sets of the quantum numbers of a structure) [4]. In this work, we offer for discussion by the nanotechnological community a non-formal classification, which is not directly related with dimensionality and chemical composition of nanostructure-forming compound or composite and it is based mainly on the less-common nanostructures. The classification includes the following sections – see **Table 1**.

Table 1.

Classic carbon-based nanostructures	Conventional non-carbon nanostructures
Carbon nanotubes, Fullerenes, Nanodiamonds, Graphene and Graphane	Simple and core-shell nanoparticles, Non-carbon nanotubes, Nanometals, Nanowires, Nanorings, Nanobelts, Nanopowders, Nanocrystals, Nanoclusters, Nanofibers, Nanodots / Quantum dots
Relatively rare nanostructures	
Simple linear 1-D, 2-D, and 3-D-nanostructures	***Prolonged 3-D nanostructures***
Nanolines, Nanopencils, Nanodumbbells, Nanopins, Nanoshuttles, Nanopeapods, Nanochains, Nanowicks, Nanobars, Nanopillars	Nanobricks, Nanocones, Nanoarrows, Nanospears, Nanospikes, Nanonails, Nanobowlings, Nanobones, Nanobottles, Nanotowers, Nanoarmors, Nanopins.
Circle- and ball-type nanostructures	***Nanocage-type structures***
Nanowheels, Nanoballs, Nanoeggs, Nanograins, Nanorices, Nanospheres	Nanocapsules, Nanocages, Nanoboxes, Nanocubes
"Nanovegetation" world	***"Nanoanimal" world***
Nanotrees, Nanopines, Nanopalms, Nanobushes, Nanograsses, Nanoacorns, Nanokelps, Nanomushrooms, Nanoflowers, Nanobouquets, Nanoforests, Nanocorns, Nanoleaves, Nanobroccoli, Nanomulberry, Nanocactus, Nanospines, Nanosheaves, Nanoonions, Nanodewdrops	Nanourchins, Nanoworms, Nanolarvae, Nanosquamae
"Nanohome" objects	***"Nanotechnical" structures and devices***
Nanobrushes, Nanobrooms, Nanocombs, Nanocarpets, Nanofans, Nanowebs, Nanospoons, Nanoforks, Nanobowls, Nanotroughs, Nanocups, Nanospindles, Nanofuns	Nanosaws, Nanosprings (Nanocoils / Nanospirals, Nanoairplanes, Nanopropellers, Nanowindmills, Nanoboats, Nanobridges, Nanocars, Nanobatteries, Nanotweezers, Nanomeshes, Nanofoams, Nanobalances, Nanojunctions, Nanopaper, Nanorobots, Nanothermometers, E-nose, E-tongue, E-eye, NEMs
Nanostructures classified as polyhedra	***Other rare nanostructures***
Nanotriangles, Nanotetrahedra, Nanosquares, Nanorectangles, Nanopyramids, Nanooctahedra, Nanoicisaedra, Nanododecahedra, Nanocubes, Nanoprisms, Nanocuboctahedra	Nano New York, Nanosponges, Nanostars, Nanoglasses, Nanodrugs

Note: This is a non-JUPAC classification!

The description is focused to the examination of less-common nanostructures (i.e., published mainly in the range of 1 – 100 reports) corresponding to the shapes above. Such structures possess unusual shapes and high surface area, which make them very useful for catalytic, medical, electronic and many other applications [5]. In addition, certain attention will be paid to the ultrasmall nanoparticles (size < 10 nm) [6] and those containing radioactive elements [7].

Some examples of rare nanospecies

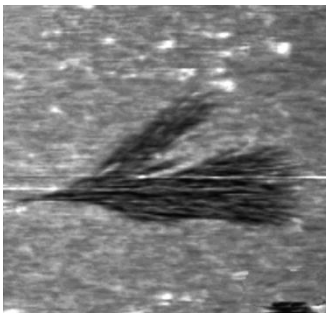
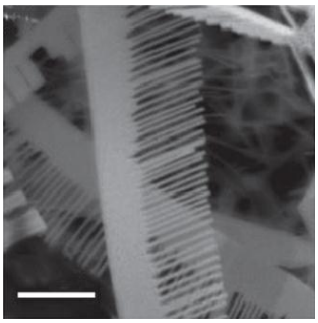
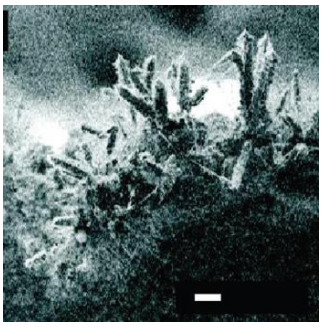
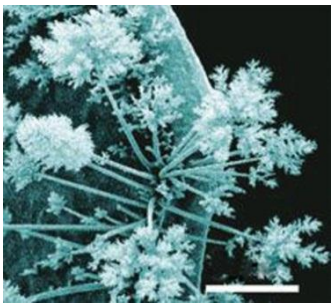
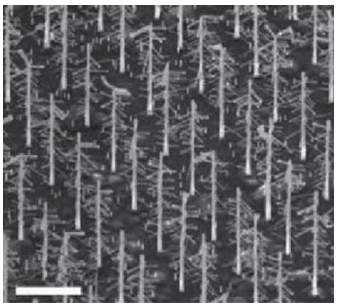
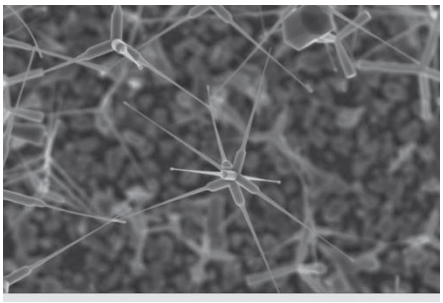

Some classic nanostructures

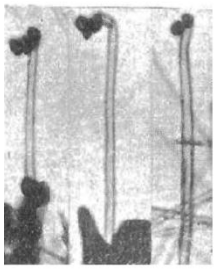

First carbon nanotubes

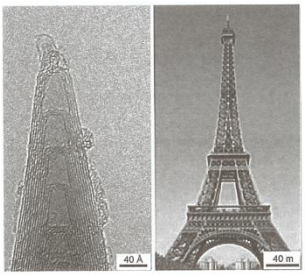

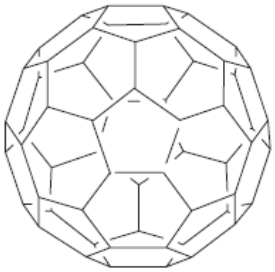

C_{60} structure

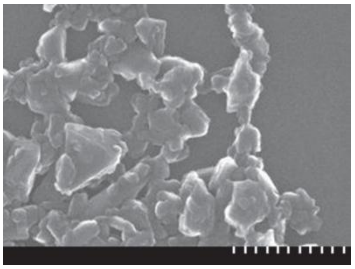
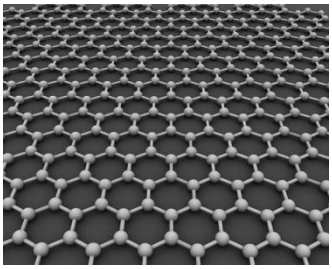

Nanodiamond

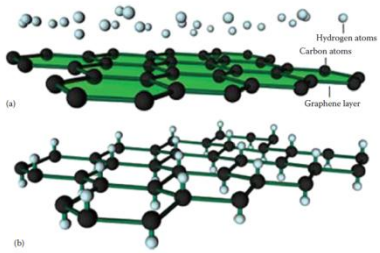

Addition of H atoms to graphene (a), resulting in graphane (b)

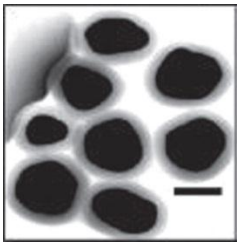

Core-shell Ag @ SiO_2 nanoparticles

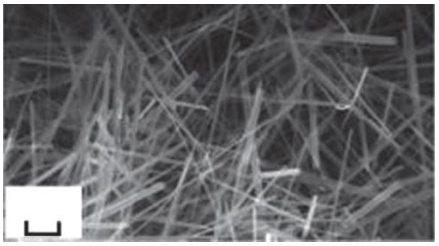

Mn_2O_3 nanowires

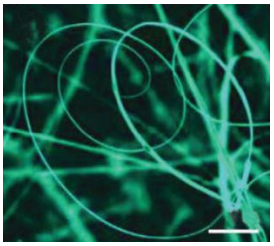

Spiral of a ZnO nanobelt

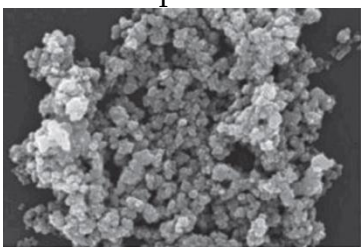

ZnO : CeO_2 nanopowders

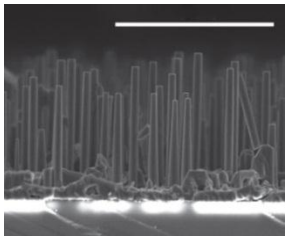

Zn-doped InN nanorods

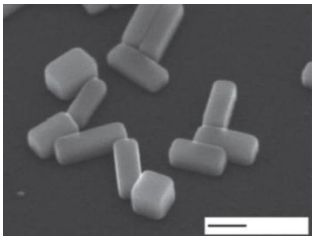

Ag nanobars

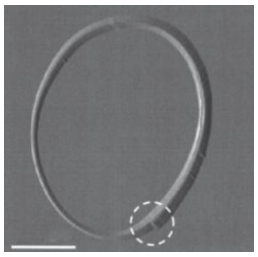

ZnO nanorings

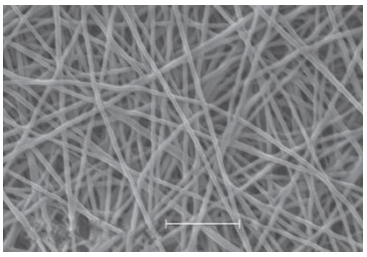

Poly(ethyleneimine) / poly (vinyl pyrrolidone) nanofibers, obtained *via* electrospinning

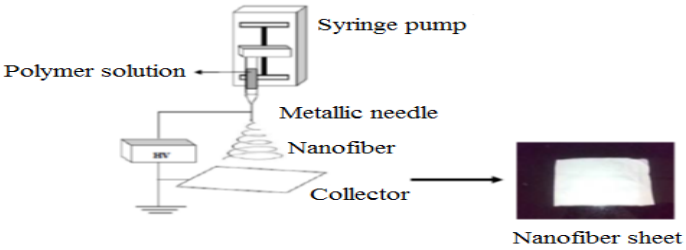

Schematic diagram of electrospinning setup.

Simple, Linear Nanostructures

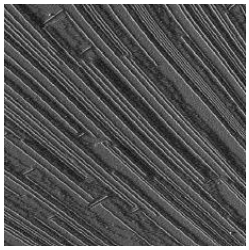

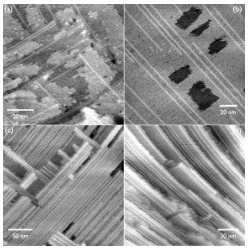

Bi nanolines

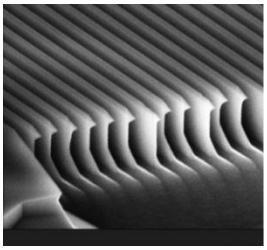

Silicon nanolines

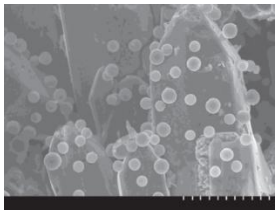

ZnO pencils decorated with carbon spheres

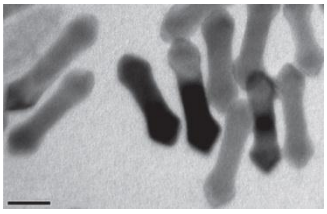

Nanoshuttle (Au/Ag)

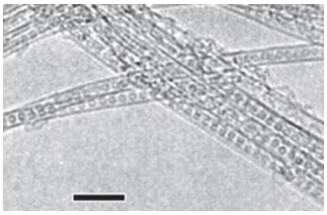

C_{60} nanopeapods

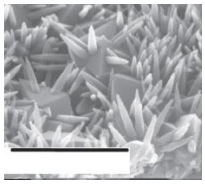

Rutile nanopins

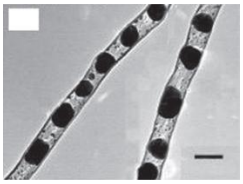

Cu nanoparticle chains

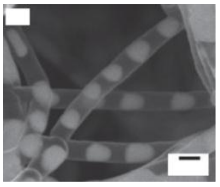

Au nanochains

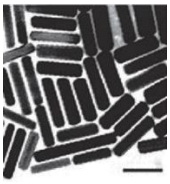

Au @ Pd core–shell nanobars

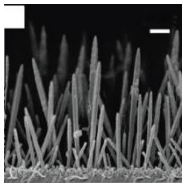

Cu nanopillars on Au / glass

Nanodumbbells

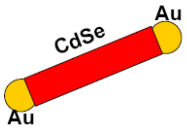

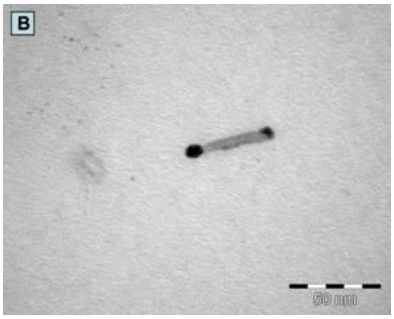

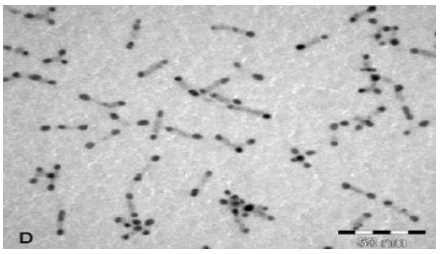

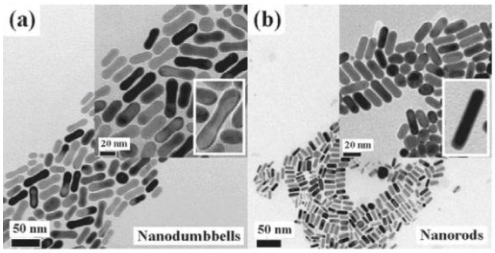

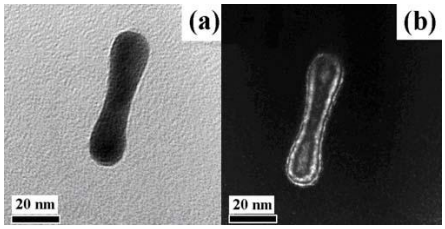

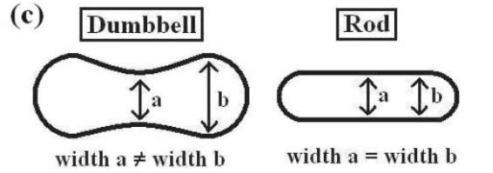

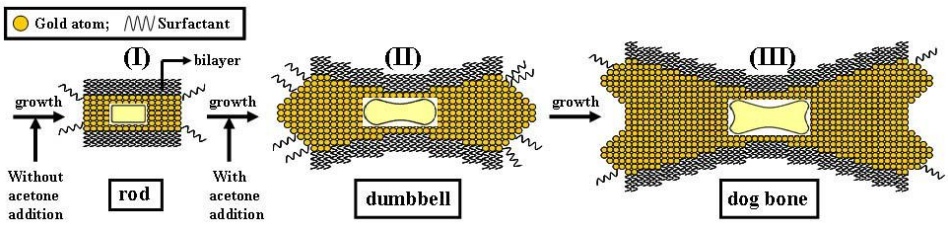

Growth mechanism of "nanodumbbells"

Preparation and characterization of gold nanodumbbells. Nanotechnol., 2006, 17, 5355: http://conf.ncku.edu.tw/research/articles/e/20071109/3.html

Various prolonged 3D Nanostructures

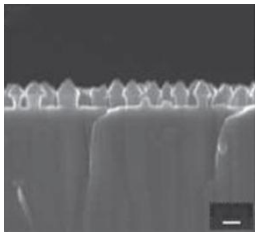

InGaN nanoarrow

MgO nanobone

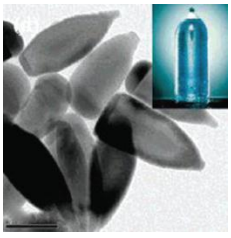

Cu–In sulfide nanobottles

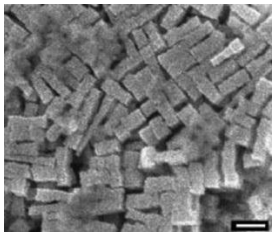

Pd nanobricks

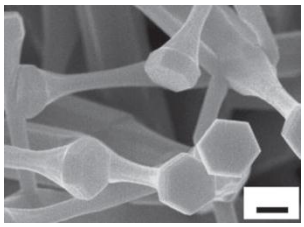

ZnO nanonail

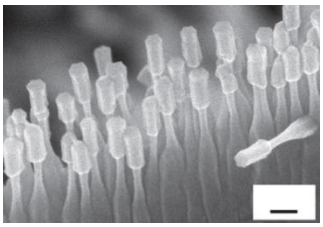

ZnO nanobowling

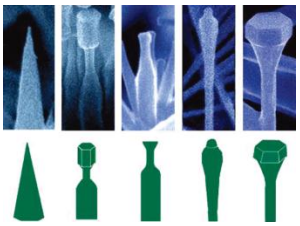

ZnO nanocone, nanobowling, nanobottle, nanoarrow, nanonail

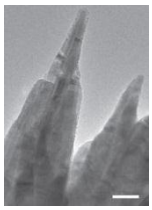

ZnO nanocone

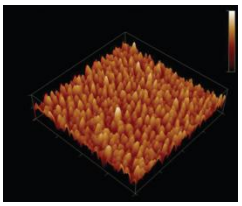

Nanocone ZnO thin film

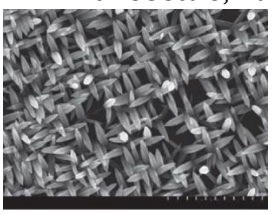

ZnO nanospears

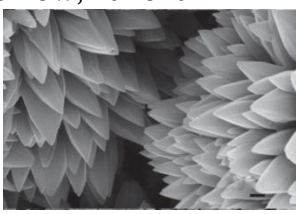

ZnO nanospikes

Circle and ball-type nanostructures

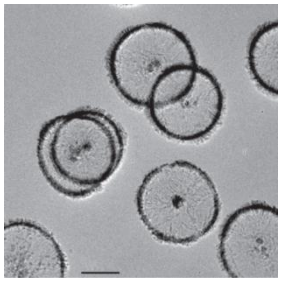

Pt nanowheel

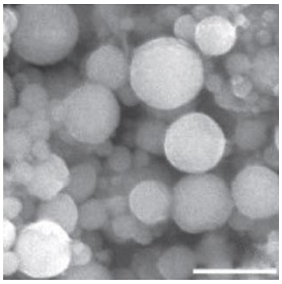

Ni nanoball

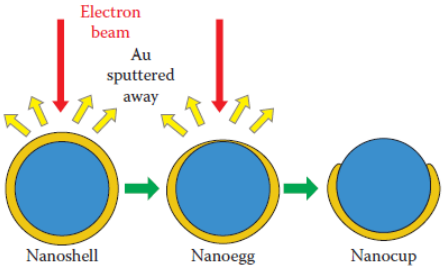

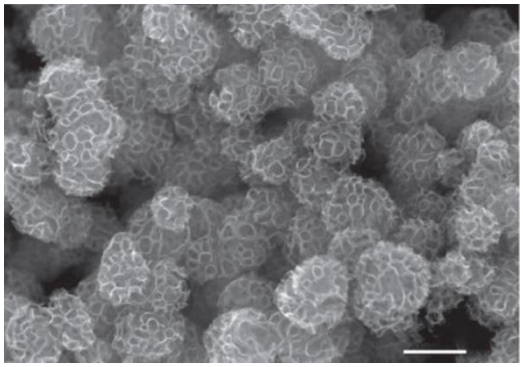

Foam-like platinum nanospheres

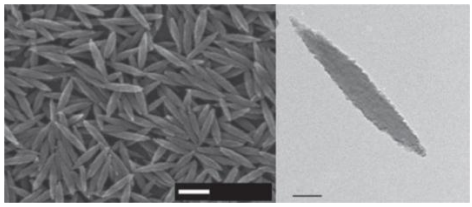

Hematite–Au core–shell nanorice particles

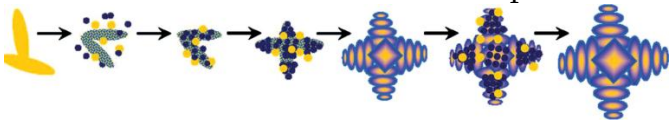

Au nanorice assemble electrolytically into mesostars

Nanocage-type structures

Nanocages, nanoboxes, and nanocubes

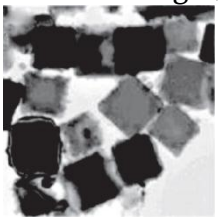

Au nanocubes

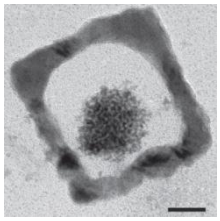

Copper oxide nanoboxes

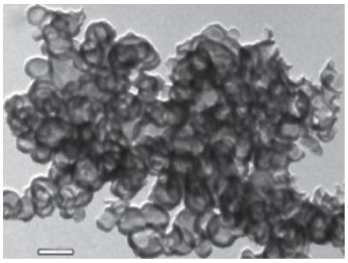

Carbon nanocapsules

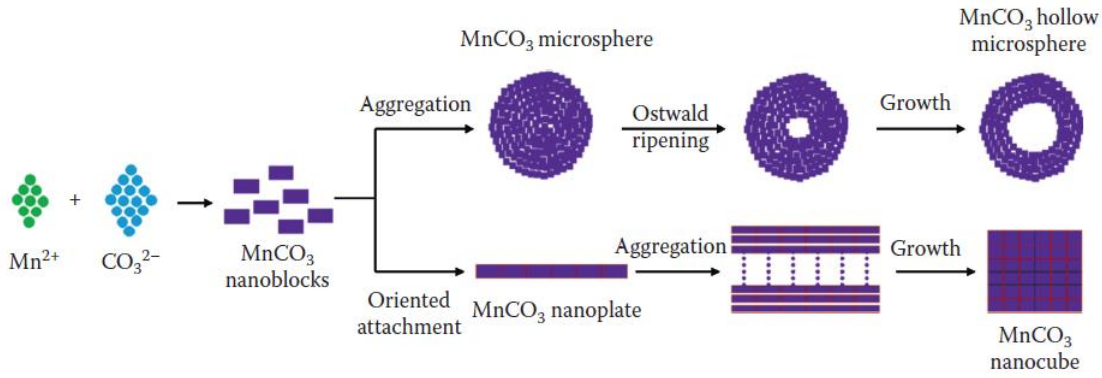

"Nanovegetation" world

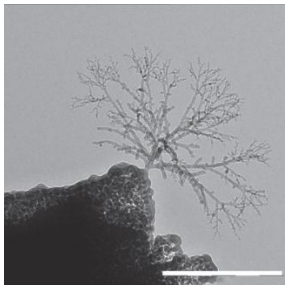

Carbon tree-like nanostructure

ZnO nanopine

Fe_2O_3

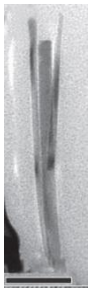

ZnO nano-palm

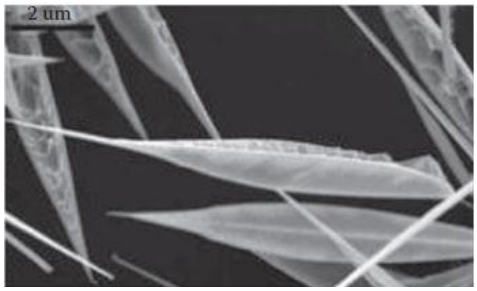

GaN leaves

Fe_2O_3 nanoforest

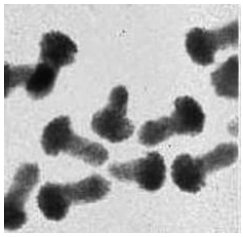

Nanomushroom (aniline–Au)

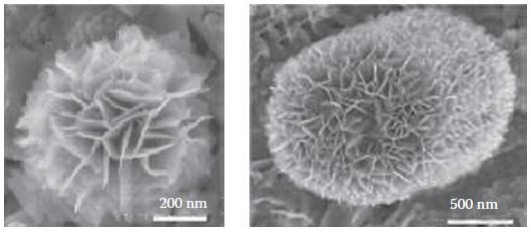

MoS_2 flower-like nanostructures

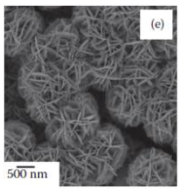

Bouquets of Bi_2Te_3 microspheres

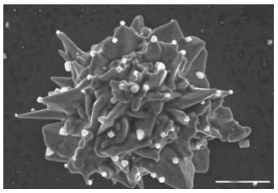

Au – Ag nanodewdrops

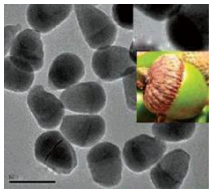

Cu – InS nanoacorns

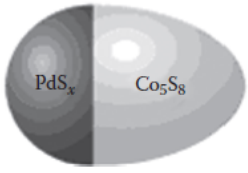

Cobalt sulfide nanoacorns

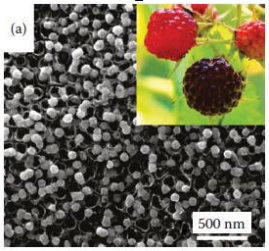

Mulberry-like CdSe nanocluster anchored TiO_2

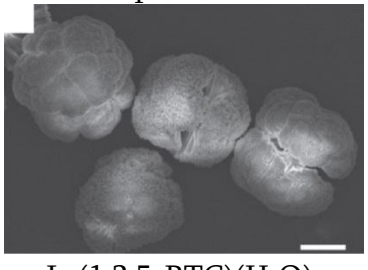

La(1,3,5-BTC)$(H_2O)_6$ broccoli-like architecture

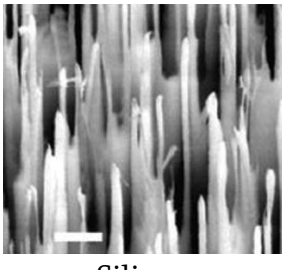

Silicon nanograss

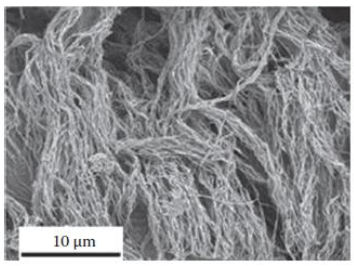

SiC nanokelps

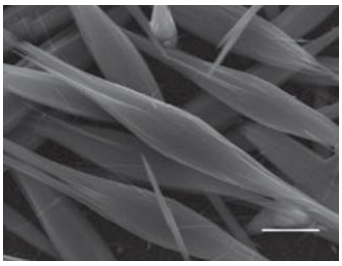

ZnO corn-like nanostructures

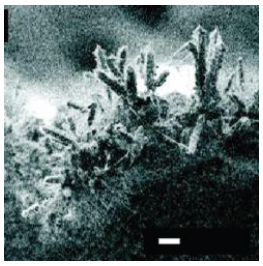

GeO_2 cactus-like formations

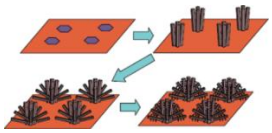

ZnO nanocactus growth

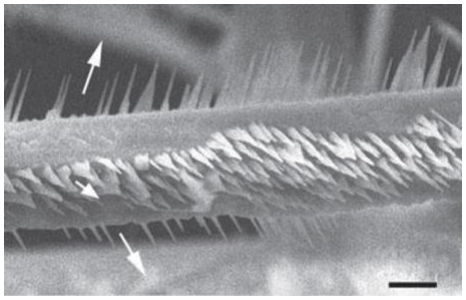

Arrays of BN sheathed ZnS nanospines

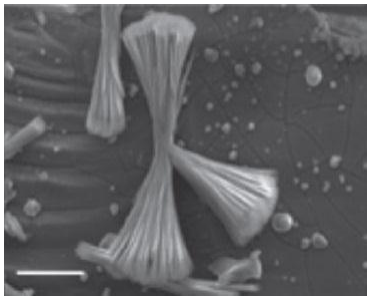

CeO_2 nanostructure with a sheaf-like morphology

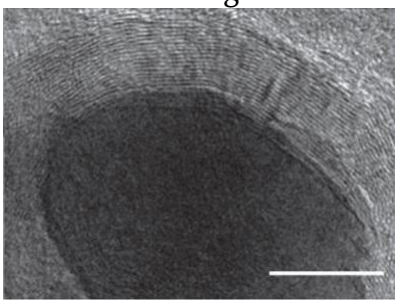

Nanoonion-like fullerenes

"Nanoanimal" world

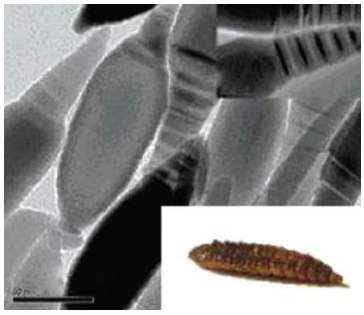

Nanolarva (Cu-InS)

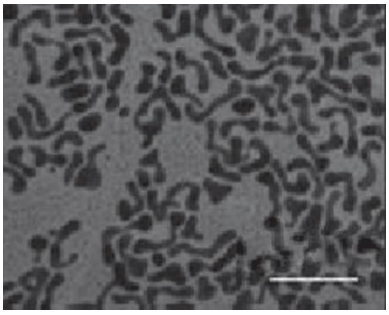

Au worm-like nanostructures

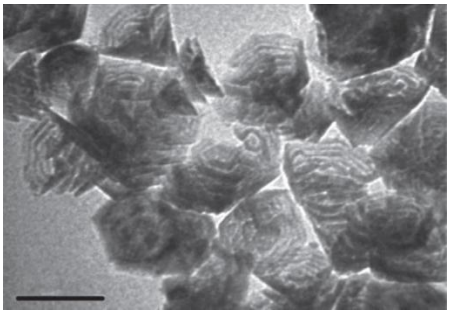

ZnO nanosquamas

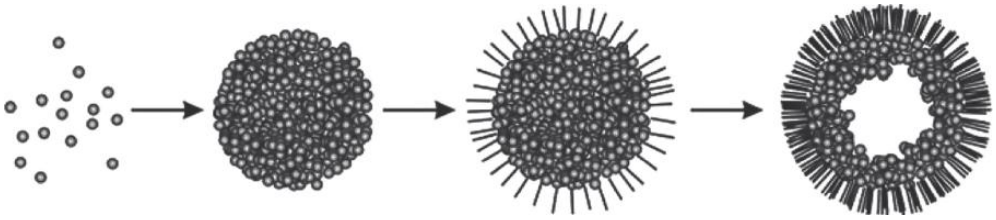

Formation of the α-MnO_2 urchin-like structures

Nanourchin (V_2O_5)

"Home"-like nanostructures

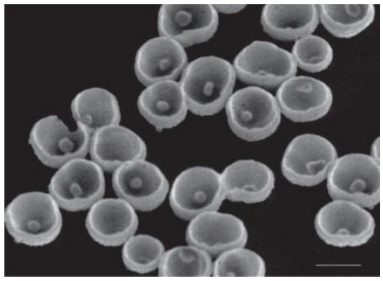

Au nanobowls

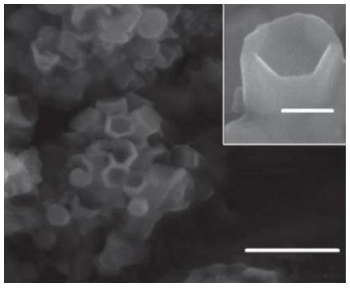

ZnO nanocups

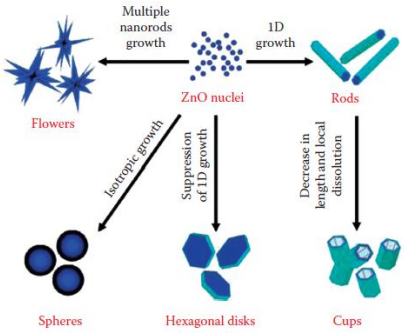

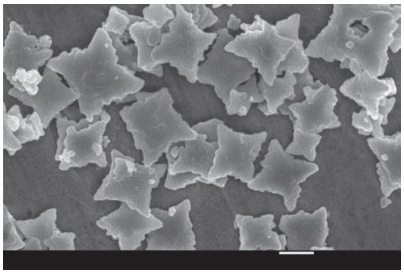

Star-like $BiVO_4$ products made of nanoplates

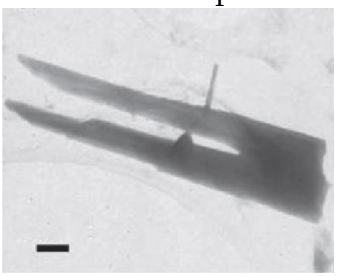

Ga_2O_3 nanofork

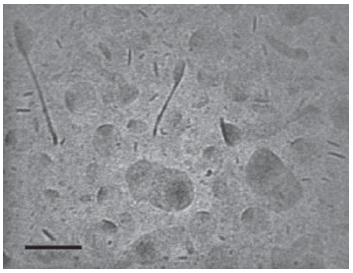

Nanospoon (solid lipid nanoparticles)

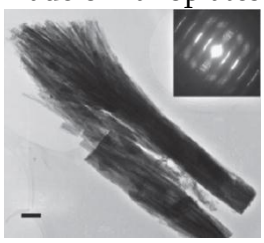

$H_2Ti_3O_7$ nanobroom

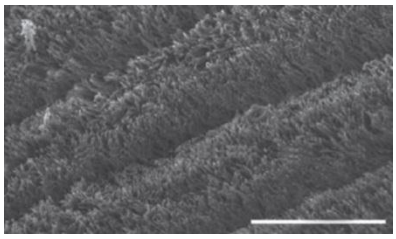

Al_2O_3 nanorod brushes

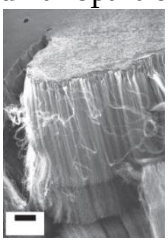

C-nanotubes nanocarpet

Au nanocombs

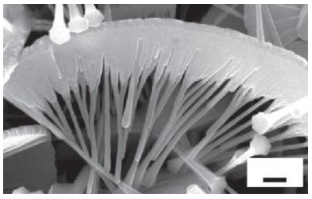

ZnO nanofan

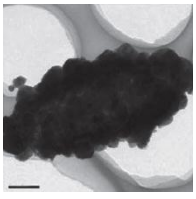

ZnS microspindles

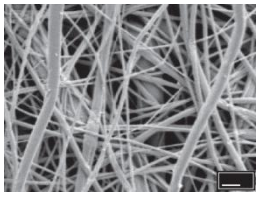

Nanoweb of cellulose acetate

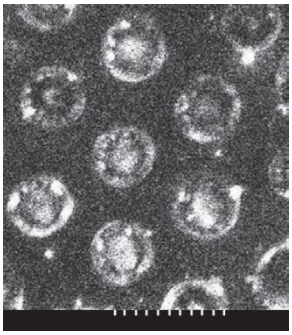

Silica nanosombrero

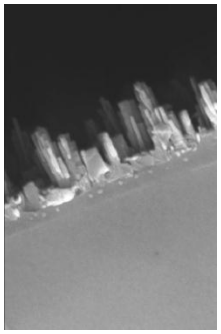

Nano New York

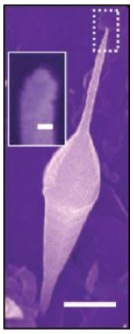

Eiffel-tower shaped SiC nanowire

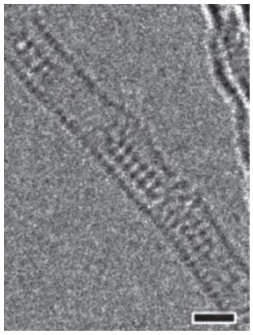

Nanoladder ($H_8Si_8O_{12}$ encapsulated inside the various CNTs)

"Nanotechnical" structures and devices

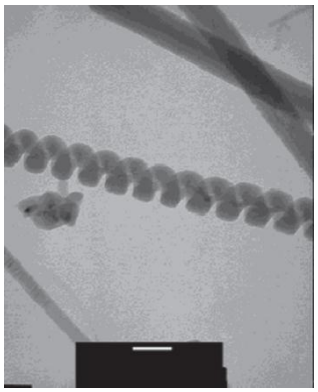

Amorphous silicon carbide nanosprings

Nanosprings / Nanocoils / Nanospirals
Nanoairplanes, Nanopropellers, and Nanowindmills

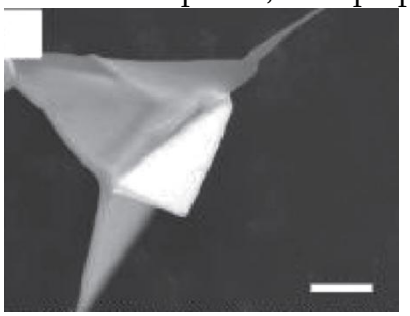

ZnO nanoairplane

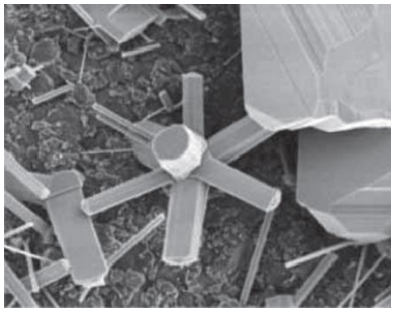

ZnS nanowindmill

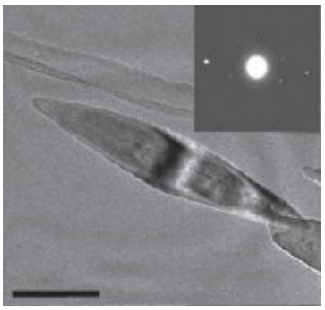

TiO_2 boat-like nanostructure

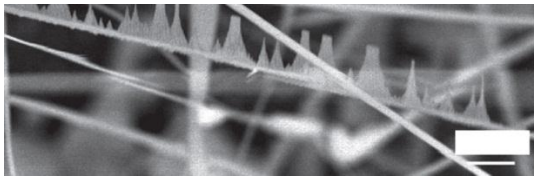

Double-side ZnS nanosaw

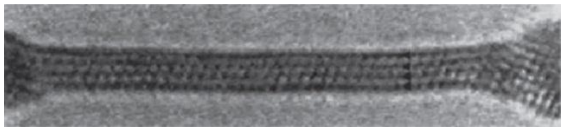

Au nanobridge

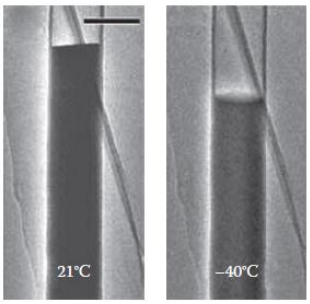

Ga – CNT nanothermometer

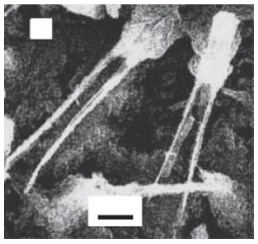

GaN nanotweezers

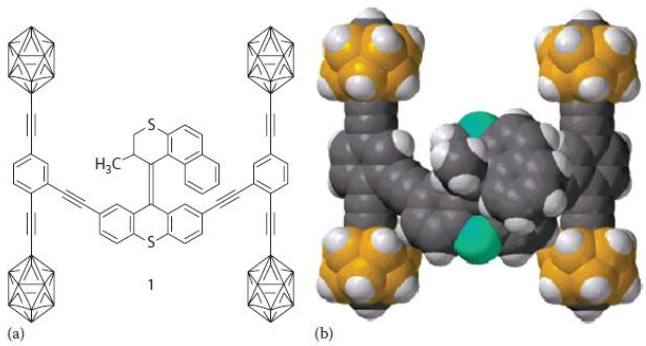

(a) Structure of motorized nanocar on *p*-carborane basis. The *p*-carborane wheels have BH at every intersection except at the top and bottom vertexes, which represent C and CH positions, *ipso* and *para*, respectively, relative to the alkynes. (b) The space-filling model of this nanocar

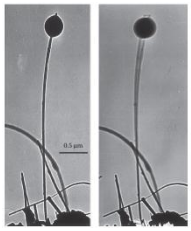

CNTs nanobalances

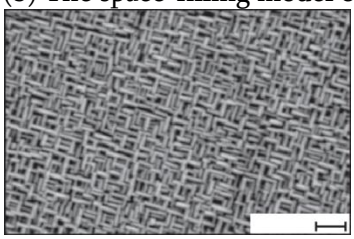

SrF_2 film on sapphire

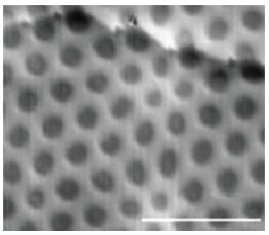

BN on Rh (111) nanomesh

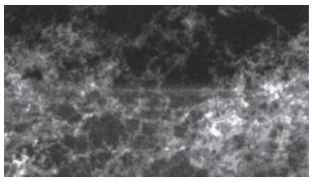

Carbon nanofoam

Nanostructures classified as polyhedra

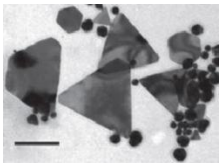

Au nanotriangles

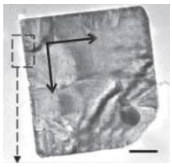

Sn nanosquare

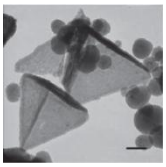

CuO nanotetrahedron

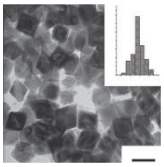

Fe_2O_3 nanooctahedron

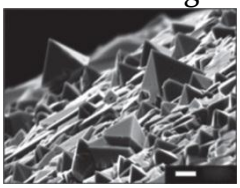

Mn-doped In_2O_3 pyramids

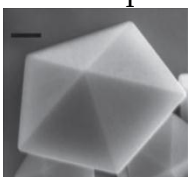

Decahedron of few micrometers

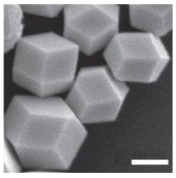

Rhombic dodecahedral Au nanocrystals

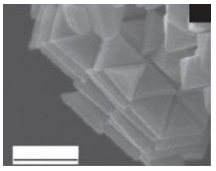

Au nanoprisms

Ultrasmall particles (< 10 nm)

In most reports on ultrasmall nanoparticles, their size is defined as lesser 10 nm (more rarely lesser 5 nm), although in a few publications such sizes as 30 and even 50 nm (standard non-ultrasmall nanoparticle size) were erroneously attributed as ultrasmall. An especial interest is given to nanoparticles with approximately 20 – 40 metal atoms per cluster and sizes < 2 nm (also referred as nanoclusters). The nanoparticles < 10 nm possess a series of useful applications, first of all in the nanomedicine area (in particular, as MRI agents).

– Overall number of reports is currently slightly more 500;

– Major part of these publications is dedicated to ultrasmall metallic gold, iron oxides, and gadolinium oxide nanoparticles;

– Other (considerably lesser): Ag, Cu, Pd, Ni / Co, Fe / Ni, C, Se, Se, SiO_2, TiO_2, CdS, $NaYF_4$, $Ln_{0.33}Gd_x$ / $[Mo(CN)_8]^{3-}$ (Ln = Eu (x = 0.34), Tb (x = 0.35)), [Fe(pyrazine){$Ni(CN)_4$}];

– Mainly biomedical applications of ultrasmall particles: Magnetic Resonance Imaging (MRI) contract agents, virus inactivation, immunoassay labeling, etc.), as well as varieties of catalysis, hydrogen sorption, as magnetic devices, ultrasmall transistors, sensors for gases or biological objects, parts of solar cells and batteries;

– In comparison with "standard" particle size in nanotechnology (20 – 50 nm), ultrasmall nanoparticles (formally < 10 nm and especially < 2 nm) contain a relatively little number of atoms, so their properties and related applications could be distinct.

Examples of their applications are:

– Catalysis (Ag – in propylene epoxidation; Pt – propane oxidative dehydrogenation; Au / TiO_2 – remarkable photocatalytic activity for both liquid and gas phase oxidation reactions;

– Frequently, ultrasmall NPs can carry out those functions, which have not been detected for their larger forms (non-ultrasmall NPs or bulk states). Thus, when supported on silica, ultrasmall **Cu** nanoclusters (1 nm) were found to efficiently catalyze C–H oxidation reactions, hitherto unknown to be catalyzed by Cu;

– Electrochemical applications: Graphene-like MoS_2 and ultrasmall Mg nanoparticles with an average diameter of 2.5 nm, used in a combination of G-MoS_2 cathode and N-Mg anode, achieved a high operating voltage of 1.8 V and a first discharge capacity of 170 mA h g^{-1}, of which 95 % is kept after 50 discharge–charge cycles, representing itself as one of the most successful configurations for rechargeable Mg batteries;

– In_2O_3 films – ethanol sensors.

Preparation:

– Their synthesis is really a more complicated than the obtaining conventional-size nanoparticles;

– The principal motif is not to allow the formed very small particles to be aggregated with use of appropriate surfactants, dispersing in polymeric and other matrices, reducing time of synthesis procedures and temperature, etc.;

– Classic wet chemistry techniques;

– Application of microwaves, hydro- and solvothermal conditions;

– Laser pyrolysis;

– Irradiation methods;

– Use of polymeric templating agents (for example, stable ultrasmall Au nanoparticles were synthesized in aqueous phase by using a tri-block copolymer (BMB) as a templating agent);

– Seeded emulsion polymerization, in which nanocrystals are used as seeds, was applied for obtaining small biocompatible polymer-coated nanocrystals with sizes close to ultrasmall region (> 15 nm).

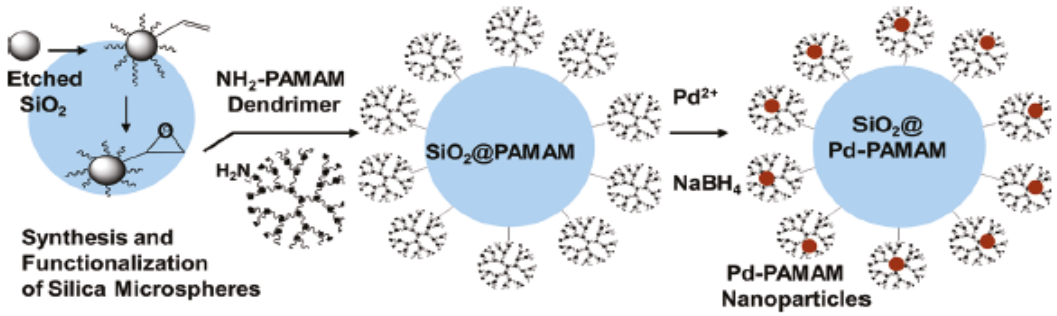

There is presented an example of synthesis: Pd nanoparticles within the cores of the SiO_2-supported PAMAM dendrimers {poly(amido amine)} were synthesized by letting Pd(II) ions complex with the amine groups in the cores of the dendrimers and then reducing them into Pd(0) with $NaBH_4$.

Radioactive nanoparticles

Most common radioactive (r/a) nanoparticles (NPs) are: isotopes of metallic gold, iodine and technetium salts, CeO_2 and other lanthanide and actinide compounds, as well as several *p*- (P, C, F, Te) and *d*- (Fe, Co, Cu, Cd, Zn) elements.

Main isotopes used are: ^{14}C, ^{125m}Te, ^{125}I, ^{124}I, ^{131}I, ^{18}F, ^{99m}Tc, ^{59}Fe, ^{198}Au, ^{60}Co, ^{137m}Ce, ^{90}Y, U (natural mixture). Among them the most frequently used isotopes are

Nanoparticles containing iodine isotopes (in organic or inorganic supports):

– Silica NPs radiolabeled them with ^{124}I (*in vivo* bioimaging, biodistribution, clearance, and toxicity studies);

– Biodegradable poly (DL-lactic acid-co-glycolic acid) nanoparticles loaded with radionuclide ^{131}I (for treatment of cancer resistant to conventional radiotherapy);

– ^{125}I on hydroxyapatite or CNTs / pingyangmycin (see the image below) composite (treatment of oral cancer lymph node metastasis).

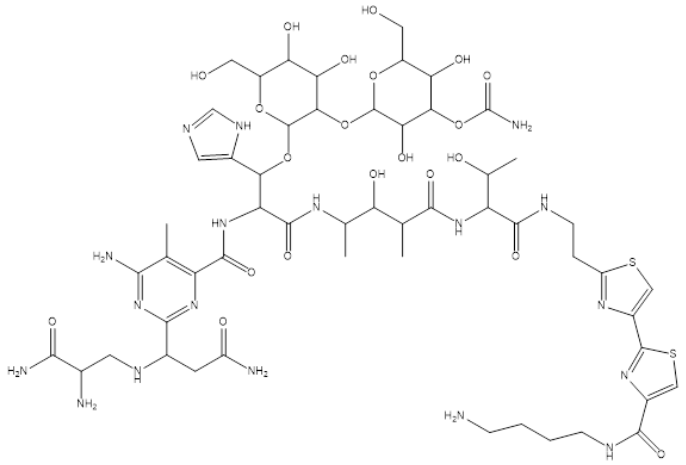

Nanoparticles containing ^{99m}Tc and ^{188}Re:

– ^{99m}Tc, important isotope for nuclear medicine, has been obtained and applied both on inorganic (iron oxides and carbon allotropes) and polymeric supports;

– ^{99m}Tc-Fe_2O_3 can be used for obtaining anatomical information about cancerous tissues and tissue functions without the need for surgery;

– ^{99m}Tc-Fe_3O_4 can be used as potential radiopharmaceuticals in nuclear medicine; for sentinel lymph node detection. Its synthesis route is: co-precipitation of $FeCl_3$ and $FeCl_2$ in the presence of NaOH and further labeled with ^{99m}Tc (having final activity of 7.4 MBq / 0.1 mL and size 50 – 60 nm);

– ^{99m}Tc was used as the radiolabeling isotope to study the biodistribution of oxidized multi-walled carbon nanotubes (OMWCNTs, 1 – 10 nm in length, 10 – 30 nm in diameter) and / or nanodiamonds (NDs, 2 – 10 nm in size, functionalized with –OH and –COOH on the surface);

– ^{99m}Tc-polymer-containing nanoparticles in technetium-tin colloid in the nanoscale size of 4 to 13 nm were prepared from SnF_2, NaF, poloxamer (special nonionic triblock copolymers), PVP, and ^{99m}Tc pertechnetate (1480 – 1850 MBq) as precursors. Use as a radiopharmaceutical in nuclear medicine, which is very useful as a radioactive tracer for identifying sentinel nodes, such as axillary lymph nodes in breast cancer;

Nanoparticles containing ^{198}Au:

– Nanoparticles, containing its radioactive isotope ^{198}Au, can be obtained from ^{197}Au nanoparticles by neutron irradiation;

– Mainly biomedical and therapeutic applications (targeted delivery of therapeutic payloads);

– Unexpected applications: radiotracer application, consisting purely of a gold and silica particles, whose particle size could be varied from tens to several hundred of nanometers by controlling the catalyzer and precipitation time, could be used to investigate multiphase system in process industries without disturbing the system operation. Also, such nanoparticles were proposed to be utilized as a tracer in petrochemical and refinery industrial processes where the internal temperature is extremely high and the conventional organic radioactive labeled compounds would be decomposed.

Other isotopes are used for different purposes: ^{14}C / SiO_2 (to trace and image the long-term behavior of nanoparticles in biological and environmental systems); Cd^{125m}Te / ZnS (biodistribution studies); ^{18}F (bioimaging); $^{59}Fe_2O_3$ (biodistribution studies); Ce isotopes (137m, 139, 141, 143) (environmental behavior of ceria nanoparticles; medical applications); ^{153}Sm, ^{152}Eu (similar applications).

Irradiation of Fe_3O_4 nanoparticles (manufactured nanomaterials increasingly used in healthcare for different medical applications ranging from diagnosis to therapy) with a proton beam was carried out to produce effectively ^{56}Co as radiolabel (nuclear reaction $^{56}Fe(p, n)^{56}Co$) – see the scheme below. Note the use of nuclear techniques for the quantification of Fe_3O_4 nanoparticles in biological systems. Current industrial uses are limited.

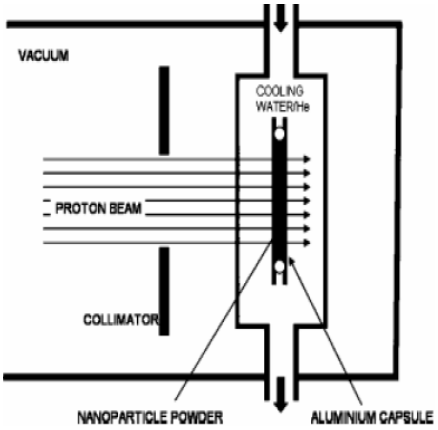

Radioactive nanoparticles can contain radionuclide alone or be supported in inorganic (silica, carbon nanotubes, nanodiamonds, iron oxides, ZnS and other salts) or organic compounds, polymers and biomolecules in the form of nanoparticles.

Methods for their obtaining include conventional chemical methods (such as, for instance, interfacial polymerization, co-precipitation, microemulsion or double-emulsion solvent-evaporation technique, hydrothermal method) and irradiation with neutron, proton, and deuteron flows.

Among disadvantages of applications of radioactive nanoparticles, only small volumes of material are required to create rather large contamination events; additionally, special permissions are needed to work with radionuclides.

Synthesis of nanoparticles from coordination compounds

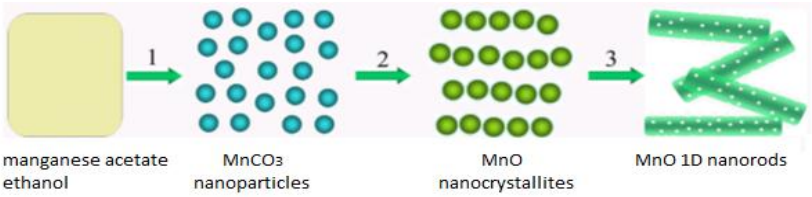

Possible formation mechanism of the MnO 1D nanorods

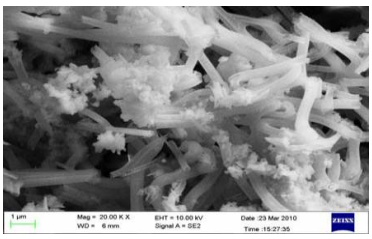

Alumina nanofiber from PVP-aluminum *iso*propoxide precursor.

Precursors

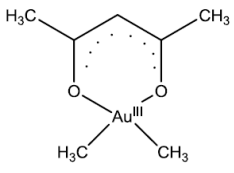

Beta-diketonates (for Au NPs)

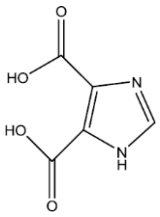

4,5-imidazoledi carboxylic acid (Ni NPs)

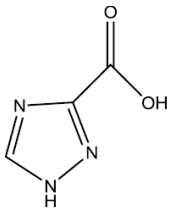

^{1}H-1,2,4-triazole-3-carboxylate (CdO NPs)

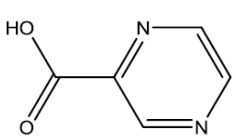

2-pyrazinecarboxylic acid (PbO NPs)

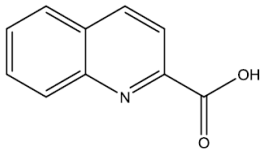

2-quinolinecarboxylic acid (PbO NPs)

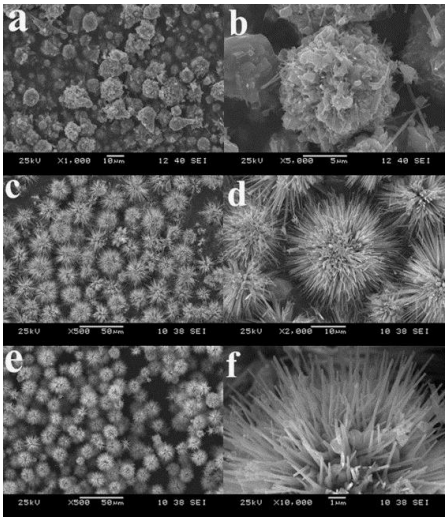

NiS nanourchins, obtained from nickel diethyldithiocarbamate [Ni(DDTC)2]

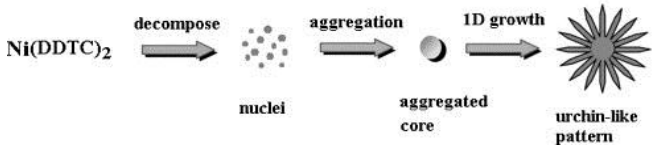

Possible formation process of the urchin-like NiS architecture.

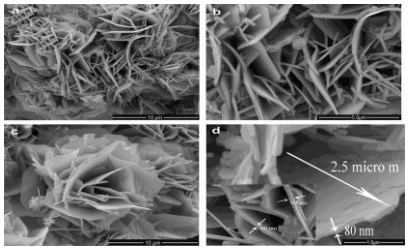

Cups powder from Cu(II) – thiourea complex

Synthesis of nanoparticles from organometallics

The picture represents 3D structures grown by exposure of a substrate to a TMGa organometallic precursor flow (~ 1 sccm). Carrier gas flow: N_2: 2 – 10 slm. Its growth depends on the reactor conditions (50 – 760 Torr), giving rise to grass leaf (450 – 550 °C), neuron (550 – 600 °C), balloon, cylinder and scepter (600 – 750 °C) shaped structures. Most of these structures are held by carbon membranes, and contain Ga inside. Growth duration is 5 to 15 min.

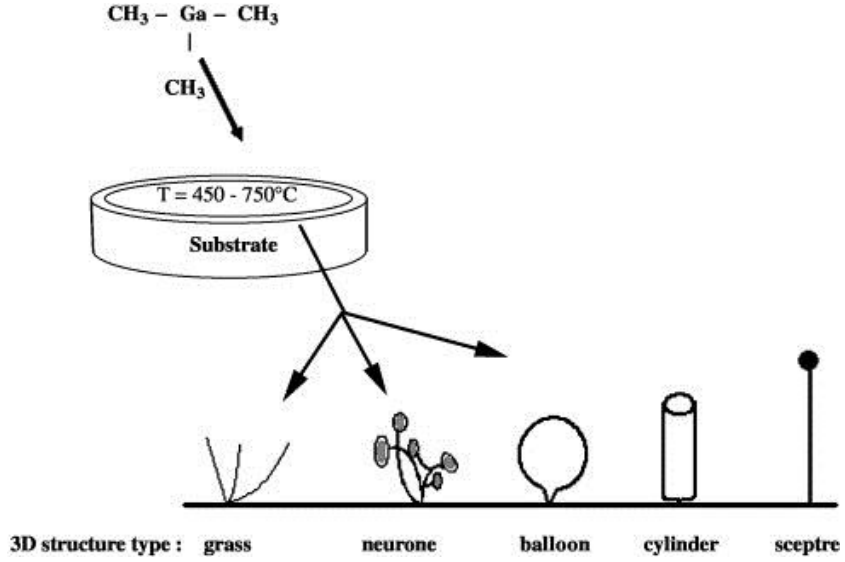

TMGa (trimethylgallium) + InP 650°C → GaInP wire capped by (Ga, In) ball + carbon radicals TMGa + TMIn + InP 650 °C → GaP wire capped by (Ga) ball+carbon radicals.

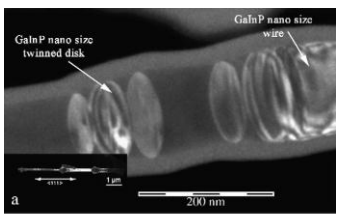

(Ga,In)P (in different conditions)

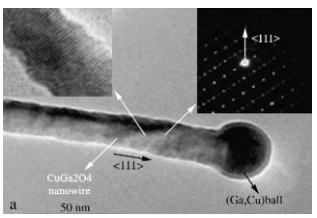

$CuGa_xO_y$

In process of electron beam induced decomposition, electron induces e.g. reactions of adsorbed $MeCpPt^{IV}Me_3$: $MeCpPt^{IV}Me_2(ads.) + e^- \rightarrow PtC_8(ads.) + H_2(g)\uparrow + CH_4\uparrow$.

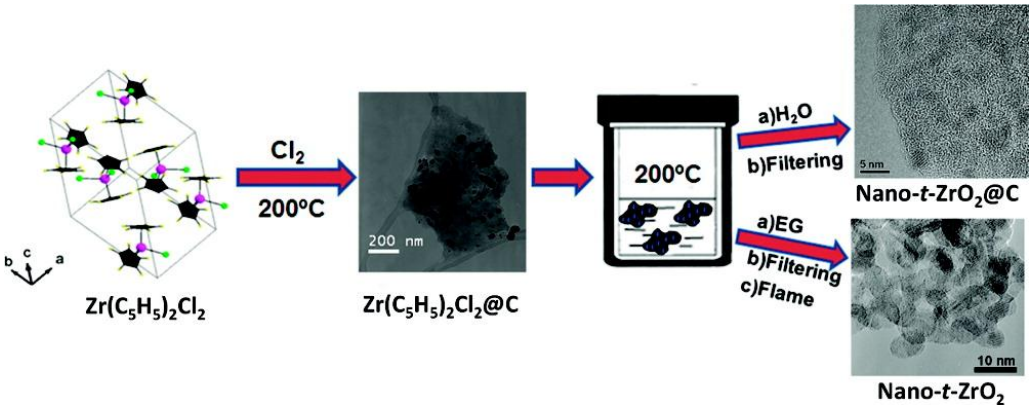

There is shown the schematic representation of the synthetic procedure followed in the synthesis of nanometric tetragonal ZrO_2. On the left a unit cell of the $Zr(C_5H_5)_2Cl_2$ precursor is drawn.

References

1. A. K. Geim, K. S. Novoselov. The rise of graphene. Nat. Mater., 2007, 6, 3, 183-191.
2. V. V. Pokropivny, V. V. Skorokhod. Classification of nanostructures by dimensionality and concept of surface forms engineering in nanomaterial science. Mater. Sci. Eng. C, 2007, 27, 5-8, 990-993.
3. V. V. Pokropivny, V. V. Skorokhod. New dimensionality classifications of nanostructures. Physica E, 2008, 40, 7, 2521-2525.
4. E. F. Kustov, V. I. Nefedov. Theory and classification system of nanostructures. Dokl. Phys. Chem., 2007, 414, 2, 150-154.
5. B. Kharisov, O. Kharissova, U. Ortiz–Mendez. Handbook of Less-Common Nanostructures. 2012, Taylor & Francis – CRC Press: http:// www.crcpress.com/product/isbn/9781439853436; ISBN: 9781439853436
6. O. V. Kharissova, B. I. Kharisov, V. M. Jiménez–Pérez,. B. Muñoz–Flores, U. Ortiz–Méndez. Ultrasmall particles and nanocomposites: State of the art. RSC Adv., 2013, 3, 22648-22682.
7. B. I. Kharisov, O. V. Kharissova, S. S. Berdonosov. Radioactive nanoparticles and their main applications: Recent advances. Recent Patents on Nanotechnology, 2014 – in press.

RECENT ADVANCE IN ELECTROPHORETIC DEPOSITION FOR NANOTECHNOLOGIAL APPLICATIONS

G. Günkaya [1], H. Kurama [2]

[1] Anadolu University
Eskişehir, Turkey
ggunkaya@anadolu.edu.tr
[2] Eskişehir Osmangazi University
Boron Research Center
Eskişehir, Turkey
hkurama@ogu.edu.tr

Accepted September 1, 2014

1. Introduction

Nanotechnology can be defined as a study and engineering of matter at the dimensions of 1 – 100 nanometers, where the physical, chemical, or biological properties are fundamentally different from those of the bulk material. A bulk material should have constant physical properties regardless of its size, but at the nano-scale size, dependent properties are often observed. With approaching the nanoscale, the percentage of atoms at the surface of materials becomes significant and the properties of materials are changed [1]. Therefore, nanoparticles are of great scientific interest as they are effectively a bridge between bulk materials and atomic or molecular structures. In order to explore novel physical properties and phenomenon, real size potential applications of nanostructure, the ability to fabricate and process of nanomaterials should clearly concerned as a priority of nanotechnology.

Nowadays, the economic and societal promise of nanotechnology has led to investments by governments and companies around the world. Nanoscale based science has numerous applications across nearly all economic sectors and allows the development of new technologies with a broad commercial potential, such as nanostructured materials, nanoscale based manufacturing processes, and nanoelectronics [2]. Especially, for developing countries, it can provide new opportunities and benefits, if research areas are prioritized on those that can address the most pressing needs of the country. In 2000, the United States launched the world's first national nanotechnology program. From 2001 through 2013, the federal government invested approximately $ 17.9 billion in nanoscale science, engineering, and technology through the U.S. National Nanotechnology Initiative (NNI) [3].

The use of nanotechnology in the knowledge intensive based products to increase the competitiveness of Turkey in global market is also concerned as a priority of Turkey's National Science and Technology Policies. In the Vision 2023 Strategy Document, nanotechnology is identified as one of the strategic technological fields with strategic focus areas; nano-photonics, nano-electronics, nano-magnetism, nano-materials, nano-characterization, nanofabrication, nanosized quantum information processing and nano-biotechnology [4, 5] Nanotechnology is also mentioned in the Turkish Industrial Strategy Document 2011 – 2014. The industrial strategy and action plan aims to expedite the transformation to an industrial structure. At present, 32 research centers consist of universities, government research and development

institutes and SMI's are conducting research studies in nanotechnology / nanoscience fields. These centers have recognized great potential on the manufacture of nanotechnology based products.

The physical, chemical, biological or hybrid methods such as vapor phase growth, liquid phase growth, solid-state reaction, hybrid growth, high-energy ball milling, sputtering, sol–gel, chemical bath deposition, molecular beam epitexy can be evaluated to fabrication of nanomaterials. However, the application of electrophoretic deposition techniques, especially to manufacturing of nanotechnology based coating materials, has shown remarkable growth in recent years.

1.1. Electrophoretic deposition

Electrophoretic Deposition is a colloidal processing method for the deposition of materials in applied electric field. The charged powder particles, dispersed or suspended in a liquid medium are forced to move toward the oppositely charged electrode with application of a DC electric field. The particles accumulate at the deposition electrode and thus create a relatively compact and homogeneous thin film (**Figure 1**). In order to effectively applying of this technique to process materials, it is essential to produce a stable suspension containing charged particles free to move when an electric field is applied. The EPD has been known since 1808 when the Russian scientist Reuss observed an electric field induced movement of clay particles in water [6]. The first practical use of the techniques occurred in 1933 with deposition of thoria particles on a platinum cathode as an emitter for electron tube application, was patented in USA. Later, it was mainly used for the processing of traditional ceramics, including enamels and porcelain. However, in recent years, the interest has been shifted to the processing of functional ceramics, composite ceramics, biomaterials and deposition of nanoparticles combined with carbon nanotubes to produce advanced nanostructured materials.

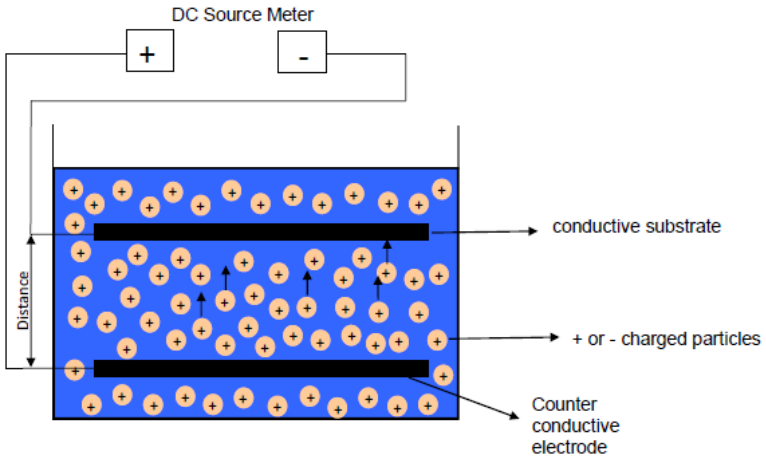

Figure 1. A schematic representation of EPD process, positively charged particles in suspension migrating towards the negative electrode [1].

1.2. Effected factors

It is evident from the literature reports [7 – 11] a large number of parameters regarding the suspension and application properties are affecting the quality of deposit formed in EPD. The physicochemical natures of suspended particle and solution, surface properties of the

powder, electrical conductivity of medium, type and concentration of the additives and the parameters related to the process, i.e. deposition time, applied voltage, concentration of solid could be given as main parameters that influence the process.

In general, a well-dispersed stable suspension is providing a better deposition during EPD compared to an unstable or agglomerated powder suspension. The particle size and the Zeta potential of solid surface (ζ), are important parameters that determine the suspension stability and mobility. Although there is no string rule to specify particle sizes suitable for electrophoretic deposition, to prevent the settle of particles during deposition resultant from gravity force and cracking of deposit at following drying steps, the particles have a range of 1 – 20 μm is generally preferred. As indicated above, electrophoresis is the phenomenon of motion of particles in a colloidal solution or suspension in an electric field, and generally occurs when the distance between particles over in which the double layer charge falls to zero and effective forces becoming larger [7]. In this condition, the particles will move relative to the liquid phase when the electric field is applied.

The stability of the colloidal system can be determined by the total potential energy of interaction between particle surfaces (V_T) as previously described by DLVO theory given in Eq. (1):

$$V_T = V_A + V_R + V_S, \quad (1)$$

where, V_A is representing the sum of these van der Waals attractive and V_R is electrical double layer repulsive forces that exist between particles as they approach each other due to the Brownian motion [12, 13]. The combination of these two functions is the fundamentals of the DLVO theory. The potential energy occurred by the solvent V_S, is only makes a marginal contribution to the total potential energy over the last few nanometers of separation. Therefore, the balance between V_A and V_R is more important on the stability of the suspension. These forces are potentially much larger and operative over a much larger distance. The DLVO theory proposes that an energy barrier resulting from the repulsive force prevents the approaching of two particles one another and adhering them together (**Figure 2**).

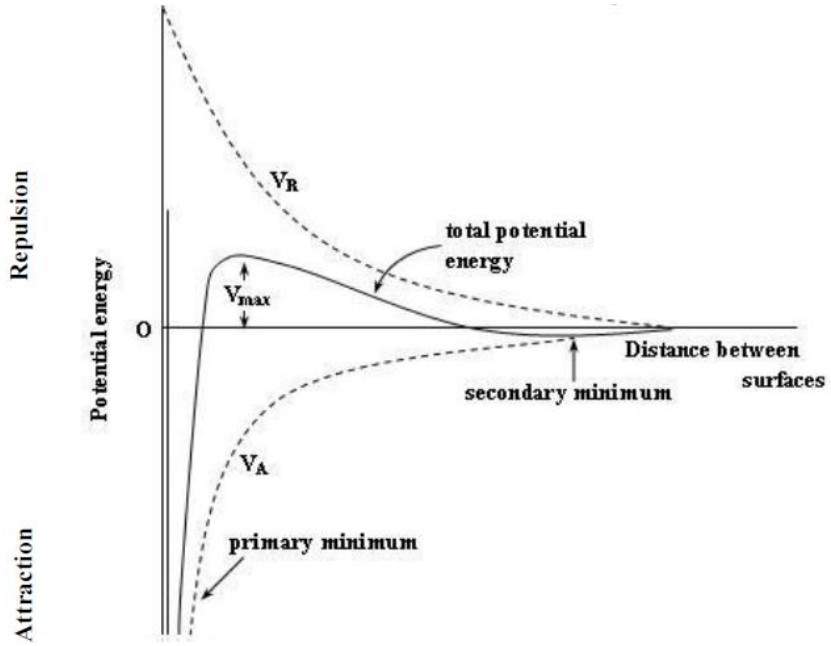

Figure 2. A variation of free energy diagram with particle separation according to DLVO theory [12].

However, if the particles collide with sufficient energy to overcome that barrier, the attractive force will pull them into contact where they adhere strongly and irreversibly together. Therefore, if the particles have a sufficiently high repulsion, the dispersion will resist flocculation and the colloidal system will be stable. The van der Waals forces dominates at both large and small separation, however, in former case its value may be too small to be significance. At small V_R must approach a finite magnitude, whereas the absolute value of the V_A increases very markedly and hence is expected to pull the surface into a deep attractive well, which called the primary minimum. On the other hand, the secondary minimum is only occurred at larger distance where a much weaker and potentially reversible adhesion between particles exists [12].

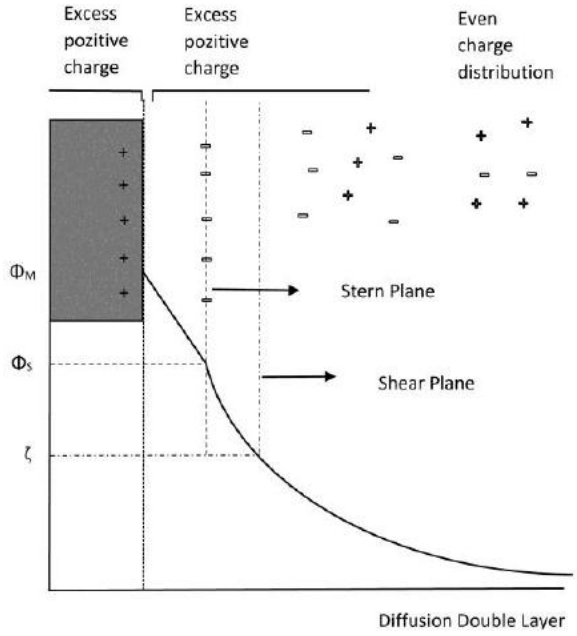

Figure 3. Typical plot of diffusion double layer and charged layers.

The magnitude of the zeta potential that can be described as the potential difference between the particle surface and the shear layer plane formed by the adsorbed ions is also referred as a key indicator to the stability of the colloidal system (**Figure 3**). If all particles in suspension have a large negative or positive zeta potential, they will tend to repel each other and there will be no tendency for the particles to come together. However, if the particles have low zeta potential values then there will be no force to prevent the particles coming together and flocculating. Although there is no string level to separate the stable and unstable regions, the general dividing line between stable and unstable suspensions is generally taken at either + 30 mV or – 30 mV. Particles with zeta potentials more positive than + 30 mV or more negative than – 30 mV are normally considered stable. However, if the particles have higher densities from the dispersant, they will eventually sediment and forming a close packed bed (i.e. a hard cake) [14].

As can be seen from **Figure 4**, the electrostatic potential decays exponentially with distance away from the shear plane. The inverse of the decay constant is a distance called the Debye double thickness. The thickness of the double layer (κ^{-1}) depends upon the concentration of ions in solution and can be calculated from the ionic strength of the medium.

The higher the ionic strength, faster the decay and hence the more compressed double layer becomes (**Figure 5**). Therefore, the thickness of the double layer determines the magnitude of zeta potentials. At high enough salt, the double layer collapses to the extent that the ever present attractive van der Waals forces overcome the charge repulsion.

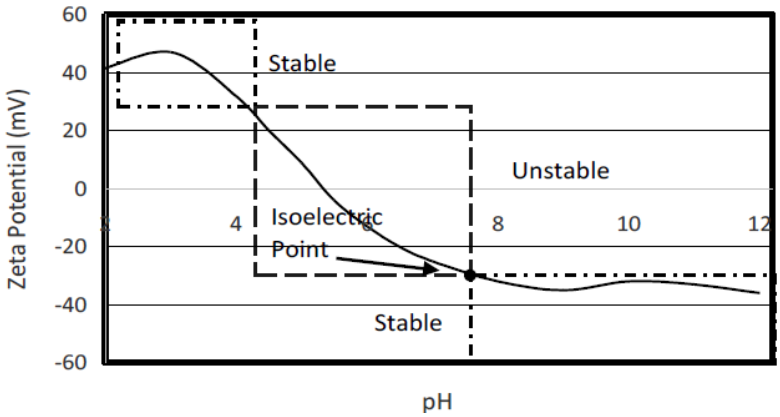

Figure 4. Typical plot of zeta potential variation versus pH Showing the position of the isoelectric point and the pH values where the dispersion would be expected to be stable.

Not only the suspension stability but also the electrical conductivity of the solution is remarkably influenced from the ion concentration of the solution. The conductivity of the solution increases rapidly with increasing ion concentration of the suspension. However, it should be noted that at high ionic concentration, the rate of agglomeration also increases. This leads to occurrence of larger agglomerates and the electrophoretic mobility of the particles reduced [15].

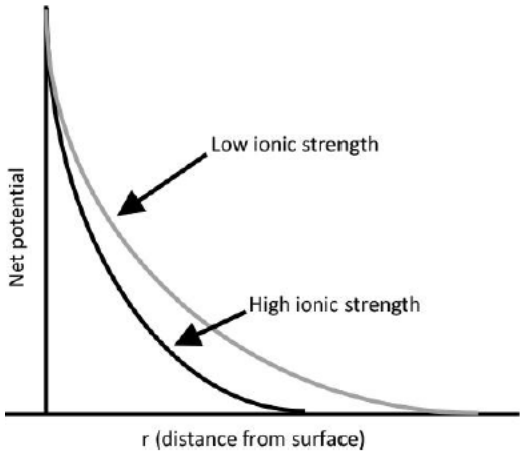

Figure 5. Effect of ion concentration of solution on the zeta potential of the surface.

Therefore the optimization of the suspension parameters is required as a first step of the indented deposition. After the parameters related to the suspension are fixed, the process parameters should be altered conveniently to obtain desired deposition. Obviously, the most dominant parameters are applied voltage, deposition time and concentration of particle in the suspension. Invariably, high applied potential leads to higher deposition rate but care has to be taken to ensure stable current density to obtain uniform deposition. Similarly, higher deposition rate is expected to increasing of the particle concentration and the deposition time [16].

2. Applications

EPD is practical and versatile method that can be used for deposition of various materials in aqueous system [17, 18]. In a wide range of industrial applications, the increased demand to use of different kind of engineering materials has also led to the increasing interest to EPD because of its low operation cost, simple equipment requirement, flexibility and high process efficiency in recent years. A performed research works focused on the production of porous surfaces by electrophoretic infiltration (EPI) can be given a new research interest. For example, the fiber materials like tows etc. can be coated by EPD or EPI, this leads to production of more effective porous membranes [19, 20]. In general the membranes used in filtration can be produced in different methods with various framework structures and pore sizes [21, 22]. However, recent advance on the membrane science showed that porous materials with increased lightweight, improved fracture toughness, damage tolerance and thermal shock resistance can be produced by EPD [19]. The production of dense membranes of zeolite and lanthanum cobaltite can be given as examples [21 – 24].

In ceramic industry, the deposition of uniform coatings made of clay based material, vitreous enamel or alumina on electrically conductive surfaces by EPD has been received extensive interests in industrial scale especially for the production of sanitary ware, tiles, table ware, etc. The main advantage's of EPD in these clay based applications was reported as achieved improvement on the formation rates compared to slip casting. The excellent smoothness and uniformity of the coated surface compared to conventional dipping or spraying processes, was also made the employment of the method to production of vitreous (or porcelain) enamel coatings on metals. EPD can be applied to any solid that is available as a fine powder (e.g. < 30 μm), therefore it has found several applications in the industrial production of domestic white ware in the early 1970s [8]. Besides than the mentioned traditional areas, within the last two decades, it has also been increasingly employed to enhance the substrate properties of the material used in advanced ceramics production. The usability of the submicron powders, d>100 nm made it more effective compared the other production methods. Boccaccini et al, reported that the hydrated alumina which was produced by sol-gel technique and coated by EPD has an several advantages than the material produced with dip coating. In this way, it's possible to obtain thicker, denser and more adherent coatings [19]. Furthermore, the EPD coatings can also be evaluated for the improvement of wear and oxidation resistance of the ceramic or composite materials. Thin or thick layer coating on the substrates surface leads the production of interlayer and this prevents the conduction or corrosion of the surface. In addition, the gaining of different features to the materials by surface coating could be considered a further benefit of the method. Therefore it was found several applications in the production of biomedical implants, electronic, magnetic and related devices [7 – 11]. Biomaterial is a synthetic material that used to make devices to replace part of a living system or to function in intimate contact with living tissue. EPD is able to produce uniform coatings with high microstructural homogeneity, is therefore, to deposition as thin and thick films on substrates of different shapes and the three-dimensional complex and porous structures of the surface make it preferable method to production of biomaterials [25]. The applications in the biomaterials field probably started with the development of hydroxyapatite (HA) $Ca_{10}(PO_4)_6(OH)_2$ coatings on Ti substrates decades ago [25, 26]. The development of

multifunctional coatings that strongly stick to bone tissue and having anti-infectious and antiallergic properties has evoked a higher synergy to selection of this method [25]. The improvement on the deposition of bioactive hydroxyapatite and related calcium phosphate films on biocompatible metallic substrates (e.g. $TiAl_4V$ alloys and Fecralloys) and the deposition of zirconia on dental crowns and bridges [27] has been marked as successful applications of EPD [28, 29]. Laminates, functionally graded materials and fiber reinforced ceramic composites are the important materials and have several applications in industry especially for the high mechanical durability of the materials is required. Therefore, in literature, comprehensive efforts have been devoted to usability of EPD to fabrication of ceramic laminates; fiber reinforced ceramic composites and functionally graded materials. In particular, the zirconia/alumina and Al_2O_3 / Y-TZP system can be given as interesting examples due to the high fracture resistance of the coated surfaces [30]. The studies [9 – 11] showed that the gradual transition to microstructure, the strength of the bond between composites increases and mechanical durability (toughness, hardness) of the material surface is enhancement [31 – 34]. The well established bonding between ZrO_2, SiC and Al_2O_3 composites reported by Askari et al. is shown in **Figure 6**.

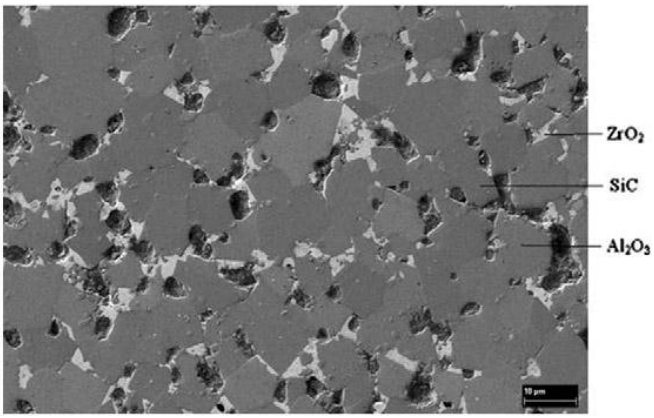

Figure 6. Microstructure images of the homogeneous layers [34].

Versatility of EPD was used to deposit different amount of SiC and ZrO_2 on the surface. Aim of this was to reach and control different mechanical properties in the layers. Beside, preferring various thermal processes porosity can be changed. As a result porosity and all these affect on mechanical and physical properties of the functionally graded material with changing hardness, fracture toughness, grain size and shrinkage of the bulk was obtained.

Fabrication of graded WC–Co composites in non-aqueous acetone suspension using WC and various amounts of Co particles can be given as a successful application of EPD in graded material production. It was reported that the amount of Co particles in suspension strongly effect the fracture resistance of the product and material has high fracture resistance can be obtained by this process [35].

Rather than the relatively higher particle sizes, the evaluation of nano particles which are below than 100 nm, and stabilization of them in various mediums, has also been subjected to several research works for the production of monolithic ceramics, ceramic coatings and ceramic films. In these studies, the deposition were performed within the special colloidal systems either aqueous or non-aqueous suspension. An electrophoretic coating of

nanocrytalline TiO_2 films on Ti-metal sheets is studied by Tan et al. [36]. It was showed that the light scattering and transparent film layers deposited on metal surface behave as a photoelectrodes and caused to significant improvement in the photo to current conversion hence enhanced the solar absorption capacity of the surface to light scattering. They proposed that this method can be used as a cost effective and simple technique in the production of dye-sensitized- solar cells with increasing conversion efficiency.

The discovery of carbon nanotubes (CNTs) by Iijima in 1991 has initiated the usability of nanometarials in production industry. An increased surface area along with enhanced electrical/optical properties makes them suitable for numerous applications such as nanoelectronics, photovoltaics and chemical / biological sensing. In the last few years the interest of the scientific community has been concentrated on the production of carbon nanotubes, both single-walled (SWCNTs) and multi-walled (MWCNTs) [37 – 40]. Many of the properties of CNTs are now well-known and their usage is spreading with current researches that focused on the expanding of the potential applications [41 – 43]. These studies recognized that homogeneous dispersion of CNTs within the appropriate polymer, ceramic or metallic matrix is fundamental to production of particular arrangements of CNTs to combine with other materials. Therefore, EPD has been found a very convenient method to manipulate CNT to form ordered, oriented nanotubes arrays [37]. In the study performed by Boccaccini et al. [37], several solvents including distilled water, mixtures of acetone and ethanol, pure organic solvents such as ethanol, isopropyl alcohol, *n*-pentanol, ethyl alcohol, tetrahydrofuran, dimethylformamide and deionised water with pyrrole have been employed to preparation of stable CNT suspension for EPD. It was reported that the presence of charger salts improved the adhesion of CNTs to substrates and also increased the deposition rate. CNTs films produced by EPD can be used for various applications like emission devices, biomedical scaffolds, catalyst supports, structural composites, fuel cells, capacitors and gas sensors [16, 37].

A porous morphology of the CNT film coated on stainless steel substrate by EPD is shown on **Figure 7**. The SEM images clearly indicated a homogeneous dense network with needle like structures that ensures the required porosity. The side view given in **Figure 7b**, also revealed a successful deposition of the CNT on the substrate.

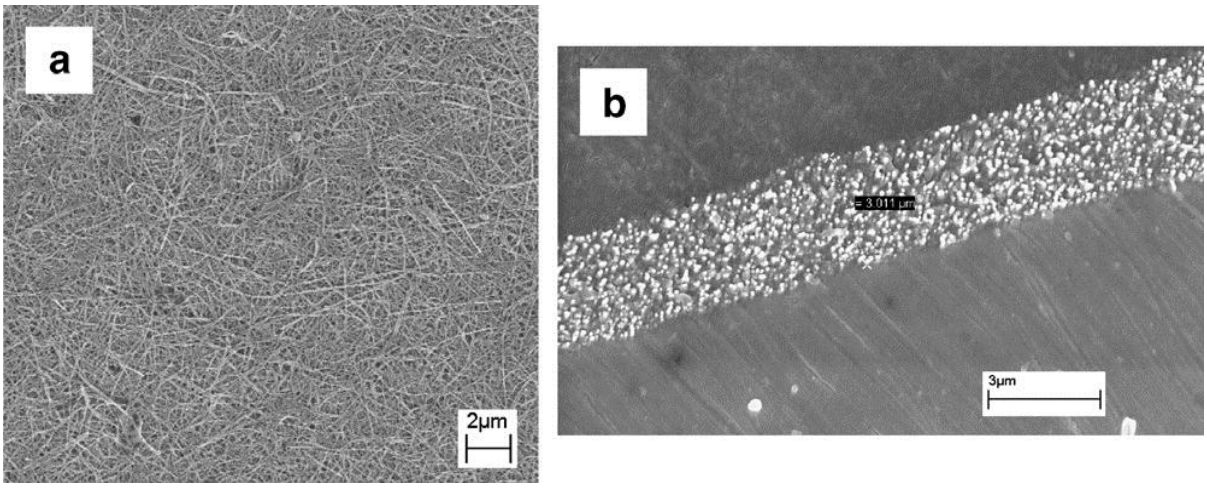

Figure 7. SEM images of CNT obtained by EPD on stainless steel substrates. (a) surface view, (b) side view.

The usage of silica nanoparticles with multi-walled CNTs by EPD was examined by Chicatun et al. [44]. They studied SiO_2 / CNT composite films on metallic substrates that can be used in the biomedical field or in thermal management devices. Another interesting approach was released by Li et al. [45]. In this study, the usability of EPD for the production of conductive substrates coated with manganese dioxide and multi-walled CNTs to obtain electrochemical super capacitors was investigated. It was found that the porous microstructure and fibrous crack free surface film layers with a pore size changes within the range of 10-100 nm can be deposited [45]. The test results also indicated that the value of specific capacitance (SC) decreases with increasing scan rate and increasing film thickness. As a result by changing the scan rate and film thickness, the magnitude of the SC can be controlled. The creating of CNT's with an oxide films of multilayered Fe_3O_4 / CNT, Eu_2O_3 / CNT or TiO_2 / CNT duo structures for optical, photocatalytic and energy-storage devices can be given remarkable studies found in literature [16]. By changing the parameters like number of the layer and thickness etc. property of the materials can be dramatically changed. TiO_2 was stated as one of the most effective material and, when TiO_2–CNT combination is used, the photocatalytic affectivity of the product was increased.

Electrophoretic deposition of nano-sized SiO_2 particles on metallic and ceramic substrates has recently been investigated by A. Charlot et al. [46]. In this study, the charging particles were stabilized by dispersing them in an alkali medium (pH=10). The results showed that silica film can be deposited with different thicknesses between 125 nm and 300 nm according to the applied electric field and deposition time. A better deposition performance obtained for thin silicate films on metallic and ceramic substrates than sol–gel process suggested that EFD can be used in the field of photonics, optics as antireflective layer or anti-corrosive coating. The applicability of EFD method to produce electroceramics coated with $BaTiO_3$ thick films [47, 48], ZnO thick films for sensor and actuator applications [49], thick films made of MgO for tunable electronic devices [50], $LiCoO_2$ electrodes for rechargeable lithium batteries [51, 52], carbon-polytetrafluoroethylene thin films for gas diffusion electrodes [53] and MgB_2 films fabricated by the diffusion of the Mg into the boron film and heat treatment of Mg/B coatings [54, 55] have also been reported by several research groups as a significant usage of EPD. In our previous studies [56 – 58], the usability of EPD to fabrication of suitable material for sensor applications has been studied. In these studies ZnO, $BaTiO_3$ and SnO_2 nano particles were concerned to obtain porous layers with high surface area on substrate. As its well know that ZnO is one of the most important oxide semiconductors for toxic and combustible gas sensing applications. Therefore, sub-micron sized ZnO particles were firstly synthesized by using homogeneous precipitation method and stabilized ZnO aqueous suspensions (5 wt. %) were than submitted to EPD tests. In deposition tests, gold-palladium electrode was used and the affect of applied voltage and deposition time on the product properties were discussed. The results indicated that a 10 μm thick homogeneous, porous layer can be obtained by EPD method. $BaTiO_3$ is also well-known dielectric material for electronic applications like multilayer capacitor, transducer, thermostat and electro optic devices. Although, some other metal oxides such as In_2O_3, TiO_2, a-Fe_2O_3, HfO_2 and $BaSnO_3$ have also been widely investigated for gas sensing applications, in literature, the use of $BaTiO_3$ was found as a relatively new research area. The performed tests showed that desired sensors with high sensitivity can be tailored by altering the substrates morphology with help of suitable dopants usage [56, 57]. $BaTiO_3$ crystals were synthesized with a novel one pot reaction nonaqueous method. In which the metallic

barium is directly dissolved in benzyl alcohol at slightly elevated temperatures. The synthesized spherical $BaTiO_3$ nanocrystals (appox. 5 nm) were stabilized in ethanol suspensions and than used for deposition process. Pt plated alumina was used as substrate. Various voltages were applied by altering the cathode to anode distance as well as deposition time for optimal process control. Because of the ethanol adsorbed on the surface of the nanoparticles, application of high voltages was possible without causing hydrolysis. The characterization test performed on the products dried in air atmosphere and sintered at different temperatures showed that relatively higher porous structure of the coated surface compare to CNT make it more preferable to gas sensor applications. The SEM images given in **Figure 8** confirmed the successful deposition of $BaTiO_3$ layers on Pt-coated alumina substrate.

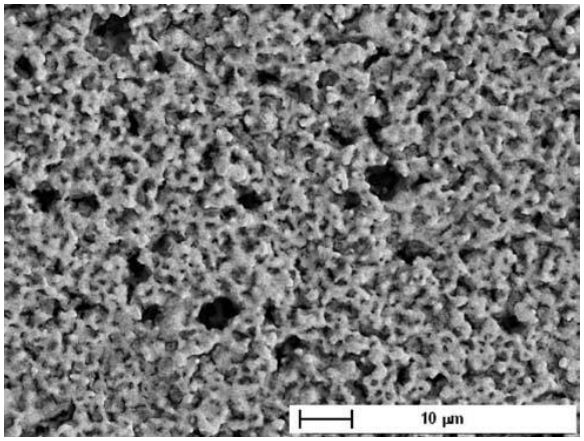

Figure 8. Microstructure of $BaTiO_3$ deposited surface by EPD.

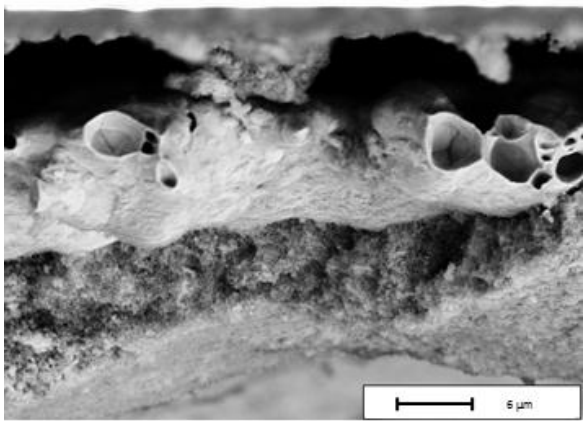

(a)

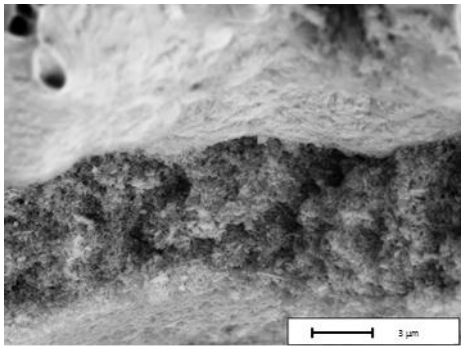

(b)

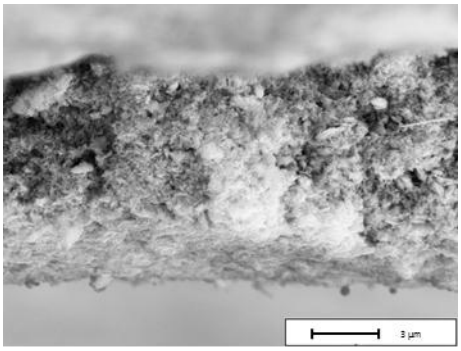

(c)

Figure 9. (a) 2500 ×, (b) 5000 × and c) 6000 × magnificated side view images of SnO_2 nanocrystallite film layers on Pt coated alumina substrate.

A further study [58] focused on the deposition of porous and homogenous SnO_2 films to production of gas sensor material showed that the deposited SnO_2film has a high sensitivity to liquefied petroleum gas (LPG) at various gas concentration and operation temperature. Nanosized SnO_2 (60 nm) particles were used in non-aqueous mediums with and without iodine to prepare stabilized EPD suspension. It was reported that highly porous, crack free and homogeneous SnO_2 films on Pt coated alumina substrate can be achieved with proposed flow sheet (**Figure 9**).

An interesting development to produce doped functional glasses was reported by Clasen et al. [59, 60]. In these studies shaping of a green body and doping were achieved in a single step and lower temperatures compared to conventional route. The doped glasses are normally created by melting silica at 2100 °C, however, at this high temperature most of the suitable dopants evaporate. As an alternative to conventional production way, the authors suggested to using of EPD, in which, the soluble salts firstly added into a silica suspension, these salts dissociate and the ions are adsorbed on the surface of the particles, which were then deposited by EPD producing a homogeneously doped green body.

Finally, it's no doubt that concentrated affords performed to using of EPD in the production of solid oxide fuel cells (SOFCs) as new electric power generation systems, should be concerned more important applications [61]. The increased interest in SOFCs is due to their high energy conversion efficiency, clean power generation, reliability, modularity, fuel adaptability, the fact that they are noise-free, have excellent long term stability and also due to the versatile nature of the technology for direct conversion of chemical energy to electrical energy. According to literature reports [62 – 64], the relative advantages of EPD in the production of SOFCs can be listed as follows; (a) deposit coatings on substrates of any shape, (b) control the deposition conditions thus being able to prepare porous coating as electrode and dense coating as electrolyte, (c) obtain laminate structures of electrodes and electrolyte and (d) produce Ni-yttria stabilized zirconia (YSZ) cermets (anodes) by electrophoretic co-deposition.

3. Boron history and its role in EPD

Boron compounds may have been known for about 6000 years, starting with the Babylonians. The Egyptians, Chinese, Tibetans and Arabians were reported to use such materials. The elemental form of boron was first recognized by Sir Humphry Davy and by Joseph Louis Gay-Lussac and Louis Jacques Thénard in 1808. It was prepared by reduction of boron trioxide with potassium and by electrolysis of moistened boric acid. Although, the purity of their products was about 50 %, in fallowing years, higher purity boron was produced by well-known Moissan process with a purity of 90 %. The product is light boron in color and is considered to be amorphous. Crystalline boron was obtained in 1856 by the German chemist Friedrich Wöhler by dissolving amorphous boron in molten aluminum. On cooling crystalline boron separates out and recovered by dissolving aluminum in sodium hydroxide. E. Weintraub of General Electric laboratory succeeded in preparing 99 % pure boron by decomposition of BCl_3 in an electric arc. Since then numerous methods have been developed to find new alternatives for the producing commercial quantities of pure boron. The discovery of boron hydrates by German chemist Alfred Stock and co-workers in 1912 has widened the utilization of boron compounds in industrial applications. Research on boron hydrides was started in the United States in 1931 by government sponsorship of various military programs to develop high-

energy fuels for rockets and aircraft during World War II. Boron fuels (alkyl penta- and decaboranes) created great interest because they possessed much higher heats of combustion than conventional hydrocarbon fuels. Large quantities of boron fuels were manufactured. Progress in borane research led to the discovery of a large number of new compounds [65].

In principle boron as a material, have many excellent surface properties, including corrosion resistance, very high hardness, refractory properties and a strong tendency to bond with most substrates. The potential benefits of the boron have not been sufficiently realized because it has high ionization energies, which make it impossible to convert into ionic form. Furthermore, its lightweight and high-melting point prevents the deposition of boron in thin film form [66]. However, in recent years, Hyam et al. 2007 reported that the deposition of thin film boron is possible by EPD, if the mobility of boron particles in solution and the stability of the suspension are provided. The degree of stoichiometry in the electrophoretic deposition is generally controlled by the degree of stoichiometry in the powder used. Therefore, it is important to use similarly charged particles and similar solvent–binder–dispersant systems for gaining better control of layer thickness. The principal driving force for EPD is the charge on the particle and the electrophoretic mobility of the particles in the solvent under the influence of an applied electric field.

In EPD tests ethylene glycol, D.M.S.O and acetone were tested as an organic media and it was found that the deposition tests performed in acetone solution showed no gravitational deposition [67]. The required surface charge on boron particles was obtained by addition of iodine in acetone solution. According to chemical reaction given in Eq. (2), the concentration of H^+ ions in the suspension increases and adsorption of H^+ ions on the neutral boron particle surfaces leads to inducing positive charge on the boron particles:

$$(CH_3)_2C{=}O + I_2 + B \rightarrow B^+ + CH_3{-}C{\downarrow}O^- CH_2I + HI. \quad (2)$$

These particles with positively charged surface repel each other and make the suspension stable due to electrostatic stabilization. The authors also suggested that EPD could be concerning as a first step to synthesis of magnesium diboride (MgB_2) superconductor. Superconductivity can be defined as a losing of all electrical resistance of an element or metallic alloy when the material cooled below a characteristic critical temperature. It was first discovered in 1911, when Dutch physicist Heike Kamerlingh Onnes cooled mercury to 4 degrees Kelvin. In recent years, the discovery of superconductivity at 39 K in binary metallic MgB_2 has attracted great interest in fundamental physics and number of potential applications. Specifically, lack of weak-links, a relatively high-critical temperature (T_c) of 39 K, and the low cost of the starting materials make MgB_2 a promising candidate for practical applications [66, 68 – 70]. The synthesis of MgB_2 as powder or thin film form can be performed by several techniques including mechanical alloying, spark plasma sintering (SPS), and boron thin films by pulsed laser deposition (PLD), magnetron sputtering, plasma enhanced chemical vapor deposition (PECVD) and electron beam evaporation [66]. As an alternative to these techniques, an electrodeposition of elemental boron films by applying high potential looks like a very promising method for further production. The authors tested the affect of particle size on the charge transfer and growth mechanism during electrophoretic deposition in suspension and reported that ZP of boron particles increases with increase in particle size, which helped to increase the stability of the suspension solution. The boron films prepared from a suspension of coarse (2.62 μm) particle size was found to be uniform, thick and suitable for magnesium diffusion as compared to the film formed from the medium (1.8 μm) and fine particle size (0.8 μm) suspension solution. The difference in particle

size of boron in suspension changes the nucleation mechanism and current density in the electrolytic cell [66].

Recently, Raddaha et al., released another interesting report titled as Chitosan/h-BN/TiO_2 composite coatings on stainless steel (316L) substrates. The article presents the results of an experimental investigation designed to deposit chitosan / hexagonal boron nitride (h-BN) and chitosan/h-BN/titania (TiO_2) composites on SS316L substrates using EPD for potential antibacterial applications. Electrophoretic deposition offers important advantages in the deposition of complex compounds. Chitosan is an interesting polymer that has been preferably used to produce a variety of coatings in combination with EPD. It is a cationic polysaccharide that has been used for biocompatible coatings and drug delivery [71]. Due to its biodegradability, biocompatibility, non-toxicity and antibacterial properties, chitosan has attracted much attention for a wide variety of biomedical applications. On the other hand, h-BN presents a layered structure with many unique engineering properties and it has been also preferred material for many biological applications due to the its improving role on the mechanical and optical properties of the final composites.

The influence of EPD parameters, i.e. voltage and deposition time and relative concentrations of chitosan, h-BN and TiO_2 in suspension on deposition was evaluated and reported that h-BN and TiO_2 particles were dispersed in the chitosan matrix through simultaneous deposition. The adhesion tests between the electrophoretic coatings and the stainless steel substrates by using tape test technique showed that the adhesion strength corresponded to 3B and 4B classes. Corrosion resistance, evaluated by electrochemical polarization curves, indicated that corrosion resistance of the chitosan / h-BN / TiO_2 and chitosan / h-BN coatings were enhanced compared to the bare stainless steel substrate [71].

Chitosan is insoluble in water and organic solvents. However, protonated form of it can be dissolved in water-ethanol mixtures at low pH. Under this condition, the amine groups of chitosan are protonated (Eq. (3)) and applied an electric field provides motion of the charged macromolecules towards the cathode:

$$Chit–NH_2 + H_3O^+ \rightarrow Chit–NH_3^+ + H_2O. \quad (3)$$

As a consequence of the pH increase at the cathode surface due to electrochemical decomposition of water, chitosan loses its charge and forms an insoluble deposit:

$$Chit–NH_3^+ + OH^- \rightarrow Chit–NH_2 + H_2O. \quad (4)$$

4. Conclusion

EPD is the most attractive surface deposition method for different kind of applications from traditional to high technology, mass production and newly employed ones. The method provides precision control of thickness and deposition rate and deposition selectivity. Mono/multilayer coatability of the material surface in the desired pore range and structure allowed to use it for the production of composites, nanotechnology materials, bio materials, sensors, optic devices, functionally graded materials from nanometer range to micrometer range as a preferable method. Furthermore, the versatility, three dimensionally controlled nano structures and building of nano composite capability in the form of dense or porous configuration expected to the expanding of it within the innovative materials production market.

References

1. K. G. Joshi, S. B. Bajaj, S. S. Ingle. IOSR–JMCE, 2013, 34.
2. M. Roco, B. Harthorn, D. Guston, P. Shapira. Nanotechnology Research Directions for Social Needs in 2020. 2011, Springer, 561.
3. J. F. Sargent Jr. The National Nanotechnology Initiative: Overview, Reauthorization, and Appropriations Issues. 2013, Congressional Research Service, 1.
4. A. Hullmann. The Economic Development of Nanotechnology – An Indicators Based Analysis. 2006, Eur. Comm., DG Res., Unit "Nano S & T – Convergent S & T", 27.
5. Nanotechnology in Turkey. http://statnano.com/news/44475, 2013, Nano Statistics, Nano Science, Technology and Industry Scoreboard.
6. I. Zhitomirsky. JOM-e, 2000, 52, 1.
7. L. Besra, M. Liu, Prog. Mater. Sci., 2007, 52, 1.
8. I. Corn, M. P. Ryan, A. R. Boccaccini. J. Eur. Ceram. Soc., 2008, 28, 1353.
9. P. Sarkar, P. S. Nicholson. J. Am. Ceram. Soc., 1996, 79, 1987.
10. A. R. Boccaccini, I. Zhitomirsky. Curr. Opin. Solid State Mater. Sci., 2002, 6, 251.
11. O. van der Biest, L. J. Vandeperre. Ann. Rev. Mater. Sci., 1999, 29, 327.
12. P. C. Himenez, R. Rajagopalan. Principle of Colloidal Surface Chemistry. 1997, New York: Marcel Dekker Inc.
13. R. J. Hunter. Foundation of Colloidal Science, 1. 1986, Oxford: Clarendon Press.
14. Malvern 30 dak içinde ZPC anlatım.
15. Malvern Haldun hoca verecek.
16. A. R. Boccaccini, J. Cho, T. Subhani, C. Kaya, F. Kaya. J. Eur. Ceram. Soc., 2010, 30, 1115.
17. N. Ogata, J. V. Tassel, C. A. Randall, Mater. Lett., 2001, 49, 7.
18. K. Kicir, C. Bayram, E. Erat, M. Türk, E. B. Denkbaş. In: Abs. 9th Nanosci. & Nanotechnol. Conf., 2013, 280.
19. A. R. Boccaccini, U. Schindler, H. G. Kruger. Mater. Lett., 2001, 51, 225.
20. S. B. Khoo, B. Yu. Electrochem. Commun., 2002, 4, 737.
21. T. Seike, M. Matsuda, M. Miyake. J. Mater. Chem., 2002, 12, 366.
22. W. Shan, Y. Zhang, W. Yang, C. Ke, Z. Gao, Y. Ye, Y. Tang, Micropor. Mesopor. Mater., 2004, 69, 35.
23. A. S. Huang, W. S. Yang. Mater. Res. Bull., 2007, 42, 657.
24. H. Negishi, N. Oshima, K. Haraya, K. Sakaki, T. Ikegami, Y. Idemoto, N. Koura, H. Yanagishita. J. Ceram. Soc. Jpn., 2006, 114, 36.
25. A. R. Boccaccini, S. Keim, R. Ma, Y. Li, I. Zhitomirsky, J. R. Soc. Interface, 2010, 7, S581.
26. C. Lin, H. Han, F. Zhang, A. Li. 2008, 19, 2569.
27. A. R. Boccaccini, O. van der Biest, R. Clasen. Key Eng. Mater., 2006, 314, 207.
28. C. Kaya, I. Singh, A. R. Boccaccini. Adv. Eng. Mater., 2008, 10, 1.
29. C. Kaya, F. Kaya, J. Cho, J. A. Roether, A. R. Boccaccini. Key Eng. Mater., 2009, 412, 93.
30. B. Ferrari, A. J. Sanchezherencia, R. Moreno. Mater. Res. Bull., 1998, 33, 4879.
31. N. Nagarajan, P. S. Nicholson. J. Am. Ceram. Soc., 2004, 87, 2053.
32. S. Put, J. Vleugels, O. van der Biest. J. Mater. Process. Technol., 2003, 143-144, 572.
33. S. Put, J. Vleugels, O. van der Biest, Scripta Mater., 2001, 45, 1139.

34. E. Askaria, M. Mehrali, I. H. S. C. Metselaar, N. A. Kadri, M. M. Rahmana. J. Mech. Behav. Biomed., 2012, 12, 144.
35. C. Kaya, F. Kaya, S. Atiq, A. R. Boccaccini. Brit. Ceram Trans., 2003, 102, 99.
36. W. Tan, X. Yin, X. Zhou, J. Zhang, X. Xiao, Y. Lin, Electrochim. Acta, 2009, 54, 4467.
37. A. R. Boccaccini, J. Cho, J. A. Roether, B. J. C. Thomas, E. J. Minay, M. S. P. Shaffer. Carbon, 2006, 44, 3149.
38. A. R. Boccaccini, J. A. Roether, B. J. C. Thomas, M. S. P. Shaffer, E. Chavez, E. Stoll, E. J. Minay. J. Ceram. Soc. Jpn., 2003, 114, 1.
39. T. Belin, F. Epron. Mater. Sci. Eng. B, 2005, 119, 105.
40. J. J. Gooding. Electrochim. Acta, 2005, 50, 3049.
41. W. A. Deheer, A. Chatelain, D. A. Ugarte, 1995, 270, 1179.
42. R. H. Baughman, A. A. Zakhidov, W. A. de Heer. Science, 2002, 297, 787.
43. A. P. Ramirez. Bell Labs Tech. J., 2005, 10, 171.
44. F. Chicatun, J. Cho, S. Schaab, G. Brusatin, P. Colombo, J. A. Roether, A. R. Boccaccini, Adv. Appl. Ceram., 2007, 106, 186.
45. J. Li, I. Zhitomirsky. J. Mater. Proc. Technol., 2009, 209, 3452.
46. A. Charlot, X. Deschanels, G. Toquer. Thin Solid Films, 2014, 553, 148.
47. J. Zhang, B. I. Lee. J. Am. Ceram. Soc., 2000, 83, 2417.
48. J. L. Zhao, X. H. Wang, R. Z. Chen, Z. L. Gui, L. T. Li. Rare Met. & Mater. Eng., 2003, 32, 370.
49. F. Hossein–Babaei, F. Taghibakhsh. Electron. Lett., 2000, 36, 1815.
50. B. Ferrari, R. Moreno, P. Sarkar, P. S. Nicholson. J. Eur. Ceram. Soc., 2000, 20, 99.
51. K. Kanamura, A. Goto, J. Hamagami, T. Umegaki. Electrochem. Solid State Lett., 2000, 3, 259.
52. K. Ui, S. Y. Funo, H. Nagase, Y. Idemoto, N. Koura. Electrochem., 2006, 74, 474.
53. K. Hayashi, N. Furuya. J. Electrochem. Soc. A, 2004, 151, 354.
54. R. S. Hyam, K. M. Subhedar, S. H. Pawar. Colloids Surf. A, 2007, 297, 172.
55. R. S. Hyam, K. M. Subhedar, S. H. Pawar. Appl. Surf. Sci., 2006, 253, 1540.
56. A. Dogan, G. Gunkaya, E. Suvaci, E. Uzgur. Key Eng. Mater., 2004, 264-268, 269.
57. A. Dogan, G. Gunkaya, E. Suvaci, M. Niederberger. J. Mater. Sci., 2006, 41, 8196.
58. G. Gunkaya, M. Gurbuz, A. Dogan. In: Proc. IEEE Sensors 2012 Conf., 2012, 1573.
59. D. Jung, J. Tabellion, R. Clasen. Key Eng. Mater., 2006, 314, 81.
60. J. Tabellion, J. Zeiner, R. Clasen. J. Mater. Sci., 2006, 41, 8173.
61. A. B. Stambouli, E. Traversa. Renew Sustain. Energy Rev., 2002, 6, 433.
62. A. R. Boccaccini, O. van der Biest, R. Clasen. Key Eng. Mater., 2006, 314, 101.
63. A. R. Boccaccini, O. van der Biest, R. Clasen, T. Uchikoshi. Key Eng. Mater., 2009, 412, 209.
64. E. Jothinathan, O. van der Biest, J. Vleugels. Adv. Appl. Ceram., 2012, 8, 459.
65. F. Habashi. In: Proc. 4th Int. Boron Symp. 2009, Eskişehir: Eskişehir Osmangazi Univ., 355.
66. R. S. Hyam, K. M. Subhedar, S. H. Pawar. Colloids & Surf. A, 2008, 315, 61.
67. R. S. Hyam, K. M. Subhedar, S. H. Pawar. Colloids & Surf. A, 2007, 297, 172.
68. E. Savaskan, B. Yanmaz, M. Başoğlu, E. T. Koparan, N. R. Dilley, C. R. M. Grovenorc. J. Alloys &Comp., 2009, 480, 203.

69. A. Gumbel, J. Eckert, G. Fuchs, K. Nenkov, K.-H. Muller, L. Schultz. Appl. Phys. Lett., 2002, 80, 2725.
70. A. M. Locci, R. Orru, G. Cao. Am. Inst. Chem. Eng. J., 2006 , 52, 2618.
71. N. S. Raddaha, L. Cordero–Arias, S. Cabanas–Polo, S. Virtanen, J. A. Roether, A. R. Boccaccini. Mater., 2014, 7, 1814.

ВЛИЯНИЕ УСЛОВИЙ ПОЛУЧЕНИЯ НА СТУКТУРНОЕ СОСТОЯНИЕ КРИСТАЛЛОВ БОРА

Д. Л. Габуния, О. А. Цагарейшвили, Л. С. Чхартишвили

Институт металлургии и материаловедения им. Ф. Н. Тавадзе
Тбилиси, Грузия
d_gabunis@hotmail.com

Принята 11 сентября 2014 года

В настоящее время бор, его соединения и сплавы, а также материалы и композиции на его основе находят широкое применение в различных отраслях современной техники. Высокие значения их прочности, твердости, износостойкости при сохранении удовлетворительных пластических свойств открывает новые возможности получения материалов с повышенными служебными характеристиками. В совокупности с радикально отличающими друг от друга нейтронопоглощающими и нейтронопрозрачными свойствами своих изотопов, бор и материалы на его основе привлекают все большее внимание ученых, исследователей и разработчиков.

Установлено, что наноразмерность структур открывает уникальные возможности создания материалов с значительно улучшенными свойствами. Такие материалы проявляют качественно новые функциональные характеристики. В этом отношении бор, с учетом его малого удельного веса, и борсодержащие материалы можно успешно использовать в электронной, атомной и авиакосмичекой промышленности. Созданные на их основе покрытия могут найти широкое применение и в медицине – для обеспечения защиты от нейтронного облучения обслуживающего персонала при диагностике и лечении онкологических заболевании. В этом аспекте возросший интерес к нанокристаллическим материалам на основе бора, способных обладать благоприятным сочетанием различных физических и химических свойств, вполне понятен.

Следует отметить, что изменение свойств наноматериалов обусловлены не только малыми размерами частиц, но и проявлением квантомеханических эффектов при доминирующей роли поверхности раздела. Эти эффекты наступают при таком критическом размере, который соизмерим с т.н. корреляционным радиусом того или иного явления, например, зарождения новой твердой фазы и кристаллизации. Эти

признаки вполне обясняют тот факт, что даже грамм нанокристалла может быть более эффективен, чем тонны обычного вещества. И дело не в количестве, а в качестве.

Как известно, основным строительным элементом структуры бора и материалов на его основе является икосаэдр с 12 атомами. Из установленных структурных модификации бора α- и β-ромбоэдрической и β-тетрагональной, наиболее стабильной является β-ромбоэдрическая. Однако ее можно получить лишь в результате отжига (> 1500 °C) или переплава (~ 2200 °C) аморфного бора. Структура β-ромбоэдрического бора достаточно сложная и ее элементарная ячейка содержит 105 регулярных узлов атомов бора. Она характеризуется наличием субъячейки B_{84} и большим количеством пустот, занимающих до 70 % объема. Следует отметить, что сложная структура, высокая температура плавления, низкая теплопроводность и большая реакционная способность в расплавленном состоянии создает серьезные технологические трудности получении кристаллов бора и в особенности его нанокристаллов.

Основные данные о получении и результатах исследовании нанокристаллических порошков бора, которых ранее называли «ультрадисперсными» представлены в [1]. Современные работы подтвердили возможность получения нанокристаллов бора, могущих существовать как в виде трехмерных так и двухмерных [2] структур.

Важное влияние на структурное состояние кристаллов бора оказывают условия его получения, температура, среда, давление. Порошки бора и наноматериалы на основе бора можно получать дроблением, конденсацией из газовой фазы, термо- и плазмохимическим синтезом, отжигом аморфных порошков и т.п. В настоящей работе рассматриваются вопросы получения нанокристаллических частиц бора и материалов на его основе в зависимости от условии получения: механическим измельчением и измельчением высоковольтным электрическим разрядом, химическим и электродуговым синтезом, термической обработкой аморфных порошков бора.

Механическое измельчение – высокоэнергетический размол кристаллического материала – можно считать наиболее продуктивным и используемым методом получения порошков β-ромбоэдрического бора. Учитывая существование нижного предела диспергирования вещества таким методом $\sim 0.7 \cdot 10^{-5}$ см, предполагается, что механическим измельчением кристаллов бора можно получать частицы порошка нанокристаллических размеров. Действительно, при тонком измельчении порошков бора ударно-истирающим воздействием на воздухе образуются частицы нанокристаллического бора размером ~ 250 нм. Фракцию таких порошков после промывки в дистиллированной воде и удаления т.н. аморфизированной части можно использовать по целевому назначению, например, для создания специальных покрытии.

Представляется, что распостраненый и широко используемый в последнее время метод механического синтеза, т.н. механосинтеза, различных веществ и композиции из соответствующих прекурсоров позволит в процессе измельчения практически при комнатной температуре получать карбид бора, нитрид бора и необходимые борсодержащие материалы и композиции.

Однако механические методы измельчения обладают радом недостатков. В первую очередь это загрязнение продуктов измельчения материалом тела измельчителя, что требует дополнительную обработку продуктов измельчения, например их химическую очистку. К сожалению, при диспергировании на воздухе порошок окисляется – это также следует принять во внимание. Необходимо учитывать и достаточно высокие энергозатраты и длительное время измельчения.

В этом отношении более привлекательным является воздействие на материал высоковольтного электрического разряда. Исследования показали перспективность его использования. Он позволяет воздействовать на дисперсные материалы как электромагнитными и термическими полями, так и волнами давления, близкими к ударным. Метод позволяет достичь сравнительно высокой степени дисперсности с незначительным загрязнением продуктов измельчения при низких затратах энергии и времени. В тоже время, использование в качестве рабочей среды соответствующей целям измельчения жидкости, например, керосина позволяет избежать окисления продуктов диспергирования и создает условия для получения требуемого вещества, например, карбида бора B_4C. В этом случае, подбирая технологические параметры композиции на основе борсодержащих веществ с точки зрения содержания в них изотопов ^{10}B или ^{11}B, можно будет получать как нейтронопоглощающие ,так и нейтронопрозрачные материалы.

Дуговой разряд в жидкой фазе все чаще используют для получения различных наноструктур, как альтернативу дуговому разряду в газовой фазе. Нами экспериментально установлена возможность получения наноразмерных частиц нитрида бора BN диспергированием в жидком азоте по методу описанном в предварительно измельченных (фракция 160 – 80 мкм) порошков β-ромбоэдрического бора.

Используя газообразные борсодержащие химические реагенты легколетучих материалов также можно получать нанокристаллические частицы бора и его соединений. Однако все же следует заметить, что применение для таких целей диборана усложняет технологию и снижает безопасность процесса получения. Это в определенной степени ограничивает их эффективное применение для получения борсодержащих нанокристаллических частиц.

Необходимо отметить,что воздействие электрического и магнитных полей является главенствующим при обработке соответствующих прекурсоров и способствует образованию нанокристаллических структур. При температурах (2000 – 6000 °C), развивающихся в столбе электрической дуге, возгоняются все металлы и соединения. С учетом этого обстоятельства можно смело сказать, что электродуговой способ получения и обработки материалов является сравнительно простым и более доступным методом получения наноструктур и композиции на основе бора и борсодержащих материалов. Образующиеся при этом продукты содержащие борные наноструктуры, могут осаждаться на катоде или на стенках реактора.

Среди многочисленных методов получения бора и материалов на его основе метод химического синтеза с использованием органических и неорганических

прекурсоров привлекает внимание своей простотой, доступностью компонентов и возможностью снижения энергозатрат.

Была показана возможность получения гетеромодульной керамики на основе B_4C. Такая керамика может быть получена и при совмещении процесса получения требуемого вещества с плакированием частиц металлической связкой. Так, была описана технология, которая позволяет совместить процесс получения B_4C и пластической связки (например, Cu / Ti), способствующей консолидации частиц. В часности, нанокристаллические порошки B_4C получали карботермическим методом пиролиза низко- и высокомолекулярных органических соединении гидроксильной группы в интервале температур 900 – 1300 °C. Для улучшения консолидации порошков их синтез совмещали с одновременным плакированием частиц связывающей фазой – твердыми растворами Cu/Mn и Cu/Ti. Консолидацию полученных композиции проводили плазменно-искровым методом, что позволяло получать плотную нанокристаллическую гетеромодульную керамику на основе B_4C. Установлено. что в такой гетеромодульной керамике содержатся компоненты, размер которых не превышает 80 – 100 нм.

Порошки нанокристаллического гексагонального BN получали химическим синтезом в атмосфере аммиака смесей, содержащих буру и карбамид или буру и хлорид аммония при температурах 870 и 1050 °C, соответственно. Размер полученных частиц BN колебался в пределах 100 – 150 нм, а их агломератов – 2 – 3 мкм. Удельная поверхность составляла порядка 8. 8 $м^2$ / г.

Исследование ряда функциональных свойств образцов, полученных из указанных материалов показали возможность их применения как для создания изделий, совмещающих высокую ударную прочность с удовлетворительной вязкостью (композиции на основе B_4C), так и для изделий, характеризующихся повышенной износостойкостью (композиции на основе BN) и т.п. Подбирая изотопический состав компшзиции по бору и технологические параметры процесса, можно получать как нейтронопоглощающие, так и нейтронопрозрачные материалы. Они могут быть использованы для создания специальных изделии или покрытии.

Анализ имеющихся в настоящее время данных показывает теоретическую и практическую возможность получения бора и нанокристаллического бора сответствующей термической обработкой аморфных порошков бора.

Изучалась кристаллизация аморфных порошков бора различного происхождения и химического состава. Удалось показать, что на процесс их кристаллизации существенное влияние оказывают способы получения, температура и время выдержки отжига. Представляет интерес более подробно рассмотреть данные по кристаллизации аморфных порошков бора.

Так, в аморфном боре, полученном пиролитическим способом, существенное изменение структуры происходит уже после его нагрева: с 1200 °C начинает формироваться α-ромбоэдрическая структура бора. При увеличении температуры выше 1300 °C на рентгенограмме исследуемого образца появляются линии α-ромбоэдрического бора и при дальнейшем повышении температуры формируется α-ромбоэдрический бор. Необходимо отметить, что при этом не наблюдаются

изменения структурной единицы – икосаэдра B_{12}. Происходит лишь их перегруппировка за счет небольших поворотов они превращаются в тетраэдры, а при их соединении образуется α-ромбоэдрическая структура. При дальнейшем нагреве от 1770 до 1900 °C образуется т.н. «промежуточная» фаза и формируется структура β-ромбоэдрического бора. Выделяемая при превращении тепловая энергия расходуется на построение более сложной β-ромбоэдрической структуры из атомов бора. Замечено, что малое содпржание примесей в исходном порошке аморфного бора – главное условие получения α-ромбоэдрического бора. Предварительное прессование исследуемого образца также способствует превращению, а проведение отжига в инертной атмосфере в 1.5-раза ускоряет процесс превращения.

После отжига при 1200 °C аморфного бора, полученного электролитическим способом, на рентгенограмме исследуемого образца постепенно появляются линии α-ромбоэдрического бора. Отметим, что в этом случае порошки не требуют прессования и единственным определяющим параметром, влияющим на процесс кристаллизации, является температура. Однако вплоть до температуры плавления β-ромбоэдрического бора (~ 2200 °C) полное превращение в β-ромбоэдрическую структуру не происходит. Это подтверждает сделанный вывод, что β-ромбоэдрическая структура образуется лишь после плавления аморфного бора. Отметим, что среда процесса кристаллизации – вакуум или инертная атмосфера – не оказывает существенного влияния на процесс кристаллизации.

При кристаллизации аморфного бора, полученного плазмохимическим методом, на рентгенограмме исследуемого образца наблюдается лишь одна линия, которую можно идентифицировать как небольшую (~ 10 %) примесь β-тетрагонального бора.

Подытоживая эти результаты можно заключить, что в одинаковых условиях кристаллизации аморфный бор быстрее всех превращается в α-ромбоэдрический, затем пиролитический и труднее всех – электролитический бор, несмотря наличие в его структуре готовых структур β-ромбоэдрического бора – B_{28}. По-видимому, основной причиной различия в процессах кристаллизации бора является различие в технологических методах получения исходного аморфного бора, влияющих на его чистоту.

Таким образом, подбирая среду, температуру и продолжительность времени отжига для кристаллизации аморфных порошков, можно получать нанокристаллы α- и β-ромбоэдрической модификации бора. Разработанные в настоящее время методы получения аморфных порошков бора позволяют прогнозировать реальные возможности увеличения количества получаемого бора как в кристаллическом, так и нанокристллическом состояниях.

В заключении необходимо отметить, что перспективность использования ряда уникальных свойств бора в различных областях современной техники будет способствовать исследованиям влияние условий получения на структурное состояние бора и таким образом стимулировать создание на его основе новых наноструктурых кристаллических материалов функционального назначения.

Ссылки

1. Д. Л. Габуния, А. А. Гачечиладзе, А. Г. Микеладзе, О. А. Цагарейшвили, Л. С. Чхартишвили. Nano Studies, 2011, 3, 123.
2. L. S. Chkhartishvili. Nano Studies, 2011, 3, 227.

APPLICATION OF STRUCTURAL NANOMATERIALS IN PETROLEUM INDUSTRY

N. Nabhani

Petroleum University of Technology
Abadan, Iran
nabhani@put.ac.ir

Accepted October 16, 2014

Intruduction

Nanomaterials, and their associated manufacturing and processing technologies, are the key enablers of the nanotechnology industry and encompass a wide range of materials. The common link across these materials is that they exhibit features only present at the nanoscale that potentially offer performance enhancement over existing materials. Nanomaterials typically measure in the range of 1 to 100 nanometer (nm).

Nanotechnology has been making its presence felt in oil industry for some time, and many applications are already standard in downstream, for example, nanostrucated zeolities are now used to extend up to 40% more gasoline than catalysts they replaced [1, 2]. The most obvious applications of nanotechnology for upstream operations is development of better materials [3 – 5]. The oil industry needs strong, stable materials in virtually all of its process, including construction sector. By building up such substances on a nanoscale, it could produced equipment that is lighter, more resistance and stronger such as weight reduction of offshore platforms and structures, corrosion resistance alloy components in the wellbore and in surface production facilities, better performing drilling parts and coating materials [4, 6]. Nanotechnology could also develop nanostructured steel alloys to provide a new class of steel with hardness fracture toughness exceeding conventional alloys. Other emerging application of nanotechnology are in the sector of developing types of smart sensor for monitoring of the structural integrity and the integrity of pipe lines in oil industry.

This paper examines and documents applications of nanotechnology that can improved the overall competitiveness of the oil and gas industry. The data and information collected is from current literature and researches and focus on applications of nanotechnology and nanomaterials in construction areas of the oil and gas industry. The purpose is to point out clear-cut direction among the nanotechnology development areas where petroleum engineering construction process would immediately harness nanotechnology by specifying clear recommendations. To conclude, the future opportunities and challenges in construction oil and gas, are highlighted.

Application of nanotechnology in construction oil and gas

Nanotechnology can be used for design and construction processes in many areas of petroleum sector, in term of materials, techniques and safe environmental operations, since

nanotechnology generated products have many unique characteristics, (summarized in **Table 1**). There are large number of applications of nanotechnology in construction area to oil and gas industry. Some of these applications are examined in detail below and followed by a summary of possible solutions that nanotechnology can offer in a number of areas of critical importance to the industry.

Table 1. Examples of use, benefits, limitations for top 5 nano-products in petroleum industry.

Product Categories	Main Uses	Key Benefits	Key Limitations
Composites	building materials (polymer, steel, piping), drilling parts, offshore structures, surface production of facilities	high strength, lightweight, durable structures, ductility, wear and corrosion resistance, earthquake resistance	technical limitations and bulk volumes, environmental impact during disposal phase
Coating	functional surfaces, exterior and interior building surfaces,piping,tanks,offshore structures	UV protection, antimicrobial, scratch, corrosion resistance, water proofing, durability, self-cleaning, longer life, aesthetics	cost to produce not available in bulk
Membranes	removal of toxic metals and volatile organic compounds (vocs), water filtration, efficient conversion of hydrocarbons and refining efficiency	better material utilization, reduces footprint, low weight and space requirement, bio-fouling resistance, low capital cost, low maintenance	technical limitations andenvironmental impact during disposal phase
Sensors	remote sensing and monitoring for example crack structural integrity of pipes lines and wells	low maintenance, minimum infrastructure requirements, precise and accurate measurement techniques	product acceptance, standards and guidelines
Cement / Concrete	bulk materials in building construction and capital structures for example oil well cement, offshore structures, supports for storage containers	strength and durability, long lasting, aesthetics, schedule. shorter curing time	manufacturing cost at the level of mass production, higher initial investment, lobbying, environmental at end of life-cycle

Nanocomposite materials

Nanocomposites are a class of materials that has gained much interest recently since the oil and gas industry need strong, stable materials in virtually all of its processes, specially in drilling operation. Because of the extremely harsh environment conditions currently present during exploration and drilling activities and even more adverse conditions as drilling operations move deeper, there is a strong need to develop harder, more resistance and durable materials. The incorporation of engineered nanoparticles into composite materials and coatings, can make materials and devices more resistant to harsh environments during drilling operation. This is due to the enhanced thermo-mechanical properties, thermal stability and flammability achieved by the addition of nanoparticles compared with conventional materials.

Industrial drilling make heavy use of superheated materials with superior wear resistance. In this respect, nanocomposite materials have better corrosion and chemical resistance characteristics, can stand better harsher operating condition. Drill bits coated with nanostructure ceramic materials have increased hardness and durability compared with their conventional counterparts [7].

US Department of Energy, has developed a novel nanosynthesis technique of high pressure and temperature ($p-T$) reactive sintering to synthesize diamond/sic nanocomposite that offer superb hardness (40 – 60 GPa), enhanced yield strength (16 GPa, comparable to diamond) and high fractured toughness (12 – 15 MPa · $m^{1/2}$). The development and deployment of these novel diamond nanocomposites will dramatically increase drilling workload and efficiency while also reducing energy and capital costs and harmful environmental and carbon effects [8].

Another example of commercial nanotechnology application is the thermosetting and thermoplastic pipes and liners created from nanocomposite materials have enhanced thermo-mechanical and creep properties, allowing for operations at the higher temperatures and pressures without increasing the thickness of the pipe or the changing the manufacturing processes involve [9].

Another major area where nanocomposite materials can make a dramatic impact is with sealants when subjected to harsher condition [10, 11]. Nanocomposite materials also offer a dramatic impact on the application of elastomers (rubber), for drilling under the extreme conditions of temperature (> 200 °C) and persuure (> 20000 Psi).

Recently, by engineering elastomer nanocomposites with carbon nanotubes and layered silicates, ensuring mixing at the molecular level and wrapping and interpenetrating network structures, a new class of elastomers has been developed, that is strong, tough, environmentally resistance and a significant weight reduction compare to the traditional elastomers [12].The use of nanocomposite in offshore engineering due to their advantage in terms of weight reduction, life cycle cost saving, etc, is another feature which can be achieved and is discussed in following sections.

Structural composities

Steel is a major construction material. Its properties, such as strength, corrosion resistance and weld ability are very important for design and application in offshore oil and gas production platforms (in which steel and concrete are the materials of choice for offshore, with steel dominant in the topside applications), oilfield tubular, piping and other equipment. In the presence of water or at high pressures, the corrosive impurities such as carbon dioxide (CO_2)

and hydrogen sulphide (H_2S), can cause rapid degradation of steel components in the wellbore and in surface production of facilities.

Sandvik Nanoflex Materials Technology has developed Sandvik Nanoflex TM which is a new stainless steel with ultra-high strength, good formability and a good surface finish. Due to its high performance, is suitable for application which requires lightweight and rigid designs. Its good corrosion and wear resistance can keep life-cycle costs low [13]. Similarly, MMFX steel Co. has produced MMFX nanostructure-modified steel which offers corrosion resistance at a cost for below stainless steel and has amazing strength (three times stronger), ductility and roughness [14]. Further more, Nanostructured steel surface technologies are enhancing the physical properties of oil field tubulars, piping and other equipment. Nanostructured alloys for thermal spray coating and weld overlay for hardfacing and wear plate applications combine high hardness and toughness properties for exceptional resistance to corrosion, erosion, impact and wear. As shown in the **Figure 1** at left, nanostructured steel alloys provide a new class of steel, with hardness fracture toughness exceeding conventional alloys. NOV Grant Prideco's Platinum® HB, developed in partnership with The NanoSteel Co. using its Super Hard Steel® technology, is engineered for drill string hardbanding applications to provide high strength for minimum casing wear performance and tool joint protection as well as high toughness to resist cracking and spalling in severe downhole applications [15].

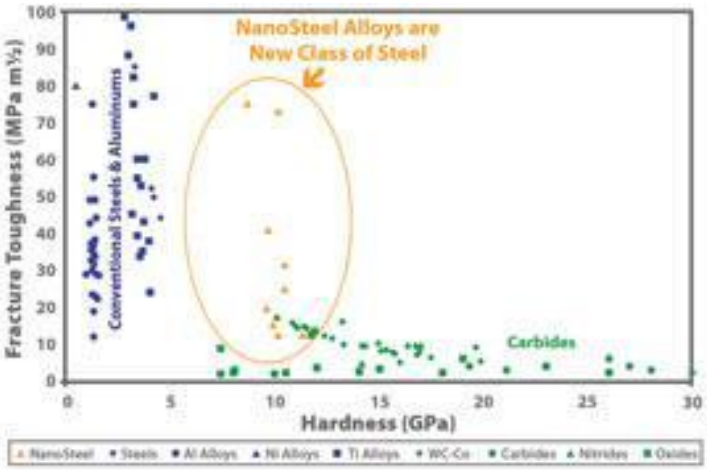

Figure 1. New class of nanosteel alloys.

The use of nanocomposite in offshore industry is another way of weight reduction, corrosion resistance, life cycle costs when compared to traditional steel. Because nanocomposite increases the performance of polymer matrices with compromising their original features. Although these materials would mostly used in secondary structural applications, they have great potential as primary load bearing members. This is particularly the case in the retrofitting of existing topside structures where increased fire and blast resistance is required. Nanocomposities are appealing in this situation as no hot working (welding) is required which would otherwise require a costly platform shutdown.As the industry moves to greater water depths, the significance of weight saving has become increasingly important in conjunction with the application of buoyant tension for the leg structures. Nanocomposities may find excellent usage in the fabrication of the following:

- Profiles for oil pollution barriers
- Granting, ladders and railings on oil drilling platforms and ships
- Walkway systems sucker rods

Nanocoating

Nanocoatings are materials that are produced by shrinking the material at the molecular to form a denser product. The coatings incorporating certain nanoparticles or nanolayers have been developed for certain purpose such as low friction, high erosion and corrosion resistance, high hardness and durability and electro chemically reactive. It is one of major application of nanotechnology in construction oil and gas industry. Drilling equipment, platforms, offshore structures and vessels, pipes and tank can be coated with nanomaterials for improved corrosion-resistance, wear-resistance, shock-resistance and enhanced thermal conductivity, [16 – 18]. These capabilities will greatly enhanced the ability of component to produce in more extreme conditions.

In production applications, the hydraulic fracture proppant was coated with nano crystals to control fines migration without decreasing productivity [19]. More recently silica nanoparticles with a polyethylene glycol (PEG) coating was used to study the mechanisms of nanoparticle retention in porous media [20].

Another major use of nanocoating is for corrosion protection in the different oil and gas industry areas, such coatings are capable of self-repair [17], reduction corrosion maintenance and increased reliability. They are used extensively to reduce corrosion in marine and offshore structures. There are usually economic advantages to using coatings as opposed to more corrosion resistance materials or cathodic protection. It has also been reported that nanocomposite coatings as thin film coatings, top layer coatings and thermal barrier coatings are excellent ways of decreasing corrosion rates to improve the lifetime of materials and devices [16, 21, 22].

A polymer nanocomposite coating can effectively combine the benefits of organic polymers, such as elasticity and water resistance to that of advanced inorganic materials, such as hardness and permeability [23]. Finally, nanocoating inhibits the adhension of microbes and marine fouling organisms. Establishment of nano-structure results in appreciable reduction in interaction between germs and surface. Nanocoating helps in reduction of germs, virus, algae by oligodynamic effect of metal component. Nanocoting can be applied in many ways including chemical vapor phase deposition, physical vapor phases deposition, electrochemical deposition, sol-gel methods, electro-spark deposition, and laser beam suface treatment.

Cementitious materials

Cement is a constructional materials used in petroleum industry for the improvement of the functionality of the oil well drilling related process and in offshore oil and gas production platforms with steel dominant in the topside applications. The incorporation of nanoscale particles into cement has catalyzed certain mechanical properties.

Oil well cement is a vitual element, which ensures the long-term durability of the borehole by providing a high-quality casing. Cementing deep wells requires materials that while satisfying performance specifications, are different from those encountered in conventional processes or macro-structural level. Because leakage of cement sheaths leads to premature access of bottom water into production, gas-water-oil crossflow, pollution of fresh water horizons, etc. Adding nano-dispersive modifiers to cement can enhance the strength of concrete and foam concrete 1.5 – 2 times [24].

Nanoparticles, especially nanosilica, nano-Fe_2O_3 [25 – 28] and nanoalumina [29 – 31] have been widely employed for increasing compressive strengths of cementitious. Abrasion

resistance [32, 33], and flextural fatigue performance [32] can be improved with the use of titania nanoparticles and nanosilica.

Further, the self monitoring capability of cement mortar with nano-Fe_2O_3 has been reported [26]. It is also been reported that adding small amount of carbon nanotube (1 %) by weight could increases both the compressive and flexural strength [34, 35]. More recently, it has been observed that macro and micro characterization of mortors produced with 0.30 % of carbon nanotube can improve the strength performance of Portland cement composities [36].

Further in the development of concrete, nanocomposite based 2D and 3D gride-type reinforcement of concrete structures would shows considerable potential for use as reinforcement of concrete, because of its corrosion and chemical resistance, its light weight and its ease of forming to fit curvatures. Grid-type reinforcement for concrete structures consist of high-performance fibres such as glass, carbon, aramid and hybrids impregnated with resin systems varying from vinyl esters and other thermosetting resin systems to thermoplastics. The significant systems-level savings could achieve due to the factors of weight. This may find excellent usage in supports for storage containers and marine and offshore structures [37].

Nanosensors

The oil and gas installations and infrastructures need continuous monitoring and upgrading and maintenance, for many decade ahead (specially in offshore oil and gas industry). Nanosensors could be embedded into structures, and would allow engineers to monitor deterioration and cracking of the structural integrity of platforms and rigs, without any physical intervention. This concept of producing a network of nanosensors that communicate with each other across the structure, offers significant advantages over traditional sensor stations comprise single monitoring points at strategic location across a structure.

Another nanosensor, smart dust, is being developed by researchers at the University of California in San Diego. Smart was created from nanostructured porous silicon crystals that can be tuned to change colour when a specific compound is detected. Within the oil and gas industry this sort of technology could be deployed to remotely sense pipeline leaks for gases, such as toxic hydrogen sulphide, or to remotely monitor the structural integrity of pipelines and wells [38].

Nanomembranes

In recent years, the membrane technologies are becoming more frequently used for separation of wide varying mixtures in the petroleum industry, due to their simplicity and low energy costs, but it has one major drawback and that is a reverse relationship between selectivity and permeability. Recently nanocomposite membranes have been developed to improve the reverse relationship problem [39 – 41]. It has shown polyimide (PI) / TiO_2 [42], nano-sized nickel carbon [43], nanocomposite membranes for gas separation have strong influence on the gas permeation properties. Among the most nanocomposite membranes, polyimide/silica materials have received the most attention for gas permeation studies [44 – 46].

The range of applications covers the supply of pure or enriched gases such as He, N_2 and O_2 from air, the separation of acid gases such as CO_2 and H_2S, the separation of H_2 in the petrochemical and chemical industries. **Table 2** shows applications established in the membrane gas separation [47]. An overview of various applications and materials can be found in the literature [48 – 53].

Table 2. Gas membrane application [47].

Gas separation	Application
O_2 / N_2	nitrogen generation oxygen enrichment
H_2 / hydrocarbons	refinery hydrogen recovery
H_2 / CO	syngas ratio adjustment
H_2 / N_2	ammonia purge gas
CO_2 / hydrocarbon	acid gas treating enhanced oil recovery landfill gas upgrading
H_2S / hydrocarbon	sour gas treating
H_2O / air	air dehydration
Hydrocarbons / air	pollution control hydrocarbon recovery
Hydrocarbons from process streams	organic solvent recovery monomer recovery

Another area of significant challenge lies in the waste treatment from petroleum industry. Reverse osmosis (RO) has been used to treat many process streams in petroleum industry. Because many of the separation performed in the petroleum industry involve chemical that damage or degrade membranes. Reverse osmosis membranes remain relatively energy intensive, non-selective and degrade membranes. Nanotechnology has produced entirely new classes of functional materials whose application to desalination and water purification need exploration. For example, recent reports on filtration and desalination membranes fabricated from carbon nanotube [54 – 56] and zeolite films [57 – 59] offers exciting new possibilities. Mixed matrix or nanocomposite membrane may exhibit improved mechanical, chemical and thermal stability as well as improved separation, reaction, and sorption capacity [60]. More recently, it has reported as a new concept, thin film nanocomposte membrane technology may offer new degree of freedom in tailoring RO membrane separation performance and material properties [60].

Future challenged and direction

There are numerous areas in construction sector of oil and gas industry in which nanotechnology can contributed to more efficient, less expensive and more environmentally sound technologies than those that are already available. The future possibilities of nanotechnology for construction oil and gas can be identified as

1. Nanotechnology-enhanced materials, which combine high strength, low weight, and to endurance to increase performance and reliability of drilling string, tubular goods, rotating equipment.
2. Nano-enhanced cements with higher tensile strength and shorter curing time than conventional materials.

3. Development of nanosttructured-steel allay for surface production of facilities and serve downhole applications.
4. Lightweight, rugged materials that reduce weight requirements on offshore platforms.
5. Nanocoatings for low friction, high erosion, corrosion resistance and assure flow.
6. Smart nanosensors for monitoring deterioration and cracking of the structural integrity of offshore platforms, and remotely monitor integrity of pipelines.
7. Improved elastomers with much better temperature and pressure resistance, and self-healing properties, critical to deep drilling and to enable drilling in higher-temperature/higher-pressure environments.
8. Improve engineered nanoparticle for enhanced imaging of the reservoir structure deep into the reservoir.
9. Improve nanocomposite materials to allow better flame retardancy and environmentally friendly.
10. Improved the structural integrity of the rubber materials applications for harsh and deepwater conditions.

As with most developing technologies, although many achievements with nanomaterials have been made in laboratory, a major number of challenges exist during the initiation and implementation of the application of the technology into reality. Most nanomaterials-based products are still in research and laboratory development stage in oil industry. Before they can be practically applied, numerous problems need to be solved, such as the fabrication of materials, health and environment issuses and the production of low-cost and easily industrialized nanomaterials and equipments. Some of the barriers that may slow implementation of future development in nano-systems for the oil and gas industry include the following factors [4 – 6]:

1. Lack of strong support for innovation in the E & P sector.
2. Barriers to entry and adoption.
3. Perceived cost and risk.
4. Lack of awareness.

With the continues heavy interest in nanotechnologies in the oil and gas industry, many potential solutions will emerge for the above referenced challenges. Once solutions to these problem are solved and the relevant technologies developed, nanotechnologies can be extensively applied in construction area of the oil and gas industry. Innovations in nanotechnology as applied to the oil and gas industry, will bring about a technological break through to the industry with many win-win rewards for rewards for both sides.

Conclusions

The present paper presented an overview of most recent research progress in nanotechnology in area of construction to the oil and gas industry. The reviewed literature suggests that the construction oil and gas is facing many materials-based and technique-based challenges, some of may well be addressed by nanotechnology, as it shows good promise. Nanomaterials are expected to play a large role in solving petroleum construction problems. These include, structural nano materials, environmentally friendly and sustainable of

construction materials, cost-effective structures, advanced nano sensors and nanocoating. Although most of nanomaterials based products are still in stage of laboratory testing, they could be extensively applied in the oil industry, once the existing problems are solved, The application of nanotechnology and nanomaterials may lead to a more efficient and greener use of current reservoirs due to smaller amounts of raw materials required, the more efficient use of rare materials (metals) and the engineering of new functionalities that have not previously been achieved using conventional technologies.

References

1. M. A. Ronter, D. Ranter. Nanotechnology: A Gentle Introduction to the Next Big Idea. 2001, New Jevesey: Prentice Hall.
2. C. Crane, M. Wilson, K. Kannangara, G. Smith, W. Wilson. Nanotechnology: Basic Science and Emerging Technologies. 2002, CRC Press.
3. S. A. Jackson. Innovation and Human Capital: Energy Security and the Quiet Crisis. 2001, Am. Petrol. Inst.
4. S. Mokhatab, M. A. Fresky, M. R. Islam. Applications of Nanotechnology in Oil and Gas E & P. J. Petrol. Technol., JPT-online: April 2006.
5. N. Nabhani, M. Emami, T. A. D. Moghadam. Application of nanotechnology and nanomaterials in oil and gas industry. AIP Conf. Proc., 2011, 1415, 128-131.
6. M. R. G. Bell. A case for nanomaterials in the oil and gas exploration and production business. In: Proc. Int. Cong. Nanotechnol. 2004, San Francisco.
7. D. Milne. Small Solutions for Big Returns, O & G Next Generation, Q4, 2009, 93-98: www.ngoilgas.com/article/small-solutions-for-big-returnspartmentofEnergy, June 2011.
8. Ultratough,Thermally Stable Polycrystalline Diamond / Silicon Carbide Nanocomposites for Drill Bits, U.S. Department of Energy.
9. S. Vincenzo, M. Gasem, S. M. Mayed. Applications of nanocomposites materials in the oil and gas industry. Adv. Mater.Res., 2010, 83-86, 771-776.
10. M. Endo, T. Noguchi, M Ito. Exterme-performance rubber nanoconposites for probing and excavating deep oil resources using multi-walled carbon nanotubes. Adv. Funct. Mater., 2008, 18, 3403-3409.
11. J. B. Slay, T. W. Ray. Dowhole seal element formed from a nanocomposte mateials. Patent # 7696275, 13 April 2010, Halliburton Energy Services Inc. (Houston TX).
12. R. Krishnamoorti. Extracting the benefits of nanotechnology for the oil industry. J. Petrol. Technol., JPT-online: November 2006.
13. Sandvik Nanoflex Materials Technology, http://www.smt.sandvik.com/nanoflex
14. MMFX Steel Crop., http://www.mmfx.com/products.html
15. K. Johnson. Advances in Nanotechnology Hold Huge Potential promise in Upstream Applications.The American Oil and Gas Reporter, July 2010.
16. V. Gariby, L. B. Diaz, A. Paniagua, G. E. Palacios, M. F. Vazquez, F. Leyte. Montesionos, nanostructured materials development with applications to the petroleum industry. Acta Microscop., 2009, 18, 1, 52-58.

17. H. G. Wheat, G. Liu. Using smart coatings in offshore structires. In: Proc. 15th Int. Offshore & Polar Eng. Conf. 2005, Seoul.
18. S. Chan–Remillard, D. Kerr, L. Marques. Applications of nanotechnology within the oil and gas industry. Exploration & Production, 2010, 8, 2.
19. S. Singh, R. Ahmad. Vital role of nanocomposities in drilling and stimulation fluid applications. In: Proc. 2010 SPE Ann. Tech. Conf. & Exhib., 2010, SPE 130413.
20. T. Huang, J. B. Crews. Nanotechnology application in viscoelastic surfactant stimulation fluids. SPE Production & Operations, 2008, 23, 512-517.
21. R. Asmatulu, O. R. Claus. Corrosion protection of materials by applying nanotechnology associated studies,. MRS Proc., 2003, 788 – online by Cambridge Univ. Press, 2011.
22. V. S. Saji, J. Thomans. Nanomaterials for corrosion control. Current Sci., 2007, 92, 1, 51-57.
23. Y. Wang, S. Limb, J. L. Luob, Z. H. Xub. Tribological and corrosion behaviours of Al_2O_3 / polymer nanocomposite coatings. Wear, 2006, 260, 976-983.
24. A. Kharkin. Nanotechnology to Boost Oil Recovery in Russia Up to 60-65, Oil & Gas, Eurasia, 2011, 4: http://www.oilandgaseurasia.com/articles/p/artcle/1473
25. F. Cadelas, M. J. Murphy, C. Hub, S. L. Bryant. Factores governing distance of nanoparticle propagation in porous media. In: Proc. 2011 SPE Production & Operation Symp., 2011, SPE 142305.
26. G. Li. Propeem. Concr.Res., 34, 2004, 1043-1049.
27. Z. G. Xu., G. Song. Effect of complexation on the zata potential of silica powder. Powd. Technol., 2003, 134, 218-222.
28. H. Li, H. G. Xiao, J. Ou. Microstructure of cement mortar with nano-partocles. Cement & Concrete Res., 2004, 34, 435-438.
29. J. Y. Shih, T. P. Chang., T. C. Hsiao. Effect of nanosilica on characterization of portland cement composite. Mater. Sci. & Eng., 2006,60, 356-359.
30. I. Compillo, A. Gurrcro, J. S. Dolado. Improvement of initial mechanical strength by nano alumina in belite cements. Mater. Lett., 2007, 61, 1889-1892.
31. Z. Li, H. Wang, S. He. Investigations on the preparation and mechanical properties of nano-alumina reinforced current composite. Matt. Lett., 2006, 60, 356-359.
32. H. Li, M. H. Zhang, J. P. Ou. Abransion resistance of concrete containing nanoparticles for pavement. Wear, 2006, 260, 1262-1266.
33. H. Li, M. H. Zhang, J. P. Ou. Flextural fatigue performance of concrete containing nano-particles for pavement. Int. J. Fatigue, 2007, 29,1292-1301.
34. I. Compillo, A. Gurrcro, J. S. Dolado, A. Porro, J. A. Ibanez, S. Goni. Improvement of initial mechnical strenght by nanoalumina in belite cement. Mater. Lett., 2007, 61, 1889-1892.
35. S. Mann. Nanotechnology and Construction, Nanoforum Report, www.Nanoforoum, May 30, 2008.
36. V. S. Melo, J. M. F. Calixto, L. O. Laderia, A. P. Silva. Macro and micro characterization of Motars produced with carbon nanotubes. Mater. J., 2011, 108, 327-332.
37. B. Soumitra, A. Mittal, G. Srikanth. Composites: A Vision of the Futher, Technology Information, Forecasting and Assessment Council (TIFAC). Department of Science and Technology, Govt .India, 2010.

38. M. J. Sailor, J. R. Link. Smart dust: Nanostructured devices in a grain of sand. Chem. Commun, 2005, 1375-1383.
39. B. M. Novak. Hybrid nanocomposite materials between inorganic glasses and organic polymers. Adv. Mater., 1993, 5, 422-433.
40. M. Smaihi, T. Jermourmi, J. Marigan, R. D. Noble,. Organic-inoirganic gas separation membranes: preparation and characterization. J. Membr. Sci., 1996, 116, 211-220.
41. C. F. Li, Q. H. Shao, S. H. Zhong. Preparation technology of organic–inorganic hybrid membrane. Progr. Chem., 2004, 16, 1, 83-89.
42. Y. Kong, H. Du, J. Yang., D. Shi, Y. Wang, Y. Zhang, W. Xin. Study on polyimide / TiO_2 nanocomposite membranes for gas separation. Desalination, 2002, 146, 49-55.
43. L. Zhang, X. Chen, Ch. Zeng, N. Xu. Preparation and gas separation of nano-sized nickel particle-filled carbon mambranes. J. Membr. Sci., 2006, 281, 429-434.
44. N. Nabhani, F. Sotude. Application and development of nanocomposite membranes in gas separation. In: Proc. Int. Conf. Nanotechnol. for the Benefits of Mankind. 2012, Khan Kaen.
45. T. Suzuki, Y. Yamada. Characterization of 6FDA-based hyperbranched and linear polyimide-silica hybrid membranes by gas separation. J. Polym. Sci. B, 2006, 44, 291-298.
46. B. H. Park, J. K. Kim, S. Y. Nam, Y. M. Lee. Imide–siloxane block copolymer / silica hybrid membranes: Preparation, characterization and gas separation properties. J. Membr. Sci., 2003, 220, 59-73.
47. Eds. S. P. Nunes, K. V. Peinemann. Membrane Technology in the Chemical Industry. 2001, Wiley.
48. R. W. Baker. Membrane Technology and Application. 2004, John Wiley.
49. M. Mulder. Basic Principles of Membrane Technology. 1996, Kluwer Acad. Publ.
50. R. W. Baker. Future directions of membrane gas separation technology. Ind. Eng. Chem. Res., 2002, 41, 1393-1411.
51. Ed. N. Toshima. Polymers for Gas Separations. 1991, Weinheim: VCH.
52. R. E. Kesting, A. K. Fritzsche. Polymeric Gas Separation Membranes. 1993, Wiley.
53. W. S. W. Ho, K. K. Sirkar. Membrane Handbook. 1992, New York: van Nostrand Reinhold.
54. D. S. Sholl, J. K. Johnson. Making high-flux mambranes with carbon nanotubes. Science, 2006, 312, 1003.
55. J. K. Holt, H. G. Park, Y. M. Wang, M. Stadermann, A. B. Artyukhin, C. P. Grigoropoulos, A. Noy, O. Bakajin. Fast transport through sub-2-nanometer carbon nanotubes. Science , 2006, 312, 1034.
56. X. F. Wang., X. M. Chen, K. Yoon, D. F. Fang, B. S. Dsiao, B. Chu. High flux filtration medium based on nanofibrous substrate with hydrophilic nanocomposite coating. Environ. Sci. & Technol., 2005, 39, 7684.
57. G. Li, E. Kikuchi, M. Matsukata. A study on the pervaporation of wateracetic acid mixtures through ZSM-5 zeolite membranes, J. Membr. Sci., 2003, 218, 185.
58. L. X. Li, J. H. Dong., T. M. Nenoff, R. Lee. Reverse osmosis of ionic aqueous solutions on a MFI zeolte membrane. Desalination, 2004, 170, 309.

59. L. X. Li, J. H. Dong, T. M. Nenoff, R. Lee. Desalination by reverse osmosis using MFI zeolite membranes. J. Membr. Sci., 2004, 243, 401.
60. H. B. Jeong, E. M. V. Hoek, Y. Yan, A. Dubramani, X. Huang, G. Hurwitz, A. K. Ghosh, A. Jawor. Interfacial polymerization of thin film nanocomposites: A new concept for reverse osmosis membranes. J. Membr. Sci., 2007, 294, 1-7.

AN ALTERNATIVE METHOD FOR OBTAINING NANOSIZE TUBES, FIBERS, MAGNETIC CLUSTERS

L. Rukhadze, L. Chkhartishvili, O. Tsagareishvili

F. Tavadze Institute of Metallurgy & Material Science
Tbilisi, Georgia
chkharti2003@yahoo.com

Accepted October 17, 2014

In recent years, it has especially increased the interest in the development of technologies of forming the carbon-based materials, which are focused on nanosystems and nanoparticles (nanotubes, fibers, clusters, etc.) obtained by the modification with doping. This will enable scientists and engineers in field of applications to control purposefully the unique properties characteristic of such materials (see, e.g., [1]).

In order to obtain carbon nanotube fibers and carbon clusters doped with ferromagnetic metals, we have developed a simple pyrolysis process of cycling hydrocarbon vapors, as well as a process of chemical vapor deposition (CVD).

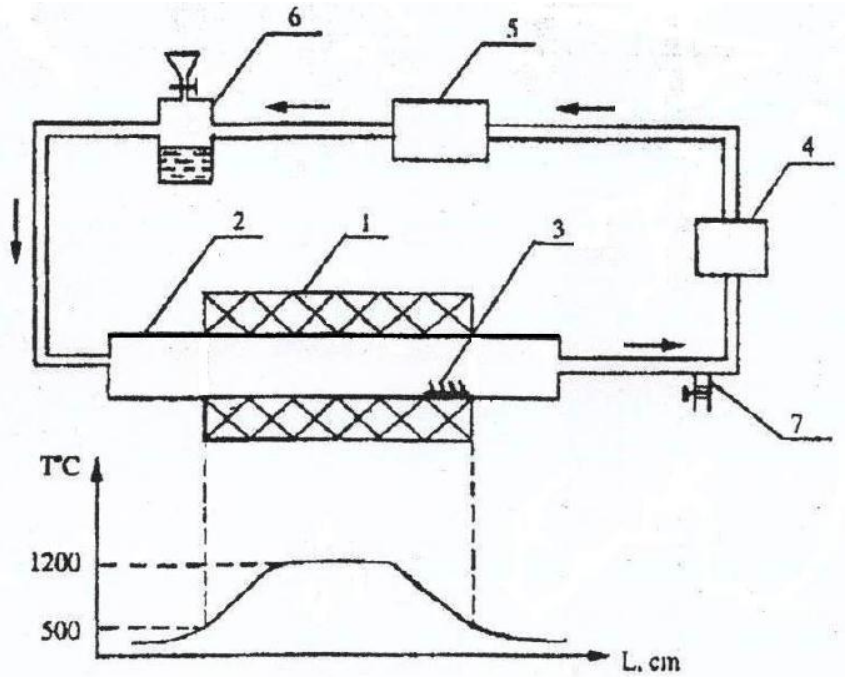

Figure 1. Experimental setup used to produce the carbon-based nanomaterials.

Figure 1 is a schematic representation of the technological process. The process set up is a closed-loop system which consists of the horizontal pipe furnace (1) to provide the given temperature distribution in the active zone of the reactor (2). A plate's shape (3) varies depending on the type of final product. The circulation circuit of the reactants within the reactor consists of the compressor (4) connected in series, the oxygen pump with the partial oxygen pressure gate (5), the hydrocarbon container (6) and the valve (7) for releasing (or collecting) the excess of hydrogen.

The proposed method allows obtaining not only nanocarbon-based materials with different shapes and structures of nanograins, but also metals in nanostates and their compounds, such are metal oxides.

Carbon nanotubes, fibers, films

Initially, the nanocarbon materials were obtained from ethyl alcohol, and then with equal success from different hydrocarbons in the temperature range 500 – 1200 °C [2]. Changing temperature, oxygen partial pressure, the amount or density of hydrocarbons, moving speed of the pyrolyzed mass in the reactor, and the conditions of substrate surface, it can be produced nanocarbon system of varying geometric size and shape (see: **Figure 2**).

(a)

(b)

(c)

Figure 2. Examples of carbon nanosystems.

Nanopowders of magnetic carbon

The carbon nanopowder synthesized at 700 °C on the surface of iron (or other ferromagnetic metals or alloys) substrate in the freely poured condition is the nanocomposite which consists of nearly spherical carbon nanoparticles (NP) with the average diameter of 80 – 200 nm (**Figure 3**) and carbon nanotubes (NT) with the diameters of 200 nm and the lengths of ~ 1 μm.

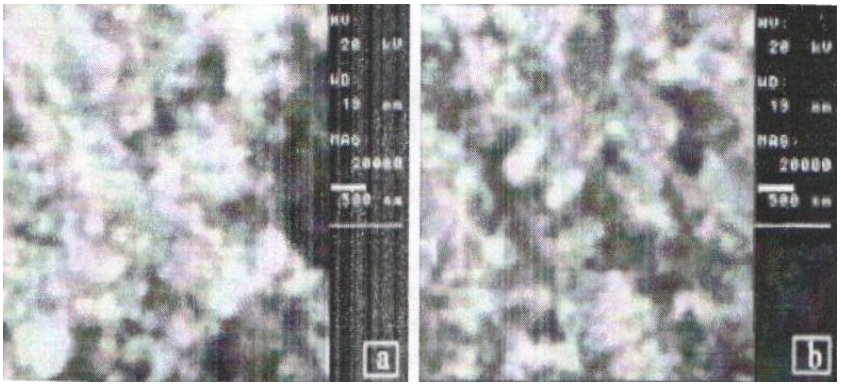

Figure 3. Electron microscopic images of magnetic powder of nanocarbon doped with iron.

In addition the carbon NPs having the structure of core & shell-type spheres, where the core represents pure iron atomic clusters, in the carbon NTs, the iron atoms' clusters are mainly concentrated at one end of the NT near the tube channel inlet. The iron concentration in the carbon NP of such a composite equals to 2.1 at. %.

The dimensions and shape of the magnetic carbon nanopowders or nanotubes can be changed not only by controlling the process's parameters, but also by the selection of hydrocarbon s used.

Under conditions of controlled oxygen partial pressure, from the nanoscale carbon it is possible to obtain a magnetic metal oxides of high purity, and then from these oxides – high purity metal in nanocrystalline state. **Figure 4** shows nanoscale powders of magnetic carbon and iron oxide (Fe_2O_3).

(a) **(b)**

Figure 4. (a) iron-doped carbon, (b) Fe_2O_3.

Unlike existing methods for producing carbon-based nanomaterials, this process is characterized as a simple one: it does not require the use of hydrogen and inert gases or vacuum. Cheap raw materials, easiness of the process control and simple hardware design allows the proposed method to obtain a diversity of carbon-based nanomaterials at low cost.

References

1. Ed. R. Jimenez–Contrares. Nanotechnology Research Developments. 2008, New York: Nova Sci. Publ. Inc.
2. L. N. Rukhadze, E. R. Kutelia, N. I. Maisuradze, B. G. Eristavi, S. I. Bakhtiyarov. Preparation and characterization of carbon nanoparticles doped with magnetic clusters. Georg. Eng. News, 2009, 4 (52), 56-59.

THE EFFECT OF ELECTROHYDRAULIC DISCHARGE FOR HIGH DISPERSIVE MAGNETIC NANOFLUID SYNTHESIS

V. Mikelashvili, J. Markhulia, Sh. Kekutia, R. Tatarashvili

V. Chavchanidze Institute of Cybernetics
Georgian Technical University
Tbilisi, Georgia
vmikelashvili@gmail.com

Accepted October 22, 2014

Introduction

The basis of electrohydraulic effect lies in the previously unknown phenomenon of a sharp increase in the hydraulic and hydrodynamic effects and amplitude of impact action. The results characterized by the realization of the pulse electrical discharge in the ion conducting liquid under the conditions of the maximum shortening of the pulse duration, maximally steep pulse edge and shape of pulse, close to the aperiodic [1].

Inside the volume liquid, locating in the open or closed vessel, the specially formed pulse electrical (spark, brush and other forms) discharge around the zone of its formation forms superhigh hydraulic pressure, capable of accomplishing the useful mechanical work accompanying by the complex of physical and chemical phenomena. The unique capabilities of electrohydraulic effect resulted in widespread use it in many areas: in the mechanical engineering and metal working, in welding and transportation systems in the mining industry and building materials industry, chemical industry, electrical engineering, in power plants, in medicine [2]. We use this phenomenon for the homogenization of magnetic nanofluid [3, 4]. However, in the scientific publications there is a lack of information using this method for magnetic nanofluid processing.

Nano materials and its research is one of the most important development frontiers in modern science. The use of nanoparticles materials offers many advantages due to their unique size and physical properties. Because of the widespread applications of magnetic nanoparticles (MNPs) in biomedical, biotechnology, engineering, material science and environmental areas, much attention has been paid to the preparation of magnetic nanofluids.

Fluids containing magnetic nanoparticles represent the colloidal dispersion of magnetic materials (ferromagnets: magnetite, ferrite) with particle size of five to several tens of nanometers which are stabilized into polar (water or alcohol) or nonpolar (hydrocarbons and silicones) environment through surfactants or polymers (surface-active substances). Principle of stability in colloidal systems is provided by interaction between particles together with Brownian motion, which compensates gravitation (the Brownian motion must overcome coprecipitation velocity). According to this, the nanoparticles (which volume fraction is no more than 25 % in liquid) are at the equilibrium state.

The stability of the magnetic colloid depends on the thermal contribution and on the balance between attractive (van der Waals and dipole-dipole) and repulsive (steric and electrostatic) interactions. The typical particle numerical density in a magnetic colloid is $\approx 10^{23}$ m^{-3}. To evaluate the typical particle diameter (D) to avoid magnetic agglomeration we compare the thermal energy with the dipole-dipole pair energy [2, 5] and get:

$$D \lessapprox \left(\frac{72kT}{\pi\mu_0 M^2}\right)^{1/3} \quad (1)$$

where k, T, μ_0 and M are the Boltzmann's constant, the absolute temperature, the permeability of free space and the intensity of magnetization. Plugging typical values one has $D \lessapprox 10$ nm.

The synthesis of uniform-sized (or monodisperse, with a relative standard deviation of < 5 %) nanocrystals is of key importance because the properties of these nanocrystals depend strongly on their dimensions. From the fundamental scientific viewpoint, the synthesis of uniform-sized nanocrystals with controllable sizes is very important to characterize the size-dependent physical properties of nanocrystals [2, 6]. For magnetic nanofluids the stability of sedimentary and aggregate condition is a major factor.

For the synthesis of magnetite (Fe_3O_4) nanoparticle containing fluids it is necessary to solve some problems: First, it is necessary to gain magnetic particles with size no more than 8 – 15 nanometers and to cover the particles of dispersive phase by the stabilizer molecules.This must prevent the agglomeration of particles and provide formation of steady colloid system of one-domain magnetic particles at the same time, dispersed in a liquid-carrier. Chemical deposition, by general point of view, do not gives finely divided (< 10 nm) homogenous dispersion (see **Figure 1**, sample 1), because in the liquid medium depending on synthesis parameters there are some micro and > 10 nm sized nanoparticles, some chemical radicals and conjugates represented [7 – 9].

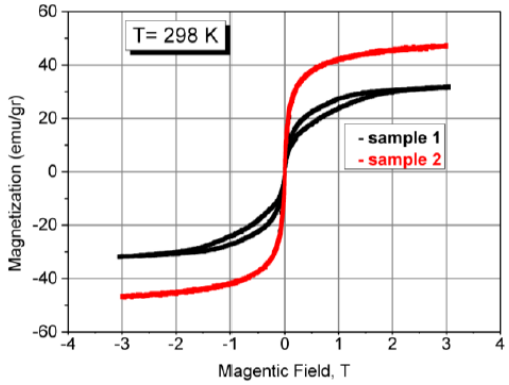

Figure 1. Magnetization vs magnetic field for magnetic naofluids synthesized by chemical co-precipitation (sample 1) and processed by electrohydraulic discharge (sample 2).

In addition, in the fluid occurs even more agglomeration and precipitation after certain amount of time from the synthesis, especially when the particles are not coat with surfactants. The disintegration of the agglomerate often cannot be achieved by agitation and stirring, there is needed an additional efforts to disperse them. One of the weapons is the ultrasonic processing. The advantage of the electro-hydraulic processing treatment discussed below with respect to the ultrasonic processing.

Electrohydraulic processing

Foundation, which ensures the varied technological opportunities of electrohydraulic effect, is the method of obtaining so-called overlong spark discharges in the conducting liquids. During the electrohydraulic discharge, cavitation bubbles generated by the pulsed arc discharge. Induced shock-like pressure rises in a cavitation zone near the discharge electrodes. These cavitated bubbles are a major source of UV emission and radical species such as ozone, OH, H_2O_2, etc. These chemical and physical reactions occur simultaneously in the cavitation zone [10, 11].

In this task, a principal scheme has developed (see **Figure 2**) which provides immediately transfer the energy through the air gap (see GAP1). Additional forming air Gap allow us to accumulate a certain amount of energy and avoid additional oscillating processes by impulse transfer, also to create sharp front of arc discharge [1]. Electrohydraulic aggregate consists of powerful transformer T2 as shown in **Figure 2**, Rectifiers diodes (D1–D4), and energy capacitor (C1). Voltage across capacitor rises until occurs the spontaneous breakdown of the air forming space, and entire energy, stored up in the capacitor, instantly enters on the Gap 2 in the liquid where release in the form of short, high power pulse. After that, the process is repeated with the frequency of a given capacity and voltage, which depends on the power of the feeding transformer.

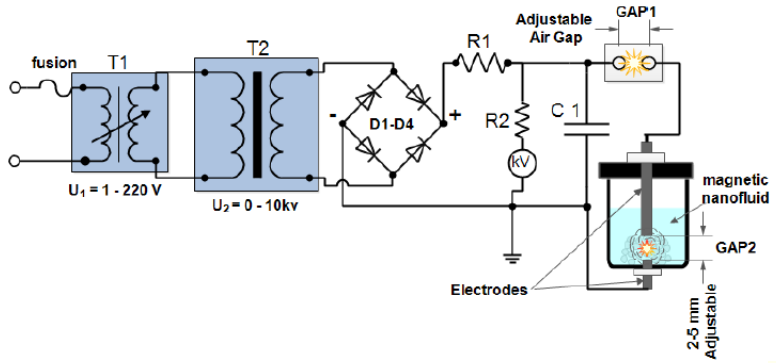

Figure 2. Principal scheme of the electrohydraulic device.

The energy emission characterized to the electrohydraulic method realized by active resistance of the contour:

$$\frac{1}{C} < \frac{R^2}{4L}, \quad (2)$$

where C is the capacitance of the condenser, R and L – active resistance and active inductance, respectively. Therefore, the main factors are the form of an electrical impulse and duration of the current.

The frontal slope of the current determines the velocity of discharge channel expansion. It is necessary to gradually accumulate energy on the condenser plates to be released at once. Adding several kV on the Discharge electrodes current pulse amplitude reaches tens of thousands of Ampere that provides immediate and significant increase in fluid pressure. This leads to the formation of a supersonic velocity wave and the fluid volume displacement speed reaches hundreds of meters per second [11]. Resonant processes and powerful infrared and ultrasonic vibrations additionally dispergate and fragmentate large materials, break down chemical bonds that are included in the medium composition and particle sorption.

Electromagnetic field during discharge significant effects on the ionic characteristics and physical and chemical changes in the medium as well.

Experiment

Magnetic nanoparticles by chemical co-precipitation of Fe^{2+} and Fe^{3+} ions in an alkaline solution prepared by the following reaction:

$$FeSO_4 + 2\ FeCl_3 + 8\ NaOH \rightarrow Fe_3O_4 + Na_2SO_4 + 6\ NaCl + 4\ H_2O. \quad (3)$$

1.9 g $FeSO_4$ and 2.2 g $FeCl_3$ dissolved in water separately, entire in 15 ml distilled water. These two solutions was thoroughly mixed and added to 20 ml, 7 % NaOH with constant stirring at 25 °C. Then, from synthesized the dark black slurry of Fe_3O_4, impurity ions such as chlorides

and sulphates removed by washing the particles several times with distilled water until pH reduced to 7.4. The resulting fluid was set on the magnet for separation of magnetitie nanoparticles from water. After that procedure, we gain 4.6 g magnetite in 100 ml volume, this corresponds 4.6 % concentration of magnetic nanofluid.

Two samples were sent to magnetic measurements. First, the sample after synthesis and the second after electrohydraulic processing (see **Figure 3**).

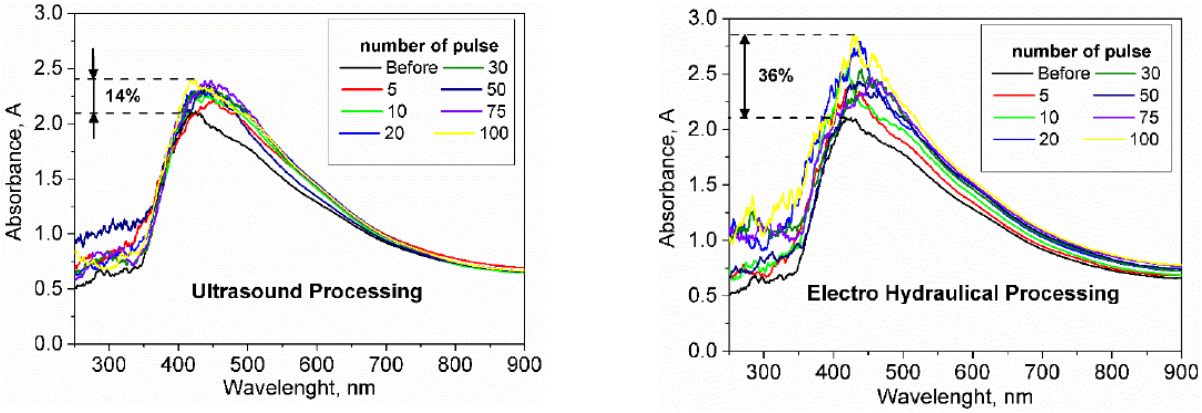

Figure 3. Changes in absorption spectrum of magnetic nanofluid after ultrasonic and electrohydraulic processing.

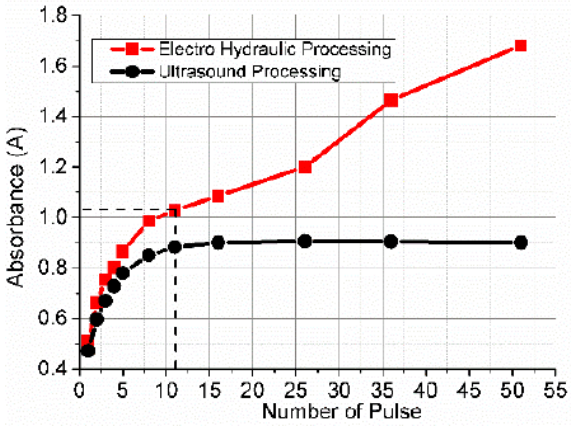

Figure 4. Optical absorbance (at $\lambda = 430$ nm) of a magnetic Nanofluid after ultrasonic and electrohydraulic processing.

For the visibility of photospectroscopy measurements the fluids with low concentration were prepared, 0.1 ml 4.6 % magnetic nanofluid dissolved in 250 ml distilled water. The concentration of solution consisted 0.00184 %. An Absorption in 430 nm wavelength measured for 100 ml samples in each case – after processing with ultrasound and electrohydraulic discharge (see **Figure 4**) – with respect to processing pulse number / time.

Discussion

The pulsed energy stored in the capacitor E was about 11.0 J, which was calculated by $E = 0.5CV^2$, where C was 0.1 μF and V the capacitor voltage was 15 kV. By the T1, (see **Figure 2**) variable transformer the output voltage from T2 varied from 2 to 10 kV. In one pulse, we consider steady pulse of a discharge with duration 70 – 100 microsecond. Time between pulses was 0.6 second. The spark discharge source in the fluid consisted of a stainless steel wire electrode (cathode) with a radius of 2 mm and an exposed length of 3 mm, and a brass cylindrical rod with diameter of 10 mm acted as anode. Distance between rods was 2 mm.

For the ultrasonic generator we used TOPT–500 ultrasonic homogenizer with operating frequency 22 kHz, ultrasonic power 10 – 500 W. Horn diameter 10 mm. Nanofluid processing carried out in 70 % of the ultrasound energy. Processing time is 1, pulse delay – 0.6 s.

For the concentration analysis we used "metash" visible spectrophotometer V–5100, with range 325 – 1000 nm, bandwidth 4 nm. We measured absorbance (A, also referred to as Optical Density or OD), the amount of light that is absorbed by a solution. We assume in a single pulse 2-3 stable Hydraulic discharge, and in the Ultrasound pulse - a single pulse, a 70 % power 2 s duration pulse.

There is a relationship between concentration and absorbance. This relationship expressed by the Lambert–Beer law – commonly known as Beer's law. This law states that the absorbance of a light absorbing material is proportional to its concentration in solution:

$$A = \varepsilon l c. \quad (4)$$

Here ε – the extinction coefficient of the substance, has units of $M^{-1}\,cm^{-1}$; l – the sample "thickness" the width of the cuvette, almost always – 1 cm, c – the concentration of the solution.

Figure 4 shows the dependence of the optical density changes in processing time. As seen in the picture concentration changes drastically after processing of sedimented nanoparticles in the liquid. In case of ultrasonic processing after certain pulse number absorbance goes through saturation. The change in particle concentration in the electrohydraulic processing relatively large, but do not saturates and continues to grow. It is associated with an increase free radicals and gas bubbles in the liquid during discharge [1, 11, 12]. Therefore, it is necessary to take into account the processing duration of electrohydraulic treatment (see the dashed area in **Figure 4**); power and volume of the fluid under processing; also discharge electrode and vessel geometry. It is the subject of our further research.

Wide absorbance range from 250 to 900 nm is shown on the **Figure 3**. As shown, the concentration increment after electrohydraulic processing of liquid is more than 22 % than after ultrasound treatment.

Vibrating sample magnetometer (VSM) is used to evaluate magnetization of the magnetic nanoparticles (MNPs) as a function of an applied external magnetic field (H) between –3 and +3 T. Based on the obtained VSM curve at room temperatures, magnetic behavior of the MNPs can be identified. For example at room temperature, the zero magnetic remanence (when H is zero), and the hysteresis loop feature indicates that the MNPs are superparamagnetic. Also, from the plateau part of the VSM curve, saturation magnetization can be determined (see **Figure 1**). The sample 1 is a magnetic nanofluid after chemical synthesis, the sample 2 – nanofluid after electrohydraulic processing. It is necessary to cover processed nanoparticles by surfactants to maintain the long-term stabilization, i.e. prevent farther sedimentation. However, covering by surfactant weakens the magnetic properties of particles. On the other hand, it is most important that the core / shell materials should possess sufficient magnetic and superparamagnetism properties for use in practical applications.

Conclusion

Experimental studies have shown the effectiveness of electrohydraulic processing on the high dispersive magnetite nanofluid synthesis. The concentration enhancement of Magnetite nanoparticle was caused by an instant increase of pressure and other physical phenomena

influence, which accompanied during electrohydraulic effect. However, the effective use of this effect closely related to the control of some physical parameters. Finally, the recorded hysteresis loops shows that the particles are superparamagnetic at room temperature, which is characteristic of a soft ferromagnetic material such as magnetite.

Acknowledgment

This work was supported by Shota Rustaveli National Science Foundation of Georgia in Scientific Program "Presidential Grants for Young Scientists", Project PG/54/3–250/13.

References

1. Л. А. Юткин. Электрогидравлический эффект и его применение в промышленности. 1986, Ленинград: Машиностроение.
2. W. Yu, H. Xie. A review on nanofluids: Preparation, stability mechanisms, and applications. J. Nanomater., 2012, 2012, 435873, 1-17.
3. ვ. მიქელაშვილი, ჯ. მარხულია, შ. კეკუტია, რ. თათარაშვილი. ელექტროჰიდრავლიკური ეფექტის გამოყენება სამედიცინო დანიშნულების მაღალდისპერსიული მაგნიტური ნანოსითხის მისაღებად. კრ.: მე-2 საერთ. კონფ. "ნანოტექნოლოგიები" მოხს. შინაარსები. 2012, თბილისი: ნეკერი, 30-37.
4. Sh. Kekutia.,V. Mikelasvili, J. Marlhulia, L. Saneblidze, S. Akhobadze. Synthesis of magnetic nanofluids and perspectives in medical application. In: Proc. Int. Conf. Phys. Meth. Res. Med. 2011, Tbilisi: Tech. Univ. 140-143.
5. R. E. Rosensweig. Ferrohydrodynamics. 1985, Cambridge – London: Cambridge Univ. Press / 1997, New York: Dover. Publ. Inc.
6. M. Faraji, Y. Yamini, M. Rezaee. Magnetic nanoparticles: Synthesis, stabilization, functionalization, characterization, and applications. J. Iran. Chem. Soc., 2010, 7, 1, 1-37.
7. H. el Ghandoor, H. M. Zidan, M. M. H. Khalil, M. I. M. Ismail. Synthesis and some physical properties of magnetite (Fe_3O_4) nanoparticles. Int. J. Electrochem. Sci., 2012, 7, 5734- 5745.
8. R. Hao, R. Xing, Zh. Xu, Y. Hou, S. Gao, Sh. Sun. Synthesis, functionalization, and biomedical applications of multifunctional magnetic nanoparticles. Adv. Mater., 2010, 22, 2729-2742.
9. И. В. Алексашкин, Е. Д. Першина, К. А. Каздобин. Оптимизация условий синтеза магнитной жидкости. Учен. зап. Таврического нац. ун-та им. В. И. Вернадского. (Сер. Биология, химия), 2010, 23 (62), 3, 227-235.
10. J. S. Chang, P. C. Loopy, K. Urashima. In: Proc. Asia–Pacific Workshop on Water & Air Treatment by AOT, 1998, 148.
11. М. А. Промтов. Перспективы применения кавитационных технологий для интенсификации химико-технологических процессов. Вест. ТГТУ, 2008, 14, 4, 861-867.
12. J. S. Chang, S. Ono, H. Ukai, Y.-C. Huang, W.-Y. Chang, P. Shou, M. Sato, S. Teii, C. Liu, K. Ting, UV and optical emissions generated by the pulsed arc electrohydraulic discharge. Int. J. Plasma Environm. Sci. & Technol., 2007, 1, 2, 1-5.

NANOSENSOR FOR THERMOELECTRIC SINGLE-PHOTON DETECTOR

A. A. Kuzanyan

Institute for Physical Research
Armenian NAS
Ashtarak – 2, Armenia
astghik.kuzanyan@gmail.com

Accepted October 22, 2014

1. Introduction

Single-photon sources and single-photon detectors are one of the most important components in the fields of quantum information and communications technology [1]. In addition to quantum information and quantum cryptography, single-photon detectors are required in research in different areas of modern science, particularly in space astronomy, single-molecule spectroscopy and high energy physics [2, 3]. They can also serve as a basis for development of a new generation of measuring systems for applications in medicine, homeland security, DNA sequencing, elemental microanalysis, traditional and quantum-enabled metrology, analysis of defects in microchips, positron emission tomography etc. [4 – 8].

Single-photon detectors (SPD) typically work by sensing an electrical signal that results from the absorption of a photon. An ideal SPD is the one for which: the detection efficiency (the probability that a photon incident upon the detector is successfully detected) is 100%, the dark-count rate (rate of detector output pulses in the absence of photons) is zero, and the count rate is as high as possible. In addition, an ideal single-photon detector would have the ability to distinguish the number of photons in an incident beam.

Conventional SPDs are based on photomultipliers and avalanche photodiodes, and are used in a wide range of time-correlated single-photon counting applications. A revolution in photon detection is now underway, with the advent of detectors based on superconductivity [9 – 12]. These new tools are dramatically improving the sensitivity of measurements across the electromagnetic spectrum, from radio waves through visible light to gamma rays. Superconducting Single-Photon Detectors (SSPD) come in two main types: thermal and pair-breaking. With both types, the energy of an individual photon (and hence its frequency) is revealed by the strength of the device's output signal. The thermal type of the detector relies on the fact that the electrical resistance of a superconductor rises sharply from zero to its normal value in the very narrow temperature range in which the material switches from superconducting to normal state. The comparison of SSPD with other fast photon counters present in the market shows that even when left unoptimized the SSPD beats other detectors in the sum of its technical characteristics. On the other hand, an extremely low temperature is required for the functioning of SSPD. The next problem was that the superconducting transition is often less than a thousandth of a degree wide, and it was very hard to keep the temperature of the device within that range. In 1993 K. D. Irwin offered to solve this problem

applying a constant voltage across the detectors, a technique called voltage biasing. This technique, however, complicates the structure of the detector.

In 1999 a group from the University of Tokyo and Japan Science and Technology Corp. lead by S. Komiyama fabricated a detector based on quantum dots (QD). They demonstrated two mechanisms of single photon detection in the THz spectral region by using gate-voltage-induced lateral GaAs/AlGaAs quantum dots. Firstly, a QD in strong magnetic fields ($B = 3 – 4$ T) is operated as a single electron transistor (SET). THz-photons (1.8 – 1.5 THz) excite the QD via cyclotron resonance, and electrical polarization is thereby induced within the QD. The polarization, in turn, affects the SET conductance. Secondly, a SET with parallel double QDs is operated without magnetic fields, where GHz-photons (about 500 GHz) excite and ionize one of the QDs, which is, in turn, probed by the other QD to change the SET conductance [13, 14]. In the first case the disadvantage of the device is its need of strong magnetic field; in the second one the "single-photon" property of the detector is lost.

Superconducting nanowire single photon detectors (SNSPD) offer single-photon sensitivity from visible to mid-infrared wavelengths, low dark counts, fast recovery times (~ 10 ns) and low timing jitter (~ 60 ps) [15]. They were introduced in 2001 by Gregory Gol'tsman and colleagues [16]. A standard detector consists of a superconducting NbN or NbTiN wire of small cross section, normally having a thickness below 10 nm and a width ~ 100 nm. The detector is operated at cryogenic temperatures well below the critical temperature of the device. Recent experimental progress in the development and application of single-photon detection techniques presented in [17 – 20]. Is there an alternative to SNSPD? Our study aims to answer this question.

2. Thermoelectric single-photon detector

The thermoelectric single-photon detector (TSPD) is one of the real competitors to superconducting detectors for single photon detection in a wide range of the electromagnetic spectrum [21 – 23]. The TSPD operation principle is based on photon absorption by absorber as a result of which a temperature gradient is generated on the edges of the thermoelectric sensor. Photon detection becomes possible by measuring the potential, emerging between the two absorbers. The scheme of the TSPD sensitive element is given on **Figure 1**. Such a sensor does not require either a separate power unit or a bias voltage. Therefore, it does not need additional leads for electronic circuitry either, and a matrix detector built on them will have a very simple engineering and electronic structure. Materials which can be used to prepare the absorber and the sensor and the achievable count rates and energy resolution are given in publications [23 – 25].

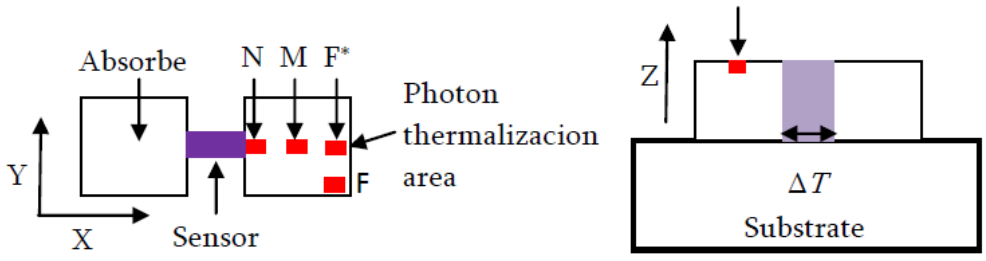

Figure 1. The detection pixel of TSPD.

A conclusion is done according which the thermoelectric detector may possess an energy resolution of 0.1 eV and a gigahertz level count rate. The conception of TSPD using a nanoscale sensor is proposed in [26]. Here we present the results of computer modeling of the TSPD. The sensor of the detector is composed of two micron-sized thin pads – photon absorbers connected by a bridge made of a thermoelectric material. The processes of heat distribution in absorption of a photon of different energy in different areas of the absorber for different sensor and absorber geometries are investigated. The calculations were performed for a tungsten absorber and a cerium hexaboride (CeB_6) sensor.

3. Computing technique

The calculations were based on the heat conduction equation:

$$\rho c \frac{\partial T}{\partial t} + \frac{\partial q_x}{\partial x} + \frac{\partial q_y}{\partial y} + \frac{\partial q_z}{\partial z} = 0,$$

where ρ is the density of the heat-conducting material, c — its specific heat capacity, and q_x, q_y and q_z — the projections of the heat flux density vector:

$$q_x = -\lambda \frac{\partial T}{\partial x},\ q_y = -\lambda \frac{\partial T}{\partial y},\ q_z = -\lambda \frac{\partial T}{\partial z}.$$

Here, λ is the thermal conductivity. The specific heat capacity at liquid-helium temperatures is determined by the equation

$$c = \gamma T + AT^3,$$

where the coefficients A and γ indicate the contribution of electrons and phonons. For simplicity of calculations in a first approximation, the phonon contribution to the heat capacity is not taken into account ($A = 0$). The calculations were carried out by the matrix method for differential equations. The operating temperature of the detector was taken to be 9 K. At this temperature, the materials used have the parameters presented in **Table 1** [27 – 31].

The modeling of thermal processes occurring in the absorption of a photon is as follows. The entire volume of the absorber and the bridge was broken down into a cell of the size Δx, Δy and Δz. These dimensions were typically of the order of 0.1 μm. Obviously, the greater the number of cells will provide the more accurate the calculation, but more time consuming.
The thermal processes were modeled according to the following algorithm.

- For all cells the initial temperature was set to 9K. The cell where the photon is absorbed was chosen in the absorber.
- According to the formula $\Delta T = E / V \rho c$, where E is the energy of the absorbed photon and V is the cell volume, the initial temperature of the cell $T_0 = 9\ \text{K} + \Delta T$ was calculated.
- Then the temperature of all the cells for each time point t_n was determined by the formula:

$$T_{ijk}(t_{n+1}) = T_{ijk}(t_n) +$$
$$+\frac{\Delta t}{\rho c}\left[\frac{\lambda(T_{i+1}) + \lambda(T_i)}{2} \cdot \frac{T_{i+1} - T_i}{\Delta x^2} + \frac{\lambda(T_{j+1}) + \lambda(T_j)}{2} \cdot \frac{T_{j+1} - T_j}{\Delta y^2} + \frac{\lambda(T_{k+1}) + \lambda(T_k)}{2} \cdot \frac{T_{k+1} - T_k}{\Delta z^2}\right].$$

Here i, j, k are the coordinates of the cell, n is number of time interval from the beginning of the process, Δt is the time interval. Obviously, the value of Δt also determines the accuracy and speed of calculation. By trial and error for each case the optimal value Δt is determined.

As can be seen in **Figure 1**, the sensor is composed of two absorbers of the same size. Red squares represent the area in which the absorbed photon is thermalized. The middle region of the absorber surface is denoted by the letter M, the closest one to the bridge – by N, and the

most distant one from the bridge – by F. The figure also shows the directions of the coordinate axes: x is parallel to the axis of symmetry of the sensor (corresponding to the length of geometric shapes), y is perpendicular to the x (width), z is perpendicular to x, y and the substrate surface (height).

One of the main characteristics of thermoelectric sensors is the time of the heat flow through the metal–insulator boundary (τ_K), which is called the Kapitza boundary [23]. This time is calculated by the formula $\tau_k = \frac{r_0 * C_{abs}}{T^3 * A_{abs}}$, where A_{abs} is the contact surface area, and at low temperatures $r_0 \sim 20$ K^4 cm^2 / W. If we substitute in this equation the heat capacity of tungsten at the temperature of 9 K (**Table 1**), we obtain the corresponding values of τ_K = 5.2, 15.6, 31.2 and 52 ps for the absorber thickness value of 0.5, 1.5, 3, and 5 μm, respectively. These are times that limit the transfer of heat of an absorbed photon from one absorber to another absorber through the thermoelectric bridge. Only for these time intervals a voltage will arise between the absorbers, by measuring which we can register the fact of photon absorption. We will try to find out below how feasible this is and what voltage may arise between the absorbers when absorbing photons with an energy of 100 eV.

Table 1. Parameters of used materials.

Parameters	Unit	W	CeB_6
Density, ρ	kg / m^3	19250	4800
Electron contribution, γ	J / kg · K^2	0.022	0.813
Thermal conductivity, λ	W / m · K	9680	0.94
Seebeck coefficient, S	μV / K	–	55–265

4. Registration of photons with an energy of 100 eV

The heat equation of heat distribution from a limited volume in a three-dimensional model was solved for various geometries of the thermoelectric sensor with boundary conditions of the absence of heat transfer to the medium and a slight loss of heat to the substrate, as in the end we will consider the initial stages occurring for times less than τ_K. **Table 2** shows the calculation numbers, data on the absorber and the sensor size (x, y, z), maximum temperature gradient value ΔT_{max} at the ends of the bridge derived from computer simulation, the time $t(\Delta T_{max})$ in which this maximum is reached, the voltage $\Delta U_{max} = \Delta T_{max} S$ (calculated using the Seebeck coefficient value S = 150 μV/ K averaged from literature reports), the time of the gradient fall to the background values $t(\Delta T = 10^{-4}$ K) and the detector count rate $R = 1 / t(\Delta T = 10^{-4}$ K).

As shown in [26], photons with an energy of 100 eV are absorbed with a 100 % probability in a 0.5 μm thick tungsten. And this thickness value of absorbers and the thermoelectric bridge is used in the calculations. Data of **Table 2** will be discussed in parallel with the consideration of the time dependence of the temperature difference at the ends of the thermoelectric bridge $\Delta T(t)$. In **Figures 2** and **3**, these dependences are given for the absorbers with the dimensions of 10 × 10 × 0.5 μm and 10 × 0.5 × 0.5 μm^3 respectively. The insets show the numbers of calculations and the size of the bridge.

Table 2. Sensor geometry, ΔT_{max}, ΔU_{max} and count rate (R) for $E = 100$ eV photon.

No.	W absorber size, μm	CeB_6 bridge size, μm	ΔT_{max}, 10^{-4} K	ΔU_{max}, nV	$t(\Delta T_{max})$, ps	t ($\Delta T = 10^{-4}$ K), ps	R, GHz
C1M	10×10×0.5	1×1×0.5	0.842	12.6	104.1	(10^{-5})>2000	<0.5
C2M	10×10×0.5	0.1×1×0.5	0.839	12.58	75.6	(10^{-5})>2000	<0.5
C3M	10×10×0.5	0.01×1×0.5	0.697	10.5	15	(10^{-5})>1500	<0.66
C4M	10×10×0.5	0.01×5×0.5	0.602	9	13.8	(10^{-5}) 330	3
C5M	10×10×0.5	0.01×10×0.5	0.47	7	13.2	(10^{-5})163	6.1
C6M	10×10×0.5	0.1×10×0.5	0.828	12.4	32.4	(10^{-5})>2000	<0.5
C7M	10×0.5×0.5	0.01×0.5×0.5	8.79	131.9	11.7	240	4.2
C8M	10×0.5×0.5	0.1×0.5×0.5	15.6	234	32.4	>2000	<0.5
C9M	10×0.5×0.5	1×0.5×0.5	15.9	238	39	>2000	<0.5
C10M	5×0.5×0.5	0.1×0.5×0.5	31.3	469	15	>5000	<0.2
C11N	5×0.5×0.5	0.1×0.5×0.5	136	2040	0.3	>5000	<0.2
C12F	5×0.5×0.5	0.1×0.5×0.5	31.2	468	21.6	>5000	<0.2
C13M[1]	5×0.5×0.5	0.1×0.5×0.5	34.4	516	14.1	>5000	<0.2
C14M[2]	5×0.5×0.5	0.1×0.5×0.5	28.1	421.5	12.3	>5000	<0.2
C15M	5×0.5×0.5	0.01×0.5×0.5	21.1	316.5	3.6	132.6	7.5
C16N	5×0.5×0.5	0.01×0.5×0.5	117.1	1756.5	0.3	119.7	8.4
C17F	5×0.5×0.5	0.01×0.5×0.5	18.1	271.5	10.2	136.5	7.3
C18M[1]	5×0.5×0.5	0.01×0.5×0.5	23.2	348	3.6	136.5	7.3
C19M[2]	5×0.5×0.5	0.01×0.5×0.5	19	285	3.6	128.1	7.8

[1] $E = 110$ eV

[2] $E = 90$ eV

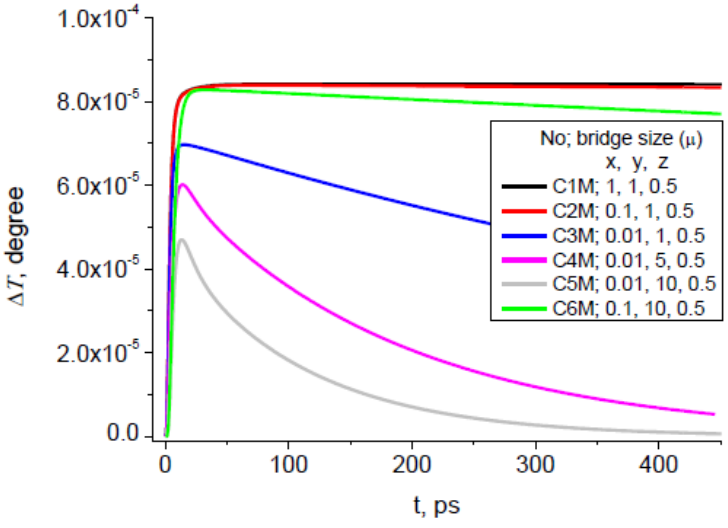

Figure 2. $\Delta T(t)$ dependence for a W absorber with the size of 10 × 10 × 0.5 μm³, bridge CeB_6 and photon energy 100 eV.

As can be seen in **Figure 2**, for the bridge length of 1, 0.1 μm and a width of 1 μm (C1M, C2M) the decline of ΔT after reaching a maximum is very slow. If we extend the bridge to the width of the absorber 10 μm (C6M), it decreases the ΔT_{max} value and the decline in ΔT is faster. However, a decrease in the length of the bridge to 0.01 μm (C3M–C5M) has a more significant impact on the variation of these parameters. The most encouraging is the curve corresponding to the calculation C5M. At the same time, according to both **Table 2** and **Figure 2** data, for the absorber size of $10 \times 10 \times 0.5$ μm^3 values ΔT less than 10^{-4} K are achieved, which is selected by us as the background for the operation of the thermoelectric detector. Reducing the volume of the absorber 20 times leads to a significant increase in the achievable ΔT_{max} values. **Figure 3** shows plots of $\Delta T(t)$ for three values of the bridge length – 1, 0.1 and 0.01 μm. And once again we see that the decrease in the length of the bridge leads, as might be expected, to some reduction of ΔT_{max} and an acceleration in the decline of ΔT after the maximum.

Let us further reduce the volume of the absorber two times and consider the influence on the $\Delta T(t)$ of the location of the photon thermalization zone (**Figure 1**) and of changes in the photon energy by 10 %. **Figures 4** and **5** show the results of these calculations for the bridge lengths of 0.1 and 0.01 μm respectively.

We first note the similarity of calculations presented in **Figures 4** and **5**. In all considered cases, ΔT_{max} values exceeding the background 20 times or more are reached. Significantly differ the $\Delta T(t)$ curves for the calculations labeled M, N and F. At the length of the bridge of 0.1 μm this difference is leveled for $t > 20$ ps, whereas for the bridge length of 0.01 μm the difference holds longer. If the photon energy is different by 10 eV, the ΔT_{max} differs by $3.38 \cdot 10^{-4}$ K. With the value of the Seebeck coefficient of 150 μV / K, this provides the build-up of a 50 nV voltage – a quantity that can be detected without the use of special electronics, distinguishing photons with an energy of 100 ± 10 eV.

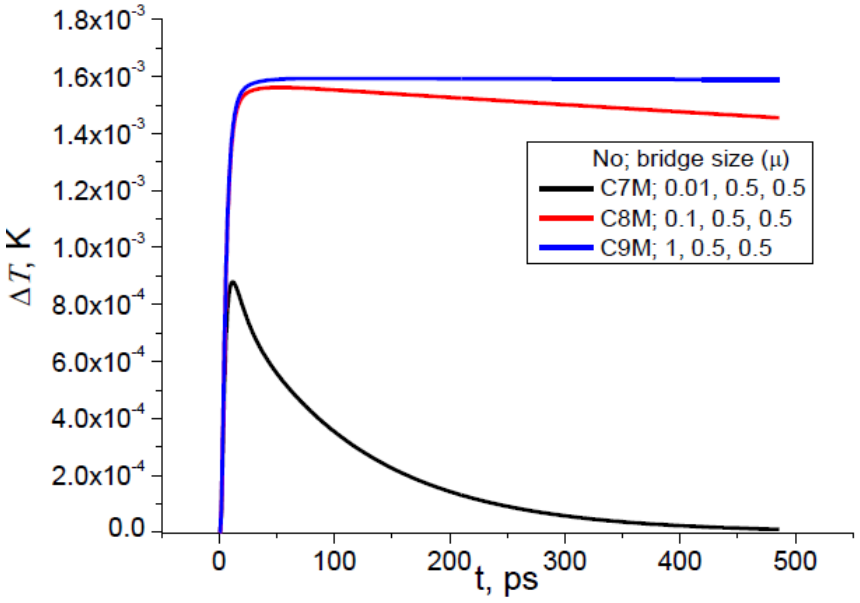

Figure 3. $T(t)$ dependence for a W absorber with the size of $10 \times 0.5 \times 0.5$ μm^3, bridge CeB_6 and photon energy 100 eV.

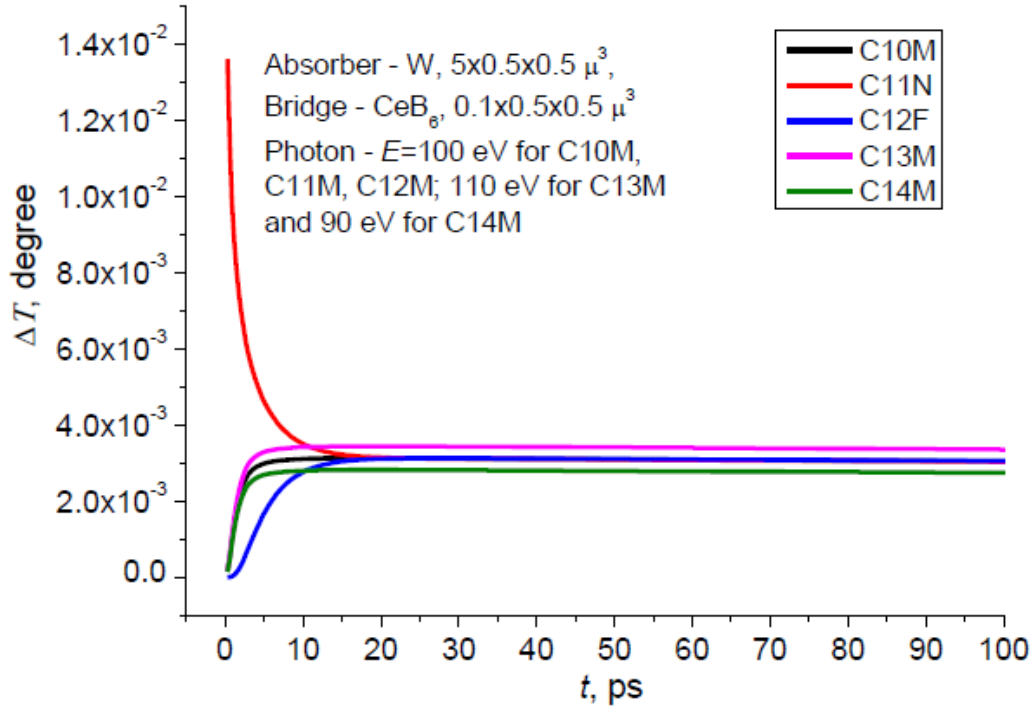

Figure 4. $\Delta T(t)$ dependence for a bridge length of 0.1 μm.

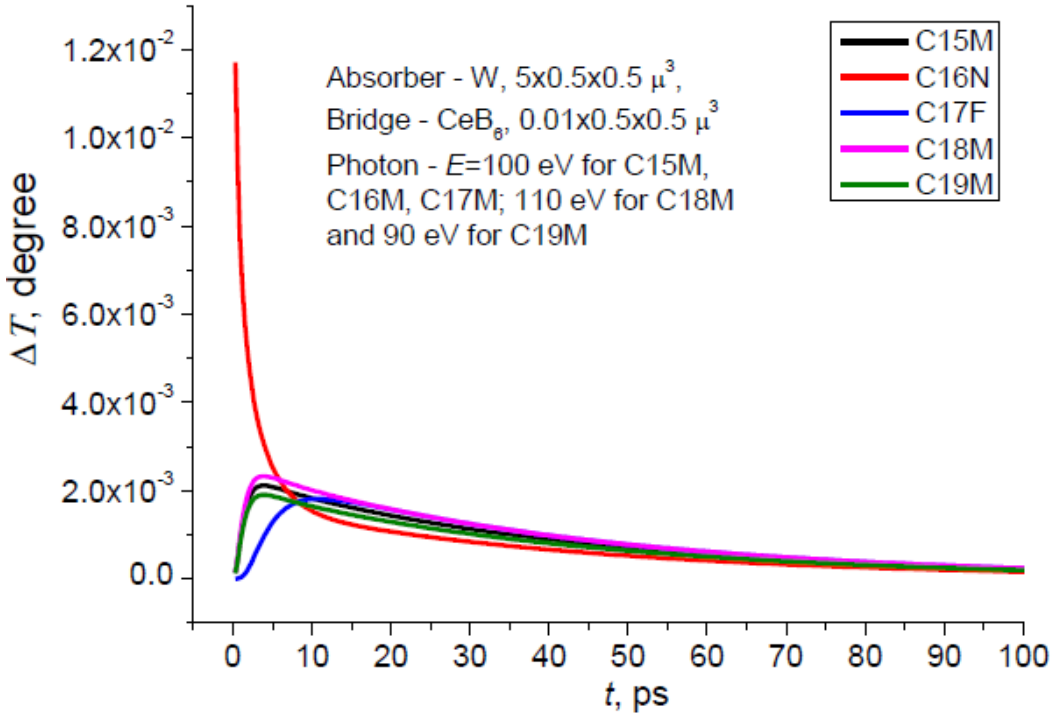

Figure 5. $T(t)$ dependence for a bridge length of 0.01 μm.

The dependences shown in **Figures 4** and **5** differ in that a shorter bridge provides a faster decline in ΔT. **Table 2** shows that according to calculations S15M–S19M one can expect a detector count rate at the level of 7.3 – 8.4 GHz.

It is time to remember about the Kapitsa boundary and the restriction imposed by it on the duration of the photon registration process. As mentioned above, for a 0.5 μm thick tungsten absorber this time is 5.2 ps. If one puts a condition that during this time the ΔT_{max} value should be reached, then to this condition correspond the calculations C15M, C16N, C18M and C19M. For sensors with corresponding characteristics, the count rate will be determined by the time of the heat flow through the Kapitza boundary. To the 5.2 ps process duration corresponds a count rate of 192 GHz!

5. Conclusion

- Using computer simulation of heat transfer processes in the three-dimensional model of a thermoelectric sensor, we have shown that the sensor with a tungsten absorber and a thermoelectric bridge of cerium hexaboride is capable of detecting photons with an energy of 100 eV and distinguishing between photons whose energies differ by < 10 %.
- For some sensor geometries, the temperature gradient decline time is more than the time of heat passage through the Kapitza contact τ_K, but during this time the ΔT reaches its maximum value and the resultant potential can be measured. In these cases, the detector count rate is determined by the time τ_K and for sensors with 0.5 μ thick tungsten absorbers it is respectively 192 GHz.
- If the thermoelectric bridge of CeB_6 possesses a Seebeck coefficient of S =150 μV/K, which corresponds to the average value reported in the literature, then as can be seen in **Table 2**, the resulting voltage can reach microvolts.

The characteristics obtained are encouraging and ensure the competitiveness of the thermoelectric detector with the superconducting single-photon detectors described in the literature. The simplicity of design of the thermoelectric sensor, the lack of stringent requirements for maintaining the operating temperature and the high operating temperature, two times higher than the boiling point of liquid helium, are additional advantages of the thermoelectric detectors based on CeB_6.

Acknowledgements

The author wishes to acknowledge the assistance of V. R. Nikoghosyan in preparation of calculation programs and A. M. Gulian and A. S. Kuzanyan for helpful discussions.

References

1. M. D. Eisaman, J. Fan, A. Migdall, S. V. Polyakov. Rev. Sci. Inst., 2011, 82, 071101.
2. R. Abusaidi, D. S. Akerib, P. D. Barnes, D. A. Bauer, A. Bolozdynya, P. L. Brink, R. Bunker, B. Cabrera, D. O. Caldwell, J. P. Castle, R. M. Clarke, P. Colling, M. B. Crisler, A. Cummings, A. da Silva, A. K. Davies, R. Dixon, B. L. Dougherty, D. Driscoll,

S. Eichblatt, J. Emes, R. J. Gaitskell, S. R. Golwala, D. Hale, E. E. Haller, J. Hellmig, M. E. Huber, K. D. Irwin, J. Jochum, F. P. Lipschults, A. Lu, V Mandic, J. M. Martinis, S. W. Nam, H. Nelson, B. Neuhauser, M. J. Penn, T. A. Perera, M. C. Perillo, B. Pritychenko, R. R. Ross, T. Saab, B. Sadoulet, R. W. Schnee, D. N. Seitz, P. Shestople, T. Shutt, A. Smith, G. W. Smith, A. H. Sonnenschein, A. L. Spadafora, W. Stockwell, J. D. Taylor, S. White, S. Yellin, B. A. Young. Phys. Rev. Lett., 2000, 84, 5699.

3. X. Michalet, O. H. W. Siegmund, J. V. Vallerga, P. Jelinsky, J. E. Millaud, S. Weiss. J. Mod. Opt., 2007, 54, 239.
4. A. Pifferi, A. Torricelli, L. Spinelli, D. Contini, R. Cubeddu, F. Martelli, G. Zaccanti, A. Tosi, A. D. Mora, F. Zappa, S. Cova. Phys. Rev. Lett., 2008, 100, 138101.
5. J.-P. Knemeyer, N. Marme, M. Sauer. Anal. Chem., 2000, 72, 3717.
6. S. V. Polyakov, A. L. Migdall. Opt. Express, 2007, 15, 1390.
7. D. A. Wollman, K. D. Irwin, G. C. Hilton, L. L. Dulcie, D. E. Newbury, J. M. Martinis. J. Microscopy, 1997, 188, 196.
8. V. C. Spanoudaki, A. B. Mann, A. N. Otte, I. Konorov, I. Torres–Espallardo, S. Paul, S. I. Ziegler. J. Inst., 2007, 2, 12002.
9. K. D. Irwin. Scientific American, 2006, November, 86.
10. B. L. Zink, J. N. Ullom, J. A. Beall, K. D. Irwin, W. B. Doriese, W. D. Duncan, L. Ferreira, G. C. Hilton, R. D. Horansky, C. D. Reintsema, L. R. Vale. Appl. Phys. Lett., 2006, 89, 124101.
11. J. N. Ullom, J. A. Beall, W. B. Doriese, W. D. Duncan, L. Ferreira, G. C. Hilton, K. D. Irwin, C. D. Reintsema, L. R. Vale. Appl. Phys. Lett., 2005, 87, 194103.
12. A. Semenov, G. N. Gol'tsman, R. Sobolewski. Supercon. Sci. & Technol., 2002, 15, R1.
13. S. Komiyama, O. Astafiev, V. Antonov, T. Kutsuwa, H. Hirai. Nature, 2000, 403, 405.
14. S. Komiyama, O. Astafiev, V. Antonov, T. Kutsuwa. Microelect. Eng., 2002, 63, 173.
15. R. H. Hadfield. Nat. Phot., 2009, 3, 696.
16. G. N. Gol'tsman, O. Okunev, G. Chulkova, A. Lipatov, A. Semenov, K. Smirnov, B. Voronov, A. Dzardanov, C. Williams, R. Sobolewski. Appl. Phys. Lett., 2001, 79, 705.
17. H. A. Atikian, A. Eftekharian, A. Jafari Salim, M. J. Burek, J. T. Choy, A. Hamed Majedi, M. Lonar. Appl. Phys. Lett., 2014, 104, 122602.
18. Y. Liang, H.-P. Zeng. Sci. China – Phys. Mech. Astron., 2014, 57, 1218.
19. D. Liu, S. Miki, T. Yamashita, L.You, Z. Wang, H. Terai. Optics Express, 2014, 22, 21167.
20. J. J. Renema, R. Gaudio, Q. Wang, Z. Zhou, A. Gaggero, F. Mattioli, R. Leoni, D. Sahin, M. J. A. de Dood, A. Fiore, M. P. van Exter. Phys. Rev. Lett., 2014, 112, 117604.
21. G. G. Fritz, K. S. Wood, D. van Vechten, A. L. Gyulamiryan, A. S. Kuzanyan, N. J. Giordano, T. M. Jacobs, H.-D. Wu, J. S. Horwits, A. M. Gulian. Proc. SPIE, 2000, 4140, 459.
22. D. van Vechten, K. Wood, G. Fritz, J. Horwitz, A. Gyulamiryan, A. Kuzanyan, V. Vartanyan, A. Gulian. NIMA, 2000, 444, 42.
23. A. Gulian, K. Wood, D. van Vechten, G. Fritzdet. J. Mod. Opt., 2004, 51, 1467.
24. V. A. Petrosyan. J. Contemp. Phys. (Arm. Acad. Sci.), 2011, 46, 125.
25. A. A. Kuzanyan, V. A. Petrosyan, A. S. Kuzanyan. JPCS, 2012, 350, 012028.
26. A. A. Kuzanyan, A. S. Kuzanyan. Proc. SPIE, 2013, 87730L.
27. T. R. Waite, R. S. Craig, W. E. Wallace. Phys. Rev., 1956, 104, 1240.
28. http://www.efunda.com/materials/elements/TC_Table.cfm?Elment_ID=W

29. S. R. Harutyunyan, V. H. Vardanyan, A. S. Kuzanyan, V. R. Nikoghosyan, S. Kunii, K. S. Wood, A. M. Gulian. Appl. Phys. Lett., 2003, 83, 2142.
30. Y. Peysson, C. Ayache, B. Salce, J. Rossat–Mignod, S. Kunii, T. Kasuya. J. Magn. & Magn. Mater., 1985, 47-48, 6365.
31. V. Petrosyan, Proc. SPIE, 2011, 7998, 18.

ENGLISH–GERMAN–RUSSIAN–GEORGIAN ELECTRONIC DICTIONARY (GLOSSARY) IN NANOCHEMISTRY, NANOPHYSICS AND NANOTECHNOLOGY

Ts. M. Ramishvili, V. G. Tsitsishvili

P. Melikishvili Institute of Physical and Organic Chemistry
I. Javakhishvili Tbilisi State University
Tbilisi, Georgia
rtsiuri@mail.ru

Accepted October 28, 2014

Nanoscience and nanotechnology are interdisciplinary branches that mandatorily require a creation of united term base. This is communication language for specialists of various branches (physicists, chemists, biologists, mechanicians, material scientists and others) who create nanoscience and nanotechnology besides, notions and terms corresponding to international standards will cause their uniform understanding and allow us to get rid of false, ambiguous interpretations. This language is created in advanced countries [1 – 4] and we have to make it understandable for Georgians using adequate terms in our native language.

There is no special Georgian-language dictionary (neither in printed nor in electronic form) in nanoscience and nanotechnologies – new and very prospective branches of science and technology, except of parts of English–German–Russian–Georgian "Short Dictionary (Glossary) in nanochemistry and nanotechnologies" [5 – 7], which was published in 2011 – 2013 in journal "Nano Studies" (Georgia), and which is the first attempt to create Georgian glossary in nanoscience and nanotechnology; it is a predecessor of electronic dictionary which creates by us together with Georgian physicists, specialists in nano- and information technology and lexicographers from the A. Chiqobava Institute of Linguistics (Tbilisi, Georgia).

Creation of Georgian electronic dictionary in nanochemistry, nanophysics and nanotechnology is timely, if not belated, since these branches develop successfully and rapidly in USA, advanced European countries (especially in Germany), China, South Korea and Japan beginning with 1980s. Nanoscience is being developed of a high rate, and the electronic format of dictionary provides possibility of its fast update.

Electronic dictionary will have one subject and different linguistic directions, particularly in special, nanoscience (nanochemistry, nanophysics) and nanotechnology directions; multilingual, translational: English–German–Russian–Georgian, illustrated and with explanations in Georgian; its volume, determined by words, word combinations and terms will count 5 340 unit per each language, total of up to 21 360 units. Based on significance of nanoscience and nanotechnology is extremely topical a creation of electronic dictionary in this branch, which will be mass consumer product. It will have a lexicographical, reference and especially educational value.

Dictionary consists of very common list of issues, among them will be nanomaterials, nanoobjects, methods of their synthesis, nanoelectronics, nanophotonics, nanomaterials for

optical, optical-electronic, electronic and magnetic systems, sensory materials, polymeric nanocomposites, nanoelectromechanical systems, functional and constructional nanomaterials, nanomaterials as energy source, chemical technologies of nanomaterials, engineering process of nanoproduction for receipt of nanomaterials using self-assemblage and self-organization, nanotechnologies for military, space, aviation technology and many other things.

For accomplishment of abovementioned goals the following tasks are set out:

1. Accumulation of English-language terms / synonyms used in nanochemistry, nanophysics and nanotechnologies according to topics and creation of their corresponding Georgian-language terms.
2. Searching a Russian and German terms / synonyms corresponding to English-language and Georgian lexical units.
3. Brief explanations of Georgian-language terms and notions used in nanochemistry, nanophysics and nanotechnologies, according to specification of two international technical committees ISO / TC 229 "Nanotechnologies" and IEC / TC 113 "Nanotechnology standardization for electrical and electronic products and systems"; also other standards elaborated by this committee for nanoscience and nanotechnology.
4. Selection of illustrative materials for every lexical unit with indication of sources.
5. Representation of obtained materials in electronic format.

The electronic dictionary, which we are going to develop, would be systematized by specialty, by subject or by branch signs. The dictionary would be Multilanguage: English-German-Russian-Georgian, illustrated and with explanations in Georgian. The e-Dictionary will have alphabetical and hierarchical structure. All preliminary chosen programs, that serves as a system that drives the developed e-Dictionary, belonged to the open source programs, distributed under GPL license (GNU GPLv3+). Those programs are already tested by other customers and are characterized as reliable, stable and they are updated in the systematic bases.

Special English–German–Russian term base is necessary for project implementation; electronic dictionary will be prepared on the basis of printed and electronic foreign (English, German, Russian) special authorial dictionaries, special scientific literature (periodicals, monographs, encyclopedias, ISO standards in nanoscience and nanotechnology, conference proceedings). Certain portion of this material will be purchased and other part can be found using Internet search systems. Difficulties expected in the process of project implementation include only disagreement of some foreign-language nanoterms with standards elaborated by international commissions and fast update of foreign-language lexical databases in nanoscience and nanotechnology. Among them the latter difficulty can be negotiated via continuous update of electronic dictionary.

Periodically, in parallel with electronic dictionary creation will be arranged presentations of its parts and discussions in Arnold. Chikobava Institute of Linguistics (Tbilisi), in University, with participation of interested persons of society; also there will be call button in computer program of electronic dictionary. We suppose it will be the best way of electronic dictionary's assessment.

Creation of **"English–German–Russian–Georgian Electronic Dictionary (Glossary) in Nanochemistry, Nanophysics and Nanotechnology"** in the era of nanotechnologies is notable for scientific culture of small-numbered Georgian nation as a bridge to ultramodern nanotechnological achievements, as means of creation of as far as possible universal communication tool in this branch. Dictionary will be unique tool for distribution of

professional knowledge of nanoscience among wide audience. Creation of electronic dictionary will be also certain contribution to Georgia lexicography.

Goal of dictionary **"English–German–Russian–Georgian Electronic Dictionary (Glossary) in Nanochemistry, Nanophysics and Nanotechnology"** is creation of multifunctional product from which is well visible its applied potential:

1. Creation of **Georgian-language lexical database, terminology** adequate to English-language terminology in nanochemistry, nanophysics and nanotechnology, which will be interesting and useful not only for researchers, students and professors, but for those who are engaged in nanotechnological manufacturing or schedule its creation: for engineers, technologists, investors, translators etc., who will create and develop Georgian nano-industry. 5 340 Georgian lexical units (words, word-combinations and terms) will be put into dictionary.
2. Dictionary will provide wide audience of readers with **basic information** about fundamental and applied aspects of nanochemistry, nanophysics and nanotechnology; basic knowledge and latest advances in branch will be united in it. Along with terms their explanations in Georgian will be presented in electronic dictionary, so dictionary will have **reference** importance.
3. Dictionary will be **one of means of Georgians communication** with people of other nationalities regarding nanoscience and nanotechnologies.

Electronic dictionary will be a product of corporate effort of Georgian scientists – chemists, physicists, lexicographer and information technologist.

Nanoscience and nanotechnology have close contact with society in the spheres such as science, technology, economics, culture, ethics, law, national safety and, of course, education. That's why students, scientists, researchers, technologists, investors, universities, scientific-research institutes, scientific-research laboratories of defense profile, teaching-scientific libraries, translators, can be among its consumers. Dictionary is meant for specialists working in nanophysics, nanochemistry and nanotechnology, who are related to chemistry, colloidal science, sol–gel technologies, aerosol technology, ceramic and chemical technology, material science, solid state physics, surface physics, supramolecular science, metallurgy, powder technology, machine building, aviation and space engineering, information technologies, computing engineering, optics, environmental protection etc.

Due to the fact that Georgian explanations will be presented in electronic dictionary along with terms, dictionary will have **reference** importance for scientists, scientific groups, universities, libraries of various institutions working in nanophysics, nanochemistry and nanotechnology.

We consider the use of following means: advertisement in internet, educational institutions, scientific-research institutes, libraries, field-oriented institutions, publishing houses as way and strategy of electronic dictionary's distribution.

As far as we know there is no multilingual dictionary in nanoscience and nanotechnology; therefore it will be also useful for foreign (English, German and Russian) readers interested in nanoscience.

After completion of electronic dictionary lexical database of dictionary will be updated, enriched, and dictionary will increase in volume on permanent basis, since electronic technologies make it possible; and second, in case of funding the issuance of dictionary in printing format will be possible too.

References

1. Dekker Encyclopedia of Nanoscience and Nanotechnology, Third Edition. 7-Volumes. Ed. by Sergey Edward Lyshevski. 2013. New York, USA: CRC Press. Ps. 6 779.
2. Encyclopedia of Nanoscience and Nanotechnology. Edited by Hari Singh Nalwa, 25-Volumes Set. 2004-2011. Valencia, California, USA: American Scientific Publishers. Ps. 20 000.
3. P. Herrmann, M. Schmitt. Wörterbuch Nanotechnologie. Deutsch–English. 2012. Berlin–Zürich: Beuth Verlag GmbH. S. 65.
4. Dictionary of nanotechnological terms and terms related to nanotechnology. Electronic dictionary. ROSNANO. 2009. http://thesaurus.rusnano.com
5. Ts. Ramishvili, V. Tsitsishvili. Nano Studies, 2011, 3, 115-150.
6. Ts. Ramishvili. Nano Studies, 2012, 6, 15-54.
7. Ts. Ramishvili, V. Tsitsishvili. Nano Studies, 2013, 8, 231-252.

MODERN THEORIES OF HOMEOPATHIC NANOPHARMACOLOGY

M. L. Chikava [1, 2], T. G. Tsintsadze [1],
Kh. T. Mishelashvili [1], N. V. Sulashvili [1, 2]

[1] Georgian Technical University
Tbilisi, Georgia
MedeaChikava@gmail.com
The University of Georgia
Tbilisi 0171, Georgia
ug@ug.edu.ge

Accepted November 26, 2014

There are a number of theories explaining the mechanism of action of homeopathic preparations. The basic theory was offered by Samuel Hahnemann, originator of homeopathy. Hahnemann believed that the whole world and all its parts are permeated by certain substance, which is too thin and inaccessible for ordinary perception. He believed that all curative substances have this power, but in its original form, like it is found in the nature.

Hahnemann observed the enhanced action of medications after every dilution and supposed that more and more **vital force** (life force) was liberated each time. This served as the basis for Hahnemann's view of low- and high-potency preparations. As the more diluted the preparation is, the less its dose is, but the stronger its action (force) becomes, Hahnemann called such conventional dose **potency** or force.

The same kind of substance, the vital force, is found in a human. In Hahnemann's view, the cause of any disease is the reduced dynamic force. So, it is the impact on the body vital force evidencing the effects of the homeopathic preparations; however, Hahnemann's views were contradicted by the developing materialistic scientific world-view as early as in Hahnemann's life and became a symbol of idealism and vitalism [1].

The experimental and clinical research in recent years have well evidenced that the medications affect the receptor mechanisms of the realization of physiological processes and cause a cascade of biochemical and physical-chemical reactions (S.. V. Anichkov, 1950, 1976; I. Cherkes, 1954, 1976; M. D. Mashkovskyi, 1960, 1989; P. V. Sergeev, 1981; I. V. Komissarov, 1983; I. S. Chekman, 1991).

The most efficient medications used in medicine affect the tissue receptors. Supposedly, there are special receptors in an organism, which react differently to the high and low doses of chemical compounds [1 – 3). The proponents of this theory tend to explain the mechanism of action of homeopathic preparations by probable impact of homeopathic preparations on their "own" homeoreceptors. Homeoreception is the means to influence on a human body by both, the medications and numerous factors of external and internal world, and the realization of modalities is closely associated with such influence. The homeopaths gain the desired effects provided the preparation is chosen accurately, in accordance with one's individual

homeoreception. One can prove the presence and functionality of homeoreceptors only pharmacologically.

Chekman, the Corresponding Member of the Academy of Sciences of Ukraine offers one more explanation of the efficiency of homeopathic preparations. According to him, the interaction of the homeopathic preparations ultralow doses with tissue receptors (homeoreceptors) causes not only biochemical and physical-chemical, but also the whole cascade of quantum-mechanical reactions resulting in the therapeutic effect [1, 2]. In other words, the action of homeopathic preparations is realized in the same way as many classic allopathic medications [1].

At present, the view of the homeopathy stimulating the immunobiological forces of a body is widely recognized. As for the ultralow doses, the clinical and experimental studies contain a number of suppositions of substances being more active at concentrations less than it is accepted in classical pharmacology. Even more so, the view of the limits of small doses expands permanently. The staging of the reaction to different doses of a stimulus is proved by L. K. Garkav, M. V. Ukolova and E. V. Kvakina, who discovered 10 levels of body reactions depending on the dose. N. P. Kravkov, with his experiment on epinephrine, showed that its high and low doses have opposite effects on blood vessels. I. P. Pavlov discovered a similar mechanism of action with caffeine. He stated that "a dose is more important when reduced rather than increased".

P. V. Simonov established that subminimal doses of substances cause retention evidenced by the clearly seen protective properties. The author called this action preventive. He writes: "The ability to cause the effect opposite to an average dose is perhaps the property of subminimal doses of many curative substances". He supposes that it is this property the reliable therapeutic effects gained by the homeopaths should owe to. As for the high dilutions theoretically not containing even one molecule of the active substance, the view of it among the homeopaths varies widely. On the other hand, the studies of some scientists evidence that the highly diluted solutions can lead to the biological effects.

In the 1930s, V. M. Person, homeopath from Leningrad, discovered the impact of the mercurous chloride of 10^{-12} dilution on starch fermentation with ptyalin, and on fibrin lysis with pepsin and tripsin, and gained reliable results. However, the regularities to equalize the use of ultralow doses to therapeutic principle have not been identified yet, as this problem is understudied in science. However, the major question of homeopathy not studied to date is the phenomenon of potentiation. Modern chemistry or physics do not offer any view of this issue. Despite this, the said doses (potentiating) are commonly used to date.

Many observers note that the reduced doses are followed by either reduced, zero or renewed and increased activity of the substance. Then, they speak about the efficiency of ultralow doses notwithstanding the fact that usually, they believe that the opposite is true. One can compare this with homeopathy, as most people, and scientists among them, consider the ultralow doses as homeopathic. In such cases, the observers do not indicate the methods of dose reductions. Perhaps, this is done by gradual dilutions, i.e. without the effect of potentiation.

Hahnemann was the first to pay particular attention to the regular dilutions and put forward the idea of drug potentiation. It should be noted that it is the homeopathic preparation prepared by using dynamization being a carrier of certain specific information. What does this mean? What are the body perception mechanisms and further reciprocal changes like? By answering these questions we will probably be able to understand the theory of homeopathy. A

number of woks, mostly by English and American homeopaths, prove the efficiency of high dilutions. These are the works in biology, biochemistry, biophysics and magnetic-nuclear resonance having left without due attention of the scientific society.

Some authors give a hypothesis of water becoming coherent as a result of interaction between the water dipole and irradiation of a diluted molecule and acquiring the property to transfer the specific information to the cell receptor, like the laser does. The surface of the cell membrane is the mediator between the electromagnetic waves and biological activity of a cell. A cell membrane rigorously retains its surface potential, which is sometimes changed by an electromagnetic field, by the virus penetration or by the connections of neurotransmitters (mediators), hormones or growth factors with its receptors. A. B. Libov in his studies presumes that specific ion currents caused by Faraday law, acts on the cell surface receptors and ion channels.

In specific cell areas, such as ion channels and cell receptors, the dissipation of waves may decline. In such cases, different ions and charged side chains, due to the influence of the electromagnetic signals on the cell receptors, will follow the exactly determined resonance circular or spiral pathway. The ions moving through ion channels are forced to move along a spiral pathway. Similarly, the receptor molecules are forced to move between the bilipid layers, resonate with specific frequencies to cause a signal transfer and thereby the periodic action typical to them will occur. Any movement or change in conformation of the growth factor receptors will lead to the signal transferring processes.

The ordered water molecules forming a by means of intermolecular hydrogen bonds, will be located between the growth factors and receptors; however, they are not essential for connecting to proteins. The ordered water molecules are placed on other surfaces of proteins and may be bounded, or unbounded to them. For example, the water molecules filling the space between the hormones and receptors in the bounded state of a ligand-receptor are totally accessible for electromagnetic activation in their unbounded state.

Thus, presumably, high dilutions of substances change the electromagnetic forces thus causing the resonance of the signal proteins of a cell surface, which transfer the biological activity through the cell receptors and ionic channels and initiate the signal transferring processes. It should be noted that the hypothesis about the information activity of homeopathic preparations was put forward as far back as in 1962, by N. Vavilova, homeopath from Moscow.

In recent years, they tried to explain the effects of homeopathic drugs by using a famous Arndt–Schultz law. However, this law is not universal. If considering the literary data, the issue as to whether the given law is effective with high dilutions is unclear, as such dilutions contain no molecules of the initial substance. Despite this, certain regularities between the effects of the maximally high and minimally small doses can be identified.

Another important issue to be taken into account when talking about the action of homeopathic preparations concerns the interaction of such preparations with blood transmission systems. The serum proteins and peptides, and albumens in the first instance, have bonding ability with different compounds. The metabolic pathways of these compounds are different depending on the degree of their affinity and value of the bonding power: the compounds with high degree of affinity mostly metabolize through liver, while those with low degree of affinity are excreted through kidneys. As there are specific bonding systems for different mediators, such as histamine, serotonin and prostaglandins, we can assume that it is through them the effects of the homeopathic preparations are realized.

There is a theory linking the mechanism of action of homeopathic drugs to the effect of contamination. Free radicals are formed in a contaminated solution resulting in the pharmacological effect. In 1971, G. Baeyer designed the first cybernetic model with the high dilution being the information carrier. Many researchers have offered the mechanisms to explain the memory of the alcohol and water mixtures. These mechanisms are described in the works of an American researcher D. Vahina, director of the department of non-traditional medicine at the National Health Institute. The information transferring action of the material particles of a substance is provided by changing the properties of the solvent. One of the models suggests that during the dynamization, the water molecules form the structures like a grape bunch corresponding to the configuration of the molecules of the substance [1].

The changes in the structure of solvents during the potentiation of homeopathic preparations were also noted by F. R. Chernikov and V. V. Maklakov, scientists of the Institute of Physical-Technical Problems of Moscow. There are many other works dedicated to this issue. Some authors explain the action of homeopathic preparations by the specific structures of Oxygen-18 and heavy isotopes of deuterium, which give signals to the biological systems. There is a view of the information being transferred through “coherent oscillations” of water molecules.

It may be said that homeopathic information in order to realize its effect in a body, affects the bioregulatory systems in the first instance. In modern view, homeostasis is regulated at different levels, including neuroendocrinal, immune, cellular and molecular mechanisms. Didier Grandgeorge was one of the first to try to explain the mechanisms of action of a homeopathic drug by means of neurophysiology. In his opinion, the central nervous system functions with the scales of homeopathy. A nerve impulse causes the changes in the state of a cell membrane and liberation of the homeopathic doses of neurotransmitters (mediators) in the synaptic gap.

At present, several tens of molecules playing the role of a neurotransmitter are known. For example, D. Grandgeorge associates the action of opium, the homeopathic preparation, with the suppression of synthesis of endomorphin, and action of Nux vomica with the changes in a glycinergic system.

References

1. А. И. Тихонов, С. А. Тихонова, Т. Г. Ярных, В. А. Соболева, А. Ф. Пиминов, В. М. Толочко, О. Н. Должникова, М. Ф. Пасечник, Л. М. Винник. Основы гомеопатической фармации. Уч. для студ. фармацев. спец. 2002, Харьков: ВУЗ. Мин. здрав. Укр. – Нац. фармацев. акад. Укр.
2. И. С. Чекман. Гомеопатия и современная фармакология. 2013, Киев. http://www.polykhrest.od.ua/other/years_articles1998_.php?id=68
3. И. С. Чекман. Клинико-экспериментальные основы фармакологии и гомеопатии. 1999, Киев.

ELECTRICAL, OPTICAL AND STRUCTURAL PROPERTIES OF TITANIUM DIOXIDE DIELECTRIC FILMS FORMED BY DC MAGNETRON SPUTTERING

A. P. Bibilashvili [1, 2], Z. S. Kushitashvili [1, 2], G. K. Skhiladze [2]

[1] I. Javakhishvili Tbilisi State University
Tbilisi, Georgia
amiran.bibilashvili@tsu.ge
zurab.kushitashvili@ens.tsu.edu.ge
[2] Institute of Micro and Nanoelectronics
Tbilisi, Georgia
givi.sxiladze@tsu.ge

Accepted December 11, 2014

1. Introduction

Progress in microelectronics and nanoelectronics has stimulated the design of fundamentally new methods for producing oxide films, as well as the further development of conventional methods. High-temperature treatment leads to the spread of diffusion regions, the diffusion of unwanted impurities, the generation of defects (dislocations, voids, cracks), the violation of the ratio between the components in binary semiconductor compounds, and so on. All these factors have a detrimental effect on the parameters of integrated circuits and the yield of devices. Taking into account the factors above, we have reason to believe that low-temperature methods are very promising. A large number of methods may be used to form thin TiO_2 layers; these include evaporation [1] or sputtering [2, 3] of TiO_2, metalorganic chemical vapor deposition (MOCVD) [4], chemical vapor deposition (CVD) [5, 6], rapid thermal oxidation (RTO) [7] and so on. All of them have in some case advantages and in some case disadvantages.

In this report we suggest reactive magnetron sputtering method for receiving thin dielectric TiO_2 layers with high dielectric constant.

2. Experiment

Titanium oxide thin films were deposited onto silicon substrates by using DC magnetron sputtering system. Pure titanium (99.999 %) of 100 mm diameter and 6 mm thickness has been used as sputtering target. High purity argon and oxygen were used as the sputtering and reactive gases respectively. Rotary and turbo pump combination was used to get the desired vacuum. The base pressure of the system is less than 10^{-5} mbar. After attaining the base pressure the oxygen partial pressure was set using aneedle valve. Before each run the target was pre sputtered in Ar atmosphere for 5 – 10 min in order to remove the surface oxide layer of the target. All the depositions were carried out at a total pressure of $1.3 \cdot 10^{-3}$ mbar. The distance between the target and substrates was kept at 45 mm.

In order to enable electrical assessment of the titanium dioxide layers produced, 1.3 mm aluminum dot MOS capacitor were fabricated. Those layers which showed a low DC leakage current were analyzed by capacitance-voltage ($C-V$) measurements at a frequency 1 MHz.

3. Results and discussion

Titanium dioxide layers were analyzed using the capacitance-voltage technique. The variation of the capacitance with gate voltage ranging from –5.0 to +5.0 V with frequency 1 MHz was obtained using Keithly Instruments Semiconductor Parameter Analyzer. The oxide capacitance is the high frequency capacitance when the device is biased for strong accumulation. The $C-V$ plot is shown in **Figure 1**, giving a flatband voltage $V_{FB} = -0.5$ V, threashold voltage $V_{TH} = 0.35$ V, oxide capacitance $C_{OX} = 5.03$ nF, the oxide charge density [8] of capacitor was calculated by

$$Q = C_{OX}\,\frac{W_{MS}-V_{FB}}{A} = -113\ \mathrm{nC/cm^2}, \qquad (1)$$

where W_{MS} is a work function between metal and semiconductor and was calculated to be 0.8 V.

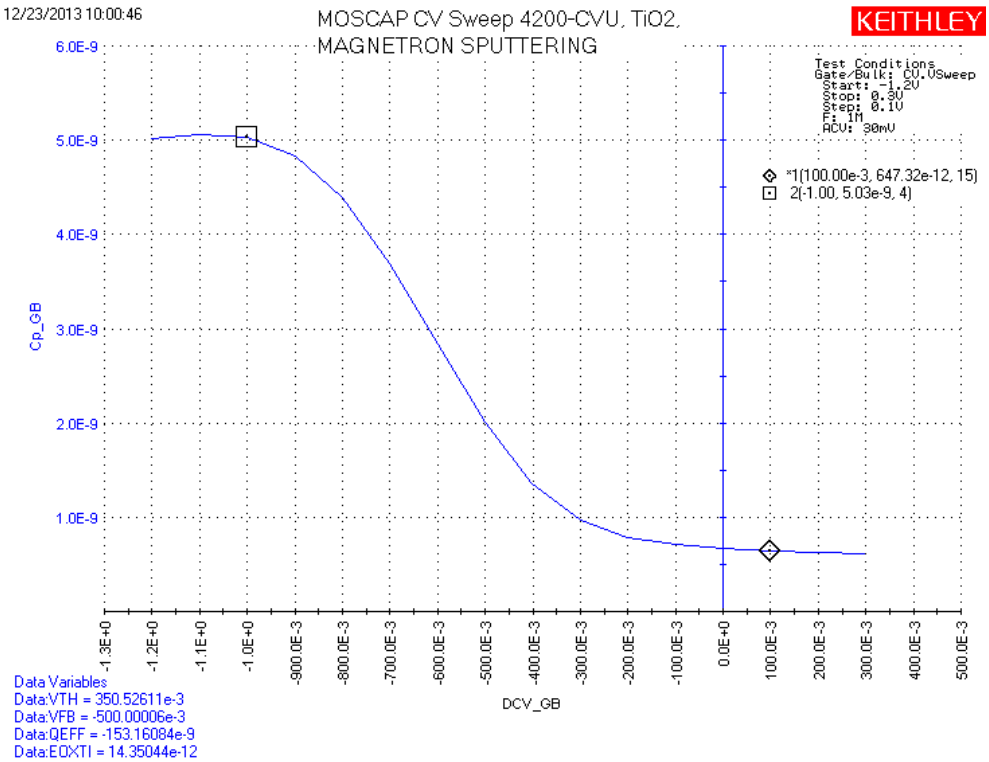

Figure 1. Capacitance–voltage characterization for magnetronsputtered TiO_2.

The dielectric constant (K) of TiO_2 was observed by calculation from the knowledge of the capacitance (C_{OX}), film thickness (T_{OX}), the free space charge permittivity (ε_0) and the area of the capacitor (A) using the relation [8]

$$K = \frac{C_{OX}T_{OX}}{\varepsilon_0 A} = 35. \qquad (2)$$

The oxide thickness was measured by Spectroscophic Elliphsometer and it found to be 85 nm.

The dielectric constant was calculated to be 35, which is lower than may be expected for titanium dioxide. The reason is relatively high leakage currents, for an applied voltage bias of 2 V leakage current is $1.5 \cdot 10^{-3}$ A. Also there is a possibility of existing of a very thin layer of silicon dioxide due to oxidation of the silicon substrate in the TiO_2 / Si interface.

Figure 2 shows the results of X-ray diffraction employing Cu K_α radiation.

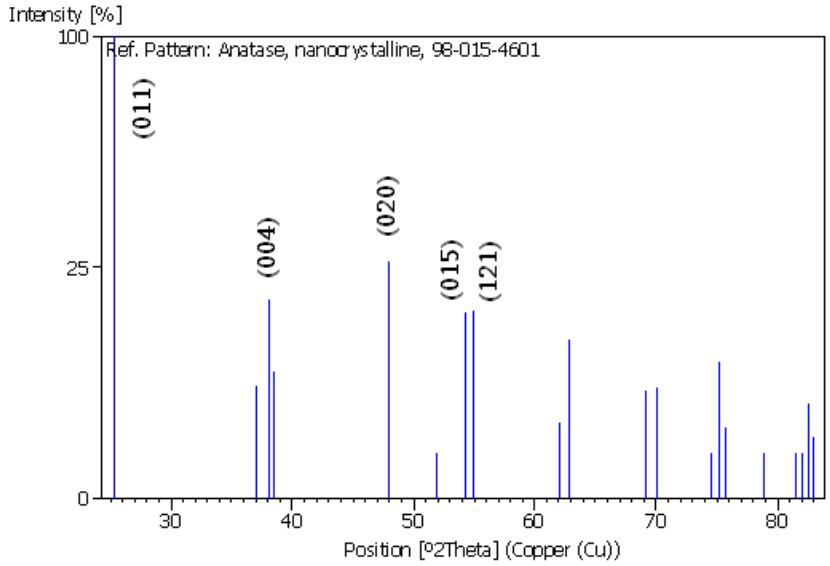

Figure 2. Intensity vs °2Theta from XRD measurement.

Crystal system is tetragonal. The (011), (004), (020), (015) and (121) diffraction peaks of the TiO_2 are high intensity peaks. Crystallographic parameters are $a = 3.7960$, $b = 3.7960$ and $c = 9.4440$ Å, calculated density is 3.9 g / cm^3. The mineral name is anatase nanocrystalline [9]. This indicates that either a low degree of crystallinity or that the films are large crystalline but with a small crystallite size.

Refractive index and the thickness of the oxide were measured by Spectroscopic Ellipsometer (**Figure 3**).

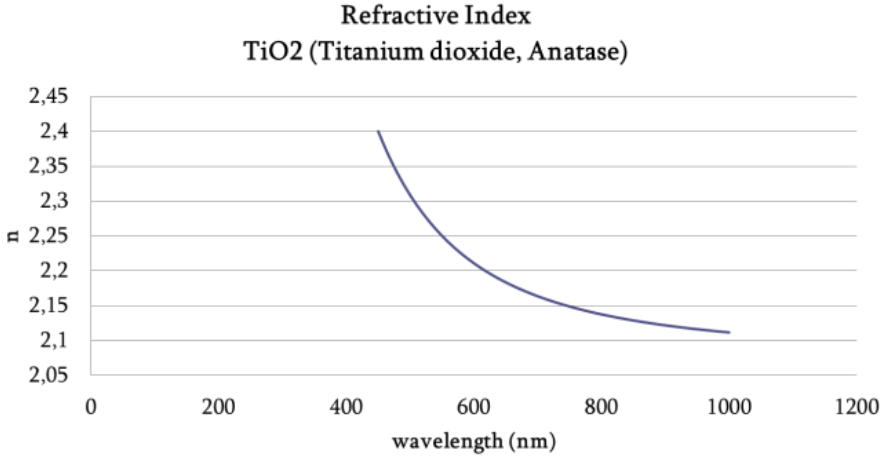

Figure 3. Refractive index of TiO_2.

In the visible light range (~ 550 nm) the refractive index is about 2.25. The optical dielectric constant can be determined from the refractive index of TiO_2 as $\varepsilon = n^2 = 2.25^2 \approx 5.43$. The band gap was calculated 3.3 eV by using equation

$$E(\text{eV}) = \frac{hc}{\lambda} = \frac{1240}{\lambda}. \quad (3)$$

E is photon energy, h – Planck constant, c – speed of light, λ – cut of wavelength by the help of Spectrophotometer, which equals $\lambda = 375$ nm.

4. Conclusion

Titanium dioxide thin films had been deposited onto silicon substrate using DC magnetron sputtering. The research was carried out on a film of thickness 85 nm. XRD analyses reveal the anatase nanocryatline nature of the film. The dielectric constant of TiO_2 thin film had been determined from the $C-V$ characterization. Relatively low dielectric constant can be explained by high leakage current and more research is needed to solve leakage current problem without decreasing effective dielectric constant.

Acknowledgments

The authors would like to thank Bilkent University, Instittutte of Materials Science and Nanotechnology (UNAM), Ankara, Turkey for support all measurements, which are given in this article.

References

1. W, D. Brown, W. W. Granneman. Solid State Electron., 1978, 21, 837.
2. D. Mardare, P. Hones. Mater. Sci. & Eng. B, 1999, 68, 42.
3. M. Takeuchi, T. Itoh, H. Nagasaka. Thin Solid Films, 1978, 51, 83.
4. T. Fuyuki, T. Kobayashi, H. Matsunami. Jpn. J, Appl. Phys., 1986, 25,1288.
5. J. P. Lu, J. Wang, R. Raj. Thin Solid Films, 1991, 204, L13.
6. K. S. Yeung, Y. W. Lam. Thill Solid Films, l983, 109, 169.
7. G. P. Burns. J. Appl. Phys., 1989, 65, 2095.
8. E. H. Nicollian, J. R. Brews. MOS Physics and Technology. 1982, New York: Wiley.
9. A. M. Tonejc, I. Djerdj. J. Alloys & Comp., 2006, 413, 159.

THE MAGNETIZATION DUE TO ACTIVITIES OF MAGNETIC PARTICLES IN MAGNETIC FLUIDS

K. V. Kotetishvili, G. G. Chikhladze

Georgian Technical University
Tbilisi, Georgia
ketinooo@hotmail.com
gurchix@gmail.com

Accepted Jenuary 21, 2014

1. Introduction

In MRI three types of the density of a magnetic flux are applied: the first – strong B_0 field in z-direction, the second – B_1 transverse radio-frequency wave, while the third – space-coded fields (G gradients) in z-directions as well.

B_0 field of about 1.5 T is induced by polarization of nuclear spins. Then relatively less will be B_1 field (approximately 0.01 T) used for transportation of induced magnetization into transverse component of the pattern as well as G gradients (~ 10 mT / m) used for the space coding of the transfer magnetization.

For high B_0 fields at ordinary MRI it shows that the equilibrium of the magnetization for magnetic fluids will be saturated and the particles of the fluid will be in accordance with B_0, i.e. will be lined in B_0 direction [1, 2].

In the paper low (sick) fields of 0.10 – 0.35 T are considered. In such kind of low fields the fluid is unable to reach saturation (is not completed) and nano-particles revolve in additional, also revolving, magnetic field.

2. Magnetization in sick fields. Basic equations

Under an action of a magnetic field the expression for relaxation of the magnetization for magnetic fluids is given as follows

$$\frac{\partial \vec{\mathrm{M}}}{\partial \mathrm{t}} + \vec{\upsilon} \cdot \nabla \vec{\mathrm{M}} - \vec{\omega} \times \vec{\mathrm{M}} + \left(\frac{1}{\tau}\right)\left(\vec{\mathrm{M}} - \vec{\mathrm{M}}_{\mathrm{sat}}\right) = 0, \quad (1)$$

which at the same time provides both the magnetization and the re-orientation of given field. $\vec{v}$ is the vector of linear velocity of the magnetic fluid, while $\vec{\omega}$ the vector of spin velocity of the magnetic fluid and τ – its time of relaxation.

The left-hand-side of (1) is straightly dependent on $\vec{v}$ velocity of the linear motion and on $\vec{\omega}$ angular (spin) velocity. The equation of state in the magnetic field possesses the time constant characteristic for the equilibrium magnetization described by the following expression:

$$\frac{1}{\tau} = \frac{1}{\tau_B} + \frac{1}{\tau_N}, \tag{2}$$

τ_B, τ_N being Brown's and Neel's times of relaxation, respectively, given as follows:

$$\tau_B = \frac{3V_h\mu_C}{kT}, \tag{3}$$

$$\tau_N = \tau_0 \cdot e^{\frac{k_\alpha V_p}{kT}}, \tag{4}$$

V_h being the hydrodynamic volume of nano-particles in m^3, while μ_C – the dynamic viscosity of the given fluid (ns / m^2), k – Boltzmann's constant, T – the absolute temperature (if no other hints are given, assume 295 K or 22 °C). V_p is the volume of nano-particles in m^3 (excluding the active external particles), k_α being the anisotropic constant (J / m^3) and τ_0 is Neel's time characteristic (in ns). Usually $\tau \approx 10^{-9} - 10^{-10}$ s. In (2) the smallest time constant is denoted by τ. Thus, at Brown's and Neel's relaxation the radius of particles increases.

Neel's relaxation, describing the rotation of the magnetization vector of particles, usually dominates for small particles of less than 4 nm radius, while Brown's relaxation, due to rotation of the particles in a fluid, dominates for the particles of radius exceeding 4 nm.

If the number of particles in a magnetic fluid is fixed (for example, being located at its surface), the only Neel's relaxation is in action, while Brown's relaxation is absent.

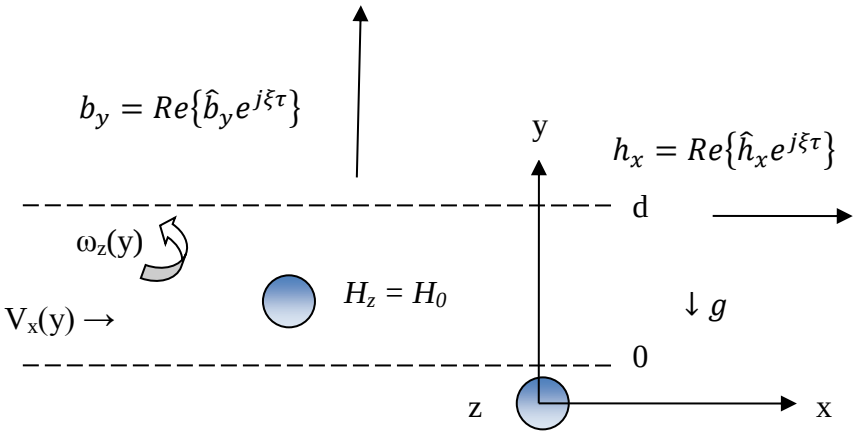

Figure 1.

In **Figure 1**, the flux of a magnetic fluid is presented in the fixed area ($y = 0$, $y = d$). The trended flux is pumped by H_0 magnetic field acting in z-direction and by the sinusoidal magnetic field in x-direction of the sick signal with the complex amplitude $\hat{h}_x$ as well as in y-direction by the sinusoidal magnetic fluctuation density of the sick signal with the complex amplitude $\hat{b}_y$. In x- and y-directions the components of the magnetic field vary due to the sinusoidal law with ξ frequency. $v_x(y)$ velocity is directed along x-axis, while the spin velocity $\omega_z(y)$ – along z-axis and both are y-dependent.

As it is seen in **Figure 1**, the velocity of the flux bleeding is directed only along x-axis while time-average spin velocity – only along z-direction. Both are space distinguished in y-dependence:

$$\vec{v} = v_x(y)\vec{\imath}_x, \qquad \vec{\omega} = \omega_z(y)\vec{\imath}_z. \tag{5}$$

Taking into account the distribution of magnetic field strengths (densities) as they are given in **Figure 1**, $\vec{\imath}_x$ and , $\vec{\imath}_z$ are space homogeneous due to corresponding zero space derivatives. Due to Ampere's law, given in the form of

$$\vec{\nabla} \times \vec{H} = \vec{J} + \frac{\partial \vec{D}}{\partial t} = 0, \tag{6}$$

when the conductivity is zero $\left(\vec{J} = 0\right)$ or the change in current density differs from it $\left(\partial \vec{D}/_{\partial t} \neq 0\right)$, the field strength should be zero and given by (6) surely.

As it is seen in **Figure 1**, both *x*- and *z*-components of the intensity of the magnetic field are homogeneous, when H_0 is invariant in space. It is seen as well that the field derivatives due to *x* and *z* are taken as zero, while the pressure gradient $\partial \rho/_{\partial x}$ may differ from zero, being additionally independent on the linear flux (at its absence as well). As it follows from (6)

$$\frac{\partial (H_0)}{\partial y} - \frac{\partial h_y}{\partial z} = 0. \tag{7}$$

From (7) yields thus

$$\frac{\partial (H_0)}{\partial y} = 0, \quad \text{and} \quad \frac{\partial h_y}{\partial z} = 0 \tag{8}$$

as well as

$$\frac{\partial h_x}{\partial z} - \frac{\partial (H_0)}{\partial x} = 0, \quad \left(\frac{\partial h_x}{\partial z} = 0 \quad \text{and} \quad \frac{\partial (H_0)}{\partial x} = 0\right) \tag{9}$$

and

$$\frac{\partial h_y}{\partial x} - \frac{\partial h_x}{\partial y} = 0, \quad \left(\frac{\partial h_y}{\partial x} = 0 \quad \text{and} \quad \frac{\partial h_x}{\partial y} = 0\right). \tag{10}$$

Gauss's law regulates densities of the fixed magnetic flux along i_y:

$$\vec{\nabla} \cdot \vec{B} = \frac{\partial b_x}{\partial x} + \frac{\partial b_y}{\partial y} + \frac{\partial (B_0)}{\partial z} = 0. \tag{11}$$

Then we get

$$\frac{\partial b_y}{\partial y} = 0, \text{ at } \frac{\partial b_x}{\partial x} = \frac{\partial (B_0)}{\partial z} = 0.$$

Based on this survey we may conclude that b_y and h_x should be constant in space and independent on *y*, while h_y may be dependent on *y*, when *y* itself depends on m_y.

The density of total instantaneous magnetic fluctuations $\vec{B}$, total instantaneous magnetic field $\vec{H}$ and total instantaneous magnetization $\vec{M}$ are given as follows

$$\vec{B} = Re\left\{\left(\hat{b}_x(y)\vec{\imath}_x + \hat{b}_y\vec{\imath}_y\right)e^{j\xi t}\right\} + B_0\vec{\imath}_z, \tag{12}$$

$$\vec{H} = Re\left\{\left(\hat{h}_x\vec{\imath}_x + \hat{h}_y(y)\vec{\imath}_y\right)e^{j\xi t}\right\} + H_0\vec{\imath}_z, \tag{13}$$

$$\vec{M} = Re\left\{\left(\hat{m}_x(y)\vec{\imath}_x + \hat{m}_y(y)\vec{\imath}_y\right)e^{j\xi t}\right\} + M_0\vec{\imath}_z, \tag{14}$$

while the relation between $\vec{B}$, $\vec{H}$ and $\vec{M}$ is given in the following way:

$$\vec{B} = \mu_0\left(\vec{H} + \vec{M}\right), \tag{15}$$

Relation between M_0 and M_{equil} is given by [3]

$$M_0 = M_{equil}L(\alpha_0), \tag{16}$$

$L(\alpha_0)$ showing the sequence of magnetic nano-particles for given magnetic field of $|H|$ magnitude. According to these circumstances for the expression (1) *x*- and *y*- (transversal) components will be given by the following formulae:

$$j\xi\,\tilde{\hat{m}}_x + \omega_z\,\tilde{\hat{m}}_y + \frac{1}{\tau}\left(\tilde{\hat{m}}_x - \frac{M_0}{H_0}h_x\right) = 0,$$
$$j\xi\,\tilde{\hat{m}}_y - \omega_z\,\tilde{\hat{m}}_x + \frac{1}{\tau}\left(\tilde{\hat{m}}_y - \frac{M_0}{H_0}h_y\right) = 0, \qquad (17)$$

where $\hat{m}_x$ and $\hat{m}_y$ are functions of the spin velocity ω_z and are given by the following expressions:

$$\hat{m}_x = \frac{M_0}{H_0}\cdot\frac{\left(j\xi\tau + 1 + \frac{M_0}{H_0}\right)\tilde{\hat{h}}_y - (\omega_z\tau)\frac{\tilde{\hat{b}}_y}{\mu_0}}{(j\xi\tau+1)\left(j\xi\tau + 1 + \frac{M_0}{H_0}\right) + (\omega_z\tau)^2},$$
$$\hat{m}_y = \frac{M_0}{H_0}\cdot\frac{(\omega_z\tau)\tilde{\hat{h}}_y + (j\xi\tau+1)\frac{\tilde{\hat{b}}_y}{\mu_0}}{(j\xi\tau+1)\left(j\xi\tau + 1 + \frac{M_0}{H_0}\right) + (\omega_z\tau)^2}. \qquad (18)$$

3. Conclusion

As it will be seen in further analysis, in the case of absence of fixed flux the spin velocity, and $\hat{m}_x$ and $\hat{m}_y$ are space invariant. When the flux is fixed, the spin velocity together with $\hat{m}_x$ and $\hat{m}_y$ varies with varying of the width *y*. The second term in (1) contributes nothing, as to the velocity of the flux along *x* and at $\partial/\partial z$ magnetization is zero.

In magnetic fluids the magnetization increases in the rotating (spiral) form, as to at the rotation it itself is responsible for movement of the fluid with the spin velocity ω_z, differing from zero, which itself changes the magnetization.

Thus, just like the relaxation of magnetic fluids, the mechanical equations should be taken into account and solutions for ω_z, $\hat{m}_x$ and $\hat{m}_y$ should be received.

References

1. D. G. Giancoli. Physics. Principles with Application. 1995, New Jersey.
2. K. M. Koch, P. B. Brown, D. L. Rothman, R. A. De Graaf. Sample Specific Diamagnetic and Paramagnetic Passive Shimming.
3. K. V. Kotetishvili, G. G. Chikhladze. Linearization of the solution of Langevin's equation in magnetic fluids. Nano Studies, 2013, 7, 225-228.

წყალმცენარის Spirulina platensis უჯრედული ზრდის პროცესში ზოგიერთი ქიმიური ელემენტის აკუმულაციის შესწავლა

ნ. კუჭავა

ე. ანდრონიკაშვილის ფიზიკის ინსტიტუტი
ი. ჯავახიშვილის სახ. თბილისის სახელმწიფო უნივერსიტეტი
თბილისი, საქართველო
e.kuchava@mail.ru

მიღებულია 2014 წლის 16 თებერვალს

დამტკიცებულია, რომ ქიმიური ელემენტების უმრავლესობა შედის ყოველი ცოცხალი ორგანიზმის შემადგენლობაში. ელემენტთა პირველი ჯგუფი: წყალბადი, ჟანგბადი, ნახშირბადი, აზოტი, გოგირდი, ფოსფორი წარმოადგენს ძირითად სასიცოცხლო სამშენებლო მასალას. ქიმიურ ელემენტთა მეორე ჯგუფი: ნატრიუმი, კალციუმი, კალიუმი, ქლორი, მარგანეცი, მაგნიუმი–მაკროელემენტებია. სხვა ჯგუფი– ე.წ. სიცოცხლის მეტალები: სპილენძი, თუთია, კობალტი და ა.შ., რომლებსაც ცოცხალი ორგანიზმები შეიცავს უმნიშვნელო რაოდენობით (მიკროელემენტები) აუცილებელია მათი ცხოველმყოფელობისათვის. ცოცხალი ორგანიზმები ასევე უმნიშვნელო რაოდენობით შეიცავს ვერცხლისწყალს, კადმიუმს, ოქროს, ტყვიას, იშვიათმიწათა ელემენტებს და სხვებს, რომელთა გავლენა ცოცხალ ორგანიზმებში მიმდინარე ფიზიოლოგიურ პროცესებზე ჯერჯერობით შეუსწავლელია ან მცირედ არის შესწავლილი [1, 2]. ჩვენს შემთხვევაში ცოცხალ სისტემად განიხილება ლურჯ-მწვანე წყალმცენარე ციანობაქტერია Spirulina platensis (S. platensis), რომელიც დღევანდელ მსოფლიოში ფართოდაა გამოყენებული ადამიანის, ცხოველთა და ფრინველთა კვების პროდუქტების ბიოდანამატის სახით და წარმოადგენს ჯანმრთელობისათვის მეტად საჭირო მასალას. ცოცხალი ორგანიზმების კვების დროს S. platensis არის ადვილად შესათვისებელი პროდუქტი და ამავე დროს ის დიდად უწყობს ხელს ნივთიერებათა ცვლის მოწესრიგებას. S. platensis აკმაყოფილებს ცოცხალი ორგანიზმების მოთხოვნილებას A, B, C, D, E ვიტამინებზე. მედიცინაში ხდება მისი ფართოდ გამოყენება როგორც მოზარდებისათვის, ასევე ზრდასრული ადამიანებისთვისაც.

ვარაუდობენ, რომ S. platensis ადამიანის ორგანიზმიდან გამოდევნის თავისუფალ რადიკალებს, რადიონუკლიდებს [3]. შრომის [4] ავტორები თვლიან, რომ S. platensis შეიძლება გამოყენებულ იქნეს ტოქსიკური ელემენტებით: კადმიუმით, ტყვიით და ვერცხლისწყლით დაჭუჭყიანებული ჩამდინარე წყლების გასუფთავებისათვის. უკანასკნელ წლებში მეცნიერთა ყურადღებას იმსახურებს S. platensis მიერ ვერცხლის, ოქროს და სხვა ქიმიური ელემენტის ნანონაწილაკების წარმოქმნის უნარი [5 – 7].

ე. ანდრონიკაშვილის სახ. ფიზიკის ინსტიტუტში გამოკვლევები ჩატარდა IPPAS B–256 ტიპის ლურჯ-მწვანე წყალმცენარის S. platensis ბიომასის გამოყენებით, რომელიც მიღებულ იქნა რუსეთის მეცნიერებათა აკადემიის კ. ა. ტიმირიაზევის სახ. მცენარეთა

ფიზიოლოგიის ინსტიტუტიდან. ექსპერიმენტების დროს დაცულიყო შემდეგი პირობები: pH > 8, მუდმივად იყო შენარჩუნებული 3500 ლქ განათება, 30 – 34 °C ტემპერატურა, უწყვეტი ბარბატირება, ხორციელდებოდა მიკროსკოპული და pH-ის მუდმივი კონტროლი, წარმოებდა S. platensis ბიომასის დაბალტემპერატურული გამოშრობა.

სამუშაოში [8] შესწავლილ იქნა ბიოგენურ ქიმიურ ელემენტთა: კობალტის, სპილენძის, თუთიის, ნიკელის, მარგანეცის, რკინის და, აგრეთვე, ტოქსიკურ ელემენტთა: ვერცხლის, კადმიუმის, ქრომის და ტყვიის შემცველობა S. platensis ბიომასაში წყალმცენარის ზრდის დინამიკაში მკვებავ Zarrouk გარემოში აღნიშნული ქიმიური ელემენტების გარკვეული რაოდენობით ჩატვირთვამდე და მათი ერთდროულად ჩატვირთვის შემდეგ. შესწავლილ იქნა, აგრეთვე, S. platensis ლიოფილურად გამოშრალ ბიომასაში სპილენძის, მარგანეცის, თუთიის, მაგნიუმის და ნატრიუმის შემცველობა ინსტრუმენტალური ნეიტრონული აქტივაციური ანალიზის მეთოდის გამოყენებით.

წინამდებარე სამუშაოში შესწავლილ იქნა ლურჯ-მწვანე წყალმცენარის ციანობაქტერია Spirulina platensis უჯრედული ზრდის დინამიკაში მკვებავ Zarrouk გარემოში ქიმიური ელემენტების: სპილენძის, თუთიის და ნიკელის ქცევის თავისებურებები მათი ცალცალკე ჩატვირთვის დროს, როცა შერჩეულ იყო თითოეული ელემენტის გარკვეული რაოდენობა.

განვიხილოთ ზემოთ აღნიშნულ ელემენტებზე ჩატარებული ცალკეული ექსპერიმენტის შედეგები.

ქიმიური ელემენტის სპილენძის როლი და მნიშვნელობა ცოცხალი ორგანიზმებისათვის, სხვა ქიმიურ ელემენტებთან შედარებით, უკეთ არის შესწავლილი. მისი თითქმის ყველა შენაერთი არის ტოქსიკური და მათ შეიძლება ჰქონდეს კანცეროგენული თვისებები [2]. ჩვენს შემთხვევაში ექსპერიმენტებისათვის შერჩეულ იქნა სპილენძის ქლორიდი.

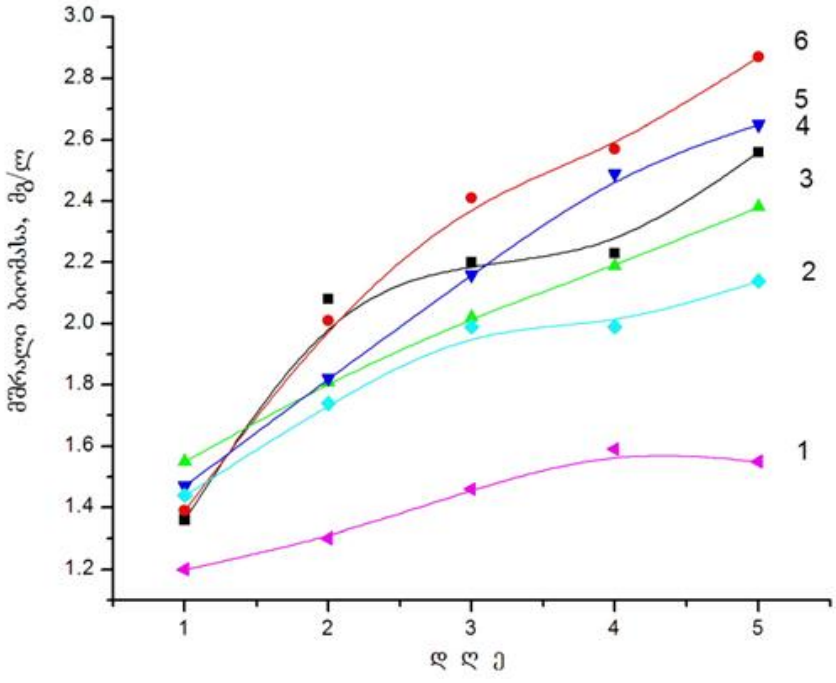

ნახაზი 1. Spirulina platensis ბიომასის ცვლილება მკვებავ გარემოში სპილენძის სხვადასხვა რაოდენობით ჩატვირთვისას საწყისი 5 დღის განმავლობაში.

ნახაზზე 1 გამოსახულია S. Platensis ბიომასის ცვლილება მისი უჯრედული ზრდის პროცესში მკვებავ გარემოში სპილენძის სხვადასხვა რაოდენობის ჩატვირთვისას. მკვებავ გარემოში ჩატვირთული S. platensis საწყისი ბიომასის რაოდენობა იყო 1.2 გ / ლ, ხოლო მკვებავი გარემოს pH – 8.6.

მრუდის ნომერს შეესაბამება სპილენძის შემდეგი რაოდენობა (მგ / ლ): 1 – 2.5; 2 – 1; 3 – 0.25; 4 – კონტროლი; 5 – 0.5; 6 – 0.05.

როგორც ნახაზიდან ჩანს, S. platensis ბიომასის შემცირება კონტროლთან (მრუდი 4) შედარებით შესამჩნევია მკვებავ გარემოში სპილენძის ყველაზე დიდი რაოდენობით ჩატვირთვისას – 2.5 მგ / ლ (მრუდი 1), ხოლო ბიომასის ზრდა ყველაზე მეტად ჩანს ჩატვირთული სპილენძის ყველაზე მცირე რაოდენობის (0.05 მგ / ლ) დროს (მრუდი 6). ამ შემთხვევაში ხდება ზრდის ფაქტიური სტიმულაცია კონტროლთან (მრუდი 4) შედარებით. კონცენტრაციულ ინტერვალში 0.25 – 0.50მგ / ლ (მრუდები 3 და 5) ხდება წყალმცენარის ბიომასის შედარებით მცირედი ზრდა. უნდა აღინიშნოს, რომ სპილენძის დამატებამ 5 მგ / ლ რაოდენობით გამოიწვია S. platensis უჯრედული ზრდის დათრგუნვა ჩატვირთვის მეორე დღესვე.

ნახაზზე 2 წარმოდგენილია მკვებავი გარემოს pHცვლილება მასში სპილენძის სხვადასხვა რაოდენობით ჩატვირთვისას.

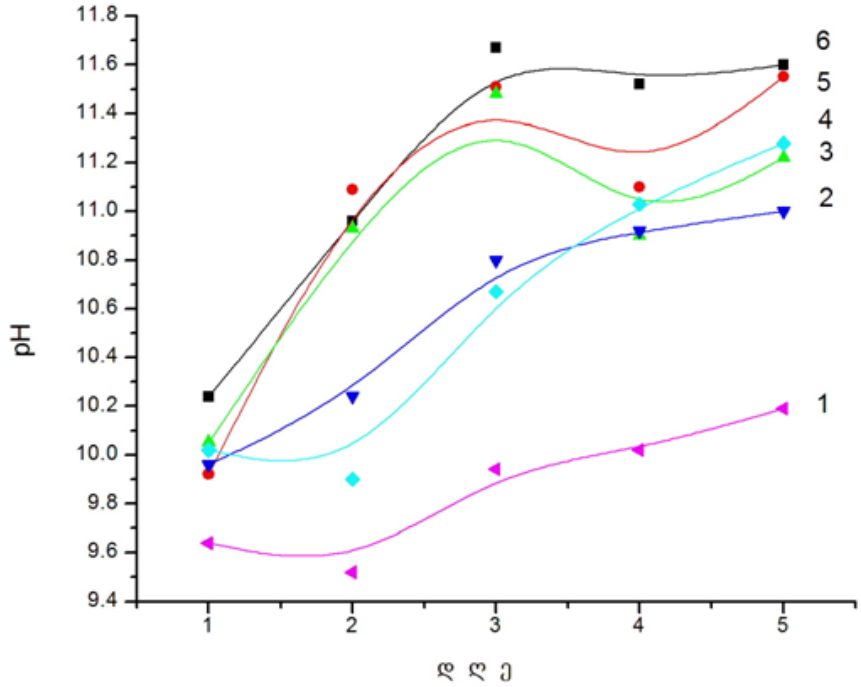

ნახაზი 2. მკვებავი გარემოს pH-ის ცვლილება მასში სპილენძის სხვადასხვა რაოდენობის ჩატვირთვისას საწყისი 5 დღის განმავლობაში.

მრუდის ნომერს შეესაბამება სპილენძის შემდეგი რაოდენობა (მგ / ლ): 1 – 2.5; 2 – 0.5; 3 – 0.25; 4 – 1; 5 – 0.05; 6 – კონტოლი.

როგორც **ნახაზიდან 2** ჩანს,მკვებავი გარემოს pH-ის კონტროლთან შედარებით შემცირდა მაშინ, როცა მასში ჩატვირთულ იქნა სპილენძი 2.5 მგ / ლ რაოდენობით (მრუდი 1), ხოლო კონტროლის pH-საგან ყველაზე ნაკლებად განსხვავდება იმ გარემოს pH, რომელშიც ჩატვირთულია 0.05 მგ / ლ სპილენძი (მრუდი 5). სპილენძის სხვადასხვა რაოდენობის ჩატვირთვისას განსხვავება pH რაოდენობებს შორის შედარებით მცირეა პირველ დღეს, რასაც ვერ ვიტყვით მეხუთე დღის შესახებ.

ცნობილია, რომ ქიმიური ელემენტი თუთია შედის ცხოველთა ორგანოებისა და მცენარეთა ყველა ნაწილის შემადგენლობაში. ჯერ კიდევ მეცხრამეტე საუკუნის მეორე ნახევარში კ. ა. ტიმირიაზევმა დაამტკიცა თუთიის დიდი მნიშვნელობა მცენარეთა ცხოველმყოფელობისათვის [9]. როგორც ვარაუდობენ, მისი უკმარისობა იწვევს მცენარეთა ზრდის შეჩერებას [2]. ინტერესმოკლებული არ უნდა იყოს S. platensis ბიომასის უჯრედების რეაგირების შესწავლა მკვებავ Zarrouk გარემოში თუთიის სხვადასხვა რაოდენობის ჩატვირთვისას. ჩვენი ექსპერიმენტის დროს შერჩეულ იქნა თუთიის სულფატი და თუთიის შემდეგი რაოდენობა: 0.5; 10; 25; 50 მგ / ლ კონტროლთან ერთად. დაკვირვება ჩატარდა ექსპერიმენტის საწყისი 5 დღის განმავლობაში. მკვებავ გარემოში ჩატვირთული S. Platensis ბიომასის საწყისი რაოდენობა იყო 1.37 გ / ლ, ხოლო მკვებავი გარემოს pH – 8.9.

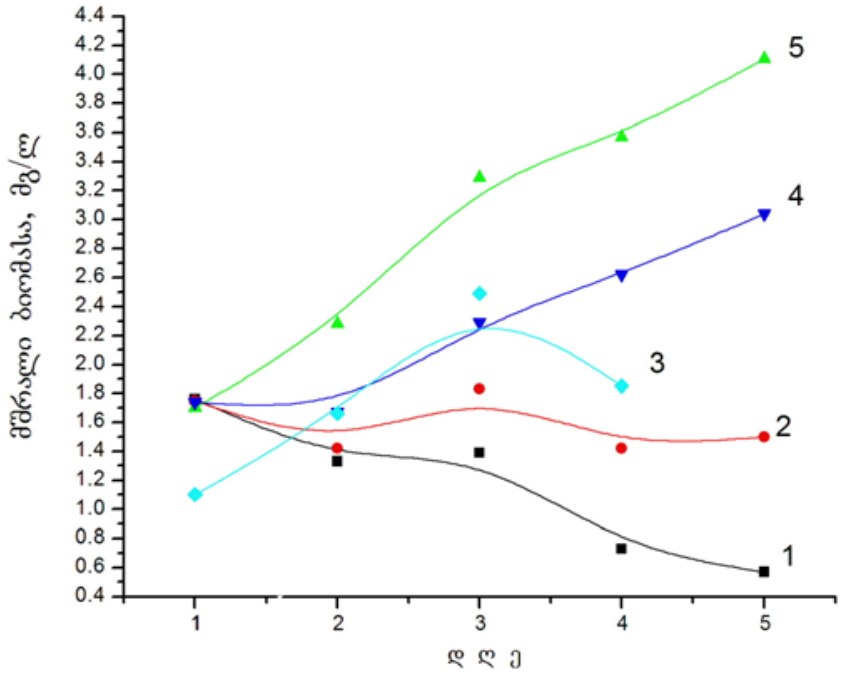

ნახაზი 3. Spirulina platensis ბიომასის ცვლილებამ კვებავ გარემოში თუთიის სხვადასხვა რაოდენობით ჩატვირთვისას საწყისი 5 დღის განმავლობაში.

ნახაზზე 3 წარმოდგენილია S. platensis ბიომასის ცვლილება მკვებავ გარემოში თუთიის სხვადასხვა რაოდენობით ჩატვირთვისას ექსპერიმენტის საწყისი 5 დღის განმავლობაში.

მრუდის ნომერს შეესაბამება თუთიის შემდეგი რაოდენობა (მგ / ლ): 1 – 50; 2 – 25; 3 – 0.5; 4 – 10; 5 – კონტროლი. რაც შეეხება თუთიის 0.5 მგ / ლ ჩატვირთულ რაოდენობას (მრუდი 3), წყალმცენარის ბიომასის და გარემოს pH-ის მნიშვნელობა მეხუთე დღეს ვერ იქნა მიღებული ტექნიკურ მიზეზთა გამო.

როგორც **ნახაზიდან 3** ჩანს, მკვებავ გარემოში ჩატვირთული თუთიის არცერთი რაოდენობა არ იწვევს საკვლევი წყალმცენარის ბიომასის ზრდას კონტროლზე მეტად. 50 მგ / ლ (მრუდი 1) და 25 მგ / ლ (მრუდი 2), მკვებავ გარემოში თუთიის ასეთ რაოდენობათა ჩატვირთვისას ხდება S. Platensis უჯრედების ბიომასის შემცირება კონტროლთან შედარებით.

ნახაზზე 4 წარმოდგენილია მკებავი გარემოს pH-ის ცვლილება მასში თუთიის სხვადასხვა რაოდენობით ჩატვირთვისას ექსპერიმენტის საწყისი 5 დღის განმავლობაში. მრუდის ნომერს შეესაბამება ჩატვირთული თუთიის შემდეგი რაოდენობა (მგ / ლ): 1 – 50; 2 – 25; 3 – 10; 4 – 0.5; 5 – კონტროლი. როგორც **ნახაზიდან 4** ჩანს, pH-ის მაქსიმალური რაოდენობა (11.99) არის კონტროლის შემთხვევაში მე-4დღეს (მრუდი 5), ხოლო მინიმალური – 1-ლ დღეს, როცა მკვებავ გარემოში ჩატვირთულ იქნა 0.5 მგ / ლ თუთია (მრუდი 4).

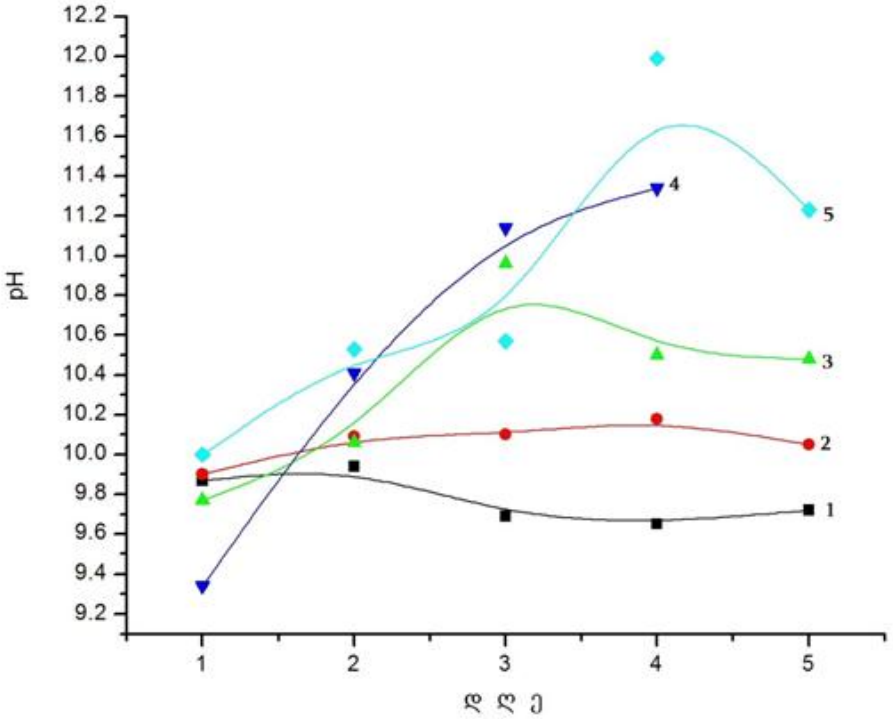

ნახაზი 4.მკვებავი გარემოს pH-ის ცვლილება მასში თუთიის სხვადასხვა რაოდენობით ჩატვირთვისას საწყისი 5 დღის განმავლობაში.

ამჯერად შევეხებით ჩვენი გამოკვლევის ბოლო ელემენტს ნიკელს.

ფიქრობენ, რომ ნიკელი მონაწილეობს ცოცხალ ორგანიზმებში მიმდინარე ფიზიოლოგიურ პროცესებში. ის შედის ნუკლეოტიდების, აგრეთვე,ზოგი ცილას შემადგენლობაში. ვარაუდობენ, რომ ნიკელი ახდენს ცილების აქტივაციას, აგრეთვე, მონაწილეობას ღებულობს გლუკოზის მეტაბოლოზმში [2].

S. platensis ბიომასის უჯრედული ზრდის პროცესებზე და მისი უჯრედების სიცოცხლისუნარიანობაზე ნიკელის ზეგავლენის შესასწავლად ჩატარდა რამდენიმე ექსპერიმენტი, რომელთაგან ამჯერად განვიხილავთ მხოლოდ ერთს. მკვებავ გარემოში ჩატვირთული S. platensis ბიომასის საწყისი რაოდენობა შეადგენდა 1.04 გ / ლ, ხოლო გარემოს pH – 8.82. აღვნიშნავთ, რომ მკვებავ გარემოში ჩასატვირთავად შერჩეულ იქნა ნიკელის გლიცინატი და ნიკელის შემდეგი რაოდენობა (მგ / ლ): 0.075; 0.25; 1.5; 2.5; 5. ექსპერიმენტი ჩატარდა 7 დღის განმავლობაში. მეექვსე დღის შედეგები ვერ იქნა მიღებული ტექნიკურ მიზეზთა გამო. მკვებავ გარემოში ჩატვირთული S. platensis ბიომასის საწყისი რაოდენობა შეადგენდა 1.04 გ / ლ, ხოლო გარემოს pH – 8.82.

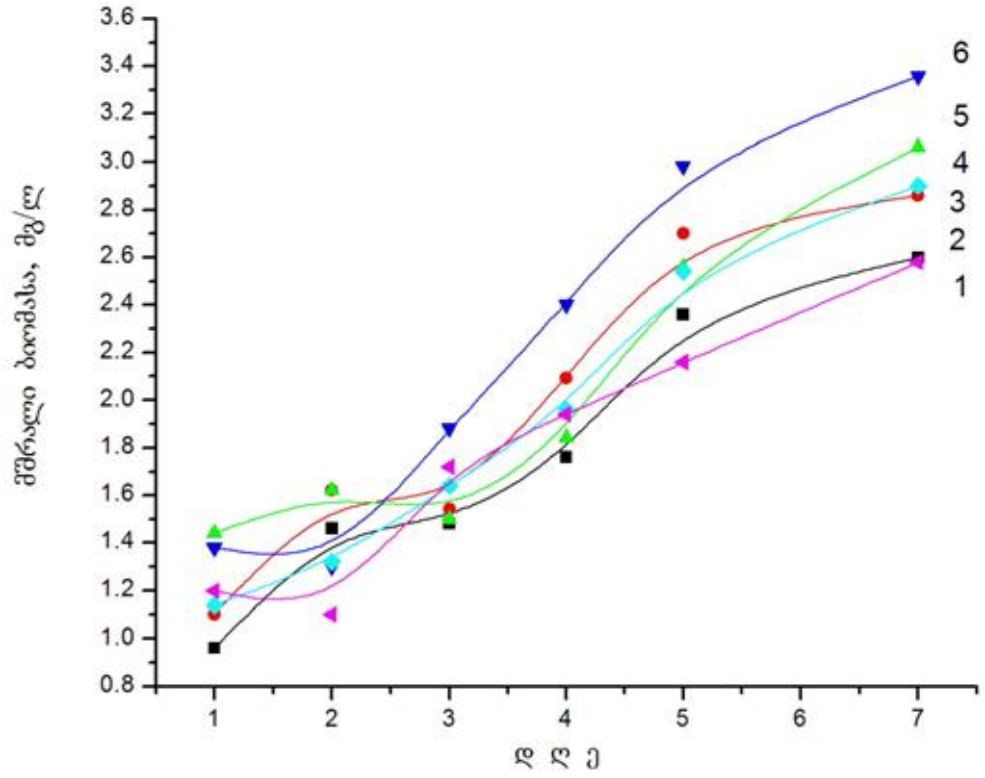

ნახაზი 5. Spirulina platensis ბიომასის ცვლილება მკვებავ გარემოში ნიკელის სხვადასხვა რაოდენობით ჩატვირთვისას საწყისი 7დღის განმავლობაში.

ნახაზზე 5 წარმოდგენილია S. platensis ბიომასის ცვლილება მკვებავ გარემოში ნიკელის სხვადასხვა რაოდენობით ჩატვირთვისას ექსპერიმენტის საწყისი 7 დღის განმავლობაში. მრუდის ნომერს შეესაბამება ნიკელის შემდეგი რაოდენობა (მგ / ლ):1 – 5; 2 – კონტროლი; 3 – 0.075; 4 – 2.5; 5 – 0.25; 6 – 1.5.

როგორც **ნახაზიდან 5** ჩანს, S. platensis ბიომასის რაოდენობა გაიზარდა ნიკელის თითქმის ყველა შერჩეული რაოდენობის დამატებისას, რაც განსაკუთრებით შესამჩნევია იმ შემთხვევისათვის, როცა მკვებავ გარემოში ჩატვირთულ იქნა ნიკელი 1.5 მგ / ლ რაოდენობით (მრუდი 6). როგორც სჩანს, ექსპერიმენტის საწყისი სამი დღის განმავლობაში ბიომასის მნიშვნელოვან ცვლილებებს ადგილი არ აქვს, ხოლო 4 დღიდან ნიკელის თითქმის ყველა ჩატვირთული რაოდენობისათვის განსხვავება ბიომასების მნიშვნელობებს შორის უფრო შესამჩნევია.

ნახაზზე 6 წარმოდგენილია მკვებავი გარემოს pH-ის ცვლილება მკვებავ გარემოში ნიკელის სხვადასხვა რაოდენობით ჩატვირთვისას ექსპერიმენტის საწყისი 7 დღის განმავლობაში. მრუდის ნომერს შეესაბამება მკვებავ გარემოში ჩატვირთული ნიკელის შემდეგი რაოდენობა (მგ / ლ): 1 – კონტროლი; 2 – 5; 3 – 2.5; 4 – 0.075; 5 – 0.25; 6 – 1.5. როგორც **ნახაზიდან** 6 ჩანს, S. platensis მკვებავ Zarrouk გარემოში ნიკელის შერჩეული რაოდენობის ჩატვირთვისას შეინიშნება მკვებავი გარემოს pH-ის ზრდის ტენდენცია კონტროლთან შედარებით, ამავე დროს დადგენილ იქნა ბიომასის უჯრედების სიცოცხლისუნარიანობა.

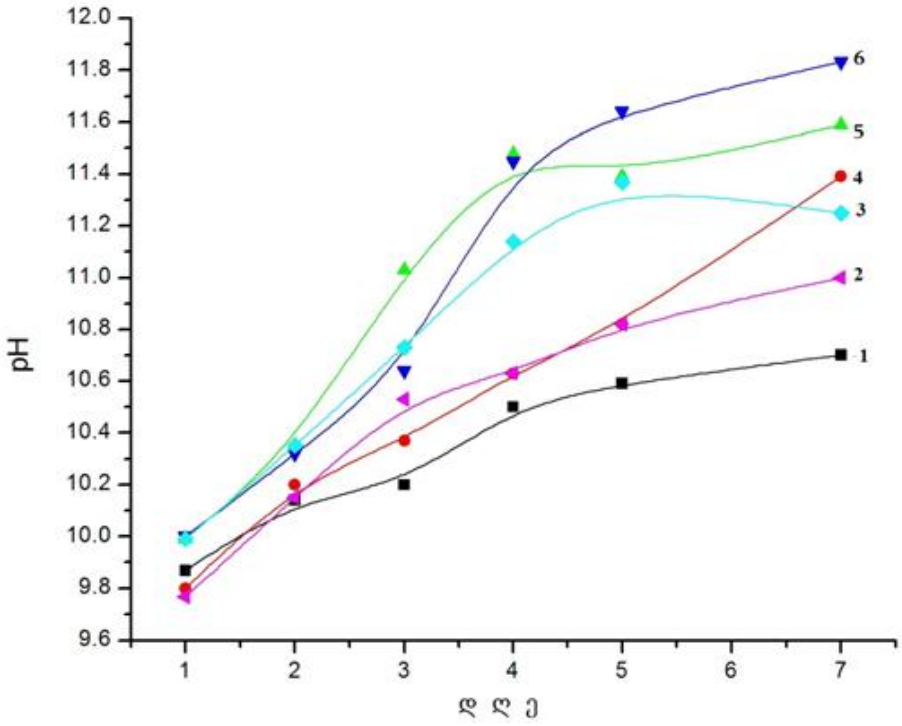

ნახაზი 6.მკვებავი გარემოს pH-ის ცვლილება მასში ნიკელის სხვადასხვა რაოდენობით ჩატვირთვისას საწყისი 7 დღისგანმავლობაში.

დასასრულს, შეგვიძლია ვთქვათ, რომ ზემოთაღნიშნული ექსპერიმენტების განხორციელებით ჩვენს მიერ დასახული მიზანი: შეგვესწავლა ლურჯ-მწვანე წყალმცენარის ციანობაქტერია Spirulina platensis უჯრედული ზრდის დინამიკაში მკვებავ Zarrouk გარემოში ქიმიური ელემენტების: სპილენძის, თუთიის და ნიკელის ქცევის თავისებურებები მათი ცალცალკე ჩატვირთვის დროს, როცა შერჩეულ იყო თითოეული ელემენტის გარკვეული რაოდენობა, ჩვენის აზრით, შესრულებულ იქნა. ვფიქრობთ, რომ საინტერესო იქნება მსგავსი საკითხის შესწავლა სხვა ქიმიური ელემენტებისათვისაც.

ჩემს სასიამოვნო მოვალეობად ვთვლი მადლობა გადავუხადო ა. ბელოკობილსკის და ა. ხიზანიშვილს ექსპერიმენტებში მონაწილეობისათვის, ხოლო ე. გინტურს ექსპერიმენტებში მონაწილეობის გარდა, წვლილისათვის, რომელიც მან შეიტანა მიღებული შედეგების განსჯაში.

მითითებები

1. Д. Уилямс.Металлы жизни.1975, Москва: Мир.
2. А. А. Кист. Феноменология биохимии и бионеорганической химии.1987, Ташкент: Фан.
3. L. Loseva, Y. Dardinskaya.In: Proc. 6th Int. Cong. Appl. Algology. 1993.Res. Inst. Radiat. Med.

4. P. Jonson, A. Shubert. Nutr. Rep. Int., 1986, 34, 6, 1053-1071.
5. N. Tsibakhashvili, T. Kalabegishvili, V. Gabunia, E. Ginturi, N. Kuchava, N. Bagdavadze, D. Pataraya, M. Gurielidze, D. Gvardjaladze, L. Lomidze. Nano Studies, 2010, 2, 179-182.
6. ნ. წიბახაშვილი, ა. რჩეულიშვილი, ე. გინტური, ნ. კუჭავა, ნ. ბაღდავაძე, ვ. გაბუნია. 1-ლისაერთ.კონფ.თეზ.კრ.: ნანოქიმია– ნანოტექნოლოგიები. 2010, თბილისი, 37-38.
7. T. Kalabegishvili, E. Kirkesali, E. Ginturi, A. Rcheylishvili, I. Murusidze, D. Pataraya, M. Gurielidze,N. Bagdavadze, N. Kuchava, D. Gvardjaladze, L. Lomidze. Nano Studies, 2012, 5, 127-136.
8. ნ. კუჭავა. Nano Studies, 2013, 7, 185-192.
9. Г. А. Бабенко, Л. П. Решеткина.Применениемикроэлементов в медицине. 1971,Киев: Здоровье.

STRUCTURAL FEATURES OF THE IRON–OXYGEN NANOPARTICLES FORMED WHEN THE ROTATION-CORROSION DISPERGATION METHOD IS APPLIED

O. M. Lavrynenko [1], Yu. M. Bolbukh [2]

[1] F. D. Ovcharenko Institute of Bio-Colloid Chemistry
National Academy of Sciences of Ukraine
Kyiv, Ukraine
alena-lavry@yandex.ru
[2] O. O. Chuiko Institute of Surface Chemistry
National Academy of Sciences of Ukraine
Kyiv, Ukraine
yu_bolbukh@yahoo.com

Accepted April 9, 2014

Introduction

The interesting in the obtaining of nanoparticles with different physical-chemical properties has been growing during recent years. Most often, the structures including magnetite $FeFe_2O_4$ (Fe_3O_4), maghemite γ-Fe_2O_3 and spinel ferrite of 3*d*-metals such as cobalt, nickel; zinc and cuprum, are used in medicine and biology. The main requirements to the nanosized iron oxide particles produced for bio-medical purposes are the particle homogeneity, the presence of ferri- or paramagnetic properties and their colloidal stability in aqueous and non aqueous solutions. Among the great number of traditional synthesis methods which permit to form iron oxides and hydroxides as well as other iron-bearing particles (spinel ferrites or composites based on iron) a new one has appeared. We called that method the rotation-corrosion dispergation (the RCD-method) [1]. The iron–oxygen nanoparticles are formed on a steel surface when its surface is brought in contact with air oxygen and aqueous dispersion medium containing ions of different types such as heavy and precious metals. A special interest in the iron oxides particles formation is focused on systems with inert (silver, gold, platinum) [2] or iron and steel electrodes [3]. In this case, the processes of the phase formation allow to avoid both the introduction of ferrous and ferric salts into the system and the additional cleaning of the particles. In this situation, the particles do not include spare components. By applying electrochemical systems, it is possible to form nanosized structures under standard conditions that are important for achieving colloidal stability and adaptability with respect to the conditions met in different practical application.

The purpose of our work is to study structural features of the iron–oxygen nanoparticles formed when the rotation-corrosion dispergation method is applied and the difference of such particles from the similar particles obtained by the co-precipitation method.

Materials and methods

The formation of iron-oxygen nanoparticles with the help of the rotation-corrosion dispergation method is carried out on the surface of the rotating disk electrode made of the finished steel (St3), the composition is the following, %: C 0.14 – 0.22; Si 0.05 – 0.15; Mn 0.4 – 0.65; Cr 0.3; Ni 0.3; P 0.04; S 0.05; N 0.01. According to its composition, such steel appears to be the iron–carbon alloy containing the phases of iron spinel ferrite $FeFe_2O_4$, graphite C and cementite $(Fe,Ni,Co)_3C$. Due to the presence of such components, a large number of micro galvanic couples, such as ferrite – graphite and ferrite – cementite, are created in the system. In these couples, the ferrite particles play the role of anodes whereas the graphite and cementite particles are cathodes. The differences in the value of standard electrode potentials of such components lead to the electrochemical red-ox reactions in the system. As it was shown in our earlier articles [4, 5], the additional components of steel, such as Si, Mn, Cr, Ni, Cu, S, P, do not participate in the processes of the phase formation: their concentration in the dispersion medium is very low. No other structures, except of iron oxides and hydroxides, are formed on the surface of a steel electrode.

The rotation of the steel disk supplies the variable contact of its surface with air and dispersion medium. As the dispersion medium distilled water, zinc, nickel, cobalt, ferric and ferrous salts (chlorides and sulphates) and argentum nitrate were chosen. The concentration of Zn(II) and Ni(II) was 100 mg / dm^3; concentrations of Co(II), Fe(II), Fe(III) were in the range from 10 to 200 mg / dm^3. The content of argentum in the dispersion medium was from 0.5 to 5.0 mg / dm^3. The pH value in all cases was 6.5.

X-ray diffraction (XRD) was used for the phase identification. The measurement was taken on computer-aided equipment (DRON 3) with filtered emission of cobalt anode in discrete conditions of plotting, with pitch of 0.1 degree and time of piling in every point 4 s. The additional module was used for recording this process *in situ* [6]. As additional visualization technique of the derived samples the scanning electron microscopy (SEM) and transmission electron microscopy (TEM) were suggested.

As the main method of the structure research we chose Fourier transform infrared spectroscopy (FTIR). The spectres were recorded for the mineral phases stirred with dry KBr. Thermo Nicolet FTIR spectrometer in the range 4000 – 400 cm^{-1} with 50 scan collected was used for measurement.

Result and discussion

As it was shown in our previous studies [7, 8], the process of the phase formation in the systems based on the iron corrosion process under oxidative conditions leads to formation of the spectrum of iron oxyhydroxides, iron oxides, iron and heavy metal spinel ferrites and core&shell nanocomposites with ferromagnetic cores and precious metal shells. The type of the nanoparticles depends on duration of the phase formation process and physical-chemical conditions such as pH value, concentration and chemical composition of dispersion medium, temperature etc. The colloid-chemical mechanism of the phase formation can be realized due to interaction of the products of iron corrosion process with metal aquahydroxoforms from the dispersion medium as well as with primary mineral phase of Green Rust or lepidocrocite [8, 9].

At the same time, disperse iron oxyhydroxide minerals γ-FeOOH, α-FeOOH can be formed when iron spinel ferrite nanoparticles are oxidized under standard conditions.

We suppose that the iron–oxygen nanoparticles formed when the rotation-corrosion dispergation method was applied have a lot of structural features. Below we will show our structure research of the iron–oxygen primary particles, iron oxides, spinel ferrites and composites $FeFe_2O_4$ & Ag^0.

Fe(II)–Fe(III) *layered double hydroxides (Green Rust) and ferrihydrite*

Two types of Fe(II)-Fe(III) LDH: hydroxysulphate or hydroxycarbonate Green Rust, respectively, can be formed on the steel surface depending on the anion composition of the dispersion medium. The structure of Fe(II)-Fe(III) LDH is usually obtained in ferric and ferrous sulphate solution after 10 – 20 min contact of steel surface with water medium. Hydroxysulphate Green Rust II ($GR(SO_4^{2-})$) has the following general composition $Fe^{II}_4Fe^{III}_2(OH)_{12}SO_4 \cdot \sim 8H_2O$ [10] with trigonal spatial group *P3m1*; the parameters of elementary lattice are $a = 0.5524_1$ nm, $c = 1.1011_3$ nm, $V = 0.29097$ nm^3 and $Z = 1/2$. The presence of $GR(SO_4^{2-})$ phase on the steel surface is not always identified by XRD (**Figures 1a** and **b**) when the initial concentration of ferric iron is low (< 10 mg / dm^3), but its presence may be confirmed by SEM (**Figure 2a**).

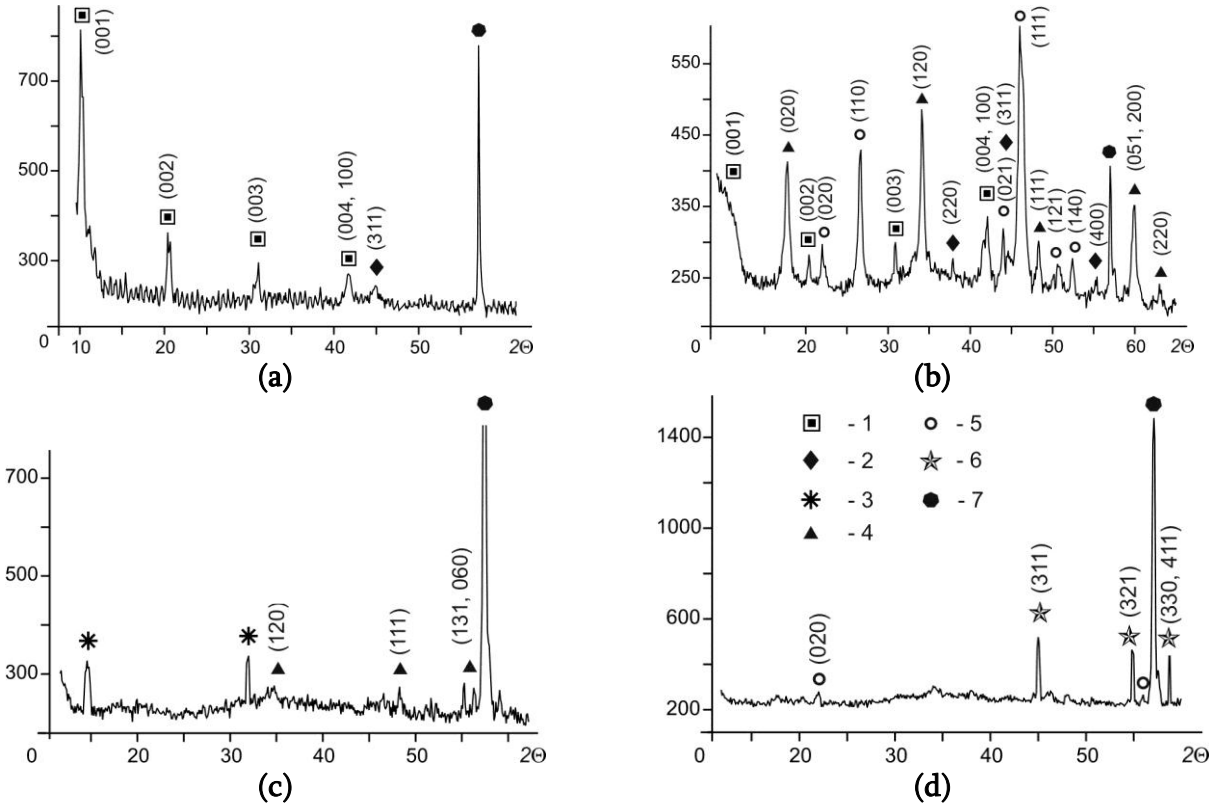

Figure 1. XRD-data of primary iron–oxygen particles formed when the rotation-corrosion dispergation method was applied: a, b – hydroxysulphate Green Rust ($GR(SO_4^{2-})$) on the steel surface; c – hydroxycarbonate Green Rust ($GR(CO_3^{2-})$) on the steel surface; d – ferrihydrite from near electrode layer. The numbers correspond to mineral phases: 1 – $GR(SO_4^{2-})$, 2 – magnetite $FeFe_2O_4$, 3 – $GR(CO_3^{2-})$; 4 – lepidocrocite γ-FeOOH; 5 – goethite α-FeOOH, 6 – ferrihydrite $Fe_5O_3(OH)_9$ and 7 – Fe^0 (from steel surface).

Hydroxicarbonate Green Rust belongs to the first type of LDH structure. It is formed when the steel electrode contacts with distilled water and air. Under such conditions the quantity of CO_2 gas in the air is enough for the primary GR(CO_3^{2-}) particles formation. The general chemical formulas are the following $Fe^{II}_4Fe^{III}_2(OH)_{12}CO_3 \cdot 2H_2O$ [2] or $Fe^{II}_4Fe^{III}_2(OH)_{12}CO_3 \cdot 3H_2O$ [11]. **Figure 1c** shows XRD-data and **Figur 2b** shows TEM-image of GR(CO_3^{2-}).

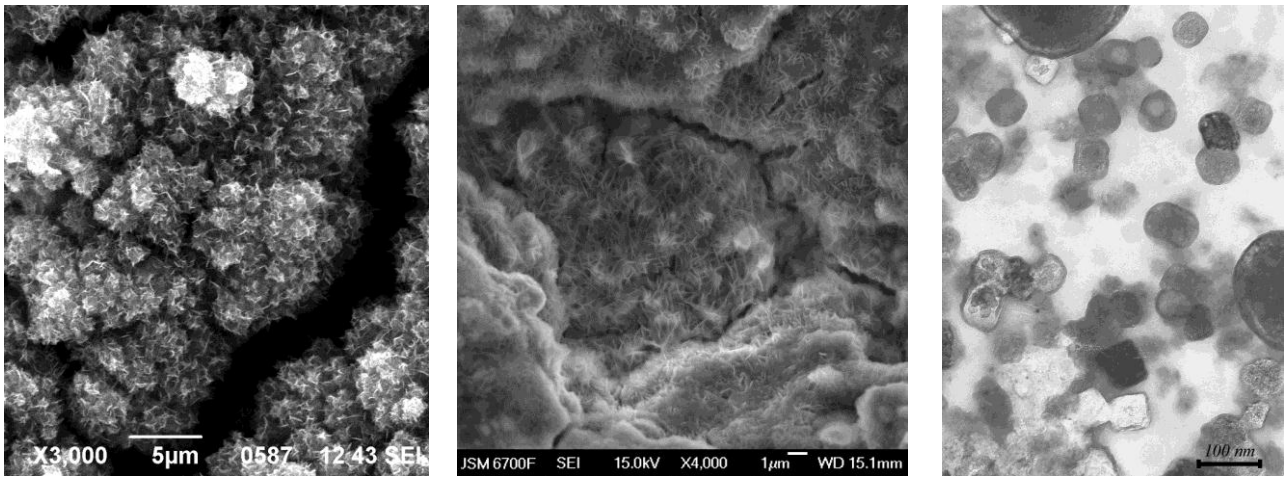

(a) (b) (c)

Figure 2. SEM-images of primary iron–oxygen particles formed on the steel surface when the RCD-method was applied: a – hydroxysulfate Green Rust (GR(SO_4^{2-}) and b – hydroxycarbonate Green Rust (GR(CO_3^{2-}); c – TEM-image of ferrihydrite formed on the near electrode layer.

Ferrihydrite particles are usually presented in near electrode layer when the rotation-corrosion dispergation method is applied. Its XRD-data are shown on **Figure 1**d and TEM-image, respectively, is shown on **Figure 2**c. The structured features of ferrihydrite strongly depend on genesis of that mineral. In our early work we analyzed the literature source devoted to structure, particle size, mineral and chemical composition of different types of ferrihydrites [12]. Such mineral can include in its structure the structural elements of iron oxyhydroxides as well as iron oxides.

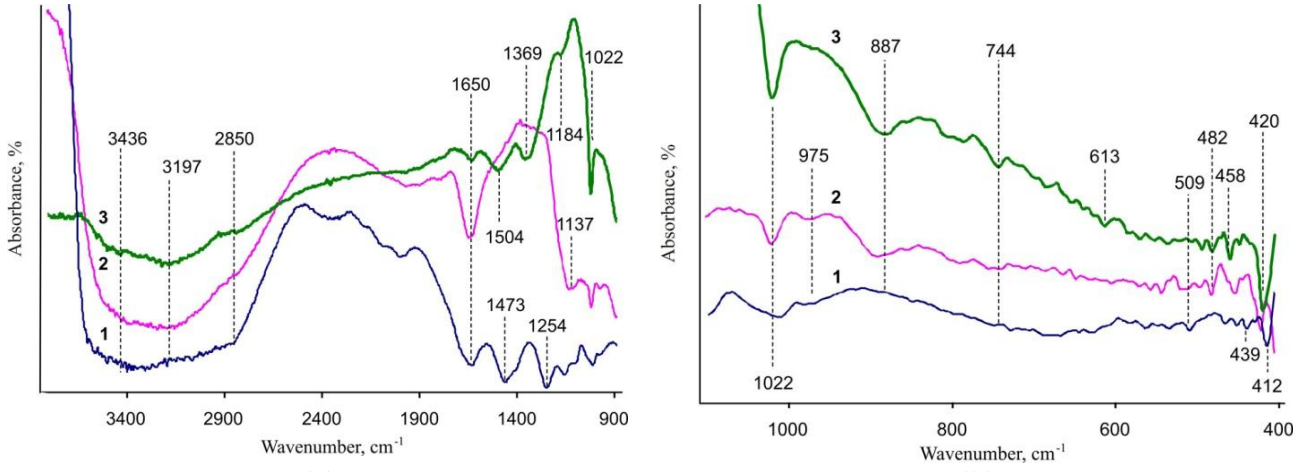

(a) (b)

Figure 3. FTIR spectra (a and b) of ferrihydrite Fh (1); hydroxysulfate Green Rust GR(SO_4^{2-}) (2) and hydroxycarbonate Green Rust GR(CO_3^{2-}) (3).

So, according to FTIR-data, in *ferrihydrite* spectra (**Figure 3**, line 1) the band at 632 cm^{-1} relates to asymmetric linkage vibration in γ-FeOOH structure. The presence of the broad band at 686 cm^{-1} coupled with the band at 728 cm^{-1} points to akaganeite β-FeOOH. At the same time the band at 450 cm^{-1} coupled with the band at 560 cm^{-1} can be considered as hematite α-Fe_2O_3 as well as the couple bands at 440 and 580 cm^{-1}. The presence of the band at 412 cm^{-1} on the spectra points to feroxyhyte δ-FeOOH formation. While the band of $Fe(OH)_2$ at 480 cm^{-1} is not found in spectra. The band at 1120 cm^{-1} relates to OH-groups in ferrihydrite structure. The sample contains a lot of coordinately fixed and physically adsorbed water. The broad intensive band at 3629 – 2873 cm^{-1} with adsorption maximum at 3340 cm^{-1} confirmed that suggestion. The band at 980 cm^{-1} can give rise to anions SO_4^{2-} or SO_3^{2-}, but together with the band at 890 cm^{-1} it could be related to bond Fe–OH as well as the band at 1114 and 686 cm^{-1}. The carbonate-ion band at 1430 cm^{-1} is absent in ferrihydrite spectra.

The *hydroxysulphate Green Rust* GR(SO_4^{2-}) FTIR spectra are presented on **Figure 3**, line 2. The band at 1137 cm^{-1} can be related to the vibration of anion SO_4^{2-} and the band at 1970 cm^{-1} relates to C=O linkage in CO_2. The valence vibrations of water molecules and OH-groups are seen due to the adsorption bands at 3401 and 3189 cm^{-1}. The band at 1369 cm^{-1} may be related to COO-groups, but carbonyl stretching vibrations at 1430, 853, 695 cm^{-1} are not found in the spectra. The intensive band at 1508 cm^{-1} points to the valence vibration of C–O linkage. The bands at 1022 and 744 cm^{-1} relate to γ-FeOOH. The IR bands at 896 and 790 cm^{-1} are typical for α-FeOOH. The intensive bands at 455 cm^{-1} belong to δ-FeOOH and bands at 482 and 542 cm^{-1} point to the presence of α-Fe_2O_3. The band at 420 cm^{-1} can be related to α-FeOOH as well as to Fe–O in oxides. The bands at 790 and 898 cm-^{1} come from traces of goethite and lepidocrocite. The bands of SO_4^{2-} are situated at 1078 and 1135 cm^{-1}; and 642 and 620 or 1075, 1130, 1198 cm^{-1}; and 975 cm^{-1}.

In *hydroxycarbonate Green Rust* GR(CO_3^{2-}) the bands at 1508 and 1646 cm^{-1} (H_2O 1650 cm^{-1}) correspond to Fe–O linkage, also the band at 136 cm^{-1} can be associated with CO_3^{2-} groups (**Figure 3**, line 3). Other bands typical for GR(CO_3^{2-}) are listed below. The bands at 1184, 1022, 748 and 478 cm^{-1} can be attributed to lepidocrocite; the bands at 790, 883 and 628 cm^{-1} – to α-FeOOH; the band at 455 cm^{-1} – to δ-FeOOH. The iron oxide bands are 550 and 482 cm^{-1} for α-Fe_2O_3 and 613 and 580 cm^{-1} for γ-Fe_2O_3. The presence of 1369 cm^{-1} band points to the near surface Fe–OH linkage and the presence of 651, 493 and 420 cm^{-1} bands points to Fe–O stretching.

Iron oxides and hydroxides

Green Rust structures as well as ferrihydrite show a great chemical activity under standard condition in the presence of oxygen. Such structures usually are kept in inert gas atmosphere. The process of their phase transformation strongly depends on red-ox conditions: under oxidative conditions the iron oxyhydroxides are formed in the system. When the entrance of the oxidant into the system is limited and ferrous species contact with the primary particles in the water dispersion medium the magnetite particles are the typical product of the phase transformation. But in the absence of ferrous species in the water medium the phase transformation of lepidocrocite leads to the formation of maghemite γ-Fe_2O_3.

When the rotation-corrosion dispergation method is applied to form iron–oxygen particles on the steel surface the phase transformation Green Rust into magnetite particles or its

mixture with maghemite particles or aggregates can be fixed on SEM-images and XRD-data. Oxyhydroxide particles can be formed on the steel surface under oxidative conditions as well as in the near electrode layer contacting with air.

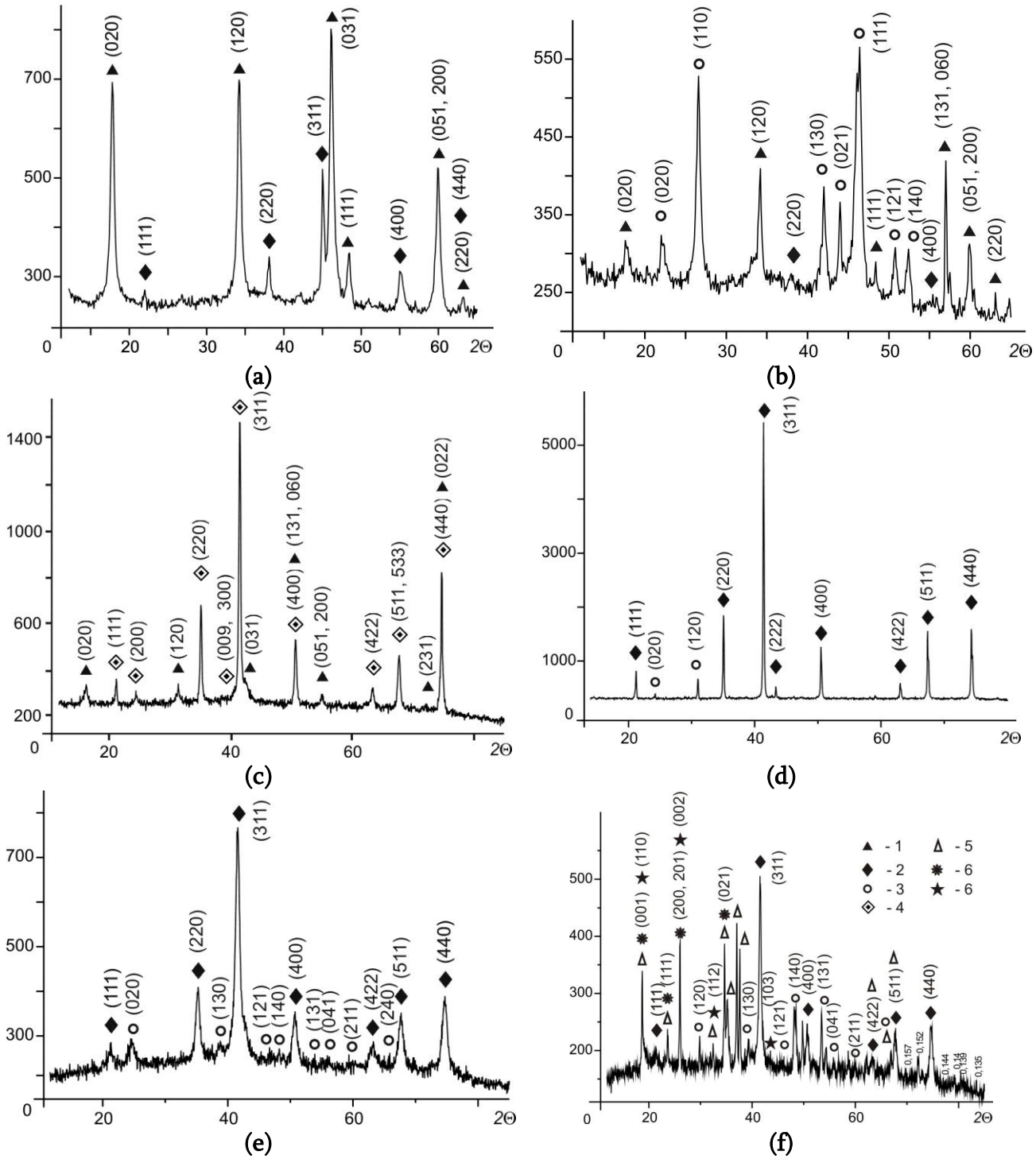

Figure 4. XRD-patterns of the iron-oxygen mineral phases formed when the RCD-method was applied: a – lepidocrocite γ-FeOOH, b – goethite α-FeOOH, c – maghemite γ-Fe_2O_3; d, e – magnetite $FeFe_2O_4$; and f – magnetite $FeFe_2O_4$ obtained by co-precipitation method. The numbers correspond to mineral phases: 1 – γ-FeOOH, 2 – $FeFe_2O_4$, 3 – α-FeOOH, 4 – γ-Fe_2O_3, 5 – $2FeCl_3\cdot 7H_2O$, 6 – $FeCl_2 \cdot 4H_2O$, 7 – $FeSO_4\cdot 4H_2O$.

The processes of the magnetite and iron oxyhydroxide formation, their properties and colloid-chemical mechanisms of their formation in our systems were in detail described in our previous works [7, 9]. **Figure 4** shows XRD-data of lepidocrocite (**Figure 4a**) and goethite particles (**Figure 4b**), maghemite (**Figure 4c**) and magnetite (**Figure 4d** and **e**) particles obtained when the RCD-method was applied, magnetite particles (**Figure 4f**) obtained by co-precipitation of ferric and ferrous salts in low alkaline medium [13]. The magnetite particles that XRD-data are presented on (**Figure 4d**) were formed on the steel surface, whereas magnetite particles that XRD-data are presented on (**Figure 4e**) were obtained in the near electrode layer. It is indicative that on the XRD-data of all samples obtained when the RCD-method was applied only iron-oxygen mineral phases are identified. On the contrary the reflexes of ferric chlorides are presented on X-ray pattern as well as reflexes of magnetite and goethite (**Figure 4f**).

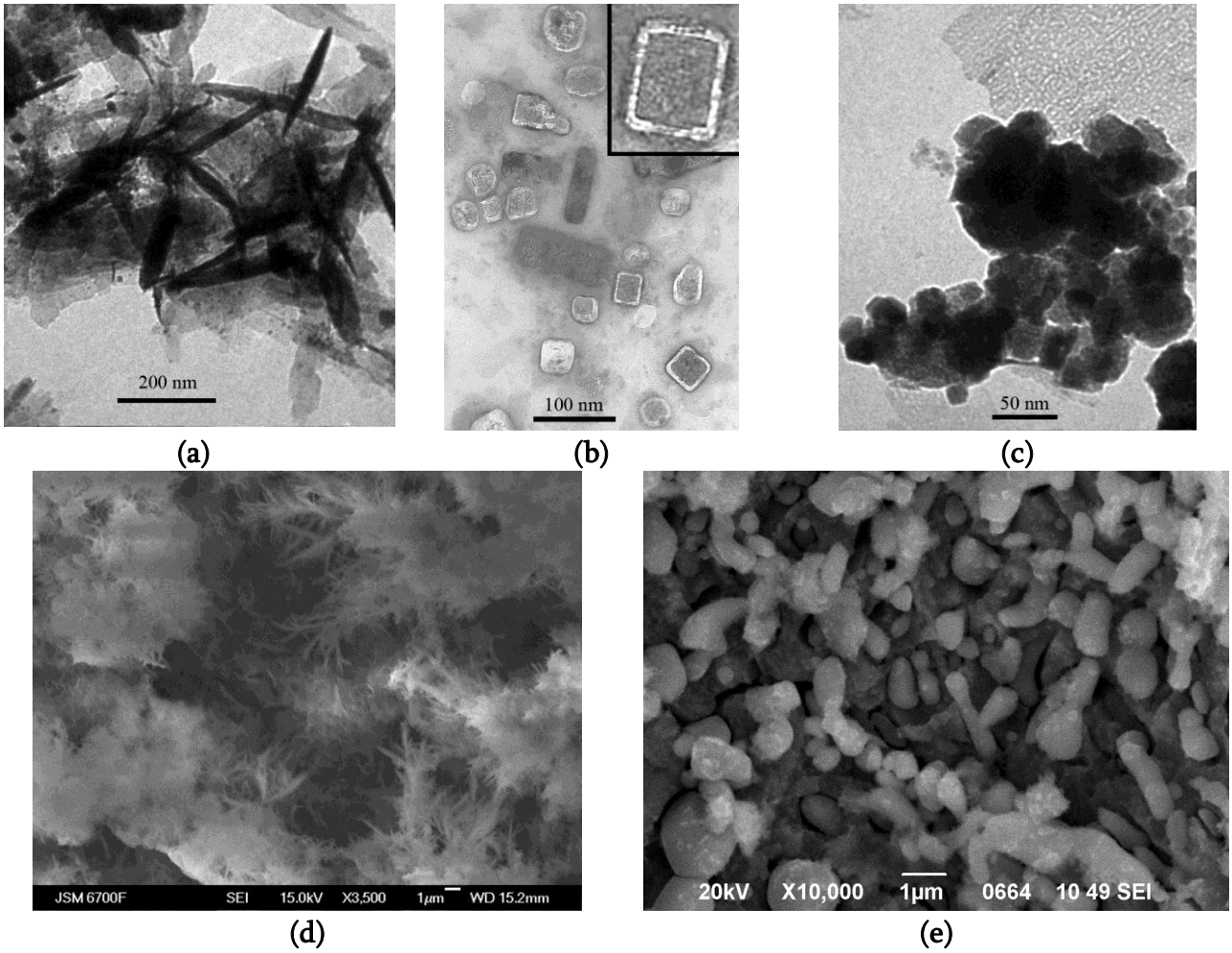

Figure 5. Iron–oxygen nanoparticles formed when the RCD-method was applied. TEM-images of: a – lepidocrocite γ-FeOOH, b – magnetite $FeFe_2O_4$, c – maghemite γ-Fe_2O_3; SEM-images of: d – lepidocrocite, e – magnetite.

The typical morphology of the iron–oxygen particles, obtained in our systems, is shown on the **Figure 5**. The lepidocrocite particles have the acicular shape (**Figures 5a** and **d**), magnetite forms the domatic crystals (**Figure 5b**) or spheres (**Figure 5e**) and maghemite shapes of globules **(Figure 5c**).

Figure 6 shows the FTRI spectra of the iron–oxygen structures (lepidocrocite and the mixture of magnetite and maghemite) formed in our system under oxidative conditions and when the concentration of ferrous iron was low in water dispersion medium.

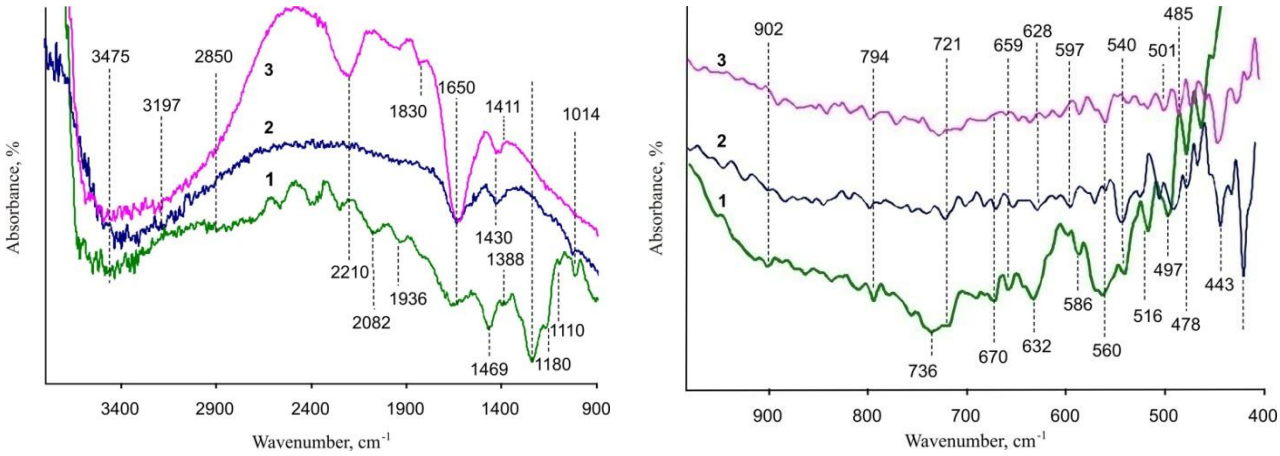

(a) (b)

Figure 6. FTIR-spectra (a and b) of lepidocrocite γ-FeOOH (line 1), the mixtures of Fe_3O_4 with γ-Fe_2O_3 (line 2) and (line 3).

The FTIR spectra of *lepidocrocite* (**Figure 6**, line 1) are characterized by the presence of following bands [14]: the broad peak with its minimum at 570 cm^{-1} and the sharp peak at 462 cm^{-1} both related to the vibrations of the Fe–O linkage. A broad peak in the interval 740 – 721 cm^{-1} appears due to the bending vibrations of –OH···O groups. The well defined widened peak is found between 1500 and 1700 cm^{-1} (minimum at 1666 cm^{-1}), it relates to OH-group vibrations. The broad peak between 3000 and 3600 cm^{-1} may be connected with the stretching vibrations of the –O–H bonds linked by hydrogen bonds. The analysis of the lepidocrocite spectra (**Figure 6**, line 1) permits to suppose the presence of goethite α-FeOOH as the additional phase. Not clearly visible band at 2850 cm^{-1} as well as the bands at 1160 and 1018 cm^{-1} relating to σOH in the plane and the bands at 742 and 540 cm^{-1} relating to γOH outside the plane point to the plate-like shape of the lepidocrocite particles. Not clearly visible band at 892 cm^{-1} and the following bands at 792, 630, 495 cm^{-1} belong to γOH outside the plane related to goethite. According to [15] the bands at 892 and 742 cm^{-1} characterize the (001) crystalline plane in the lepidocrocite structure. When the band at 636 cm^{-1} that qualifies the Fe–O vibration in the (010) plane together with the band at 656 cm^{-1} characterizing less crystalline phase are present in the spectra then the structure of the sample is heterogeneous. But the absence of the structure-depending band at 412 cm^{-1} proves a small size of the particles. The band at 1103 cm^{-1} can be associated with SO_4^{2-} anions.

The typical bands relating to *magnetite* structure are the following [16 – 21]: 440, shoulder 480, 580, 670 or the intensive peak 590 cm^{-1}. The groups of the bands characteristic for maghemite γ-Fe_2O_3 are the following [22 – 25]: 418, 560 – 585, 631, 691; 720 670; 650 550; 620 and 516 cm^{-1}. The bands at 620 and 580 cm^{-1} correspond to linkages M_{th}–O–M_{oh} (metal in tetrahedral site links with oxygen and links with metal in octahedral site) and M_{th}–M_{oh} (metal in tetrahedral site links with metal in octahedral site), respectively. All bands become weaker as crystallinity decreases and finally they almost disappear. A peak at around 3425 cm^{-1} in the spectra could be attributed to the metal–OH stretching vibrations of the hydroxyl group.

The following bands are presented on the *first spectra of the mixture of maghemite with magnetite* phases (**Figure 6**, line 2): the bands at 1025 cm^{-1} relating to goethite; the bands at 725 and 670 cm^{-1} corresponding to Fe–O asymmetric vibration in γ-Fe_2O_3, the band at 682 cm^{-1} characterizing the Fe–O–Fe vibration in metal oxides. Other bands 655 and 543 cm^{-1} as well as the bands at 628 and 524 cm^{-1} are associated with tetrahedral and octahedral sites in bulk of γ-Fe_2O_3 or with its surface. The strong band at 570 cm^{-1} as well as the bands at 478, 443, 670 and 543 cm^{-1} correspond to the magnetite phase. The band at 420 cm^{-1} may be related to Fe–O bonds in α-FeOOH as well as the band at 505 cm^{-1}. The band at 1130 and 1164 cm^{-1} can correspond to SO_4^{2-}. The band at 1430 cm^{-1} points to CO_3^{2-}-anions.

For the *second sample of the mixture of maghemite with magnetite* (**Figure 6**, line 3) the bands at 447 and 559 cm^{-1} are related to magnetite. The band shift from 570 to 586 cm^{-1} can be explained by a coating of $FeFe_2O_4$ with its oxidized layer. The shift of the band at 655 to 640 cm^{-1} as well as the correlation of the bands at 458 and 428 cm^{-1} coupled with the intensity lowering of the band at 458 cm^{-1} point to reduction of sample's crystallinity. Moreover the band feature at 428 cm^{-1} may be assigned to Fe–O bonds in iron oxide mixture. The weakening of the band at 1164 – 1130 cm^{-1} points to the decrease of the SO_4^{2-} quantity. The appearance of two bands at 1427 and 1411 cm^{-1} points to the presence of different complexes of carbonate ions in the mineral structure. The absence of the bands at 1025 and 505 cm^{-1} shows the decrease of the hydroxyl content.

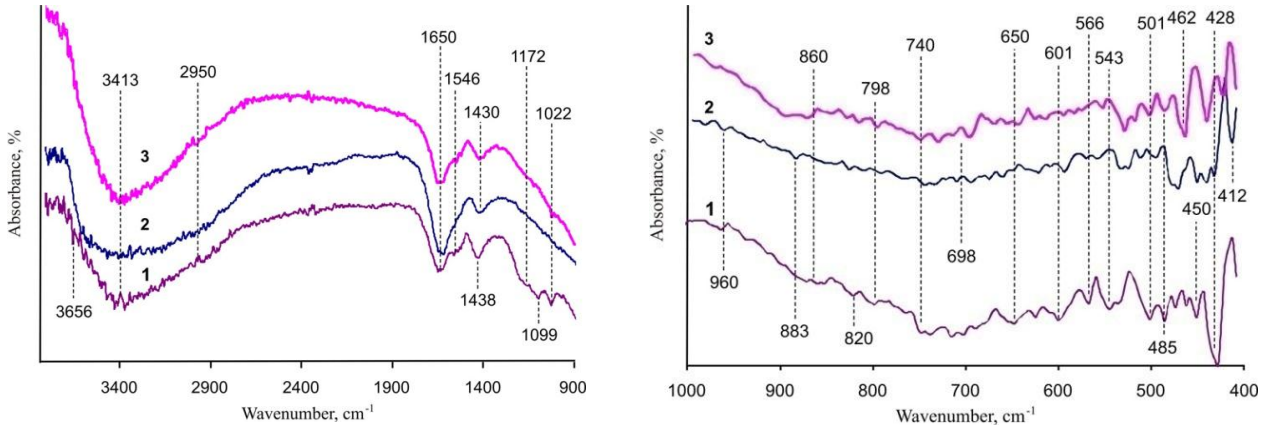

Figure 7. FTIR spectra (a and b) of the magnetite samples: Fe_3O_4 nm_1 (line 1), Fe_3O_4 nm_2 (line 2), Fe_3O_4 nm_3 (line 3).

Figure 7 shows the spectra of magnetite obtained when the RCD-method was applied. So, the bands at 1195, 1122 and 1099 cm^{-1} correspond to stretching asymmetric vibration of the SO_4^{2-} inner-sphere complexes in *nanosized magnetite* Fe_3O_4 nm_1 (**Figure 7**, line 1). The bands at 968 and 883 cm^{-1} point to the Fe–OH bonds. The bands at 550 and 450 cm^{-1} as well as strong band at 570 cm^{-1} correspond to magnetite. The presence of the band at 628 cm^{-1} can be evidenced by the predominance of the M_{th}–O–M_{oh} linkages and the band at 501 cm^{-1} together with the band at 860 cm^{-1} points to the surface hydroxyl groups. The couple of the bands at 462 and 550 cm^{-1} as well as the bands at 474, 570 and 628 cm^{-1} can be related to hematite α-Fe_2O_3. At the same time the presence of the bands at 748 and 651 cm^{-1} point to lepidocrocite γ-FeOOH; the bands at 883 and 798 cm^{-1} correspond to goethite α-FeOOH, but the band at 694 cm^{-1} is typical of the GR structure.

The shift of the band at 601 to 597 cm^{-1} in the spectra of the Fe_3O_4 nm_2 sample (**Figure 7**, line 2) as well as the increasing of the band at 412 cm^{-1} intensity points to the increase of the particle size. The bands in the interval from 1195 to 1130 cm^{-1} do not appear. But the widening of the band with maximum at 748 cm^{-1} points to prevalence of γ-FeOOH. The band's strengthening at 474 cm^{-1} points to the increase in the quantity of α-Fe_2O_3. Whereas the band at 485 cm^{-1} does not appear but the appearance of the band at 532 cm^{-1} is confirms the presence of γ-Fe_2O_3.

On the Fe_3O_4 nm_3 spectra (**Figure 7**, line 3) the following bands point to the presence of SO_4^{2-} (the band at 1122 cm^{-1}); α-FeOOH (the band at 1022 cm^{-1}); γ-Fe_2O_3 (the bands at 439 and 698 cm^{-1}); α-Fe_2O_3 (the band at 525 and the strong band at 424 cmα[1]); γ-FeOOH (the bands near 752 cm^{-1}). The band at 485 cm^{-1} is related to the surface Fe–O or FeO and the band at 898 cm^{-1} corresponds to Fe–OH linkage. The band at 871 and 732 cm^{-1} can be associated with carbonate ions.

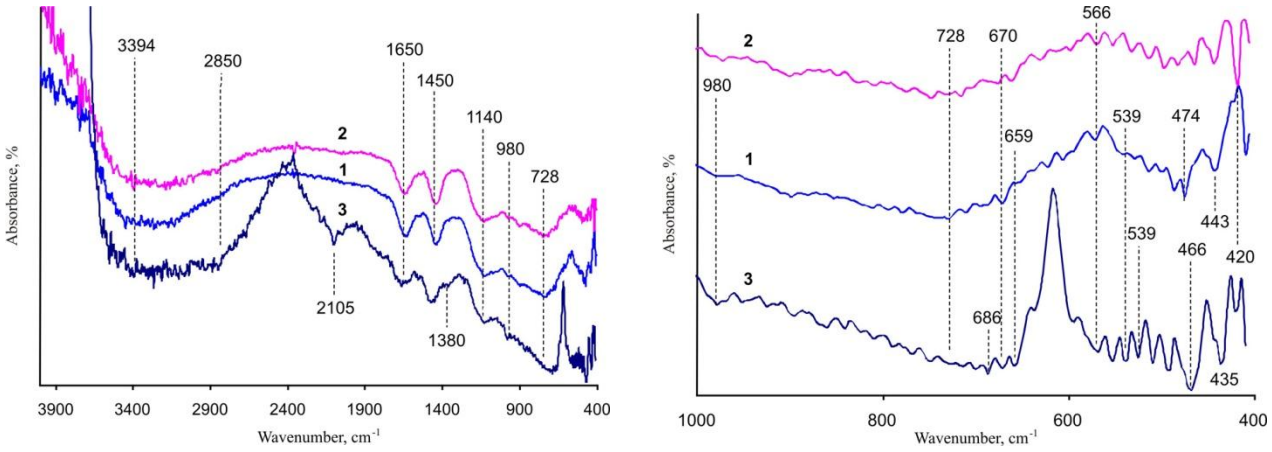

Figure 8. FTIR spectra (a and b) of magnetite: Fe_3O_4 mkm_mid (line 1), Fe_3O_4 mkm_max (line 2), Fe_3O_4_NH_4OH (line 3).

Figure 8 shows the spectra of microsized magnetite particles obtained at co-precipitation of ferrous and ferric sulphate salts in the water solutions. So, the bands at 597 – 593 cm^{-1} relating to magnetite are weak when the oxidative layer applied on its surface (the sample Fe_3O_4 mkm_mid (**Figure 8**, line 1)). The band at 570 cm^{-1} is presented on every spectrum. The bands at 728 and 670 cm^{-1} are related to γ-Fe_2O_3, but the bands at 485 and 443 cm^{-1} together with the band at 570 cm^{-1} can be associated with magnetite. The band at 620 cm^{-1} indicates the M_{th}–O–M_{oh} linkages and the strong band at 408 cm^{-1} tells about the presence of a great number of the octahedral species. The band at 978 cm^{-1} relates to Fe–OH linkages and the band at 898 cm^{-1} corresponds to σOH in the plane of α-FeOOH vibration. The bands at 1643 and 1450 cm^{-1} (σH_2O), at 1133 cm^{-1} (SO_4^{2-}) and 1068 cm^{-1} (complex ν_{as} SO_4^{2-} and ν_{as} SO_3^{2-}) on the spectra 2 of the sample Fe_3O_4 mkm_max are similar to the spectra 1 (**Figure 8**). The main changes get the bands at 750 and 674 cm^{-1} related to γ-Fe_2O_3. Inside the interval from the band 560 cm^{-1} to the band 500 cm^{-1} the new bands at 551 and 532 cm^{-1} appear. Together with the new band at 462 cm^{-1} they relate to α-Fe_2O_3. But the magnetite phase due to the presence of the bands at 482, 443, 570 cm^{-1} is predominant. The band displacements from 408 to 416 cm^{-1} give the evidence of the change of crystallite size.

The band at 686 cm^{-1} related to γ-Fe_2O_3 shifts in the sample Fe_3O_4_NH_4OH (**Figure 8**, line 3) and that shift can point to the less quantity of such iron oxide in the presence of α-Fe_2O_3. To the opposite the great increase of the band intensity at 466 cm^{-1} points to the increase of crystalline degree. The bands at 593 and 570 cm^{-1} confirm the presence of magnetite. But two peaks obviously observed at the bands 570 and 420 cm^{-1} can correspond to Fe–O stretching vibration in α-Fe_2O_3. New bands at 493 and 539 cm^{-1} point to the presence of FeO phase. The band at 1068 cm^{-1} is absent, but other new peaks are observed at 1660 and 1558 (NH), 1473 (NH_3 on the surface), 1361 cm^{-1} (Fe–O linkages near surface). Two peaks are clearly observed at 979 and 898 cm^{-1} in all spectra, particularly strongly they are developed in Fe_3O_4_NH_4OH sample.

Nickel, zinc and cobalt spinel ferrites

The addition of the heavy metal cations to the dispersion medium complicates the process of the phase formation when the rotation-corrosion dispergation method is applied. Among the iron-oxygen structures formed under such conditions apart from iron oxyhydroxides and oxides the spinel ferrites and basic salts of heavy metals appear. For practical usage in biology and medicine the most interesting are the individual nanoparticles of iron, cobalt, nickel and zinc spinel ferrites.

Colloid-chemical processes occurred in the systems based on the iron depending on physical-chemical conditions were described in following works [1, 7, 8]. The formation of iron-oxygen particles in this system occurs in a wide range of the pH values with the participation of different ionized forms of ferric and ferrous iron, zinc and cobalt. In such systems the concentration of heavy metals in the dispersion medium plays an important role for the phase composition. So, at relatively high concentrations of those ions (100 – 500 mg / dm^3) the spinel ferrite phases dominate in the iron-oxygen structure composition on the steel surface, whereas at low concentrations (1 – 10 mg / dm^3) the most developed phase is magnetite.

The applying of the RCD-method does not permit to obtain the stoichiometric spinel ferrites and regulate the cation correlation in their structure. The mass distribution (mass %) of Fe:Co in the $(Co_xFe_{1-x})Fe_2O_4$ structure was studied under following conditions: the ranges of initial Co^{2+} concentrations from 1.0 to 1000.0 mg / dm^3, pH value 2.5 – 12.0 and temperature 3 – 70 °C. The mass distribution is found in the ratio from 100:0 to 85.8:14.2 mass %. The mass distribution of Fe:Zn in $(Zn_xFe_{(1-x)})Fe_2O_4$ structure averages 99.13:0.87 mass % in the near electrode layer and 99.48:0.52 mass % on the steel surface. When the content of cobalt cations in the spinel ferrite structure is increased from 0 to 12.7 % the particle size is growing from 12.6 ± 0.2 nm to 15.8 ± 0.2 nm. When the temperature of the phase formation is increased from 3 to 70 °C the magnetite Fe_3O_4 ($FeFe_2O_4$) particle size is growing from 24.3±0.2 nm to 28.4±0.2 nm as well as spinel ferrite $(Co_xFe_{(1-x)})Fe_2O_4$ particle size is growing from 19.6 ± 0.2 to 21.0 ± 0.2 nm. But under all physical-chemical synthesis conditions the spinel ferrite particles are homogenous and at 300 K belong to magnetically soft materials with M_s 30 – 50 kOe, M_r 6,.5 – 18.0 kOe and H_c ~ 0.03 – 0.05 T. **Figure 9** shows the X-ray patterns of the following non-stoichiometric spinel ferrite phases: nickel ferrous spinel ferrite (**Figures 9a – d**), zinc ferrous spinel ferrite (**Figures 9e –** f) and cobalt ferrous spinel ferrite (**Figures 9g** and **h**) obtained when the rotation-corrosion dispergation method was applied as well as the particles formed due to co-precipitation of ferric and ferrous salts.

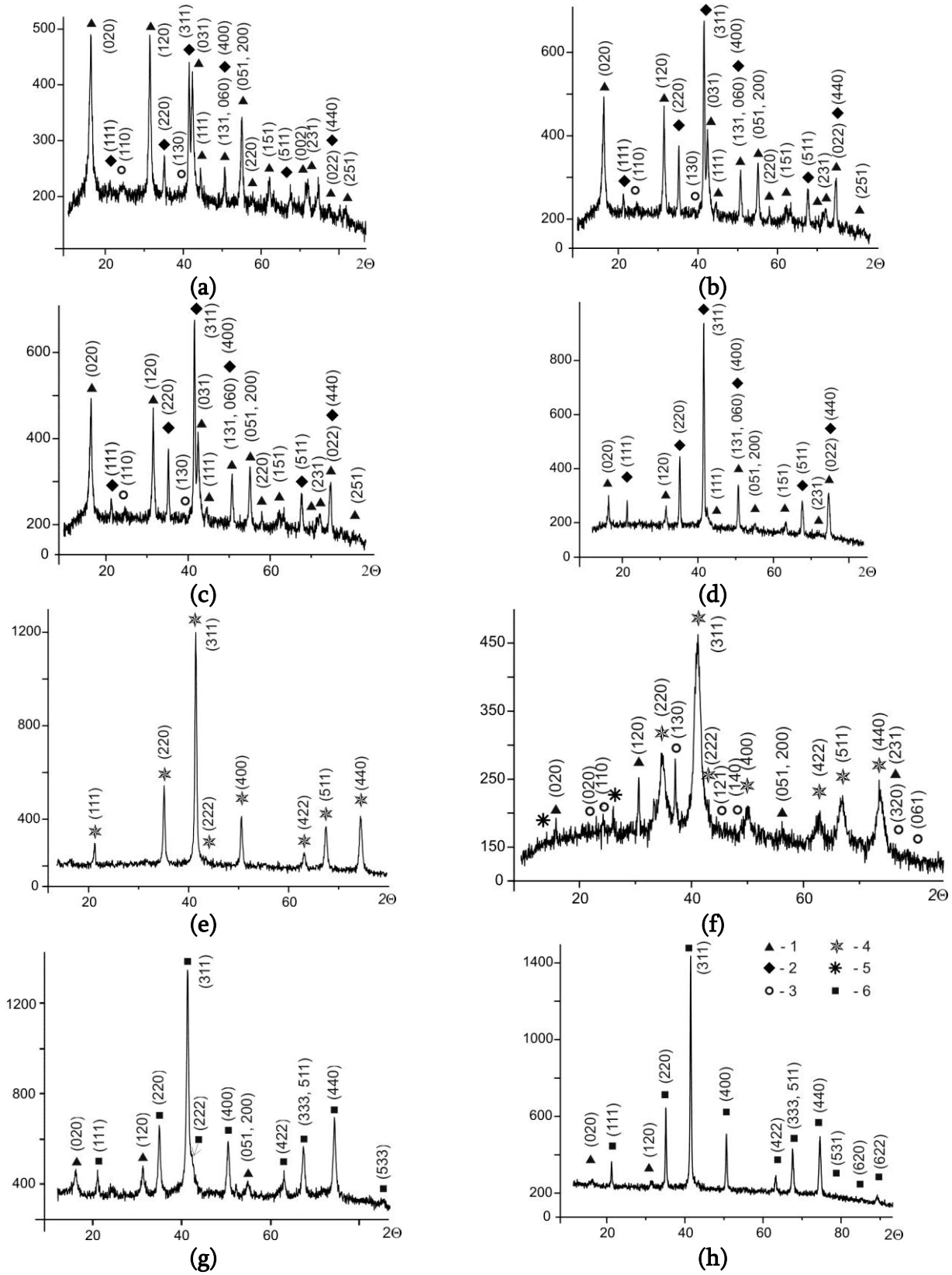

Figure 9. XRD-data of the disperse spinel ferrites: a – d the intermediate products of the $(Ni_xFe_{1-x})Fe_2O_4$ formation (the RCD method); e – nanosized particles of $(Zn_xFe_{1-x})Fe_2O_4$ (the RCD method); f – $(Zn_xFe_{1-x})Fe_2O_4$ (the co-precipitation method); g – $(Co_xFe_{1-x})Fe_2O_4$ (the RCD method), $C_{Co(II)}$ = 100 mg / dm³, h – $(Co_xFe_{1-x})Fe_2O_4$ (the RCD method), $C_{Co(II)}$ = 10 mg / dm³. Numbers correspond to: 1 – γ-FeOOH, 2 – $(Ni_xFe_{1-x})Fe_2O_4$, 3 – α-FeOOH, 4 – $(Zn_xFe_{1-x})Fe_2O_4$, 5 – GR(CO_3^{2-}), 6 – $(Co_xFe_{1\ x})Fe_2O_4$.

TEM images of the nickel, zinc and cobalt spinel ferrites obtain when the RCD-method was applied are shown on the **Figure 10**. All particles have similar morphology and shape of the domatic crystals.

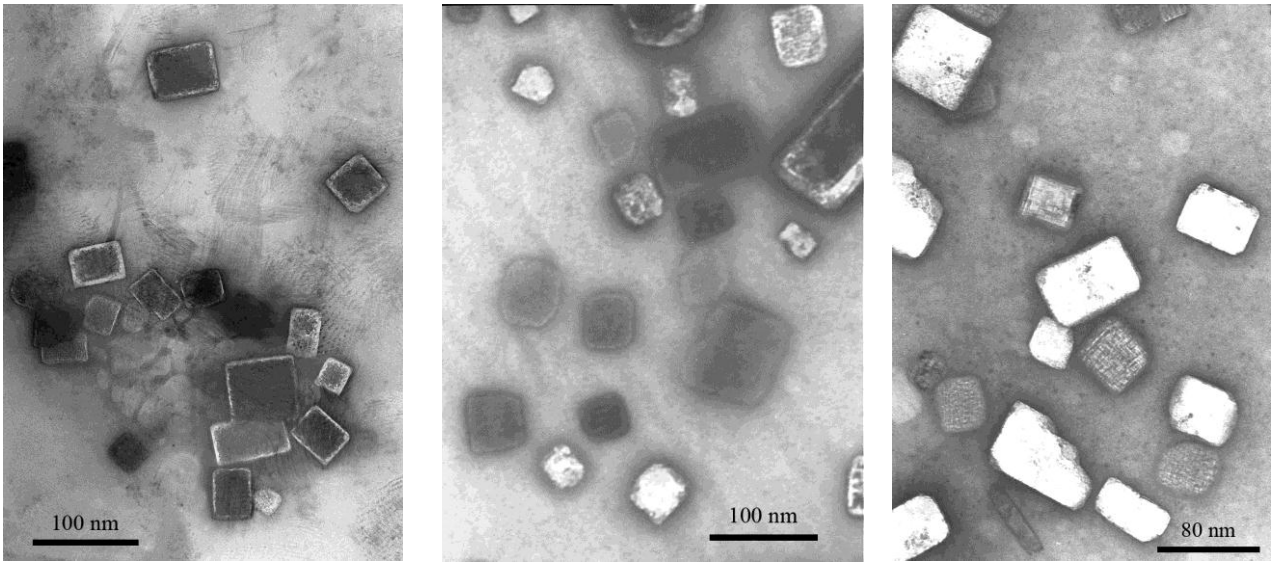

(a) (b) (c)

Figure 10. TEM-images of spinel-ferrite nanoparticles obtained when the RCD-method was applied: a – $(Ni_xFe_{1-x})Fe_2O_4$, b – $(Zn_xFe_{1-x})Fe_2O_4$, c – $(Co_xFe_{1-x})Fe_2O_4$.

As it is known the spinel type oxides of transition metals can be divided into normal or inverse structures. Nickel ferrite belongs to inverse spinel structure. There are four IR active bands in the spectral region under the study: υ_1 (630 – 560 cm^{-1}) and υ_2 (525 (465) – 390 (445) cm^{-1}) that are assigned to the vibrations of the tetrahedron and octahedron for the ferric iron cations respectively [26].

Figure 11, line 1 shows the FTIR spectra of the nickel ferrite precursor. The broad band between 3441 – 3219 cm^{-1} appears due to the O–H stretching corresponding to the surface hydroxyl group disturbed by hydrogen bonds and the water molecules adsorbed onto oxide particles (associated water content). Two strong bordering bands at 1978 and 1901 cm^{-1} associate with adsorbed CO_2; the strong band at 1640 cm^{-1} corresponds to the vibration in OH-group in the adsorbed water. The IR spectrum of the precursor material (**Figure 11**, line 1), shows the typical bands associated with the spinel ferrite structure. The most intensive bands at 1349 and 879 cm^{-1} relate to the Ni–O–Fe bond stretching of the tetrahedral building units that formed the structure of spinel ferrite. The bands at 1558 and 1349 cm^{-1} can point to the presence of carboxylat ions as well as can be associated with the deformation vibration of OH-hydroxyl groups. The presence of CO_3^{2-} ions are confirmed by the band at 1473, 880 and 717 cm^{-1}. Simultaneously the bands at 829 (Fe–OH), 956 (Fe-O), 1349 and near 1500 cm^{-1} (line 1) confirm the presence of $Fe_2(OH)_2CO_3$ structure. In the range of 1100 – 400 cm^{-1} the structure-sensitive and intrinsic absorption bands characterized of the metal–oxygen bonds are found. So, following vibrations belong to α-FeOOH (879 and 794, 505 cm^{-1}), γ-FeOOH (1029, 1164, 750 and 667 cm^{-1}), δ-FeOOH (462 and 863 cm^{-1}), α-Fe_2O_3 (551 and 420, 524 and 443 cm^{-1}), γ-Fe_2O_3 (698 cm^{-1}), spinel or inverse spinel structure of Fe_3O_4 (667 cm^{-1}). The band at 590 cm^{-1} can be associated with both the Fe–O in Fe_3O_4 and the intrinsic vibration of the metal at the tetrahedral sites. The appearance of the band at 590 cm^{-1} (Fe–O) points to the intrinsic

vibrations of the tetrahedral complexes, whereas the bands in the range of 443 – 462 cm^{-1} are attributed to the intrinsic vibrations of the octahedral complexes. Therefore, the vibration mode of tetrahedral clusters is higher than the vibration mode of octahedral clusters. The spectrum bordering with the inflection at 698 cm^{-1} indicates the predominance of the tetrahedral structures. At the same time the broadening of such peak may point to weak crystallinity of the ferrite sample [27]. The band at 613 cm^{-1} shows the presence of $Ni(OH)_2$, but the well defined bands of $NiFe_2O_4$ in spectrum 1 (**Figure 11**) are not observed.

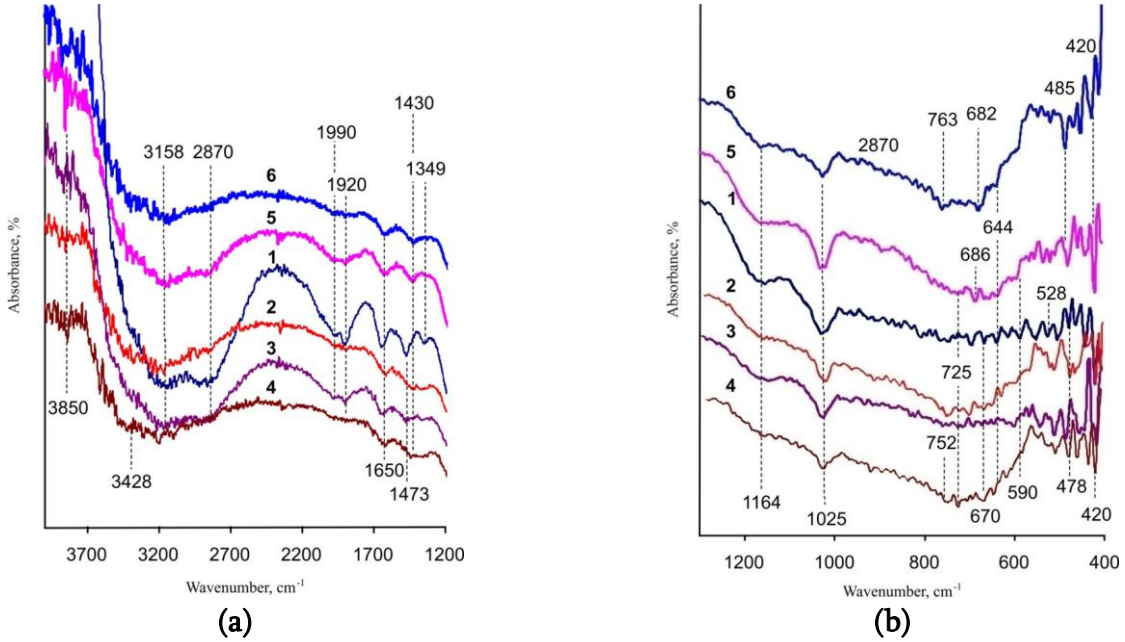

Figure 11. FTIR spectra (a and b) of the nickel ferrites $(Ni_xFe_{1-x})Fe_2O_4$: Ni_1 (line 1), Ni_2 (line 2), Ni_3 (line 3), Ni_4 (line 4) and zinc spinel ferrites $(Zn_xFe_{1-x})Fe_2O_4$: Zn_100_1 (line 5), Zn_100_2 (line 6).

The main changes on the spectra 2 (**Figure 11**) are observed in the region of the absorption bands belonging to hydroxyl groups and surface water molecules (3800 – 2800 cm^{-1}). The intensity of moisture adsorption bands is considerably decreased with their displacement into the area of big wave numbers, whereas the band at 2850 cm^{-1} and the broad band's at 2075, 1982 and 1920 cm^{-1} are weakly developed. When the intensity of the band at 1430 cm^{-1} belonging to CO_3^{2-} ion vibrations is noticeably decreased, the band at 1380 cm^{-1} can be related to α-FeOOH and this confirms the increase of the goethite content. On the other hand the broadening of the band in the range of 1470 – 1300 cm^{-1} together with appearance of weak reflex at 1540 cm^{-1} confirms the presence of carboxilate groups. The smoothing band at 1164 cm^{-1} gives the evidence of the γ-FeOOH quantity decrease. The appearance of the shoulder at 1070 cm^{-1} related to valence vibrations –OH between CO_3^{2-} and iron atoms [28] points to the formation of complexes on the phase interface. The bands at 914, 899 and 752 cm^{-1} confirm the formation of plate-type goethite [15]. The strong band at 590 cm^{-1} disappeared on the spectra, but the appearance of new bands at 683 cm^{-1} (nickel salts), 652 and 521 cm^{-1}, as well as, new shoulder at 571 cm^{-1} and the band at 408 cm^{-1} (Ni–O) correspond to intrinsic stretching vibrations of the metal–oxygen at the tetrahedral and octahedral sites, respectively, indicate the obtaining of the $NiFe_2O_4$ structure. Moreover, such absorption bands give the evidence to the formation of the individual spinel ferrite phases [29]. But the bands at 478 and 548 cm^{-1} point to

the presence of well crystallined hematite α-Fe_2O_3 phase whereas the bands at 530 and 440 cm^{-1} characterize the protohematite phase.

The band at 1153 cm^{-1} in the spectra 3 (**Figure 11**) is increased with the splitting of the bands at 1473 and 1365 cm^{-1}. The strong band at 601 cm^{-1} with the shoulder at 590 cm^{-1} related to intrinsic vibration of the metal at the tetrahedral sites (Fe–O) and the band at 416 cm^{-1} related to vibration in octahedral sites (Ni–O) can be associated with $NiFe_2O_4$. The splitting of the main tetrahedral band shows that some of the Ni^{2+} ions are shifted from octahedral to tetrahedral sites. Also the spectra 3 (**Figure 11**) have strong bands at 543 and 466 cm^{-1} (α-Fe_2O_3 phase), two bands at 582 and 617 cm^{-1} ($NiFe_2O_4$), the band at 690 cm^{-1} (nickel salt), the band at 509 cm^{-1} (α-FeOOH), and the band at 485 cm^{-1} that points to the presence of adsorbed nickel ions on the spinel ferrite surface. The strong bands at 629 and 440 cm^{-1} with the band splitting at 459 cm^{-1} correspond to α-Fe_2O_3 phase. The band at 659 cm^{-1} relates to –OH as well as the inclusion of the Fe_3O_4 phase. Two bands at 562 and 428 cm^{-1} belong to the sub-bands of tetrahedral sites. The difference in band positions for tetrahedral and octahedral complexes corresponds to the differences of the band distances of Fe^{3+}–O^{2-}. The kink 833 cm^{-1} appears due to Fe–O–H linkage and the band at 6907 cm^{-1} points to Fe–O linkage in γ-FeOOH structure.

The peculiarity of the spectrum 4 (**Figure 11**) lies in the displacement of the band at 543 cm^{-1} that pointed to Fe–O linkage in α-Fe_2O_3 (**Figure 11**, line 3) to the band at 551 cm^{-1}. Such displacement is explained by the structure reconfiguration accompanying of the spinel ferrite degradation. The band at 582 cm^{-1} relating to the spinel ferrite is not developed, whereas the intensity of the band at 670 cm^{-1} that is characteristic to Green Rust as well as Fe_3O_4 is growing. Reinforcement of the band at 620 cm^{-1} points to the tetrahedral building of spinel ferrite. The strong band at 755 cm^{-1} relates to asymmetric vibrations of Fe–O linkage and it is typical for α-FeOOH as well as γ-FeOOH, but the band at 725 cm^{-1} coupled with the band at 670 cm^{-1} confirms the presence of γ-Fe_2O_3. The change of spectrum profile in the area below 500 cm^{-1} points to recrystallization of the sample accompanied by the formation of the following structures: M_{th}–O–M_{oh} linkage at 620 cm^{-1}, the surface Fe–OH linkages at 3840 and 3614 cm^{-1} and α-Fe_2O_3 as the main phase at 551 and 462 cm^{-1}. The presence of spinel ferrite is confirmed by duplet 532 – 524 and 647 cm^{-1}. The weak shoulder at 586 cm^{-1} in couple with the bands at 482 and 420 cm^{-1} can point to the presence of adsorbed nickel ions as well as spinel ferrite phase with characteristic bands at 483, 586 and 705 cm^{-1}. Whereas the presence of $Ni(OH)_2$ phase at 620 (626), 524 (428) and 420 (417) cm^{-1} is possible. The kink at 836 cm^{-1} appears due to the Fe–O–H linkage and the band at 694 cm^{-1} points to Fe–O linkage in γ-FeOOH. Correlation of the hematite bands at 462 and 435 cm^{-1} provide the evidence of low cryslallinity of the sample. The bands near 819 – 806 and 879 – 836 cm^{-1} point to the differences in hydrate layer; the band at 435 cm^{-1} coupled with the bands at 725 and 586 cm^{-1} corresponds to micro porous ferrite structure.

The compound zinc-iron oxide has a spinel structure AB_2O_4 with tetrahedral A sites occupied by Zn^{2+} ions and octahedral B sites occupied by Fe^{3+} ions, respectively. According to the cation distribution into the spinel lattice it can be either normal zinc spinel ferrite structure or its inverse structure with half of the trivalent ions in the tetrahedral position and the other half together with the divalent ions in the octahedral sites [30].

The typical IR bands for the zinc spinel ferrite structure are the following: the high frequency band is found in the range of 595 – 600 cm^{-1} and the lower frequency band v2 is found in the range of 480 – 490 cm^{-1}, respectively [30, 31]. The typical bands at 1349 and

879 cm^{-1} that correspond to the stretching Zn–O–Fe linkages of the tetrahedral building units of the spinel skeleton are not observed on the IR spectra of $(Zn_xFe_{1-x})Fe_2O_4$ (**Figure 11**, line 5). The wide absorption band in the high energy area, centred at 3158 cm^{-1}, associates with the water molecule vibrations (from –OH stretching) in the spinel ferrite structure. The broadening of this band as well as the lowering of its frequency can point to the formation of the H-bridges in the spinel ferrite precursor, which subsequently disappear after the completion of the phase transformation. The band at 1632 cm^{-1} gives the evidence of the H–O–H deformation mode. The broad band situated below 700 cm^{-1} belongs to the maghemite γ-Fe_2O_3 nanoparticles that are present in both $(Zn_xFe_{1-x})Fe_2O_4$ and $(Ni_xFe_{1-x})Fe_2O_4$ structures. The broad band near 686 cm^{-1} was observed only on the $(Zn_xFe_{1-x})Fe_2O_4$ spectrum. It points to the presence of $Fe(OH)_3$ on the outer surface of the nanoparticles. Very small shoulders around the 713, 667 and 536 cm^{-1} appearing on the IR spectra 5 of $(Zn_xFe_{1-x})Fe_2O_4$ (**Figure 11**) point to the tetrahedral sites, but such bands completely disappear on the $(Zn_xFe_{1-x})Fe_2O_4$ spectra 6 (**Figure 11**). According to [32] the absorption bands splitting or shoulder formation can be connected with the presence of the Fe^{2+} in the spinel ferrite structure. Moreover it is attributed to the Jahn–Teller distortion due to the presence of Fe^{2+} ions which produce the local deformation in the crystal field potential and lead to the splitting of the absorption bands. The presence of the couple bands at 597 and 482 cm^{-1} as well as 566 and 420 cm^{-1} point to the zinc iron spinel ferrite structure. But the last pair can be attributed to α-FeOOH. The absorption bands at 640 and 555 cm^{-1} correspond to the metal–oxygen (Fe–O) stretching vibrations and give the evidence of the zinc spinel ferrite structure [33]. The bands at 555 and 450 cm^{-1} can correspond to α-Fe_2O_3. This result is also in agreement with [34] that assigned the high-frequency bands to the tetrahedral groups (640 and 555 cm^{-1} areas) and the low-frequency bands to octahedral group (450 cm^{-1}). The peaks at 3182 and 1630 cm^{-1} correspond to hydration water [31].

On the $(Zn_xFe_{1-x})Fe_2O_4$ spectrum 6 (**Figure 11**) the broad band profile changes due to the appearance of moisture peaks at 3880 and 3749 cm^{-1} that are attributed to the isolated surface hydroxyls. The peak at 1095 cm^{-1} points to the appearance of the overtone. The band at 1078 cm^{-1} associates with the stretch motion, where the oxygen atom moves back along a line parallel to the axis along two metal atoms [35]. The bands at 559 and 428 cm^{-1} relate to zinc spinel ferrite, where the peak 428 cm^{-1} corresponds to the vibration of Zn–O. Also the band at 763 cm^{-1} corresponds to Fe–O–Zn linkage and the strong band at 590 cm^{-1} corresponds to Fe_3O_4 present in the spectra. The band at 485 cm^{-1} relates to $Fe(OH)_2$ and the band at 470 cm^{-1} relates to α-Fe_2O_3 increase in the spectrum (**Figure 11**, line 6) whereas the new strong band at 412 cm^{-1} appears. Such condition confirms the Fe–O vibrations in normally orientated crystal plane and points to the increase of the particle size. The bands at 763, 640, 485 and 455 cm^{-1} can be attributed to the (001) crystal plane of α-FeOOH. The same way as the bands at 763, 640, 485 and 455 cm^{-1} can point to the presence of α-FeOOH with crystal plane (001). The bands at 640 and 470 cm^{-1} can be related to γ-Fe_2O_3 and the bands at 455 and 547 cm^{-1} are attributed to α-Fe_2O_3, respectively. The presence of the ZnO phase with the typical bands placed at 496 and 558 cm^{-1} is not detected.

The cobalt ferric spinel ferrites $(Co_xFe_{1-x})Fe_2O_4$ were formed under the following conditions (**Figure 12**): the concentration of the cobalt ions was 10 mg / dm^3 where the line 1 attributed to the particles obtained into the near electrode layer and the line 2 and line 3 correspond to the samples obtained on the steel surface. Other particles were formed on the steel surface at $C_{Co(II)}$ = 100 mg / dm^3 (line 4) and $C_{Co(II)}$ = 200 mg / dm^3 (line 5).

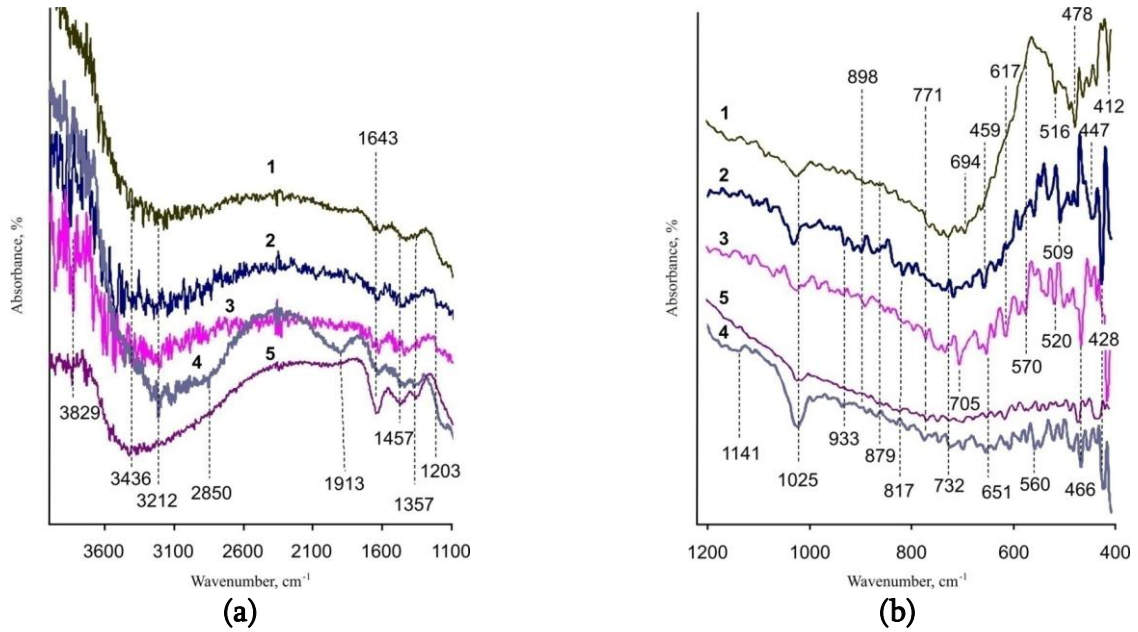

Figure 12. FTIR spectra (a and b) of the cobalt ferric spinel ferrites $(Co_xFe_{1-x})Fe_2O_4$.

The typical cobalt spinel ferrite structure is characterized by the following IR bands: the antisymmetric stretching at 1629 cm^{-1}, the symmetric stretching at 1388 cm^{-1}, the totally symmetric stretching at 1052 cm^{-1}, the out of plane bending at 870 cm^{-1}, the antisymmetric in-plane bending at 729 cm^{-1} and the symmetric in-plane bending at 664 cm^{-1} [36]. Two broad bands in the frequency ranges of 3450 – 3550 and 1600 – 1650 cm^{-1} correspond to O–H stretching and H–O–H bending vibrations of the water molecules, which confirm the water components, present in the spinel structure.

The shift of the broad band corresponding to the moisture vibration to the lesser wave numbers (the band centered at 3282 cm^{-1}) in comparison with Fe_3O_4 (the band near 3480 cm^{-1}) or mixture of Fe_3O_4 and γ-Fe_2O_3 (the band near 3420 cm^{-1}) is detected for the cobalt spinel ferrite. The following bands appeared in the spectrum 1 (**Figure 12**): two bands at 1630 and 1658 cm^{-1} (σOH vibration of water); the bands at 1430 and 710 cm^{-1} (CO_3^{2-}); the bands at 1160, 1122 and 1087 cm^{-1} (ν_{as} SO_4^{2-} and ν_{as} SO_3^{2-}). In the area of the Fe–OH vibrations at 890 – 960 cm^{-1} the characteristic bands do not appear. The most signal intensity corresponding to γOH vibration out of the plane in the γ-FeOOH and α-FeOOH structure is found in the interval of 780 – 690 cm^{-1}. The wave length area 400 – 800 cm^{-1} characterizes the Me–O and Me–O–Me linkage vibrations in the metal oxides. The typical absorption of Fe_3O_4 at 580 cm^{-1} relating to Fe–O bond is absent but two bands at 435 and 478 cm^{-1} are present on the spectrum. The bands at 462 and 450 cm^{-1} correspond to the δ-FeOOH and α-FeOOH. Due to the presence of the band complex at 435, 478, 528 and 640 cm^{-1} it is possible to suppose the α-Fe_2O_3 metastable phase formation characterized by the absence of Fe ions in its tetrahedral sites as well as the presence of γ-Fe_2O_3 phase with the bands at 435, 478, 640, 694, 728 cm^{-1}. The bands at 694 cm^{-1}, in the area of 728 – 763 cm^{-1}, the bands at 543, 516 and 489 cm^{-1} can relate to hydrated Co–Fe centers. The last band at 489 cm^{-1} may be examined as a typical one.

The following bands appear on the spectrum 2 (**Fig.ure 12**): 590 (Fe_3O_4), 560 (γ-Fe_2O_3) and the intensive band 428 cm^{-1}. The bands at 435 and 451 cm^{-1} are not seen in the spectra but the band at 447 cm^{-1} appears. Together with the new bands at 509 and 875 cm^{-1} they can point to the increase of the content of the α-FeOOH phase, whereas the bands at 447 and 559 cm^{-1}

can be associated with the Fe_3O_4 phase. The band at 659 cm^{-1} as well as the strong band at 1640 cm^{-1} relates to –OH vibrations on the surface. New band at 686 cm^{-1} can relate to hydrated Co–Fe centers. The bands at 613 and 532 cm^{-1} are seen on the spectrum and the band at 547 cm^{-1} becomes stronger. The band at 489 cm^{-1} (FeCo) shifts to 485 cm^{-1} but its intensity does not change. The correlation of the band intensities at 462 cm^{-1} and the band near 450 – 420 cm^{-1} points to the decrease of the phase crystallinity.

The intensive band at 520 cm^{-1} relating to α-Fe_2O_3 as well as the couple of bands at 574 and 636 cm^{-1} relating to the coated Fe–O in octahedral sites appear in the spectrum of the spectrum 3 (**Figure 12**). The band at 536 cm^{-1} is absent. The main changes take place in the area of the vibrations of Fe–OH groups near 890 cm^{-1} and in the range from 1623 to 1666 cm^{-1}. The band at 659 cm^{-1} splits into 651 and 667 cm^{-1}. Such change confirms the sample hydration. The most intensive bands are the following: at 705, 667 and 466 cm^{-1} (δ-FeOOH) and the band at 416 cm^{-1} corresponding to the phases $CoFe_2O_4$ as well as γ-Fe_2O_3. The bands at 466 and 447 cm^{-1} can also associate with complicate Co–γ-Fe_2O_3 structure or with the surface Fe–O linkages of Fe_3O_4 particles. The complex of bands at 732, 520, 489 cm-^{1} can be explained as CoFe units. According to the obtained data the particles include the following structure elements: Fe_3O_4, γ-Fe_2O_3 and α-Fe_2O_3. The strong band at 720 cm^{-1} corresponding to β-FeOOH or γ-Fe_2O_3 in the presence of Co ions shifts to 705 cm^{-1}.

The structural elements of both spectrum (line 1 and line 3) are present on the spectrum 4 (**Figure 12**). The band at 455 cm^{-1} appears but the bands at 536 and 447 cm^{-1} as well as the couple of strong bands at 651 and 667 cm^{-1} and the band at 705 cm^{-1} do not appear. The bands at 424 and below 408 cm^{-1} become stronger. The most significant changes are seen on the spectra Co_200, where the typical bands of the following phases: Fe_3O_4 at 590 cm^{-1}, α-Fe_2O_3 at 520 cm^{-1} and δ-FeOOH at 466 cm^{-1} are not found. The strong bands at 439 cm^{-1} (γ-Fe_2O_3), 474 and 578 cm^{-1} more probably relate to the Fe–O linkages in the mixture of γ-Fe_2O_3 with α-Fe_2O_3. The broadening and smoothing of the bands in the interval of 900 – 500 cm^{-1} point to the crystallinity decrease. But the increase of the band intensity at 474 cm^{-1} and the shift of the band from 435 to 439 cm^{-1} give the evidence to the intercalation of cobalt ions into iron–oxygen particles [36].

The $FeFe_2O$ & Ag^0 *nanocomposite*

The physicochemical properties of the $FeFe_2O$ & Ag^0 nanocomposites were described in [37]. **Figure 13** shows XRD-data and **Figure 14** shows TEM-images of such structures. The $FeFe_2O$ && Ag^0 composites were formed under following conditions: the pH value was chosen 6.5 and the argentum concentrations were chosen 0.5 (**Figure 15**, line 1), 1.0 (**Figure 15**, line 2), 2.0 (**Figure 15**, line 3), 3.0 (**Figure 15**, line 4) and 5.0 mg / dm^3 (**Figure 15**, line 5).

Infrared spectra of the magnetite situated in the core of the composite particles show the typical bands at 590 and 450 cm^{-1} corresponding to the Fe–O linkages in tetrahedrical and octahedrical positions [16]. The peculiarity of the $FeFe_2O_4$ & Ag^0 composite with $C_{Ag(I)}$ = 0.5 mg / dm^3 (**Figure 15**, line 1) is the availability of the band at 3509 cm^{-1} in the interval of the moisture vibration. The following bands are present in the area of the CO_3^{2-} vibration: the band at 1473 cm^{-1} is similar to the bands on certain spinel ferrites and lepidocrocite spectra and the band at 1430 cm^{-1} is similar to the band on magnetite spectrum. The band at 1369 cm^{-1} can relate to the Fe–O linkages of the near α-FeOOH surface. The band at 1149 cm^{-1} points to the presence of oxygen bridges or Fe–OH groups. The bands at 1029, 1164 and 759 cm^{-1} correspond

to γ-FeOOH and the band at 682 cm^{-1} can prove the presence of γ-Fe_2O_3. The band at 674 cm^{-1} points to normal or inverse spinel structure and characterises the ferrimagnetic core whereas the couple of bands at 628 and 586 cm^{-1} corresponds to uncoated ferrimagnetic surface. The band at 570 cm^{-1} can be related to Fe–O–Fe linkage of uncoated magnetite surface Fe_3O_4 as well as the bands at 555, 570, 647 and 655 cm^{-1} may be corresponding to γ-Fe_2O_3 and the bands at 570 and 424 cm^{-1} point to Fe–O linkages in α-FeOOH. Moreover the combination of the bands at 887, 759, 628, 497 and 455 cm^{-1} can relate to the (001) crystal plane of α-FeOOH.

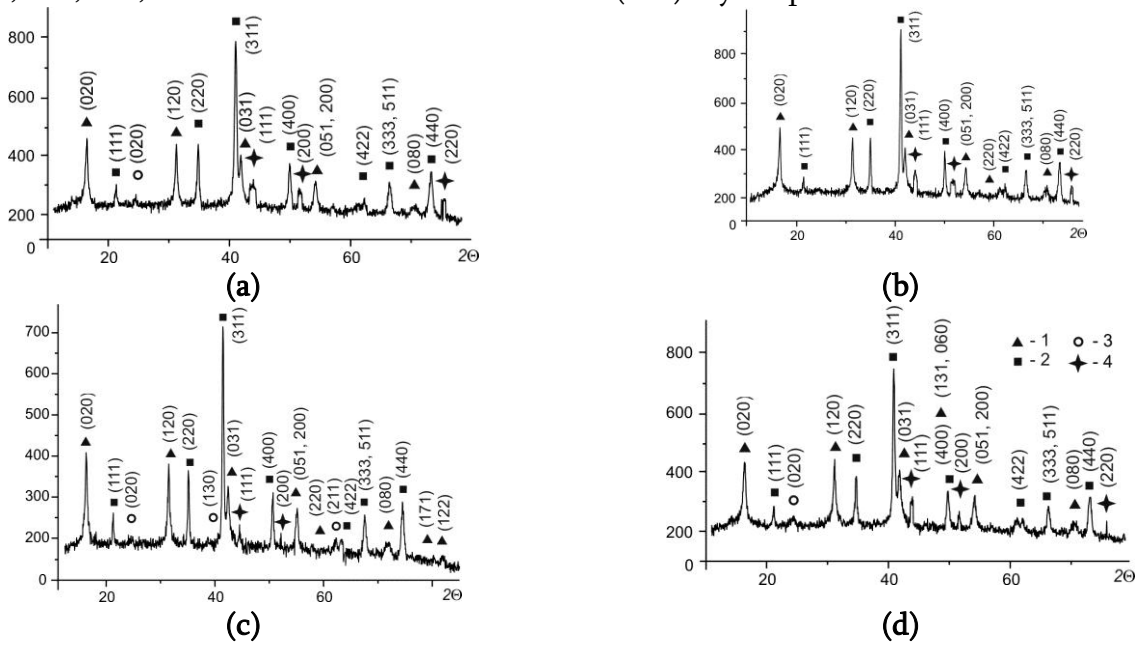

Figure 13. XRD-data of the $FeFe_2O_4$ & Ag^0 composite particles obtained when the RCD-method was applied: a – $C_{Ag(I)}$ = 1 mg / dm^3; b – $C_{Ag(I)}$ = 2 mg / dm^3; c – $C_{Ag(I)}$ = 3 mg / dm^3; d – $C_{Ag(I)}$ = 5 mg / dm^3. The numbers correspond to mineral phases: 1 – γ-FeOOH, 2 – $FeFe_2O_4$, 3 – α-FeOOH, 4 – Ag^0.

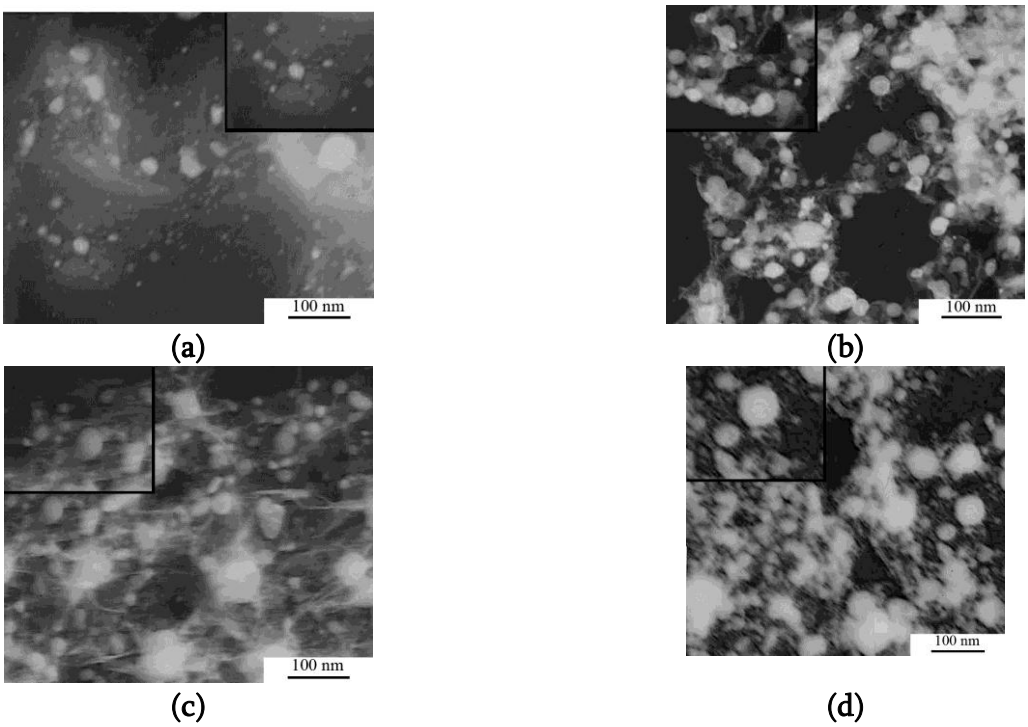

Figure 14. TEM-images of the $FeFe_2O_4$ & Ag^0 composite particles Obtained when the RCD-method was applied: a – $C_{Ag(I)}$ = 1 mg / dm^3; b – $C_{Ag(I)}$ = 2 mg / dm^3; c – $C_{Ag(I)}$ = 3 mg / dm^3; d – $C_{Ag(I)}$ = 5 mg / dm^3.

When the quantity of silver on magnetite surface is increasing (**Figure 15**, line 2) the bands at 3509 and 887 cm^{-1} disappear but the intensity of the band near 755 cm^{-1} increases. Together with the bands at 1150 and 1029 cm^{-1} (the σOH linkage in the plane), very intensive bands at 613 and 509 cm^{-1} and the band at 482 cm^{-1} (γOH out of plane) it relates to the vibrations of the rode-like γ-FeOOH. At the same time the strong band at 509 cm^{-1} corresponding to α-FeOOH appears on the spectrum but the band at 474 cm^{-1} corresponding to the vibrations of the surface group in Fe_3O_4 structure disappears. Whereas the bands at 497 and 528 cm^{-1}, relating to the α-Fe_2O_3 do not appear. It confirms the transition from octahedral to tetrahedral structure. The band at 586 cm^{-1} splits into two bands centered at 593 and 582 cm^{-1} corresponding to Fe–O linkages in Fe_3O_4 that were broken due to argentum interaction. The shape of the sensitive band at 605 cm^{-1} is not detected as well as the band at 674 cm^{-1} corresponding to normal or inverse spinel structure is not changed. Whereas the band at 628 cm^{-1} relating to Fe_3O_4 splits into three bands at 632, 624 and 613 cm^{-1}.

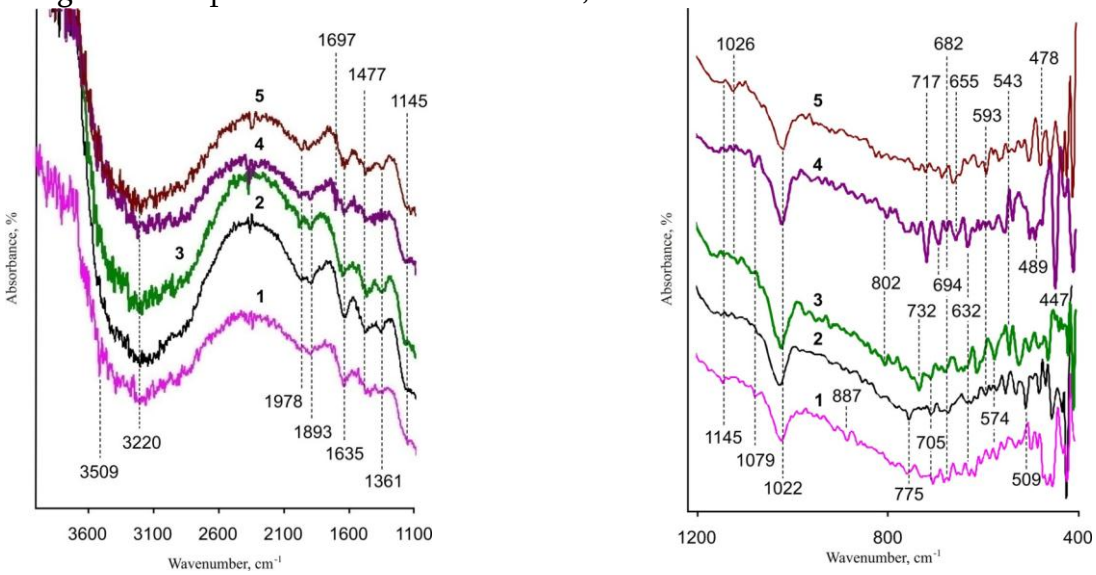

Figure 15. FTIR spectra (a and b) of the $FeFe_2O_4$ & Ag^0 composites: $C_{Ag(I)}$ = 0.5 mg / dm^3 (line 1); $C_{Ag(I)}$ = 1 mg / dm^3 (line 2); $C_{Ag(I)}$ = 2 mg / dm^3 (line 3); $C_{Ag(I)}$ = 3 mg / dm^3 (line 4); $C_{Ag(I)}$ = 5 mg / dm^3 (line 5).

The intensity of the band at 447 cm^{-1} is strongly growing due to the increase of argentum quantity on the magnetite particles on the spectrum 4 in comparison with spectrum 3 (**Figure 15**). Such changes give the evidence of the reinforcement of the octahedral magnetite structure. That band shifts to 458 cm^{-1} on the spectrum 5 (**Figure 15**). The vibration of the band at 474 cm^{-1} relating to the surface Fe-O linkages points to the change of the composite shell due to the formation of the island structures when the quantity of the shell's argentum increases.

The shape of the bands at 460 and 437 cm^{-1} points to the crystallinity changes from strong (spectrum 2) to weak (spectrum 3) and back to strong (spectrum 5) (**Figure 15**). The appearance of the bands at 408 and 412 cm^{-1} corresponds to nanocrystalline structure of the samples. The band at 1079 cm^{-1} (ν_{as} SO_4^{2-} and ν_{as} SO_3^{2-}) is present only on the spectrum 1 and spectrum 4 but the sulfate vibrations at 1106 cm^{-1} (ν_{as} SO_4^{2-}) and 1064 cm^{-1} (HSO_4^-) are weak on the spectrum 5 (**Figure 15**).

On the whole the increase of the argentum layer (**Figure 15**, spectrum 5) leads to the shift of the vibration bands of the Fe–O linkages to the area of great wave numbers. So, the shift

of the band at 570 to 578 cm^{-1} points to predominance of the M_{th}-M_{oh} structure, the shift of the band at 586 to 593 cm^{-1} gives the evidence of the interaction with argentum. The band at 489 cm^{-1} relating to the surface Fe–O vibration disappears but the band of the OH vibrations at 1018 cm^{-1} becomes intensive that points to the formation of new hydrate coverage. The presence of the bands at 609, 578 and 478 cm^{-1} confirms the γ-Fe_2O_3 increase on the phase interface. The appearance of the band at 566 cm^{-1} gives the evidence to the inclusion of the argentum ions into magnetite structure. The strong band at 412 cm^{-1} appears due to the increase of the particle size. The absence of the intensive bands in the area 795 – 890 cm^{-1} points to the small amount of α-FeOOH, but the bands at 794 and 632 cm^{-1} relate to the residual of α-FeOOH. The following bands are presented on the spectra: at 686 and 721 cm^{-1} (γ-Fe_2O_3), at 740 and 663 cm^{-1} (γ-FeOOH). The bands at 505, 458 and 420 cm^{-1} can relate to α-Fe_2O_3.

Conclusions

1. According to XDR data the iron-oxygen particles obtained when the rotation-corrosion dispergation method was applied contain the products of the phase transformation of the main phase and structural elements of its phase-precursors in their structure. Ferrihydrite and Fe(II)-Fe(III) layered double hydroxides (Green Rust) relate to the phase-precursors in the systems based on the iron (steel). So, some structural elements of iron oxyhydroxides as well as hematite are included into ferrihydrite structure. Whereas Green Rusts contain the corresponding anions, water and iron oxide admixtures in its structure alongside with the lepidocrocite and goethite phases.
2. The process of the phase transformation of the phase-precursors strongly depends on red-ox conditions. While under oxidative conditions the iron oxyhydroxides are formed in the system, under reductive condition in the presence of the ferrous species the magnetite particles are the typical product of the phase transformation. But in the absence of ferrous species in the water medium the lepidocrocite □-FeOOH transformation leads to the maghemite □-Fe_2O_3 formation. Lepidocrocite has a plate-like morphology, it is heterogeneous and contains goethite phase as admixture. The following structural elements were found in the magnetite structure: sulphate and carbonate anions, goethite, hematite, maghemite and lepidocrocite admixtures.
3. Spinel ferrites obtained when the RCD-method was applied correspond to the non-stoichiometric structures where zinc, nickel or cobalt atoms replace ferrous atoms. The FTIR spectra of such particles have a few differences from stoichiometric spinel ferrites due to the presence of the anions as well as structural elements of Green Rust and iron oxyhydroxides.
4. The structure of the core&shell composite $FeFe_2O_4$&Ag^0 includes the following features: 1) the core degradation under condition when the colloidal particles are instable; 2) the presence of argentum atoms in the magnetite structure as well as silver on its surface; 3) the silver shell porosity or its island-like structure etc.

References

1. O. M. Lavrynenko, V. I. Kovalchuk, S. V. Netreba, Z. R. Ulberg. Nano Studies, 2013, 7, 295.
2. S. Peulon, H. Antony, L. Legrand, A. Chausse. Electrochem. Acta, 2004, 49, 2891.
3. L. Legrand, M. Abdelmoula, A. Géhin, A. Chaussé, J.-M. R. Génin. Electrochim. Acta, 2001, 46, 1815.
4. O. M. Lavrynenko. Sci. News Natl. Tech. Univ.Ukr. “KPI”, 2007, 5, 110.
5. Е. Н. Лавриненко. Наносистеми, наноматеріали, нанотехнології, 2008, 6, 2, 529.

6. O. M. Lavrynenko, S. V. Netreba, V. A. Prokopenko, Ya. D. Korol. Хімія, фізика та технологія поверхні, 2011, 2, 93.
7. O. M. Lavrynenko. Nano Studies, 2011, 4, 5.
8. O. M. Lavrynenko. The obtaining of the composition structured systems based on the iron-oxygen minerals, their structure and properties. Автореф. дис. на здобуття наук. ступеня доктора хім. наук: спец. 02.00.11 «Колоїдна хімія». 2013, Київ, 40 с.
9. O. M. Lavrynenko, S. V. Netreba, P. O. Kosorukov. Nano Studies, 2012, 6, 93.
10. J.-M. R. Genin, A. A. Olowe, Ph. Refait, L. Simon. Corros. Sci., 1996, 38, 1751.
11. J.-M. R. Genin, M. Abdelmoula, Ch. Ruby, Ch. Upadhyay. C. R. Geosci, 2006, 338, 402.
12. О. М. Лавриненко. Мінералогічний журнал, 2011, 33, 12.
13. U. Schwertmann, R. M. Cornell. Iron Oxides in the Laboratory: Preparation and Characterization. 2000, Wienheim: Wiley–VCH.
14 L. Carlson, U. Schwertmann. Clays and Clay Minerals, 1980, 28, 272.
15. R. M. Cornell, U. Schwertmann. The Iron Oxides: Structure, Properties, Reactions, Occurrence and Uses. 2003, Weinheim: Wiley–VCH.
16. P. E. G. Casillas, C. A. R. Gonzalez, C. A. M. Pérez. Infrared Spectroscopy of Functionalized Magnetic Nanoparticles, Infrared Spectroscopy – Materials Science, Engineering and Technology. 2012, InTech: http://www.intechopen.com/books/infra red-spectroscopy-materials-science-engineering-andtechnology/infrared-spectroscopy-of-functionalized-magnetic-nanoparticles
17. M. Ma, Y. Zhang, W. Yu, H. Shen, H. Zhang, N. Gu. Colloids Surf. A, 2003, 212, 219.
18. H. C. Liese. Am. Mineralogist, Mineralogical Notes, 1967, 52, 1198.
19. F. Zhao, B. Zhang, L. Feng. Mater. Lett., 2012, 68, 112.
20. M. Sundrarajan, M. Ramalakshmi. E-J. Chem., 2012, 9, 1070.
21. F. Márquez, T. Campo, M. Cotto, R. Polanco, R. Roque, P. Fierro, J. M. Sanz, E. Elizalde, C. Morant. Nanosci. Lett., 2011, 1, 25.
22. P. S. Sidhu. Clays and Clay Minerals, 1988, 36, 31.
23. D. K. Bora, P. Deb. Nanoscale Res. Lett., 2008, 4, 138.
24. C. Pecharromán, T. González–Carreño, J. E. Iglesias. Phys. Chem. Minerals, 1995, 22, 21.
25. Y.-S. Li, J. S. Church, A. L. Woodhead. J. Magn. Magn. Mater., 2012, 324, 1543.
26. G. Dixit, J. P. Singh, R. C. Srivastava, H. M. Agrawal, R. J. Chaudhary. Adv. Mater. Lett., 2012, 3, 21.
27. S. Singhal, Sh. Jauhar, K. Chandra, S. Bansal, Bull. Mater. Sci., 2013, 36, 107.
28. D. L. Melissa. Am. Mineralogist, 2007, 92, 118.
29. M. Khairy, M. E. Gouda. J. Adv. Res., 2014: http://www.sciencedirect.com/science/article/pii/S2090123214000101
30. Ch. A. Ladole. Int. J. Chem. Sci., 2012, 10, 1230.
31. M. C. Chhantbar, U. N. Trivedi, P. V. Tanna, H. J. Shah, R. P. Vara, H. H. Joshi, K. B. Modi. Ind. J. Phys. A, 2004, 78, 321.
32. V. A. Potakova, N. D. Zverv, V. P. Romanov. Phys. Status Solidi A, 1972, 12, 623.
33. T. Marykutty, K. C. George. Ind. J. Pure Appl. Phys., 2009, 47, 81.
34. P. M. P. Swamy, S. Basavaraja, A. Lagashetty, N. V. S. Rao, R. Nijagunappa, A. Venkataraman. Bull. Mater. Sci., 2011, 34, 1325.
35. S. Ponce–Castañeda, J. R. Martínez, S. A. Palomares Sánchez, F. Ruiz, J. A. Matutes–Aquino. J. Sol–Gel Sci. Technol., 2002, 25, 37.
36. N. Sanpo, J. Wang, Ch. C. Berndt. J. Australian Ceram. Soc., 2013, 49, 84.
37. O. M. Lavrynenko. Nano Studies, 2012, 5, 27.

RADIOACTIVE WASTE MANAGEMENT IN GEORGIA

G. Nabakhtiani, L. Chkhartishvili, A. Gigineishvili, K. Gorgadze

Georgian Technical University
Tbilisi, Georgia
giorgi.nabakhtiani@gmail.com
chkharti2003@yahoo.com

Accepted April 14, 2014

1. Introduction

Georgia takes active steps for establishment of radioactive waste management system in the country:

- Based on the international support the Centralized radioactive waste Storage Facility (CSF) was constructed and commissioned;
- Georgia joined to "Join Convention on the Safety of Spent Nuclear Fuel Management and on the Safety of Radioactive Waste Management". According to the convention's requirement the first country status report was prepared and sent to the International Atomic Energy Agency (IAEA) at 2011. (The country status report covers all aspects of radioactive waste management system existed within the country);
- IAEA experts reviewed draft Georgian law "On radioactive waste Management";
- The first radiological Survey of disposal site was conducted together with Swedish experts at 2011;
- EU Project G.4.01.08 "Survey and Strategic Assessment of Georgian Radwaste Interims Storage and Disposal Facilities" was conducted at 2012–2013;
- EU Project G.4.01/09 aim conducting of safety assessment of CSF and disposal was started at 2013.

2. Elements for radioactive waste management system

Generally speaking radioactive management system should contain four major elements:

1. Legal basement – Laws and regulations defining main requirements for safe handling with radioactive waste;
2. Administrative structure – Governmental institutions (Regulatory Body (RB), Radioactive Waste Management Agency (RWMA) and others), which conduct state regulation and handling with radioactive waste;

3. Infrastructure for handling with radioactive waste – Facilities (storage facility, disposal and others) and means, using of what handling with radioactive waste should be conducted;
4. Financial system – financial mechanism for handling with radioactive waste.

Only some parts of above-mentioned elements are exist in Georgia now:

1. Legal Basement

Only some requirements are adopted. The whole system should be established.

2. Administrative Structures

Georgian Ministry of Environment and Natural Resources Protection through its Department for Nuclear and radiation Safety (Georgian Law "On Nuclear and Radiation Safety", Art. 6) acts as a regulatory body. The main task is establishment of RWMA which on behalf of state should conduct radioactive waste management within whole country.

3. Infrastructure for handling with radioactive waste

CSF is under operation (some addition improving of safety system components is desired). Closed near surface disposal is also existed. Is it possible or not to use (and how) the disposal site for further disposing - the answer can be obtained based on the results of Project G.4.01.09.

It is taken the first step within IAEA Project GEO/9/011 to establish simple radioactive waste processing facility at the CSF.

4. Financial system

The system is not defined well. Financial support is provided by the state.

RWMA should meet 9 basic principles defined by IAEA [1]. Based on these first it is possible to define more detailed principles:

a) Openness;
b) Involvement of stakeholders;
c) A deliberative and accessible process;
d) Provision of adequate time for the resolution of issues;
e) Final disposal is regarded as the ultimate step in the radioactive waste management process;
f) The aim shall be to achieve a maximum degree of passive safety in storage facility and disposal;
g) The design, construction, commissioning, operation, decommissioning and closure of waste generating and disposal (close up for disposal) facilities shall be in accordance with all applicable regulatory requirements;
h) The following hierarchy of waste management options shall be followed where practicable;
    h.a) Avoidance and minimization of waste trough:
    h.b) Re-use, reprocessing and recycling;
    h.c) Storage;
    h.d) Conditioning and disposal.
i) The national radioactive waste management strategy shall cover the total life cycle of waste management – generation to institutional control;
j) The competent regulatory body must specify the period for which an active institutional control may be assumed for purposes of safety assessments.

k) The transfer of waste among generators shall be considered provided all issues pertaining to ownership and liability and safety are addressed.

l) To minimize the burden on future generations, decommissioning and closure of facilities should be implemented as soon as practicable.

m) The deliberate dilution of radioactive waste is not acceptable, however in the case of NORM waste the dilution of higher concentration material with lower concentration material will be considered provided all relevant regulatory concerns are addressed.

3. Radioactive waste framework

Georgia as all other countries should develop its policy for radioactive waste management and strategy for practical implementation of the policy [2]. One requirement for the policy is defined by Georgian law "On Nuclear and Radiation Safety", Art. 36 to ban import of radioactive west generated in other countries. Georgia also set requirements to return all imported radioactive sources after completion of their using in the country. Therefore the following main routes for radioactive west generation in Georgia can be considered:

1. Demolition of large facilities (Ssuch as nuclear reactor).
2. Renovation of the disposal site (some radioactive waste probably should be retrieved and reprocessed).
3. Generation of new waste due developing of industry and medical application of radioactive sources.
4. Generation of secondary radioactive waste.

Besides of all Disused Radioactive Sources (DSRS) and so-called historical waste should be also considered.

Whole process for handling with radioactive waste can be divided into following three main phases:

1. Establishment of national system for radioactive waste management (elaboration of legal basement, establishment of radioactive waste management agency).
2. Predisposal activity (processing of the waste, preparation of the disposal).
3. Disposing.

According to IAEA radioactive waste classification [3] the maximum level of radioactive waste can be generated at near future is Intermediate Level Waste (ILW); Therefore based on IAEA [4] requirements the following waste framework can be developed (**Table 1**).

Disposal of liquid waste is preferable to conduct after their solidification (immobilization in concrete matrix is one practical way for this). Taking into account limited quantity of DSRS, they can be disposed into depth boreholes. Engineering Barrier System (EBS) for these boreholes should be considered (especially for SHARS).

Based on all above-mentioned the main task is establishment of RWMA, which on behalf of state will operate all radioactive waste management facilities (storage facility, waste processing facility and disposal facility). Functions of RWMA also cover handling with DSRS on all steps and decontamination activity.

Table 1.

Radioactive waste stream		End point						
		Long term Storage (*)	Decay Storage	Surface trench	Engineering surface facility	Intermediate depth facility	Geological disposal	BOSS
VSLV	Low volume	NR	+ +	+	+	NR	NR	NR
	Large volume	NR	+ +	+	NR	NR	NR	NT
VLLV	Low volume	NR	N	+ +	+	NR	NT	NR
	Large volume	NR	N	+ +	+	NR	NT	NT
LLW	Low volume	+	N	+	+ +	+ +	NR	+
	Large volume	+	N	NR	+ +	+ +	NR	NT
ILW	Low volume	+	N	N	N	+ +	NR	+
	Large volume	+	N	N	N	N	NR	N
DSRS	Short lived	+	+	+	+	+	NR	+
	Long lived	+	N	N	N	NR	+ +	+
	SHARS	+	N	N	N	NR	+ +	+
NORM	Low volume	NR	N	+ +	N	+	NR	NR
	Large volume	NR	N	+	NR	NR	NR	NT

(*) Long-term storage is an end point only for radioactive waste stored for decay; otherwise it must be followed by disposal option.

\+ Acceptable solution

++ Preferable solution

N Not possible for safety reason

NT Not possible for technical reason

NR Possible but not recommended for technical or economic reason

BOSS Borehole disposal facility

SHARS Spent sealed high radioactive sources

The main function of RWMA can be defined as followings:

a) To carry out the long term management of radioactive waste according to established safety and security requirements at facilities during their operation or in periods of institutional control including monitoring;

b) To perform ecological rehabilitation of territories contaminated by radionucldes for which the State is responsible or for other territories based on agreement with the organization which has caused the contamination;

c) To transport radioactive waste to its own facilities;

d) To carry out segregation, slection.processing, storage and disposal of radioactive waste;

e) To elaborate and submit to RB working plans based on the followings:

e.a) Periodical and routine monitoring of radioactive waste management facilities;

e.b) Assessment of radioactive waste stream;

e.c) Elaboration and analyze of methods for long-term handling with radioactive waste;

e.e) Systematic analyze of each method taking into account safety requirement, technological issues, their acceptance and cost effectiveness and social factors;

e.f) Defining of best methods by avoiding cost increasing;

e.g) Elaboration of mechanisms for reviewing of working plans;

f) To create radioactive waste inventory;

g) Periodical conducting of Safety Assessment (SA) and preparation of Safety Case (SC) and their submission to RB;

h) Based on the conducted SA defining of Safety Functions (SF) and Safety System Components (SSC);

i) Based on analyze of SF, elaboration of Waste Acceptance Criteria (WAC) and it submission to RB for approval;

j) To elaborate and submit to RB for approval long-term working plan (considering period of the facility operation, its close up or decommissioning);

k) To elaborate and submit to RB for approval working rules (radiation minting, audit, record keeping, acceptance and transfer of waste, emergency response and others).

RWMA should meet all requirements set by IAEA [5].

There are different forms for establishing of RWMA. Taking into account the Georgian reality can be considered two major ones:

1. RWMA under some ministry;
2. Transfer of RWMA function to CSF operator.

The both cases can be briefly analyzed.

The first case

Pros: The agency is comparably independence and focused on its activity.

Cons: Problems with qualified specialist and high cost for equipment.

The second case

Pros: Qualified personnel. the possibility to use technical base of the CSF operator (Dosimeters, laboratories, hot cells, workshops for creation of technical means and others). All of these sufficiently increases the safety level and decreases the cost for RWMA operation. It meets IAEA requirement: "Ensuring that staff are trained, qualified and competent"…).

It should be considered that CSF operator successfully implemented three IAEA projects. Another new IAEA project GEO/9/012 is officially approved and will be implemented soon.

Cons: Subordination to another Ministry.

Financial support to RWMA is very important task. The special, mechanism should be elaborated to support activity of RWMA. Two main financial sources can be considered:

1. State budget;
2. Private finances.

State budget should provide financial support for handling state owned radioactivity. Private sector should pay for handling with waste generated by them (principle – polluter pays). There is also possible existion of two ways for accumulation of finances form private sector:

1. Payment for each action according to defined price list;
2. Establishment of radioactive waste insurance foundation.

Let briefly analyze these two ways.

The first way

Pros: Payment is correctly defined considered chemical-physical characteristic and volume of the waste.

Cons: Payment can be very high and difficult for to conduct for some small enterprises.

The second way

Pros: Payment is not very high and periodically collected form waste potential producers.

Cons: Waste generating organization can be assigned as bankrupt. Payment is not strictly corresponded to the waste volume.

References

1. Principles for Radioactive Waste Management. IAEA Safety Series, 1995, 111–F.
2. Policies and Strategies for Radioactive Waste Management. IAEA Nuclear Energy Series, 2009, NW–G–1.1.
3. Classification Radioactive Waste. IAEA General Safety Guide, 2009, GSG–1.
4. Disposal of Radioactive Waste. IAEA, Specific Safety Requirements, 2011, SSR–5.
5. Predisposal Management of Radioactive Waste. IAEA General Safety Requirements, 2009, GSR–5.

METHOD OF STANDARD DEVIATION FOR ANALYSIS OF HYDROGEODYNAMIC PARAMETER

A. Gevorgyan [1], A. Khangaldyan [2], S. Cth. Mavrodiev [3], M. Adibekyan [1], G. Melikadze [4], A. Sborshchikovi [4], G. Kobzev [4], T. Jimsheladze [4]

[1] SNTO "Western Survey for Seismic Protection"
Yerevan, Armenia
adibekyan@yahoo.com
ani_gevorkjan@mail.ru
[2] "Survey for Seismic Protection" Agency
Mministry of Emergency Situations of of Armenia
Yerevan, Armenia
arminenem@mail.ru
[3] Institute Nuclear Research & Nuclear Energy
Bulgarian Academy of Sciences
Sophia, Bulgaria
schtmavr@yahoo.com
[4] M. Nodia Institute of Geophysics
I. Javakhishvili Tbilisi State University
Tbilisi, Georgia
melikadze@gmail.com
rossoneri08@yandex.ru m

Accepted May 6, 2014

Introduction

Seismological investigations in the Caucasus, and particularly in Armenia, have been conducted since late 21st c. They were related mainly to investigations of strong earthquakes. The regional seismic network of Armenia was a part of the USSR United System of Seismic Observation (USSO). The "Spitak" earthquake showed the necessity of developing the existing seismic network and its technical re-equipment with contemporary high technology equipment and software. After the establishment of National Survey for Seismic Protection (NSSP) of the Republic of Armenia in 1991, new tasks were posed for Armenian seismology, directed to the population protection against strong earthquakes. Since then, the seismic network was being developed through its upgrading and e increase of the number of seismic stations.

Experiment was done for earthquakes in time-series have been studied using the variation of water level in boreholes and earth tidal. Short introduction of method Standard deviation: the signal for imminent increasing regional seismic activity is the hydrogeodynamic

parameter (water level) where is defined as a jump of daily averaged standard deviation function (SDF). Such approach permits to compare by numbers the daily behavior of the hydrogeodynamic field with those in other days. Among the earthquakes occurred on the territory under consideration in certain time period, the "predicted" one is the earthquake with magnitude M and epicenter distance which is identified by the maximum value of the function: The physical meaning of the function is the surface density of earthquakes energy in the point of measurement.

Investigated period of several earthquakes and hydrogeodynamic parameter in Armenia and Georgia. For comparative analysis using data of water level from the network:

Analysis Comparison of ground-water level in borehole "Noemberyan" (Observatory Network, NSSP of Armenia) and "Akhalkalaki" (Water Observatory, DSH Georgia) for "Van" (Turkey, 23.10.2011, $M = 7.2$) [I], "Zaqatala" (Azerbaijan, 07.05.2012, $M = 5.4$) [II], "Mingachevir" (Azerbaijan, 07.04.2013, $M = 3.8$) [III] earthquakes.

I. Van (Turkey, 23.10.2011, $M = 7.2$ (Figure 1))

Figure 1. Map of the epicenters with magnitude $M \geq 3.5$ for time period 01 Sep –f 01 Nov 2011.

On the figures below at the first graph in the left corner is the picture of tidal behavior [m], the next shows the energy (J / km^2), the next – magnitude, and the last describes precursors (red columns) and water level signals (blue points). The blue points has been count using normal standard deviation and the red columns, so-called precursors, were obtained by subtraction of the daily standard deviation of today and the previous day. The first graph in the right corner is water mean during 23 October, the period of great Turkey (Van) earthquake and the next describes standard deviation of water level.

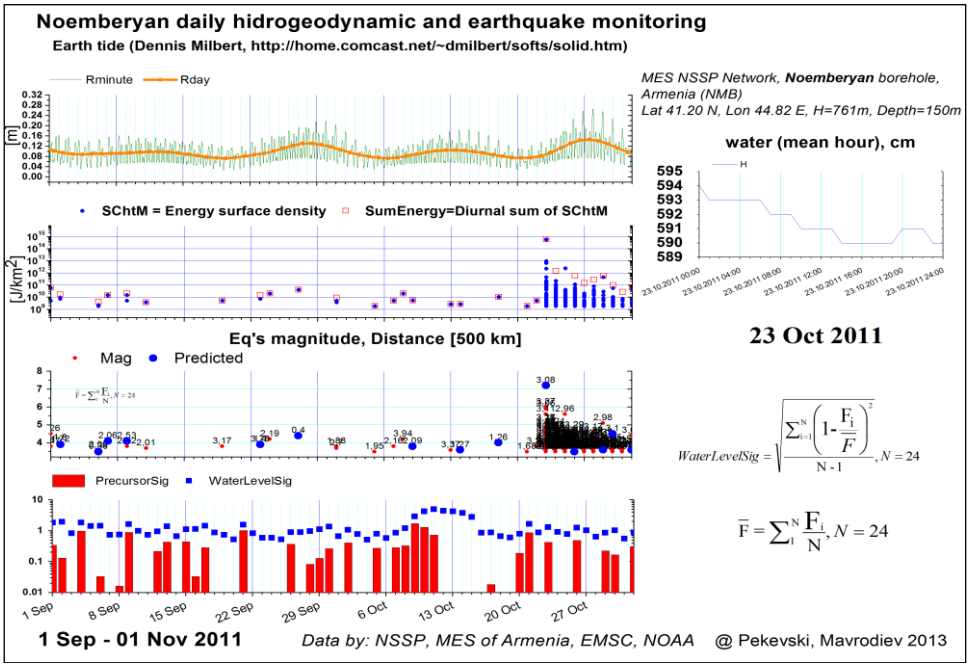

Figure 2. "Noyemberyan" borehole daily monitoring including period of earthquake in Van (2011).

On this figure, on "Noemberyan" borehole during 23 October Turkey (Van) earthquake $M = 7.2$ we can see anomaly, which is expressed by the falling of water level signal during one week before "Van" earthquake (**Figure 2**). The anomaly has place to be during aftershocks too.

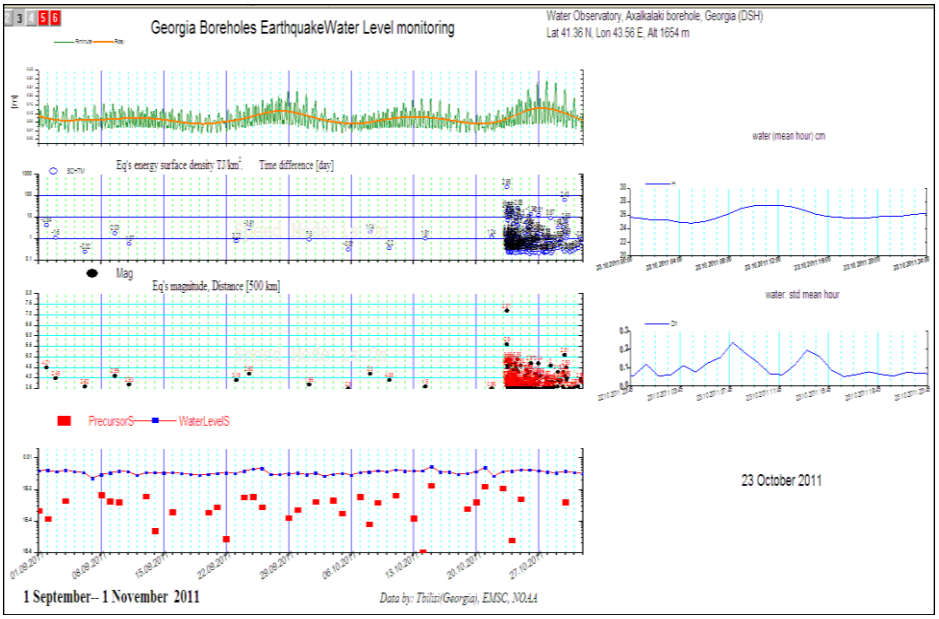

Figure 3. "Akhalkalaki" borehole daily monitoring including period of earthquake in Van (2011).

The same situation is on this figure. Here we have "Akhalkalaki" borehole data for 23 October (**Figure 3**). As we have mentioned above, one week before the earthquake we have the same anomaly at "Akhalkalaki" borehole.

Zaqatala (Azerbaijan, 07.05.2012, $M = 5.4$ (Figure 4))

Figure 4. Map of the epicenters with magnitude $M \geq 3.5$ for time period 01 Apr – 01 Jun 2012.

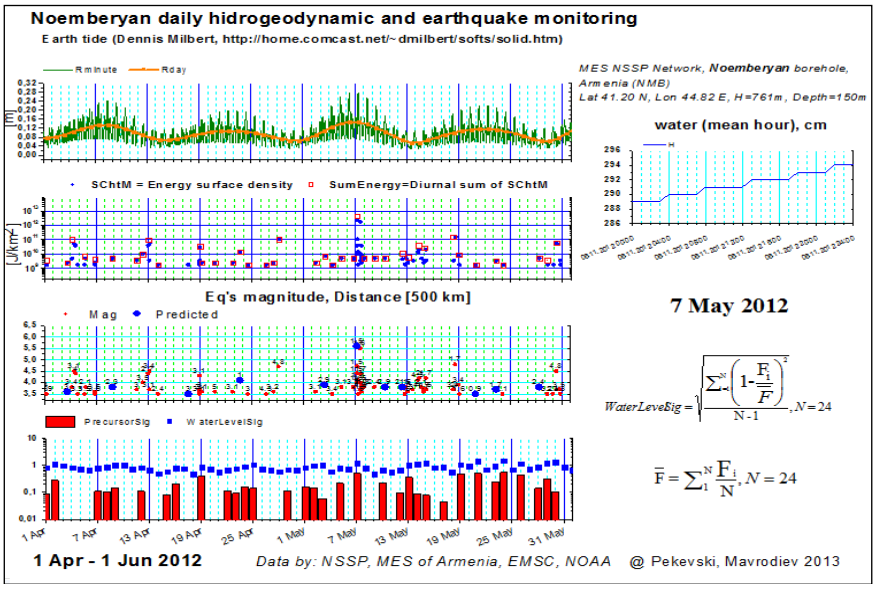

Figure 5. "Noyemberyan" borehole daily monitoring including period of earthquake in Zaqatala (2012).

On this figure, which describes "Noemberyan" borehole during "Zaqatala" earhquake (07.05.2013 $M = 5.4$), we also have an anomaly, which appears in falling of water level signal during 3 days before an earthquake (**Figure 5**). Also the anomaly continues during the earthquake.

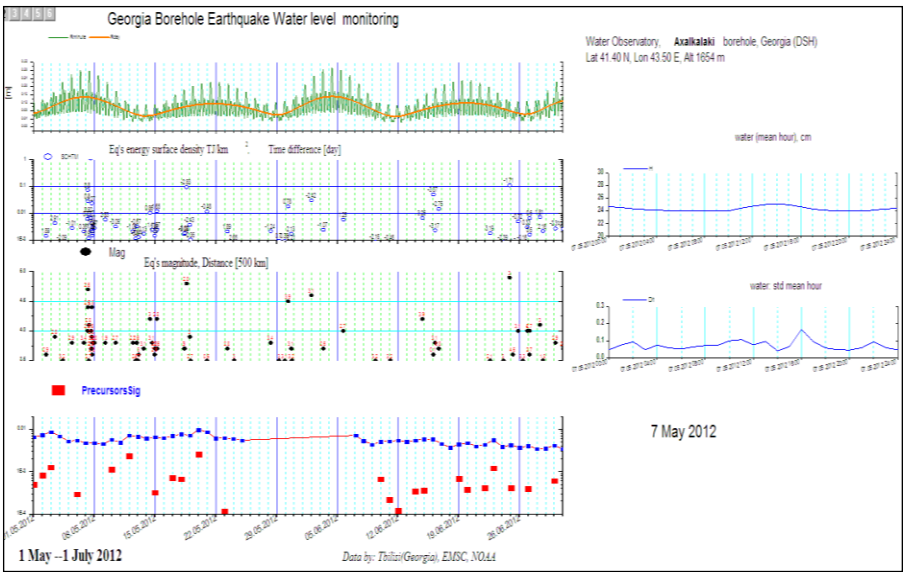

Figure 6. "Akhalkalaki" borehole daily monitoring including period of earthquake in Zaqatala (2012).

The same situation is on "Akhalkalaki" borehole (**Figure 6**). As we see the anomaly starts during 3 days before an earthquake and ends after it.

Mingachevir (Azerbaijan, 07.04.2013, M = 3.8 (Figure 7))

Figure 7. Map of the epicenters with magnitude $M \geq 3.5$ for time period 01 Mar – 01 May 2013.

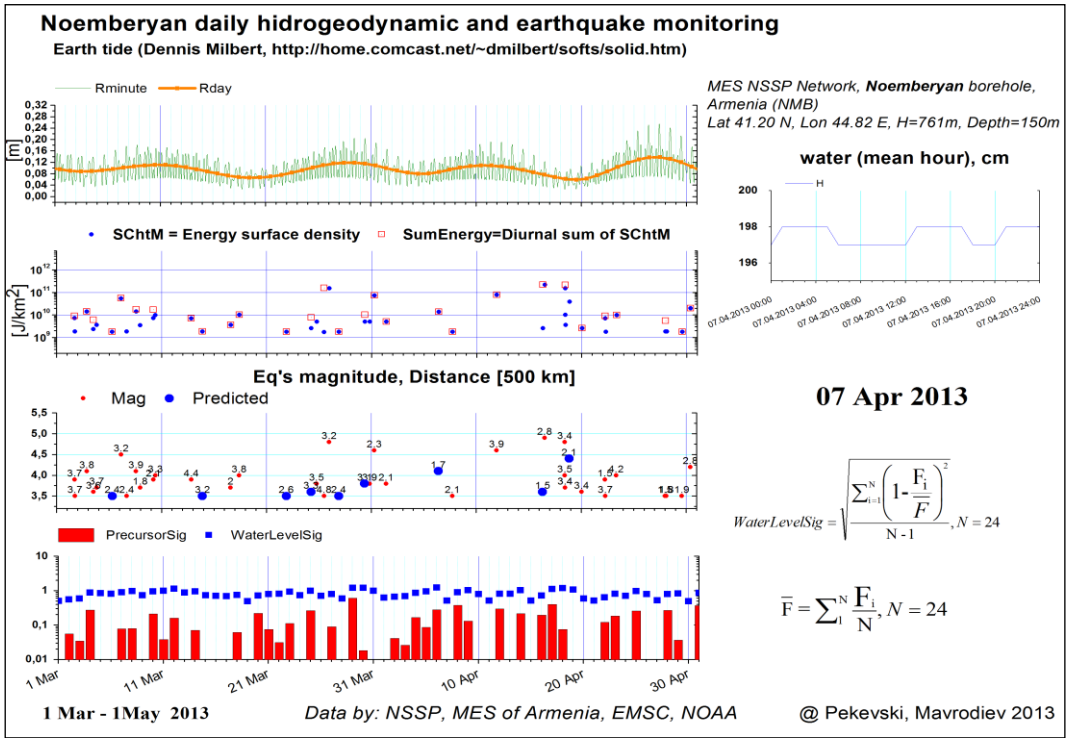

Figure 8. "Noyemberyan" borehole daily monitoring including period of earthquake in Mingachevir (2013).

One more figure of "Noemberyan" borehole for the period of "Mingachevir" earthquake (07.04.2013 $M = 3.8$) has anomaly too (**Figure** 8). We see the growing of water level signal during one week before this earthquake and falling after earthquake.

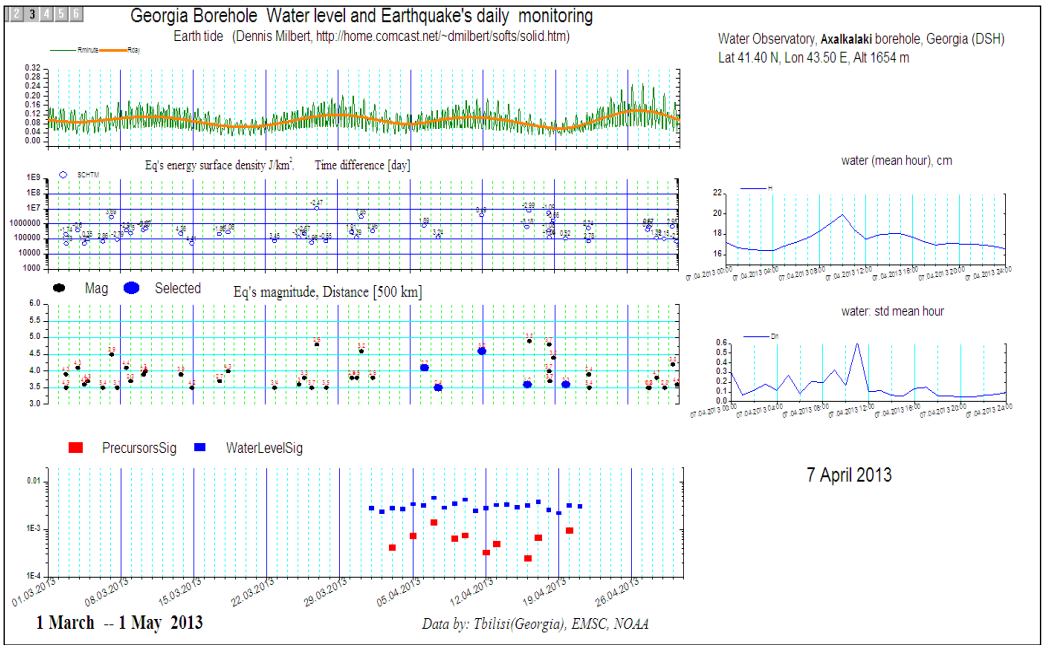

Figure 9. "Akhalkalaki" borehole daily monitoring including period of earthquake in Mingachevir (2013).

The same effect as on "Noemberyan" borehole we have on "Akhalkalaki" well too (**Figure 9**). Growing of water level signal before an earthquake and then falling down after earthquake.

Conclusion

1. Before the earthquake "Van" (Turkey, 23.10.2011, $M = 7.2$), the water level variation in the boreholes "Noemberyan" and "Ahalkalaki" is falling during one week before the earthquake, which means that the expansion process has occurred.
2. The water level variation in boreholes "Noemberyan" and "Ahalkalaki" before the earthquake "Zaqatala" (Azerbaijan, 07.05.2012, $M = 5.4$) also is falling during three days before the earthquake, which means that the expansion process has occurred.
3. The water level variation in boreholes "Noemberyan" and "Ahalkalaki" before the earthquake "Mingachaur" (Azerbaijan, 07.04.2013, $M = 3.8$) is growing during one week before an earthquake and then during it starts to fall down, which means that we have compression process before the earthquake and then expansion process.

The results of the monitoring of water level variation parameter indicated a direct connection between deformation processes to strong earthquakes.

References

1. S. Cht. Mavrodiev, L. Pekevski. On reliability of the geomagnetic quake as regional imminent-earthquake precursor, complex researchof earthquake's forecasting possibilities, seismicity and climate change correlations. In: BlackSeaHazNet Methodological-Coordination Workshop, 2 – 5 May 2011, Republic of Macedonia. 2011, Ohrid,. BlackSeaHazNet Series, 1, 49-63.
2. S. Cht. Mavrodiev, L. Pekevski. On the FP7 BlackSeaHazNet Project and its possible application for harmonic existence of the regions. In: Black Sea Energy Resource Devlopment and Hydrogen Energy Problems, 7 – 10 October 2012. Published in Cooperation with Nato Emerging Security Challenges Division, 2012, Springer, 253-271.
3. T. Jimsheladze, G. Melikadze, G. Kikuashvili, S. Cht. Mavrodiev, L. Pekevski, M. Chkhitunidze. Study of geomagnetic variations in Georgia and establishment the anomaly nature of Eearthquake precursors, complex research of earthquake's forecasting possibilities, seismicity and climate change correlations. In: BlackSeaHazNet Training-Seminar Workshop, 13 – 16 September 2011, Georgia. BlackSeaHazet Series, 2, 2011, Tbilisi, 205-214.
4. G. S. Vartanyan. Regional geodynamic monitoring system for ensuring safety in geological and exploratory production of oil and gas. Izvestia: Atmospheric and Oceanic Physics, 2010, 46, 8, 952-964.

5. С. Ю. Баласанян. Сейсмическая защита и ее организация. 2004, Гюмри: Эльдорадо, 164 -169.
6. A. Sborshchikovi, G. Kobzev, S. Cht. Mavrodiev, G. Melikadze. Boreholes water level and earthquake's daily monitoring. Nano Studies, 2013, 8, 203-212.
7. http://theo.inrne.bas.bg/~mavrodi/everyday_monitoring.html
8. http://www.emsc-csem.org/#2
9. http://home.comcast.net/~dmilbert/softs/solid.htm

MOBILITY OF Cr (VI) BY *Spirulina platensis* AND *Arthrobacter* SPECIES

E. Gelagutashvili, E. Ginturi, A. Rcheulishvili

E. Andronikashvili Institute of Physics
I. Javakhishvili Tbilisi State University
Tbilisi, Georgia
eterige@gmail.com

Accepted July 17, 2014

Introduction

Due to regular interaction, life could sustain on the Planet with a well-organized deposit of minerals. Recently, scientists become more and more interested in the interaction between inorganic molecules and biological species. Studies have found that many microorganisms can produce inorganic nanoparticles through either intracellular or extracellular routes. Sinha & Khare demonstrated that mercury nanoparticles can be synthesized by *Enterobacter sp.* cells [1]. *Pyrobaculum islandicum*, an anaerobic hyperthermophilic microorganism, was reported to reduce many heavy metals including U (VI), Tc (VII), Cr (VI), Co (III), and Mn (IV) with hydrogen as the electron donor [2]. The formation of heavy metallic nanoparticles can be attributed to the metallophilic microorganism's developed genetic and proteomic responses to toxic environments [3]. Heavy metal ions, for example, Hg^{2+}, Cd^{2+}, Ag^{+}, Co^{2+}, CrO_4^{2+}, Cu^{2+}, Ni^{2+}, Pb^{2+}, and Zn^{2+} cause toxic effects to the survival of microorganisms. To counter these effects, microorganisms have developed genetic and proteomic responses to strictly regulate metal homeostasis [4]. The form, when metal partition from aqueous solution onto the mineral surface, a process generally referred to as sorption. Environmental systems are always dynamic and often far from equilibrium. In spite of this, the biotic ligand model assumes that the metal of interest and its complexes are chemical equilibrium with each other and with sensitive sites on the biological surface [5]. Constants for the interaction of the metal with the biological surface have been estimated by measuring metal internalization fluxes, metal loading, and metal toxicity [6]. To develop an efficient biosorbent and its reuse by subsequent desorption processes, knowledge of the mechanism of metal binding is thus very important.

The mobility of Cr (VI) on *Arthrobacter* species and *Spirulina platensis* was examined in this study simultaneous application dialysis and atomic absorption analysis.

Materials and methods

Arthrobacter bacterials were cultivated in the nutrient medium [7]. Cells were centrifuged at 12 000 rpm for 10 min and washed three times with phosphate buffer (pH 7.1). The centrifuged cells were dried without the supernatant solution until constant weight. After solidification (dehydrated) of cells (dry weight) solutions for dialysis were prepared by dissolving in phosphate buffer. This buffer was used in all experiments. *Spirulina platensis* IPPAS B–256 strain was cultivated in a standard Zaroukh alkaline water-salt medium at 34 °C, illumination ~ 5000 lux, initial pH 8.7 and at constant mixing [8]. K_2CrO_4 was analytical grade.

A known quantity of dried bacterium suspension was contacted with solution containing a known concentration of metal ion. For biosorption isotherm studies, the dry cell weight was kept constant (1 mg / ml), while the initial chromium concentration in each sample was varied in the interval (10^{-3} – 10^{-6} M). All experiments were carried out at ambient temperature. Metal was separated from the biomass with the membrane Visking (serva) and analyzed by an atomic absorption spectrophotometer. Dialysis carried out during 72 h.

Data analysis. The isotherm data were characterized by the Freundlich [9] equation $C_b = K C_t^{1/n}$, where C_b is metal concentration adsorbed on either live or dried cells of *bacterium* species in mg g^{-1} dry weight. C_t is the equilibrium concentration of metal (mg l^{-1}) in the solution. K is an empirical constant that provides an indication log C_b as a function of log C_t of the adsorption capacity of either live or dry cells, n is an empirical constant that provides an indication of the intensity of adsorption. The adsorption isotherms were obtained by plotting log C_b as a function of log C_t.

Results and discussions

Cr (VI) uptake by cells of *Spirulina platensis*, *Arthrobacter globiformis* 151B and *Arthrobacter oxidas* 61B was studied as a function of metal concentration. The linearized adsorption isotherms of Cr – bacterium species at room temperature are shown in **Figures 1** and **2** by fitting experimental points. Freundlich parameters evaluated from the isotherms with the correlation coefficients are given in **Table 1**. In **Figure 1**, it is presented biosorption isotherm for Cr (VI) – *Spirulina platensis*. In **Figure 2**, it is presented biosorption isotherms for Cr (VI) – *Arthrobacter globiformis* and Cr (VI) – *Arthrobacter oxidas* for dry (A, B) and living cells (C, D). As shown in **Figures 1** and **2** the adsorption of Cr (VI) in all cases of *Spirulina platensis*, *Arthrobacter* species to living and dry cells was dependent on their concentrations, and thus fitted the Freundlich adsorption isotherm. The correlations between experimental data and the theoretical equation were extremely good, with R above 0.90 (**Table 1**) for all the cases. The higher correlation coefficient show that the Freundlich model is very suitable for describing the biosorption equilibrium of Chromium by the *Spirulina platensis* and *Arthrobacter* species in the studied concentration range. (The constants determined in a given concentration range will not necessarity be the same as constants determined in another concentration range, because each determination will have its own detection window [10].)

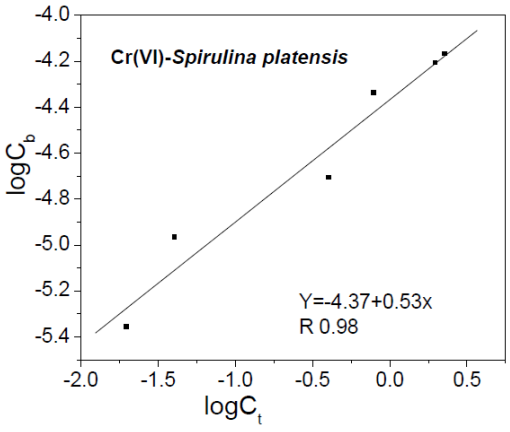

Figure 1. Linearized Freundlich adsorption isotherm for Cr (VI) – *Spirulina platensis*.

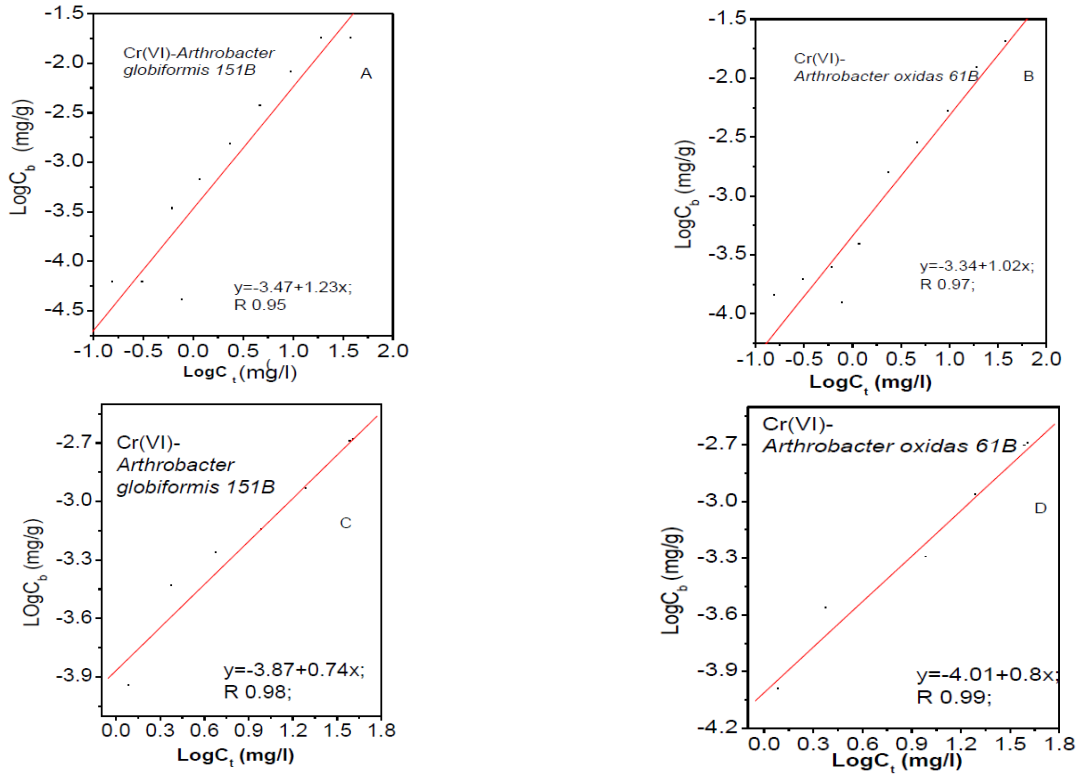

Figure 2. Linearized Freundlich adsorption isotherms of Cr (VI) ion – *Arthrobacter globiformis* and *Arthrobacter oxidas* (A and B – dry cells, C and D – living cells).

Table 1. Biosorption characteristics for Cr (VI) – *Arthrobater Oxidas* 61B, Cr (VI) – *Arthrobacter Globiformis* 151B and Cr (VI) – *Spirulina platensis* at 23 °C.

	Cr (VI)		
Biosorption characteristics	K, $\times 10^{-4}$	n	R
Arthrobater oxidas (dry cells)	4.6	0.98	0.98
Arthrobacter globiformis (dry cells)	3.4	0.81	0.96
Arthrobater oxidas (living cells)	1.0	1.25	0.94
Arthrobacter globiformis (living cells)	1.3	1.35	0.91
Spirulina platensis	0.4	1.89	0.98

The adsorption yields determined for each *Arthrobacter* were compared in **Table 1**. The data in **Table 1** show a significant difference between the binding constants for Cr (VI) – *Arthrobacter oxidas* and Cr (VI) – *Arthrobacter globiformis*. Decrease in bioavailability has been observed experimentally for Cr (VI) – *Arthrobacter globiformis* as compared with *Arthrobacter oxidas*. It is in good agreement, with literatute data by which, there is a large difference in the efficiency of adsorption in each species of microorganisms, since the sorption depends on the nature and the composition of the cell wall [11]. Metal concentrations sorbed by bacterium and those in solution at equilibrium obeyed the Freundlich equation, suggesting the presence of heterogeneous sorption sites on bacterium surfaces. On the other hand, Gram-positive bacteria have a greater sorptive capacity due to their thicker layer of peptidoglycan which contains numerous sorptive sites [12]. It is known, that plasma membrane is the primary site of interaction of trace metal with living organisms. All biological surfaces contain multiple sites including biotic ligands, transport sites, or specific sites and non-specific active sites that are unlikely to participate in the internalization process, including cell wall polysaccharides,

also proteins, and lipids, which act as a basic binding site of heavy metals. Functional groups within the wall provide the amino, carboxylic, sulfydryl, phosphate, and thiol groups that can bind metals [13]. It was shown, that the carboxyl groups were the main binding site in the cell wall of gram positive bacteria [14]. Proceed from the assumption, may be speculate, that first binding sites for Cr (VI) on the surface of *Arthrobacter* species are carboxyl groups. Our results indicated that Cr (VI) sorption is depended of species of bacterial *Arthrobacter*. Differences between *Arthrobacter* species in metal ion binding may be due to the properties of the metal sorbates and the properties of bacterium (functional groups, structure and surface area, depending on the species). Functional groups, such as amino, carboxylic, suphydryl, phosphate and thiole groups, differ in their affinity and specifity for metal binding. *n* values which reflects the intensity of sorption presents the same trend but, as seen from table 1 for both *Arthrobacter* species *n*-values are not significantly different and their sorption intensity indicator are generally small. Comparative Freundlich biosorption characteristics Cr (VI) – *Arthrobacter* species of living and dry cells are shown (**Table 1**) that *n*-values are in both cases nearly the same. Dry cells have larger biosorption constant for both species ($K = 4.6 \cdot 10^{-4}$, $3.4 \cdot 10^{-4}$), than living cells ($1.0 \cdot 10^{-4}$, $1.36 \cdot 10^{-4}$). This may confirm the hypothasis that metal sorption by this bacterium is independent of the metabolic state of the organism [15]. In regard to *Spirulina platensis* biosorption constant for Cr (VI) – *Spirulina platensis* is small.

Thus, different species of bacterium displayed a different sorptive relationship. Biosorption is often followed by a slower metal binding process in which additional metal ion is bound, often irreversibly. This slow phase of metal uptake can be due to a number of mechanisms, including covalent bonding, crystallization on the cell surface or, most often, diffusion into the cell interior and binding to proteins and other intercellular sites [16].

References

1. A. Sinha, S. K. Khare. Biores. Technol., 2011, 102, 4281-4284.
2. K. Kashefi, D. R. Lovley. Appl. Environ. Microbiol., 2000, 66,1050-1056.
3. F. Reith, M. F. Lengke, D. Falconer, D. Craw, G. Southam. ISME J., 2007, 1, 567-584.
4. D. H. Nies. Appl. Microbiol. Biotechnol., 1999, 51, 730-750.
5. V. I. Slaveykova, K. J. Wilkinson. Environ.Chem., 2005, 2, 9-24.
6. M. Ghaedi, E. Asadpour, A. Vafaie, Spectrochim. Acta A, 2006, 63, 182-188.
7. N. Ya. Tsibakhashvili, L. M. Mosulishvili, T. L. Kalabegishvili, D. T. Pataraya, M. A. Gurielidze, G. S. Nadareishvili, H.-Y. Holman. Fresenius Environ. Bull., 2002, 11, 352-361.
8. L. Mosulishvili, A. Belokobilsky, E. Gelagutashvili, A. Rcheulishvili, N. Tsibakhashvili. Proc. Georg. Acad. Sci. (Biol. Ser.), 1997 23, 1997, 105-113.
9. H. Freundlich. Phys. Chem., 1906, 57, 384-410.
10. R. M. Town, M. Filella. Limnol. Oceanogr., 2000, 45, 1341-1357.
11. O. Hammouda, A. Gaber, N. Raouf–Abdel. Ecotoxicol. Environ. Safety, 1995, 31, 205-210.
12. E. D. van Hullebusch, M. H. Zandvoort, P. N. L. Lens. Rev. Environ. Sci. Bio. Technol., 2003, 2, 9-33.
13. Y. P. Ting, F. Lawson, I. G. Prince. Biotechnol. Bioeng., 1991, 37, 445-455.
14. C. Cervantes, J. Campus–Garcia, S. Davars, F. Gutierrez–Corona, H. Loza–Tavera, J. C. Torres–Guzman, R. Moreno–Sanches. FEMS Microbiol. Rev., 2001, 25, 335-347.
15. D. L.. Parker, L. C. Rai, N. Mallick, P. K. Rai, H. D. Kumar. Appl. Environ. Microbial., 1998, 64, 1545-1547.
16. H. B. Xue, L. Sigg. Water Res., 1990, 22, 917-926.

ОБЕЗЗАРАЖИВАНИЯ ПИТЬЕВОЙ ВОДЫ ОТ ПОСЛЕДСТВИЙ АНТРОПОГЕННЫХ И СТИХИЙНЫХ БЕДСТВИЙ МЕТОДОМ НАНОТЕХНОЛОГИИ

Д. В. Эристави, Н. Ш. Бибилури, Ш. Н. Андгуладзе, А. Р. Гогишвили, М. К. Гугешидзе, Е. Л. Мацаберидзе, З. Л. Мацаберидзе

Грузинский технический университет
Тбилиси, Грузия
deristavi@hotmail.com

Принята 18 октября 2014 года

Коллоидное серебро – продукт нанотехнологий, состоящий из микроскопических частиц серебра, взвешенных в деминерализованной и деионизированной воде. Этот продукт высоких научных технологий производится электролитическим методом [1].

Проблема бактериального загрязнения питьевой воды остро стоит повсеместно. Получение безопасной питьевой воды всегда являлось не простой задачей. Особенно усложняется проблема при отсутствии централизованного водоснабжения, обеспечивающего высокое качество воды за счет сложной и дорогостоящей аппаратуры и квалификации обслуживающего персонала. Применяемые при этом хлор, фтор, озон в переизбытке так же наносят вред потребителям воды.

В полевых условиях для получения питьевой воды не достаточно профильтровать воду взятую из родника, колодца или любого другого природного источника воды. Кипячение не всегда возможно и часто не достаточно для обеззараживания воды. Применяемые дезинфицирующие концентраты (порошковые или таблетированные), при повторном и частом употреблении воды с ними, могут привести к тяжелым последствиям. В мирных условиях применение таких препаратов недопустимо.

Использование серебра для обеззараживания воды не только увеличивает арсенал существующих реагентов, но и является одним из наиболее эффективных методов дезинфекции и консервирования питьевой воды. В настоящее время коллоидное серебро с успехом применяется на кораблях, в плавательных бассейнах, в полевых условиях и т.п., а так же тогда, когда хлор при взаимодействии с применением воды даёт токсические или сильно пахнущие соединения.

На сегодняшний день этот метод применяется в России на Украине, в США, Англии, Швейцарии, ФРГ, Чехии, Франции и других странах.

С Этой целью создаются во многих странах генераторы коллоидного серебра, как для применения в промышленных целях (плавательные бассейны, морские суда, авиация и космонавтика), так и для индивидуального применения в быту. Однако, все эти генераторы коллоидного серебра довольно сложны в эксплуатации и дорогостоящи.

Коллоидное серебро по бактерицидным свойствам в разы выше других известных и применяемых веществ [2, 3], поэтому разработка приборов для получения коллоидного серебра является своевременным и важным. Планируется спроектировать и изготовить опытные образцы четырех типов простых в эксплуатации и главное дешёвых приборов:

1. Прибор индивидуального использования в полевых условиях для нужд туристов, командированных, армии и т.д., для обработки коллоидным серебром не менее 15 000 литров воды, с автономным питанием от аккумуляторов или пальчиковых батареек;
2. Прибор для семейного использования, непосредственно надевающиеся на любой кухонный кран для обработки 150 000 литров воды с применением аккумулятора;
3. Прибор для использования в объектах общепита, так же надеваемый на кран любой конструкции, для обработки 1 500 000 литров воды;
4. Прибор для обеспечения питьевой водой населения, могущий очистить и обеззаразить в сутки не менее 90000 литров питьевой воды.

Целью нашего исследования являлось, кроме разработки этих приборов и, в конечном счете, их производства, изучить влияние деиствия ионов серебра на неорганические вещества в питьевой воде г. Тбилиси [4]. Нами также, создан электролизер, для получения концентрата раствора коллоидного серебра в воде, предназначающийся для различных целей в том числе и медицинских.

Получение водных растворов ионов коллоидного серебра основано на электролитическом методе – пропускании постоянного электрического тока через погруженные в воду электроды. При этом серебряный электрод (анод), растворяясь, насыщает воду ионами серебра Ag^{+}. Концентрация получаемого раствора зависит от силы тока, времени работы источника тока и объема обрабатываемой воды [5].

Ссылки

1. Биозащита: www.bio.su/page
2. Л. А. Кульский. Серебряная вода. 1977, Киев: Наукова думка.
3. Коллоидное серебро: www.silver-maks-kolloidnoe.html
4. Н. Ш. Бибилури, Н. Г. Чхубианишвили, Ш. Н. Андгуладзе, Д. В. Эристави, А. Р. Гогишвили, Н. А. Куциава, М. Л. Кавтарадзе. Разработка приборов для обеззараживания питьевой воды ионами серебра и определение влияния коллоидного серебра на основные неорганические анионы в питьевой воде г. Тбилиси. В сб.: Труды Междунар. научно-тех. конф. «Устойчивое развитие и охрана окружающей среды». 2010, Тбилиси: Изд. дом Техни. унив., 48-51.
5. Серебряная вода: www.zen-zen.ru/catalogue/.../servodgeorg/

ვაკუუმური ВУ–1А ტიპის დანადგარის მოდერნიზაცია მრავალშრიანი პერიოდული სტრუქტურის მქონე ოპტიკური დანაფარების მისაღებად

ზ. ვ. ბერიშვილი, ი. ი. კორძახია, დ. გ. ზარდიაშვილი,
გ. გ. აბრამიშვილი, ი. მ. ავალიანი, დ. მ. შალამბერიძე, ი. დ. ივანიძე

სსიპ ინსტიტუტი "ოპტიკა"
თბილისი, საქართველო
zaurberi7@yahoo.com

მიღებულია 2014 წლის 20 ოქტომბერს

მრავალშრიანი პერიოდული სტრუქტურის მქონე ოპტიკური დანაფარების, კერძოდ, ოპტიკურ დეტალებზე გაშუქოვნების ფენების მისაღებად საჭიროა, სპექტრის მოცემულ უბანში სხვადასხვა გარდატეხვის მაჩვენებლების და მინიმალური ოპტიკური დანაკარგების მქონე თხელფენოვანი დიელექტრიკული შრეების დაფენა. ამ შემთხვევაში თხელფენოვანი დიელექტრიკული მასალების ვარგისიანობის ძირითადი პარამეტრებია: გამჭვირვალობა, გარდატეხვის მაჩვენებელი, ერთგვაროვნება, სიმკვრივე, ადგეზია, სისალე, მექანიკური დაძაბულობა, მდგრადობა გარემოს ზემოქმედების მიმართ და სხვა. სხივური დანაკარგები – შთანთქმა და გაბნევა – დიელექტრიკულ ფირებში, რომლებიც გამოიყენება გაშუქოვნებისათვის, უნდა იყოს მინიმალური. მრავალშრიან დანაფარებში თითოეული ფენის შთანთქმის კოეფიციენტი k არ უნდა აღემატებოდეს $1 \cdot 10^{-2}$. თხელფენოვანი დიელექტრიკული შრეების ოპტიკური თვისებები მნიშვნელოვნადაა დამოკიდებული მათი მიღების მეთოდებზე და ტექნოლოგიურ რეჟიმებზე, როგორებიცაა: ოპტიკური დეტალების ტემპერატურა, დაფენის სიჩქარე, ნარჩენი წნევა ვაკუმურ კამერაში და სხვა. დაფენის პრიცესში დიელექტრიკული შრეების ოპტიკურ თვისებებზე გავლენას ახდენს აგრეთვე დასაფენი ოპტიკურ დეტალის მასალა, ჩვენს შემთხვევაში – ოპტიკური პოლიმერი. აღნიშნული მასალის თვისებების გათვალისწინებით სასურველი და აუცილებელიცაა დაფენის პროცესების მართვა მაღალი განმეორადობით, რომელიც უზრუნველყოფს მაღალი ხარისხის ფუნქციონალური დანაფარების მიღებას.

შრომაში [1] მოყვანილია 200-ზე მეტი ნივთიერება, რომლებიც გამოიყენება თხელფენოვანი ოპტიკური დიელექტრიკული შრეების მისაღებად. ამათგან ელექტრომაგნიტური გამოსხივების სპექტრის ოპტიკურ დიაპაზონში გამოიყენება დაახლოებით 20 ნივთიერება. ამ ნივთიერებებიდან მაღალი ხარისხის მრავალშრიანი პერიოდული სტრუქტურების მქონე ოპტიკური დანაფარების მისაღებად ჩვენს მიერ შერჩეული იქნა სილიციუმის ორჟანგის (SiO_2) და ცირკონიუმის ორჟანგის (ZrO_2) მასალების თხელი შრეები. აღნიშნული მასალებისგან ფორმირებულ დიელექტრიკულ შრეებს გააჩნიათ მაღალი მექანიკური სიმტკიცე და ქიმიური სტაბილურობა. ისინი ხასიათდებიან მაღალი გამჭვირვალობით ხილული სპექტრის მიმართ. ამ წყვილს, სპექტრის ინფრაწითელ დიაპაზონში გარდატეხვის მაჩვენებლების ერთმანეთისაგან

მცირე განსხვავებისა და შესაბამისი სქელი შრეების ძლიერი მექანიკური დაძაბულობის არსებობის გამო პრაქტიკულად არ იყენებენ.

მიუხედავად ამისა, დიელექტრიკული შრეების ეს წყვილი ხშირად გამოიყენება მრავალშრიანი პერიოდული სტრუქტურების მქონე ოპტიკური დანაფარების მისაღებად, რომლებიც ერთნაირი წარმატებით მუშაობენ როგორც ხილულ, ისე ახლო ინფრაწითელი სპექტრის არეში.

ცნობილია, რომ ვაკუუმში გაფრქვევის თერმულ მეთოდებთან (მაგალითად: თერმული (რეზისტიული) აორთქლება, ელექტრონულ-სხივური და ლაზერული აორთქლება) შედარებით, მაგნეტრონულ-პლაზმური გაფრქვევის მეთოდებს გააჩნიათ მთელი რიგი უპირატესობები. ასე მაგალითად, ოპტიკური დეტალების ზედაპირზე დაცემისას გაფრქვეული ნაწილაკების საშუალო კინეტიკური ენერგია გაცილებით მეტია ვიდრე ზემოთ ჩამოთვლილი თერმული მეთოდების შემთხვევაში, ეს მნიშვნელოვან გავლენას ახდენს მიღებული ფირების სისალეზე, ადგეზიურობაზე და მათ სიმკვრივეზე. მიღებულ დანაფარებს გააჩნიათ ძალიან წვრილი საკუთარი ზედაპირის სიმქისე და, რაც მთავარია ჩვენი ამოცანებისათვის, შესაძლებელია დიელექტრიკული შრეების მიღება დაბალტემპერატურული ტექნოლოგიურ რეჟიმებში.

მოკლედ განვიხილოთ მაგნეტრონული გაფრქვევის მოწყობილობის ფიზიკური საფუძვლები [2]. ჯვარედინა ელექტრული და მაგნიტური ველების გამოყენება პლაზმაში ელექტრონების ჩაკეტილი სპირალური მრუდის სახის ტრაექტორიების ფორმირებისათვის. მაგნიტური ველი, რომლის ძალწირები გასაფრქვევი სამიზნის ზედაპირის პარალელურია, აკავებს ელექტრონებს უშუალოდ სამიზნის მახლობლობად ჯვარედინი ელექტრული და მაგნიტური ველებით შექმნილ ე.წ. ელექტრონების "ხაფანგში". ელექტრონების ოსცილაცია და მათი მოძრაობა სპირალურ ტრაექტორიებზე ზრდის იონიზირებადი დაჯახებების რიცხვს, რის შედეგადაც იზრდება პლაზმის სიმკვრივე, რომლის ზემოქმედება სამიზნეზე უზრუნველყოფს სამიზნის მასალის გაფრქვევის მაღალ სიჩქარეს. მაგნეტრონული გაფრქვევის მოწყობილობის განსხვავებულ თავისებურებას წარმოადგენს პლაზმის დიდი კონცენტრაცია უშუალოდ გასაფრქვევი სამიზნის მახლობლობაში, რაც გამოწვეულია მაგნიტური ველის არსებობით. ამ მიზეზით ელექტრონები ვერ აღწევენ დასაფენ ოპტიკურ დეტალებამდე, რაც იცავს ამ დეტალებს ზედმეტი გადახურებისაგან. აღნიშნულ მეთოდს გააჩნია მთელი რიგი უპირატესობები, კერძოდ: შესაძლებელია ლითონების, ნახევარგამტარების, დიელექტრიკების, ოქსიდების, ნიტრიდების და სხვა თხელფენოვანი დანაფარების მიღება კარგი ადგეზიითა და ფიზიკო-ქიმიური თვისებებით, ამასთან, არ ხდება ეკოლოგიურად მავნე ნივთიერებების გამოყოფა. აგრეთვე, მეთოდს არ გააჩნია ეკოლოგიურად მიუღებელი ნივთიერებების ნარჩენები.

წარმოდგენილი სამუშაოს მიზანია მაგნეტრონული გაფრქვევის ექსპერიმენტალურ-ტექნოლოგიური დანადგარის შექმნა ვაკუუმური ВУ–1А ტიპის დაფენის დანადგარის მოდერნიზაციის გზით, რაც უზრუნველყოფს ოპტიკურ დეტალებზე მრავალშრიანი პერიოდული სტრუქტურის მქონე ოპტიკური დანაფარების მიღებას ერთიან ტექნოლოგიურ ციკლში. აღნიშნული დანადგარის დანიშნულებაა ოპტიკურ დეტალებზე გაშუქოვნების ფენების მიღების ოპტიმალური ტექნოლოგიების დამუშავება და მიღებული შრეების გამოყენება სხვადასხვა კვლევებში, ოპტიკური ხელსაწყოების საწარმო ნიმუშების დამზადებასა და პერსპექტივაში, მათი მცირე წარმოებაში.

ვაკუუმური დანადგარის ხუფქვეშა მოწყობილობის კონსტრუქციის დაგეგმარებისას ჩვენი მთავარი მოთხოვნა იყო მაგნეტრონული გაფრქვევის ორი მოწყობილობის და მბრუნავ დისკოზე დამაგრებული დასაფენი ოპტიკური დეტალების განლაგების ისეთი გეომეტრიის განსაზღვრა, რომელიც უზრუნველყოფდა ოპტიკური დეტალების დაფარვას ერთნაირი სისქის ფენით.

ვაკუუმური დანადგარის ხუფქვეშ მაგნეტრონული გაფრქვევის ორი მოწყობილობის, მბრუნავი დისკოს და მასზე განლაგებული ოპტიკური დეტალების დამჭერის მქონე ნახვრეტები (ათი პოზიცია), უძრავ დისკოზე განლაგებული ნახვრეტები (2 პოზიცია) და მაგნეტრონების საფარის ოპტიმალური განლაგება შესრულებულია კონსტრუირების 3D ფორმატში. ამან მოგვცა აღნიშნული დეტალების ვაკუუმური დანადგარის ხუფქვეშ კომპაქტურად განლაგების შესაძლებლობა და რაც ერთ-ერთი წინაპირობაა იმისა, რომ, დიდი წარმადობით, ერთიან ვაკუუმურ ციკლში განხორციელდეს ოპტიკური დეტალებზე მაღალი ხარისხის გაშუქოვნების შრეების მიღება.

დასმული ამოცანის განსახორციელებლად შესრულდა შემდეგი სამუშაოები:

- ვაკუუმური დანადგარის ხუფქვეშ ჩვენს მიერ კონსტრუირებული და დამზადებული გადამყვანების და ვაკუუმური განმხოლოებების გამოყენებით დამონტაჟდა პლანარული მაგნეტრონული გაფრქვევის ორი მოწყობილობა. დამონტაჟებული მაგნეტრონები წარმოადგენენ კლასიკურ პლანარული მაგნეტრონული გაფრქვევის მოწყობილობებს, წყლის გაცივების სისტემით და 100 მმ დიამეტრის სამიზნით;
- ორივე მაგნეტრონული გაფრქვევის მოწყობილობისთვის დამონტაჟებულია საფარი;
- ვაკუუმური ხუფის ზედა ნაწილზე ჩვენს მიერ კონსტრუირებული და დამზადებული გადამყვანის და ვაკუუმური განმხოლოებების გამოყენებით დამონტაჟდა RGA 200 ტიპის კვადრუპოლური მას-სპექტრომეტრი [3];
- განხორციელდა აირის სისტემის კონსტრუირება, დამზადება და მონტაჟი;
- დამზადდა მუდმივი და იმპულსური ძაბვის კვების ბლოკები და მაღალი ძაბვის გადამრთველის (RFDC “PlasmaSwitch”) გამოყენებით მიეერთდა მაგნეტრონული გაფრქვევის მოწყობილობას.

ხშირ შემთხვევაში, მიღებული დანაფარების ხარისხი დამოკიდებულია არა მარტო ვაკუუმური სისტემის და მაგნეტრონული გაფრქვევის მოწყობილობების მახასიათებლებზე, არამედ მათი კვების ბლოკზეც, განსაკუთრებით მაშინ, როცა საქმე გვაქვს რეაქტიულ მაგნეტრონულ გაფრქვევასთან და გვინდა მივიღოთ სილიციუმის ორჟანგი (SiO_2). ამ შემთხვევაში მუდმივი კვების წყაროს გამოყენებისას პლაზმაში გარკვეული სიხშირით წარმოიქმნება მცირე სიდიდის რკალური განმუხტვები, რაც ართულებს ტექნოლოგიურ პროცესის კონტროლს და უარყოფითად მოქმედებს მიღებული შრეების ხარისხზე. თუ მაგნეტრონული გაფრქვევის მოწყობილობაზე ნაცვლად მუდმივი ძაბვისა მოვდებთ იმპულსურ ძაბვას, მისი სიხშირის გაზრდისას რკალური განმუხტვები კლებულობს და 50 – 60 კჰც სიხშირის ზევით საერთოდ ქრებიან.

ამის გათვალისწინებით ჩვენი მაგნეტრონების ელექტრომომარაგების სისტემა შედგება ორი ავტონომიური ბლოკისაგან. ერთი, მუდმივი ძაბვის კვების ბლოკი, რომელსაც შეუძლია უზრუნველყოს ძაბვა 800 ვ, დენით 1.5 ამპერამდე. და მეორე, რეაქტიული გაფრქვევების რეჟიმებისათვის, იმპულსურ ძაბვის კვების ბლოკი

(სიხშირით 50 – 100 კჰც). აღნიშნული სისტემა იძლევა საშუალებას მიეწოდოს მუდმივი ან იმპულსური ძაბვები ორივე მაგნეტრონული გაფრქვევის მოწყობილობებს და უზრუნველყოს მათი როგორც ერთდროული, ისე ცალცალკე მუშაობის რეჟიმი.

როგორც ცნობილია [4], ვაკუუმური დანადგარის ხუფქვეშ ნარჩენი გაზების მთლიანი წნევის გაზომვა არ არის საკმარისი დაგეგმილი ტექნოლოგიური ამოცანების გადასაჭრელად. ჩვენს შემთხვევაში აუცილებელია არა მარტო ხუფქვეშ არსებული ნარჩენი გაზების შემადგენლობის ცოდნა, რომლის გარემოში მიმდინარეობს ტექნოლოგიური პროცესები, არამედ ამ შემადგენლობის კონტროლიც.

ვაკუუმური სისტემის ხუფქვეშ ნარჩენი გაზების შემადგენლობა განისაზღვრება ტუმბოების სისტემების მახასიათებლებით, ვაკუუმური ხუფის კედლების და ხუფქვეშ დამონტაჟებული კონსტრუქციების გაუაირიანების ხარისხით, დასაფენი ობიექტის შემადგენლობით და მიწოდებული გაზების სისუფთავით. გარდა ამისა, ნარჩენი გაზების შემადგენლობების ანალიზით შესაძლებელია დადგინდეს ნორმებიდან გადახრის ძირითადი მიზეზი. მაგალითად, ვაკუუმური სისტემის გერმეტიზაციის დარღვევა. ჩვენს შემთხვევაში ვაკუუმურ ხუფქვეშ პარციალური წნევის გასაზომად გამოიყენება, ჩვენს მიერ დამონტაჟებული RGA 00 ტიპის ნარჩენი გაზების ანალიზატორი.

მუშა აირის (ინერტული და რეაქტიული) ნაკადის ავტომატური მართვის და რეგულირების მოწყობილობა AALBORG (ორი კომპლექტი) ჰერმეტულად მიერთებულია, ერთი მხრივ, მაგნეტრონული გაფრქვევის მოწყობილობებთან უშუალოდ გაფრქვევის ზონაში (რეაქტორში), ხოლო მეორე მხრივ, აირის სისტემასთან და შემდეგ არგონის და ჟანგბადის ბალონებთან შესაბამისად, ისე, როგორც **ნახაზზე 1** არის ნაჩვენები.

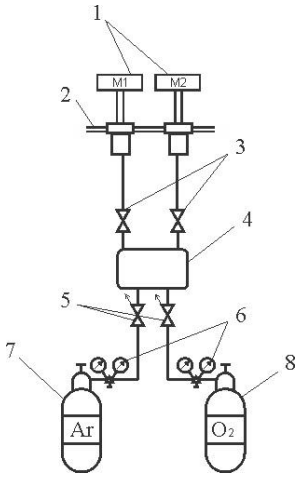

ნახაზი 1. მოდერნიზირებული ვაკუუმური ВУ–1А ტიპის დანადგარის აირის სისტემის სქემა: 1 – M_1 და M_2 პლანარული მაგნეტრონული გაფრქვევის მოწყობილობები; 2 – ვაკუუმური ხუფქვეშა ფილა; 3 – ვაკუუმური ონკანი; 4 – აირების შერევის რეზერვუარი; 5 – AALBORG ტიპის აირის ნაკადის ავტომატიური მართვის და რეგულირების მოწყობილობა; 6 – რედუქტორი; 7 – არგონის ბალონი; 8 – ჟანგბადის ბალონი.

აღნიშნული სქემა საშუალებას იძლევა მაგნეტრონული გაფრქვევის მოწყობილობების რეაქტორს მიეწოდოს, როგორც მხოლოდ ერთი აირი (მაგალითად,

Ar), ასე ორი აირის ნარევი (მაგალითად, Ar და O_2) მათი კონტროლირებადი შემცველობით. ჩვენს მიერ კონსტრუირებული და დამზადებული სისტემა უზრუნველყოფს რეაქტორში აირების – არგონის და ჟანგბადის – სასურველ პარციალური წნევების რეგულირებას ხელსაწყოზე ფიქსირებული მნიშვნელობის ± 1 % სიზუსტით.

მრავალშრიანი პერიოდული სტრუქტურის მქონე ოპტიკური დანაფარების მიღების ვაკუუმური ВУ–1А ტიპის დაფენის მოდერნიზირებული დანადგარის კონსტრუქცია მოყვანილია ნახაზზე 2.

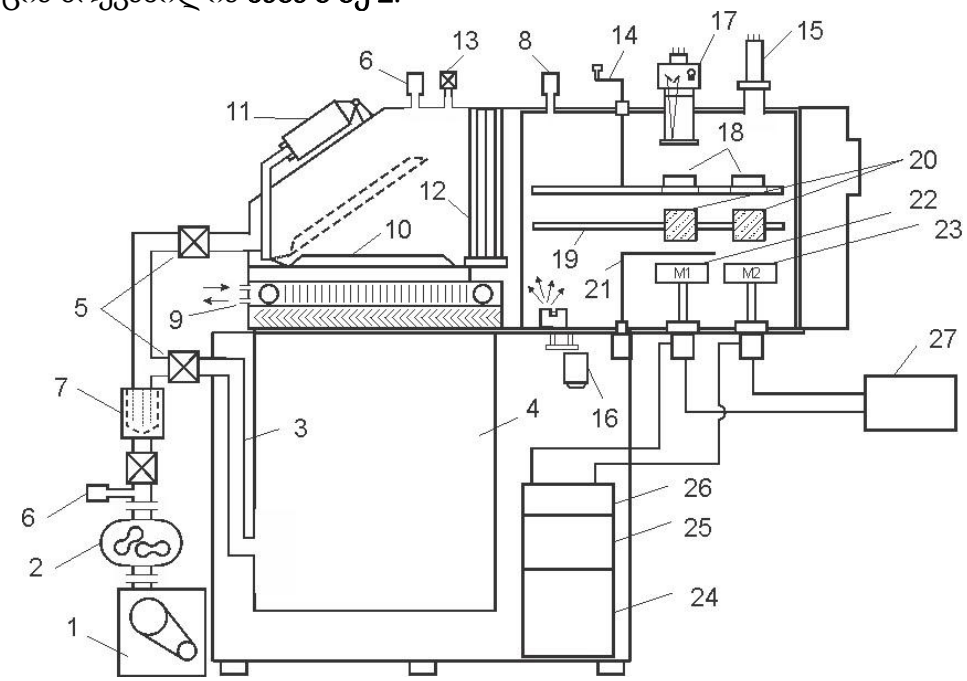

ნახაზი 2. ვაკუუმური ВУ–1А ტიპის დაფენის მოდერნიზირებული დანადგარის კონსტრუქცია: 1 – ფორვაკუუმური ტუმბო; 2 – ორროტორიანი ტუმბო; 3 – ფორვაკუუმური გამოტუმბვის ხაზი; 4 – დიფუზიური ტუმბო; 5 – ფორვაკუუმური სარქველები; 6 – თერმოწყვილური წნევის გადამწოდი; 7 – სორბციული ჩამჭერი; 8 – მაღალი ვაკუუმის გადამწოდი; 9 – კრიოგენული ჩამჭერი; 10 – მაღალვაკუუმური საკეტი; 11 – საკეტის ჰიდროამძრავი; 12 – დამცავი ცხაურა; 13 – ჰაერის შემშვები სარქველი; 14 – დასაფენი ობიექტის ბრუნვის ამძრავი; 15 – კვადრუპოლური მასსპექტრომეტრი; 16 – ტიგელის ამძრავი (დაკონსერვებულია); 17 – სპექტროფოტომეტრი (დაკონსერვებულია); 18 – მბრუნავი დისკო ოპტიკური დეტალების დამჭერით; 19 – უძრავი დისკო; 20 – ცილინდრული ეკრანი; 21 – საფარი; 22 – M_1 პლანარული მაგნეტრონული გაფრქვევის მოწყობილობა სილიკონის სამიზნით; 23 – M_2 პლანარული მაგნეტრონული გაფრქვევის მოწყობილობა ცირკონიუმის სამიზნით; 24 – მუდმივი ძაბვის კვების ბლოკი; 25 – იმპულსურ ძაბვის კვების ბლოკი; 26 – მაღალი ძაბვის გადამრთველის (RFDC “PlasmaSwitch”), 27 – აირის სისტემის სქემა.

ვაკუუმური ВУ–1А ტიპის დაფენის დანადგარის ხუფქვეშ მაღალი წნევის მისაღებად სისტემაში ჩართულია ფორვაკუუმური ტუმბო (1), ორროტორიანი ტუმბო (2), რომელიც ფორვაკუუმური გამოტუმბვის ხაზით (3), სორბციული ჩამჭერით (7) და ფორვაკუუმური სარქველებით (5) მიერთებულია დიფუზიურ ტუმბოსთან. მაღალვაკუუმური საკეტი (10) საკეტის ჰიდროამძრავით (11) უზრუნველყოფს

დიფუზიური ტუმბოს დაცვის ცხაურას (12) გავლით დაფენის ვაკუუმურ ხუფთან ჰერმეტიულ მიერთებას და განმხოლოებას. სორბციული ჩამჭერი (7) და კრიოგენული ჩამჭერი (9) ზღუდავენ ტუმბოებიდან დაფენის ვაკუუმურ ხუფქვეშ ზეთის ნაწილაკების მოხვედრას. წნევის თერმოწყვილური გადამწოდების (6) და წნევის მაღალვაკუუმური გადამწოდის (9) დანიშნულებაა, შესაბამისად, დაბალი და მაღალი წნევების გაზომა და კონტროლი. ტექნოლოგიური პროცესების დამთავრების შემდეგ ვაკუუმურ ხუფფვეშ ჰაერის შეშვება ხდება ჰაერის შემშვები სარქველის (13) მეშვეობით. კვადრუპოლური მასსპექტრომეტრი (15) განკუთვნილია ვაკუუმურ ხუფქვეშ ნარჩენი გაზების შემადგენლობის კონტროლისა და ანალიზისათვის. საფარის (21) დანიშნულებაა გაფრქვევის ზონისა და დასაფენი ოპტიკური დეტალების განმხოლოება.

ფუძეშრე (ჩვენს შემთხვევაში პოლიმერული მასალისაგან დამზადებული ოპტიკური ლინზა), რომლის ზედაპირზე ეფინება მრავალშრიანი პერიოდული სტრუქტურების მქონე გაშუქოვნების დანაფარები, დამაგრებულია მბრუნავ დისკოზე ოპტიკური დეტალების დამჭერით (18). დისკოს ფიქსირებული კუთხით შემობრუნება ხორციელდება ხელით ოპერატორის მიერ. მანძილი დისკოსა და მაგნეტრონული გაფრქვევის მოწყობილობის სამიზნის ზედაპირს შორის 95 მმ-ია. აღნიშნული სამიზნის ზედაპირიდან 80 მმ მანძილზე მოთავსებულია მეორე უძრავი დისკო (19), რომელსაც ორივე მაგნეტრონული გაფრქვევის მოწყობილობის გასწვრივ ამოჭრილი აქვს 80 მმ დიამეტრის ნახვრეტი. ამ ნახვრეტზე გაფრქვეული ნაწილაკების მოძრაობის გასწვრივ დამაგრებულია 80 მმ დიამეტრის და 35 მმ სიმაღლის ცილინდრული ეკრანი (20). უძრავ დისკოს (19) გააჩნია ნულოვანი პოტენციალი. ცილინდრული ეკრანი (20) ზღუდავს მაგნეტრონული გაფრქვევის მოწყობილობების განსხვავებული სამიზნეებიდან გაფრქვეული მოლეკულების ურთიერთ გადაფარვას და მნიშვნელოვნად ზრდის დანაფარების სისქეების ერთგვაროვნებას [5]. ორი ფიქსირებული პოზიციის მქონე საფარი (21) ყოფს სივრცეს გაფრქვევის ზონასა და მბრუნავ დისკოზე დამაგრებულ ოპტიკური დეტალებს შორის. მისი დანიშნულებაა დაიცვას ოპტიკური დეტალები გაჭუჭყიანებისაგან, გამოწვეული დაფენის პროცესის საწყის პერიოდით და აგრეთვე, მათ ზედაპირზე დაფენის პროცესის შეწყვეტა (ან დაწყება), საფარის (21) შემობრუნება ხორციელდება ელექტრომაგნიტური მოწყობილობის გამოყენებით.

მოდერნიზირებული ვაკუუმური ВУ–1А ტიპის დანადგარი მუშაობს შემდეგნაირად: დაფენის ტექნოლოგიური პროცესი იწყება მბრუნავ დისკოზე ოპტიკური დეტალების დამჭერის (18) მეშვეობით წინასწარ გაუცხიმოებული ოპტიკური დეტალის (ლინზის) ჩატვირთვით. ვაკუუმური დანადგარის ხუფქვეშ ზღვრული ვაკუუმის (10^{-4} პა) მიღების შემდეგ სამუშაო აირის ნაკადის ავტომატიური მართვის და რეგულირების მოწყობილობის AALBORG მეშვეობით მაგნეტრონული გაფრქვევის ორივე რეაქტორში მიეწოდება სამუშაო აირი (არგონი + ჟანგბადი კონცენტრაციით 75 : 25) და ხუფქვეშ იქმნება 10^{-1} პა რიგის სამუშაო წნევა. მაღალი ძაბვის გადამრთველის (RFDC “PlasmaSwitch”) (26) გამოყენებით კვების ბლოკის წრედში ჩაირთვება M_1 მაგნეტრონული გაფრქვევის მოწყობილობა სილიკონის სამიზნით. ამის შემდეგ ირთვება იმპულსური ძაბვის კვების ბლოკი (25) და გამოსავალი იმპულსური ძაბვის თანდათანობით მომატებით M_1 მაგნეტრონული გაფრქვევის მოწყობილობაზე მიიღწევა ღვივადი განმუხტვა. ცდების საფუძველზე წინასწარ დადგენილი ტექნოლოგიური რეჟიმების დამყარების შემდეგ დასაფენი ობიექტი ბრუნვის ამძრავის (14) მეშვეობით გადადის M_1 მაგნეტრონული გაფრქვევის მოწყობილობის დაფენის

პოზიციაზე. საფარი (21), რომელიც ყოფს სივრცეს გაფრქვევის ზონაში, სპეციალური ტუმბლერის ჩართვით გადაადგილდება M_2 მაგნეტრონული გაფრქვევის მოწყობილობის პოზიციაზე. ამასთან, ირთვება წამზომი და დაიწყება ლინზაზე სილიციუმის ორჟანგის (SiO_2) პირველი შრის დაფენის პროცესი. წინასწარი გამოთვლებით დადგენილი დაფენის პროცესისთვის საჭირო დროის ამოწურვის შემდეგ ტუმბლერი გამოირთვება და საფარი (21) გადაინაცვლებს გაფრქვევის ზონაში. ამით ლინზაზე SiO_2 პირველი შრის დაფენის ტექნოლოგიური პროცესი მთავრდება. იმპულსური ძაბვის თანდათანობით დაკლებით M_1 მაგნეტრონული გაფრქვევის მოწყობილობაზე იმპულსური ძაბვა გამოირთვება.

ამის შემდეგ მაღალი ძაბვის გადამრთველის (RFDC "PlasmaSwitch") (26) გამოყენებით კვების ბლოკის წრედში გადაირთვება M_2 მაგნეტრონული გაფრქვევის მოწყობილობა ცირკონიუმის სამიზნით. შემდეგში ირთვება იმპულსური ძაბვის კვების ბლოკი და გამოსავალი იმპულსური ძაბვის თანდათანობით მომატებით M_2 მაგნეტრონული გაფრქვევის მოწყობილობაზე მიიღწევა ღვივადი განმუხტვა. ცდების საფუძველზე წინასწარ განსაზღვრული ტექნოლოგიური რეჟიმების დამყარების შემდეგ დასაფენი ობიექტის ბრუნვის ამძრავის (14) მეშვეობით ოპტიკური დეტალი გადადის M_1 მაგნეტრონული გაფრქვევის მოწყობილობის დაფენის პოზიციაზე. საფარი (21) სპეციალური ტუმბლერის ჩართვით გადაადგილდება M_2 მაგნეტრონული გაფრქვევის მოწყობილობის პოზიციაზე და ყველაფერი მეორდება, რის შედეგადაც ლინზაზე ეფინება ცირკონიუმის ორჟანგის (ZrO_2) მეორე შრე. დიელექტრიკული შრეების დაფენის ზემოთ მოყვანილი ტექნოლოგიური პროცესები მეორდება იმდენჯერ, რამდენი გაშუქოვნების შრის მიღებაც არის დაგეგმილი. ჩვენს შემთხვევაში სამჯერ. ამის შემდეგ იხსნება ჰაერის შემშვები სარქველი (13) და დაფენილი ოპტიკური დეტალი ჩამოიტვირთება.

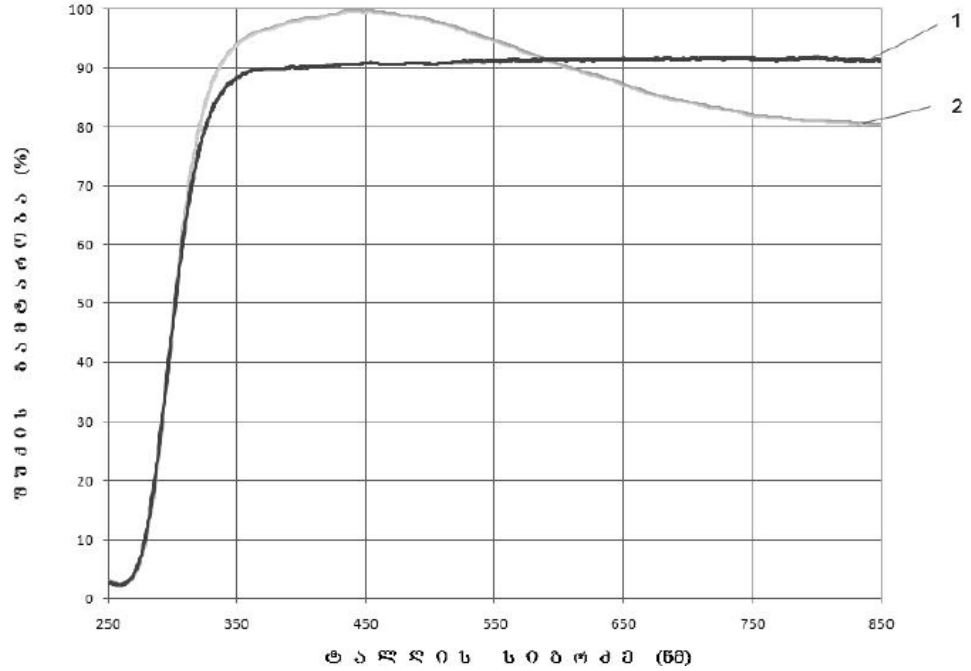

ნახაზი 3. პოლიმერული მასალისაგან დამზადებული ოპტიკური ლინზის სპექტრალური მახასიათებელი გაშუქოვნების ფენის დაფენამდე (1) და დაფენის შემდეგ (2).

მოდერნიზირებული ვაკუუმური ВУ–1А ტიპის დანადგარის ტესტირებისათვის განხორციელდა მრავალშრიანი პერიოდული სტრუქტურების მქონე გაშუქოვნების ფენების მიღება λ = 350 ნმ-დან λ = 900 ნმ-მდე სპექტრის ზონაში. ცალკეული ფენების სისქეები აღნიშნულ სისტემებში იცვლებოდა დიაპაზონში: სილიციუმის ორჟანგისათვის SiO_2 (n = 1.47) – (59 – 153) ნმ და ცირკონიუმის ორჟანგისათვის ZrO_2 (n = 1.97) – (44 – 114) ნმ. კონკრეტულად, გათვლილი და მიღებულია პოლიმერული მასალისაგან დამზადებულ ოპტიკურ ლინზაზე სამი ფენისაგან შემდგარი გაშუქოვნების შრეები: პირველი შრე SiO_2 სისქით 74 ნმ, მეორე შრე ZrO_2 სისქით 55 ნმ, მესამე შრე SiO_2 სისქით 74 ნმ.

ჰოლანდიური ფირმის Avantes Avaspec სპექტრომეტრით ULS 2040 გამოკვლეული იქნა პოლიმერული მასალისაგან დამზადებული ოპტიკური ლინზის სპექტრალური მახასიათებელი გაშუქოვნების ფენის დაფენამდე და დაფენის შემდეგ (**ნახაზი 3**).

სპექტრალური მახასიათებლებიდან ჩანს, რომ გაშუქოვნების შემდეგ ლინზის მიერ გატარებული სინათლის ინტენსივობას გააჩნია მაქსიმუმი X_{max} სპექტრის 434 ნმ მნიშვნელობისათვის. სპექტრის აღნიშნული უბანში ლინზის მიერ გატარებული სინათლის ინტენსივობა დაფენამდე 90.72 %-ია, ხოლო დაფენის შემდეგ 99.81 %.

მითითებები

1. Э. С. Путилин. Оптические покрытия. 2010, Санкт Петербург: СПб ГУИТМО.
2. P. J. Kelly, R. D. Arnell. Magnetron sputtering: A review of recent developments and applications. Vacuum, 2000, 56 , 159-172.
3. Г. С. Ануфриев, Б. С. Болтенков, А. И. Рябинков. Масс-спектры высокого разрешения остаточного газа в металлической вакуумной системе. ЖТФ, 2006, 76, 61-66.
4. გ. დ. დგებუაძე, ზ. ვ. ბერიშვილი, ს. ვ. სიხარულიძე. პლანარული მაგნეტრონული გაფრქვევის მოწყობილობა. საქართველოს პატენტი, № 2013 5725 B, 2013.

FORMATION OF TITANIUM ALLOYS 3D NANOSTRUCTURES

K. Gorgadze, T. Berikashvili, G. Nabakhtiani,
T. Berberashvili, Sh. Khizanishvili

Georgian Technical University
Tbilisi, Georgia
kakha-gorgadze@mail.ru

Accepted December 14, 2014

1. Setting the scene

Very active investigation of Titanium alloys were provoked by the discovery of thermoplastic martensit transformation and the possibility to fix within this transformation the thermoplastic equilibrium. These alloys are characterized by special properties as are Shape Memory Effect (SME) and Super Elasticity (SE). All these characterizations have practical application for different sphere including medicine.

It was fixed that only Ti-Ni alloys have the highest hardness and plastic properties with unique SME, and high corrosion resistance and reliability. It is also should be noted that metallurgic and thermomechanic processing of the alloys is comparably easy.

According to the conducting investigations some negative properties of Ti–Ni alloys were also fixed. Sometimes it is not possible to reach physico-mechanical properties of the alloy by its thermomechanical processing. During the processing the extraction of “free” nickel is fixed, which creates defined difficulties to use the alloy for medical purpose [1]. (Nickel provokes allergic actions in human body). All usual methods for improving of physic-mechanical properties of the alloy (alloying, thermomechanical processing) are already tested without valuable results; Therefore the new task is set to create new material with new chemical composition an nanostructure (nanocrystalline or submicrocrystallline).

The production of update medical technique and human body implants together with high reliability of the equipments sets other strong requirements for them: miniaturization, relevance of biomechanical properties to human tissue characteristics. So, elastic modules of the equipment material should be corresponded to bone elastic modules, yield strength should be increased approximately 1.5 – 2 times with the same SME and SE [2].

2. The way to solve the problem

To solve the above-mentioned problem the new method was developed considering formation in titanium alloys 3D submicrocrystalline or nanostructure by cold rolling method. The method allows enhance mechanical properties of the alloys by preserving their biochemeical characteristics. This situation differences are caused by the processes held in nanostructure metals, where main of them are developed not in crystal structure, but on the borders of crystalline seeds; Therefore no dislocation or vacancies have main impacts on the processes and material properties, but the borders among the crystalline seeds. More precisely it can be said that material properties are defined mainly by interaction between the seeds border and dislocation and defects formulated by strong deformation.

Using high purity components and electrical beam melting method the different Titanium alloys were prepared and investigated. The main idea of the investigation was to find

other elements which can replace nickel in alloys to enhance the alloy property and making it more appropriate for medical application. A number of alloys were produced and processed thermomechanicaly. All alloys were investigated by X-ray and thermo differential methods. The electroresistance, internal friction, dilatometrial and torsion investigations also were conducted. based on the results two alloys were chosen Ti–33Nb–7Zr and Ti–26Nb–4Ta–7Zr. (The numbers give weight percentage.)

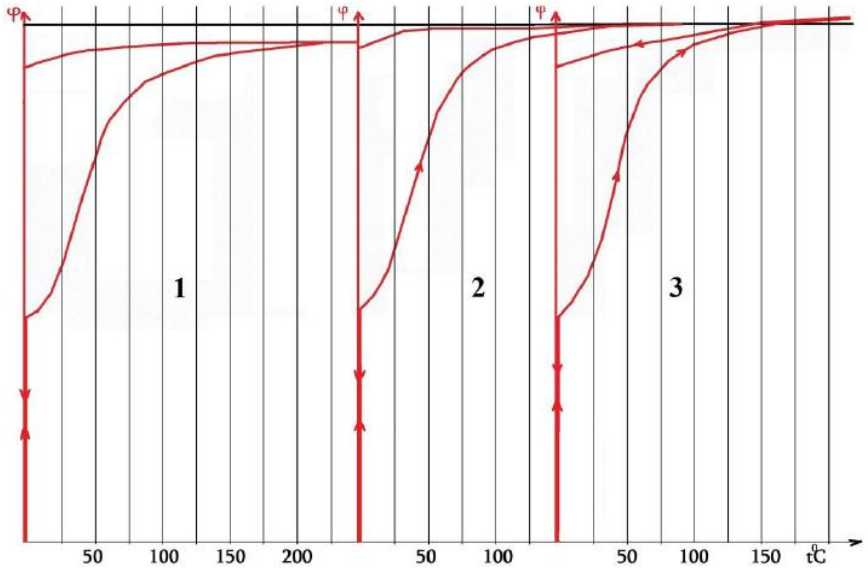

Figure 1. The shape recovery for Ti–33Nb–7Zr alloy.

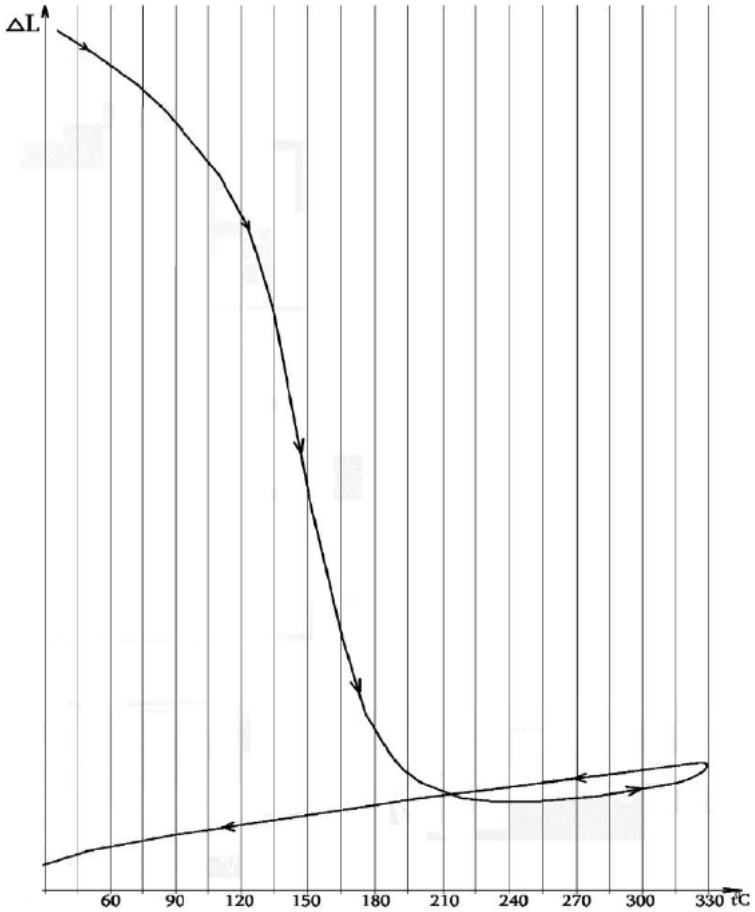

Figure 2. Dilatometric curve for Ti–33Nb–7Zr alloy sample.

The shape recovery characteristics for the first alloy are shown on **Figure 1**. The torsion deformation $\varepsilon = 6.5\ \%$ is conducted at room temperature. After that the sample temperature was increasing until the shape recovery process conducted. As the **Figure 1** shows the shape recovery was conducted at 25 – 60 °C temperature interval which is comparably close to human body temperature. Dilatometric characteristics of the same alloy are given on **Figure 2**. The recovery temperature on **Figure 2** is higher which is caused by the dilatometer properties. The same characteristics of the second alloy are given on **Figures 3** and **4**. The initial torsion deformation for the second alloy sample was $\varepsilon = 6.8\ \%$. The shape recovery is conducte within 80 – 120 °C temperature interval. The both alloys are characterized by high SME and SE.

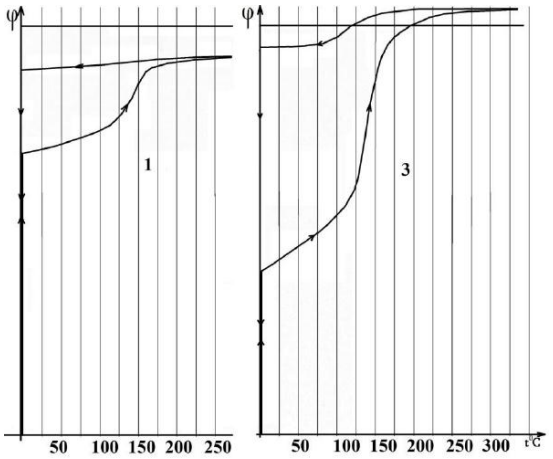

Figure 3. The shape recovery for Ti–26Nb–4Ta–7Zr alloy.

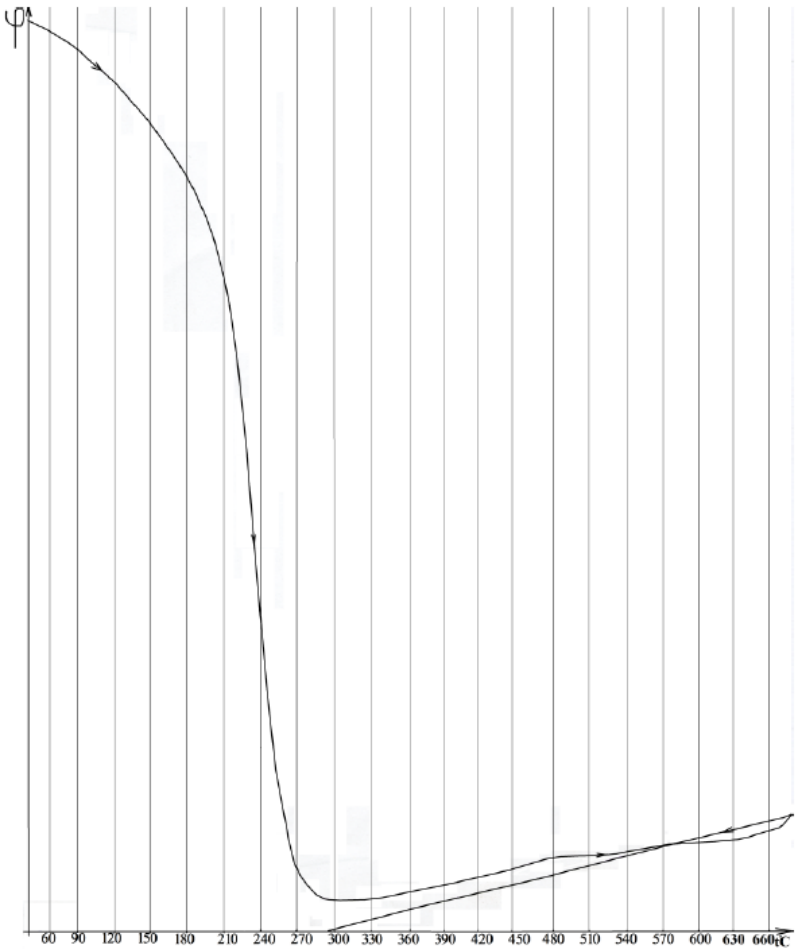

Figure 4. Dilatometric curve for Ti–26Nb–4Ta–7Zr alloy sample.

3. Conclusion

According to the investigations results the given alloys consist of metastable β-phase, orthorhombic α˝ martensit phase and thin dispersion hexagonical ω phase. The experiments proved high reliability of alloys samples and confirmes their acceptability for using in medical sphere.

References

1. Т. Перадзе, Ю. Стаматели, Т. Берикашвили, Т. Челидзе, К. Горгадзе. Эффект памяти форми в многокомпонентных сплавах на основе титана. Материаловед., 2006, 10, 20-22.
2. ICCMNM–2013 Conf. “Virtual Nanotitanium VIANT”.

რადიაციული ეფექტები იონურ კრისტალებში
(ე. ანდრონიკაშვილის ფიზიკის ინსტიტუტის კვლევები)

ვ. კვაჭაძე

ე. ანდრონიკაშვილის ფიზიკის ინსტიტუტი
ი. ჯავახიშვილის სახ. თბილისის სახელმწიფო უნივერსიტეტი
თბილისი, საქართველო
vkvachadze@yahoo.com

მიღებულია 2013 წლის 2 ნოემბერს

მყარი სხეულების ფიზიკა იყო კვლევის ერთ-ერთი ძირითადი მიმართულება, კოსმოსური სხივების ფიზიკის პარალელურად, რომლის საფუძველზეც დამოუკიდებელ ინსტიტუტად ჩამოყალიბდა საქართველოში ფიზიკის ინსტიტუტი (1950 წლის დეკემბერი). თავდაპირველად იგი მოიცავდა მყარი სხეულების ფიზიკის განყოფილებას, რომელშიც შედიოდა ლითონების ფიზიკისა და დიელექტრიკების ფიზიკის ლაბორატორიები. მოგვიანებით (1957 წელი) კი, კვლევების არეალის გაფართოებასთან დაკავშირებით, ამ ლაბორატორიებმა განყოფილების სტატუსი შეიძინეს. შედეგად ჩამოყალიბდა ლითონთა ფიზიკის განყოფილება და ნახევარგამტარებისა და დიელექტრიკების ფიზიკის განყოფილება.

თემები, რომელიც შეისწავლებოდა ახლად დაარსებულ ფიზიკის ინსტიტუტში (მაგალითად, დიელექტრიკების ფიზიკაში: "მეორადი მოვლენები ტუტე-ჰალოიდური მარილების ფოტოგამტარ კრისტალებში და კრისტალური დეფექტების როლი ამ მოვლენებში"; "შეღებვის ცენტრები KCl-ისა და KCl+Ag-ის კრისტალებში და გამა-სხივების გავლენა მათი წარმოქმნის პროცესებზე"; „სტიმულირებული ლუმინესცენციის მექანიზმები" და სხვ.) არა მარტო იმდროინდელ მოთხოვნებს შეესაბამებოდა, არამედ დღესაც აქტუალურია.

ბირთვული რეაქტორის შექმნამ (1959 წელი) განვითარების მნიშვნელოვნად მაღალ დონეზე აიყვანა მყარი სხეულების ექსპერიმენტული ფიზიკა. საქართველოში მყისიერად იწყო აღმავლობა ახალმა დარგებმა (მყარი სხეულების რადიაციული ფიზიკა და რადიაციული მასალათმცოდნეობა). გამომდინარე დარგის მნიშვნელობიდან, განვითარების ტემპიც ძალიან მაღალი იყო. მით უმეტეს, რომ უმოკლეს დროში შეიქმნა და ჰპოვა გამოყენება მყარ სხეულებზე ზემოქმედების კიდევ ერთმა საშუალებამ – რადიაციულმა კონტურმა, რომელიც ნეიტრონების ენერგიას გარდაქმნიდა გამა-კვანტების ენერგიად. კვლევისათვის ეს, მეტად საჭირო ბირთვული დანადგარი, სხვა მსგავს მოწყობილობასთან შედარებით, უმძლავრესი იყო საბჭოთა იმპერიაში (რადიაციული დოზა – 400 კგ რადიუმის ექვივალენტი).

კვლევის განვითარებამ მოითხოვა ორგანიზაციული ცვლილებები და ზემოთ ჩამოთვლილმა განყოფილებებმაც 1962 წლისთვის მიიღეს საბოლოო სახე, როგორც მყარი სხეულების ფიზიკის განყოფილება და დაბალტემპერატურული რადიაციული მასალათმცოდნეობის განყოფილებამ (ყველაზე ხანგრძლივად სწორედ ასეთი სახით იარსებეს მათ – თითქმის 90-იან წლებამდე, სანამ საბოლოოდ არ დაკონსერვდა რეაქტორზე მიმდინარე სამუშაოები).

დაბალტემპერატურული რადიაციული მასალათმცოდნეობის განყოფილებაში დამუშავდა და შეიქმნა ბირთვული რეაქტორის უნიკალური კრიოარხები. მათი საშუალებით უშუალოდ ბირთვული რეაქტორის აქტიურ ზონაში შექმნილ ტემპერატურათა ფართო დიაპაზონში (10 – 400 კ) ხორციელდებოდა საკვლევ ობიექტთა (ლითონები, დიელექტრიკები, სხვადასხვა შენადნობები და სხვ.) დასხივებაცა და შიგაარხული გაზომვებიც. სწორედ ამიტომ, ფიზიკის ინსტიტუტს დაევალა სსრკ-ში მეთაური ორგანიზაციის ფუნქციების შესრულება დაბალტემპერატურული რადიაციული მასალათმცოდნეობის დარგში (1962 წელი).

მყარი სხეულების ფიზიკისა და დაბალტემპერატურული რადიაციული მასალათმცოდნეობის განყოფილებების დამსახურებაა ის, რომ ყოფილი საბჭოთა კავშირის მეცნიერებათა აკადემიაში შემდგომში (1973 წელს) შეიქმნა მყარი სხეულების რადიაციული ფიზიკის საპრობლემო საბჭო (თავმჯდომარე ფიზიკის ინსტიტუტის დირექტორი ე. ანდრონიკაშვილი), ხოლო მისი ბაზური ინსტიტუტის ფუნქციები დაეკისრა საქართველოს მეცნიერებათა აკადემიის ფიზიკის ინსტიტუტს. თვალსაჩინო წარმატებების შედეგია იმ საერთაშორისო დონის ღონისძიებების ჩატარებაც, რომელიც იმ ხანებში ხორციელდებოდა: საერთაშორისო სკოლები მყარი სხეულების რადიაციულ ფიზიკაში: 1965 წლის ოქტომბერი, თელავი, და 1973 წლის ოქტომბერი, თბილისი; 1966 წლის ნოემბერში, თბილისში ჩატარებული XV სიმპოზიუმი კრისტალების ლუმინესცენციაში; კარგად ცნობილი ახალგაზრდა ფიზიკოსთა ბაკურიანის საზაფხულო სკოლა (1973 – 1991 წლები.) და სხვ.

მყარი სხეულების ფიზიკის განყოფილებაში უმთავრესად შეისწავლებოდა სამოდელო სისტემების – იონური კრისტალების – ფიზიკური თვისებები, რომელიც განსაკუთრებით მგრძნობიარეა მიკროსტრუქტურის ცვლილების მიმართ. მიზანს წარმოადგენდა რადიაციული თუ სხვა დეფექტების ტიპისა და ბუნების კვლევა და, აგრეთვე, მათი როლის დადგენა კრისტალის სახეშეცვლილი (ახალი) თვისებების ჩამოყალიბებაში. ცხადია, ამ ფუნდამენტურ კვლევას ყოველთვის ახლდა პრაქტიკული ინტერესიც.

ფიზიკის ინსტიტუტში მყარი სხეულების რადიაციული ფიზიკის განვითარება შეიძლება პირობითად ორ ეტაპად დავყოთ. პირველი ეტაპი, რომელიც დიდი ხანია რაც დამთავრდა, მოიცავს პირველადი რადიაციული დეფექტების შექმნის, მათი ურთიერთქმედებისა და გარდაქმნის (ევოლუციის) პროცესების შესწავლას იმ პირობებში, როცა მყარ სხეულებზე, საგანგებოდ, მხოლოდ ერთი – რადიაციული ველი მოქმედებს. ეს არის ეტაპი მყარი სხეულების რადიაციულ დეფექტურ სტრუქტურაზე ფუნდამენტური წარმოდგენების შექმნისა და განვითარებისა, ამ სფეროში ფუძემდებლური ფიზიკური კანონზომიერების დადგენისა, პოსტრადიაციული რელაქსაციის შესწავლისა და ა.შ. რადიაციული დეფექტების კვლევა პირველ ეტაპზე მიმდინარეობდა სხვადასხვა მიდგომით, როგორიცაა ოპტიკური მეთოდები (შთანთქმისა და გამოსხივების სპექტრები) – თ. დავითაშვილი, ლ. ვოროჟეიკინა, მ. აბრამიშვილი, მ. ჟვანია; კინეტიკური მოვლენები (დაბალტემპერატურული ფონონური სითბოგამტარობა, ელექტროგამტარობა) – ვ. კვაჭაძე, თ. ჯანდიერი, დ. იგითხანიშვილი; დინამიკური მოვლენები (ინფრაწითელი სპექტრომეტრია, დაბალ-ტემპერატურული სითბოტევადობა) – ზ. ახვლედიანი, კ. ყვავაძე, მ. ნადარეიშვილი, ლ. თარხნიშვილი; მექანიკური თვისებები – მ. გეთია, მ. გალუსტაშვილი, დ. დრიაევი; ელექტრონული მაგნიტური რეზონანსი (ეპრ) – თ. ყალაბეგიშვილი, ი. ახვლედიანი, ს. სობოლევსკაია; ელექტრონული მიკროსკოპია – გ. ნაცვლიშვილი, პ. მეტრეველი,

ს. გეტცი. ასეთი კომპლექსური მიდგომა კვლევისადმი ქმნიდა საიმედო საფუძველს მიღებული ექსპერიმეტული შედეგების სრულფასოვანი ანალიზისათვის.

აღსანიშნავია, რომ კრისტალების ფონონური სითბოგამტარობისა და სითბოტევადობის გასაზომი აპარატურა ადგილობრივი ძალებით იყო შექმნილი და მუშაობდა ფართო ტემპერატურულ ინტერვალში (1.3 – 300 კ). რაც შეეხება სითბოტევადობის საკვლევ კალორიმეტრს (ავტორები: კ. ყვავაძე და მ. ნადარეიშვილი) იგი მეტად ორიგინალურია. მასში შერწყმულია როგორც იმპულსური, ასევე დიფერენციალური კალორიმეტრიის პრინციპები და შესაბამისად, მაღალ მგრძნობიარობასთან ერთად (10^{-8} ვტ / ნვ) ხასიათდება გაზომვების მაღალი სიზუსტითაც. სწორედ ამან განაპირობა ისეთი ეფექტების დამზერა, რომელიც სხვა ცნობილი კალორიმეტრებისთვის მიუღწეველი იყო. დღეს იმპულსური დიფერენციალური კალორიმეტრი [1] ერთადერთი დიფერენციალური კალორიმეტრია მსოფლიოში, რომელიც მუშაობს იმპულსური გახურების მეთოდით და, შესაბამისად, გაზომვები ხორციელდება თერმოდინამიკური წონასწორობის პირობებში. ეს განაპირობებს გაზომვების მაღალ სიზუსტეს: $\Delta C / C \approx 10^{-4}$, სადაც C არის ნიმუშის სითბოტევადობა, ხოლო ΔC – მისი გაზომვის აბსოლუტური ცდომილება. მსოფლიოში ლიდერი კომპანიის (Setaram) მიერ წარმოებული დაბალტემპერატურული კალორიმეტრისათვის BT2.15, რომელიც მუშაობს უწყვეტი გახურების მეთოდით, აღნიშნული სიდიდე უარესია: $\Delta C / C \approx 10^{-3}$. თერმოდინამიკური მოვლენების ცნობილმა სპეციალისტმა ნ. მომონომ და მისმა კოლეგებმა ჯერ კიდევ 1999 წელს აღიარეს ამ აპარატურის მაღალი შესაძლებლობები [2].

აღნიშნულ კვლევებს სხვადასხვა დროს ხელმძღვანელობდნენ ნ. კალაბუხოვი, ნ. პოლიტოვი, ე. ანდრონიკაშვილი, თ. დავითაშვილი, ლ. ბუიშვილი, ზ. სარალიძე, კ. ყვავაძე, ვ. კვაჭაძე. რაც შეეხება ე. ანდრონიკაშვილს – აქ აღნიშნულია ის ფაქტი, რომ გარკვეული პერიოდის განმავლობაში ის იყო იმ განყოფილების ოფიციალური ხელმძღვანელი, რომელიც იონურ კრისტალებს შეისწავლიდა. თორემ რეალურად ე. ანდრონიკაშვილი მუდმივად კურირებდა რადიაციულ მოვლენებთან დაკავშირებულ ყველა კვლევას და თუ კაშკაშა შედეგს აღმოაჩენდა, ძალისხმევას არ იშურებდა ამ შედეგის ქვეყნის გარეთ გასატანად.

მყარი სხეულების რადიაციული ფიზიკის კვლევის პირველ ეტაპს მიეკუთვნება შედეგი, რომელსაც დიდი გამოხმაურება მოჰყვა: რეაქტორის არხში დასხივებულ ტუტე-ჰალოიდურ კრისტალებში ახალ, ანუ დასხივების პროცესში გაჩენილ ელემენტარულ სტრუქტურულ დეფექტებთან ერთად (წერტილოვანი დეფექტები) აღმოჩენილი იქნა ახალი დისლოკაციებიც – ხაზოვანი დეფექტები [3, 4]. ამ შედეგმა საბოლოოდ დაასაბუთა მანამდე გამოთქმული ჰიპოთეზა იონურ კრისტალებში დისლოკაციების რადიაციული გზით შექმნის შესაძლებლობის თაობაზე, რომელსაც ბევრი უარყოფდა, მიუხედავად იმისა, რომ სხვა მასალაზე (ლითონის ფოლგებში) ეს მოვლენა უკვე დამზერილი იყო ინგლისელი მკვლევრების მიერ [5].

დამუშავდა მოვლენის მექანიზმიც რადიაციული წერტილოვანი დეფექტების კოალესცენციის მოდელის ფარგლებში (ე. ანდრონიკაშვილი, ზ. სარალიძე): დასხივებით წარმოქმნილი წერტილოვანი დეფექტები განიხილებოდა როგორც “ორთქლი”, რომლისგანაც მიიღება ახალი ფაზა – დისლოკაციები. სწორედ ასეთი მექანიზმის სასარგებლოდ მეტყველებდა რადიაციული სტრუქტურული დეფექტების (ვაკანსიებისა და დისლოკაციების) წარმოქმნის არამონოტონური, პოლიმოდალური ხასიათი, რაც ექსპერიმენტულ ფაქტს წარმოადგენდა (მ. გეთია, ლ. ვოროჟეიკინა,

მ. აბრამიშვილი) [6]. აშკარა გახდა, რომ წერტილოვანი დეფექტებისა და დისლოკაციების რადიაციული დაგროვების პროცესები მჭიდროდ შეუღლებულია ერთმანეთთან [7]: დასხივების გარკვეული კრიტიკული დოზებისათვის დაიმზირება ერთდროულად შეღებვის ცენტრების სახით წერტილოვანი დეფექტების რაოდენობის შემცირება და დისლოკაციების სიმკვრივის ზრდა. შემდგომ ეტაპზე ხდება ახლად შექმნილი დისლოკაციების დაშლა და ვაკანსიების ინჟექცია მესერში, რაც განაპირობებს შეღებვის ცენტრების რაოდენობის შესაბამის ზრდას. ამ შედეგებმა ხელი შეუწყო ზოგიერთი სპეციფიკური რადიაციული პროცესების კომპიუტერულ მოდელირებას (რ. დოხნერი, ი. თოფჩიშვილი) [8], ამ მიმართულების გზამკვლელის პ. ვინიარდის კვალდაკვალ. განიხილებოდა ვაკანსიური კომპლექსების შექმნა და მათი ურთიერთქმედება სხვა დეფექტებთან, აგრეთვე, აღნიშნული კომპლექსების ევოლუცია და გარდაქმნა უფრო რთულ წარმონაქმნებად, რომელთა უშუალო შესწავლა ექსპერიმენტულად იქნებოდა შესაძლებელი.

სხვა ნაერთებისაგან განსხვავებით, იონურ კრისტალებში დისლოკაციები დამუხტულია. სკურპულოზურად და სრულად იყო შესწავლილი (მ. გალუსტაშვილი) [9] დამუხტვის მთელი პროცესი დაწყებული დისლოკაციის გაჩენის მომენტიდან (პლასტიკური დეფორმაცია) და დამთავრებული იმ დიფუზური პროცესებით, რომლებიც დეფორმირებულ კრისტალს აბრუნებენ ელექტრულად წონასწორულ მდგომარეობაში. დეფორმაციის პროცესში კრისტალიდან მოხსნილი სიგნალის ყოფაქცევა საშუალებას იძლევა შევაფასოთ დისლოკაციების მოძრაობის სიჩქარის მიმართულება და სიდიდე და მათი განაწილება კრისტალში.

აღმოჩენილი იყო ელექტრომექანიკური ეფექტი [10] (დ. დრიაევი), რომლის არსსაც წარმოადგენს LiF-ის მონოკრისტალის რხევა ცვლადი ელექტრული ველის ზეგავლენით. იგი გამოწვეულია ცვლადი ელექტრული ველისა და იონური კრისტალის დამუხტული დისლოკაციების ურთიერთქმედებით.

ცნობილია, რომ ტუტე-ჰალოიდურ კრისტალებში ჩანაცვლებული ჰიდროქსილის მოლეკულური იონები არა მარტო უშუალოდ იწვევს ახალ მოვლენებს (მაგალითად, ლოკალური რხევების წარმოქმნა), არამედ მნიშვნელოვნად მოქმედებს კრისტალის თვისებებზე არაპირდაპირი გზითაც. ჰიდროქსილის იონები და მათი დაშლის პროდუქტები მონაწილეობს რადიაციული სტრუქტურული დეფექტების შექმნის, გარდაქმნის (ევოლუციის), თუ დაშლის თითქმის ყველა პროცესში. ამიტომ ამ უცნაური მინარევის შესწავლა, რომელიც, როგორც წესი, მეტნაკლებად ყოველთვის იმყოფება ნომინალურად სუფთა კრისტალებში, მეტად მნიშვნელოვან ამოცანას წარმოადგენს. საბოლოოდ დასაბუთდა, რომ ჰიდროქსილის იონების რადიაციულ დაშლას ტუტე-ჰალოიდებში ალტერნატივა არ გააჩნია [11] (ზ. ახვლედიანი). რეაქტორში დასხივებული ლითიუმის ფტორიდის კრისტალების ოპტიკური სპექტრის ინფრაწითელ უბანში აღმოჩენილ იქნა ოთხი ახალი ზოლი (1900 – 2200 სმ$^{-1}$ დიაპაზონში), გამოწვეული ჰიდროქსილის რადიოლიზის შედეგად წარმოქმნილი უარყოფითი წყალბადიონების (ე.წ. U_1-ცენტრები) ლოკალური რხევებით. კვანძთაშორის სივრცეში მოთავსებული ეს მსუბუქი იონი ასე მგრძნობიარედ (ოთხი სიხშირე!) ეხმაურება გარემოცვის ოდნავ ცვლილებასაც კი. გარდა ამისა, დასაბუთდა, რომ აღნიშნული იონების განთავსებისთვის ანიონურ ვაკანსიებში (U-ცენტრები) სრულებით არ არის საჭირო კრისტალის პოსტრადიაციული გამოწვა, როგორც ეს მანამდე იყო ცნობილი.

წყალბადის ატომები, კიდევ ერთი პროდუქტი ტუტე-ჰლოიდურ კრისტალებში ჰიდროქსილის იონების რადიოლიზისა, შეიძლება მოთავსებული იყოს კვანძთაშორის,

ანიონურ და კათიონურ ვაკანსიებში, აგრეთვე კრისტალების პლასტიკური დეფორმაციის დროს შექმნილ ფორებში. მაგრამ ლითიუმის ფტორიდის შემთხვევაში წყალბადის ატომები ვერა და ვერ აღმოაჩინეს კათიონურ ვაკანსიებში. ეს ფაქტი საკმოდ ძლიერ სტიმულს ქმნიდა მკვლევართათვის (თ. ყალაბეგიშვილი, ი. ახვლედიანი), რომელთაც გამა-დასხივებულ ლითიუმის ფტორიდის კრისტალებისათვის პირველად მიაკვლიეს წყალბადის ატომების ეპრ-სპექტრის შვიდკომპონენტიან ზეფაქიზ სტრუქტურას, გამოწვეულს კათიონურ ვაკანსიებში (ანუ ლითიუმის მატრიცაში) არსებული წყალბადის ატომებით [12]. მოგვიანებით, კვლევის მეორე ეტაპზე (დეფორმაცია პლუს მაიონებელი გამოსხივება), კიდევ ერთხელ დადასტურდა ის, რომ წყალბადის ატომს, განსაკუთრებულ პირობებში, მეორე, ანიონურ მატრიცაშიც შეუძლია დამკვიდრება [13].

კვლევის პირველ ეტაპს უნდა მივაკუთვნოთ აგრეთვე იონურ კრისტალებში კოლოიდური და კვაზიკოლოიდური ნაწილაკების ადრინდელი კვლევები [14], რომელიც სხვა სამეცნიერო ცენტრებში მიმდინარე ანალოგიურ კვლევებთან ერთად შეიძლება ჩაითვალოს დღევანდელი ნანონაწილაკების კვლევების წინაპერიოდად. შეისწავლებოდა ლითიუმისა და მაგნიუმის დისპერსული (20 – 50 ნმ) კოლოიდური ნაწილაკების (აგრეთვე, პრეციპიტატების) წარმოქმნა რეაქტორში დასხივებულ ტუტე-ჰალოიდურ კრისტალებში; აგრეთვე, ადიტიურად შეღებილ კრისტალებში მიღებული კოლოიდური თუ კვაზიკოლოიდური ნაწილაკების რადიაციული მდგრადობა (ლ. ვოროჟეიკინა, მ. აბრამიშვილი).

ამ პირველ ეტაპზე ისეთ აღმავლობას მიაღწია მყარი სხეულების რადიაციულმა ფიზიკამ ე. ანდრონიკაშვილის ფიზიკის ინსტიტუტში (როგორც საერთოდ, ასევე – იონური კრისტალების განხრით), რომ საქართველოში უცხოელი მეცნიერები ჩამოდიოდნენ სათანამშრომლოდ, თუ სტაჟირებაზე. საკმაოდ ნაყოფიერი იყო გერმანელი მეცნიერების კ. ბერგისა და პ. გრუს (ქ. ჰალე, გერმანია) თანამშრომლობა ინფრაწითელი სპექტრომეტრიის ლაბორატორიასთან (დადგინდა ჰიდროქსილის იონების რხევის ოსცილატორის ძალა!) იგივე ლაბორატორიაში გაიარას სტაჟირება ბ. ზლატოვმა ბულგარეთიდან. იონურ კრისტალებში მიმდინარე რადიაციული მოვლენებით დაინტერესებამ მივლინებით ჩამოიყვანა თბილისში ცნობილი პოლონელი მეცნიერი ჯ. დამი. აქაურ მკვლევარებთან ერთად განიხილავდნენ პრობლემურ საკითხებს შეღებილი კრისტალების ოპტიკიდან ფ. ფრიოლიხი (ქ. ჰალე, გერმანია), პ. ავაქიანი (ქ. ვილინგტონიდან, აშშ). ა. ბერტრანი, რომელიც კრისტალების მექანიკური თვისებებით იყო დაინტარესებული, საფრანგეთიდან (ქ. გრენობლი) ჩამოვიდა სტაჟირებაზე და სხვ.

საქართველოსა და ესტონეთის მეცნიერებათა აკადემიების ხელშეკრულების დონეზე იქნა გაფორმებული თანამშრომლობა საქართველოს და ესტონეთის ფიზიკის ინსტიტუტებს კრისტალების ფონონური სითბოგამტარობის ერთობლივი კვლევის თაობაზე. ყველა ამ შემთხვევაში თანამშრომლობის საფუძველს აქაური ექსპერიმენტი და / ან იქაური თეორიული დებულება თუ მოდელი და, საბოლოო ჯამში, ამ ორი მიდგომის შერწყმა წარმოადგენდა [15 – 20]. (ნათქვამთან დაკავშირებით უპრიანია გავეცნოთ თუ რას წერდა რ. პაიერლსი 1962 წელს ფონონური სითბოგამტარობის შესახებ [21]: « .... в современной физике едва-ли найдется еще одна такая проблема, которая насчитывала бы столько неверных начинаний и столько теорий, не принимавших во внимание ряд существенных явлений, как это было в проблеме теплопроводности непроводящих кристаллов ... »). აღსანიშნავია, აგრეთვე თანამშრომლობა რუსეთისა

(ქ. მოსკოვი, ქ, ირკუტსკი, ქ. ტომსკი და სხვ.) და ყოფილ სსრკ-ში შემავალ სხვა რესპუბლიკების სხვადასხვა სამეცნიერო ცენტრებთან.

კვლევის მეორე ეტაპად, რომელმაც განვითარება იწყო გასული საუკუნის 70-იანი წლებიდან, შეიძლება ჩაითვალოს კომბინირებული ზემოქმედების შესწავლა მყარ სხეულებზე. იგულისხმება მათზე ერთდროული ზემოქმედება სხვადასხვა გარე ველისა – უმეტეს შემთხვევაში ეს არის კომბინაცია ბირთვული გამოსხივებისა დატვირთვის სხვადასხვა სახეობასთან (ტემპერატურული, ელექტრომაგნიტური, მექანიკური ველები). მსგავსი ექსპერიმენტული სიტუაციების შესწავლა განსაკუთრებით მნიშვნელოვანია, რადგანაც ასეთ შემთხვევაში ექსპერიმენტის პირობები უფრო მეტად უახლოვდება იმ რეალურ პირობებს, რომელშიც ხშირად უხდება ფუნქციონირება მყარ მასალებს. შესაბამისად შეიქმნა კვლევის ორიგინალური მეთოდები, რომელთა შორის ერთ-ერთი მნიშვნელოვანია კრისტალებზე რადიაციული და მექანიკური ველების ერთდროული ზემოქმედების შესწავლა (დენადობის ზღვარის ფარგლებში), რამაც განაპირობა მთელი რიგი ახალი მოვლენების დაკვირვება [22]. ასე მაგალითად, მიღებული იქნა იმ დროისთვის მოულოდნელი შედეგი (ე. ანდრონიკაშვილი, ნ. პოლიტოვი, ი. პაპერნო, ა. რაზმაძე [23]), რომ მაიონებელი რადიაციისა და მექანიკური ძაბვის ერთდროული მოქმედების პირობებში კრისტალის სიმტკიცის მნიშვნელოვან ზრდასთან ერთად მიიღწევა მისი პლასტიკური თვისებების შენარჩუნება ან გაუმჯობესება – ე.წ. პლასტიფიკაციის ეფექტი (მრუდები 3 და 4, **ნახაზზე 1**). მარტოოდენ რადიაციით ანდა მარტო დეფორმაციით გამოწვეულ განმტკიცებას, ჩვეულებრივ, თან სდევს მასალის გამყიფება ანუ პლასტიკური თვისებების გაუარესება მათ სრულ გაქრობამდე (მრუდი 2, **ნახაზი 1**). საკითხის თეორიულმა დამუშავებამ ეს მოულოდნელი შედეგი კანონზომიერების ლოგიკას დაუმორჩილა. გაკეტდა დასკვნა, რომ ეფექტი უმთავრესად განპირობებულია წარმოქმნილი ანიზოტროპული დეფექტების სხვადასხვა ველებთან ურთიერთქმედების ორიენტაციული დამოკიდებულებით.

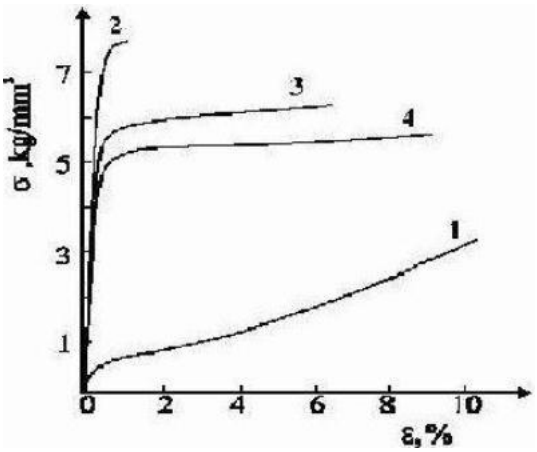

ნახაზი1. დიაგრამა მექანიკური ძაბვა – დეფორმაცია LiF-ის მონოკრისტალებისათვის: 1 – ზემოქნედებამდე; 2 – დასხივების შემდეგ; 3 და 4 – დაჭიმულ მდგომარეობაში დასხივების შემდეგ (ძაბვის სხვადასხვა მნიშვნელობებისათვის).

პლასტიფიკაციის ეფექტის მიღება შესაძლებელია ნებისმიერ კრისტალურ მყარ სხეულში მიუხედავად იმისა, თუ რა სახის ბმებია შემადგენელ ატომებს ან იონებს შორის. მაგალითად, ლითონებზე ჩატარებული მსგავსი ექსპერიმენტების თანახმად, რამდენჯერმე იზრდება ლითონთა დენადობის ზღვარი მათი პლასტიკურობის

შესამჩნევი შემცირების გარეშე [24]. აღსანიშნავია, რომ ლითონთა ჩვეულებრივი რადიაციული გამტკიცებას თან სდევს პლასტიკურობის კატასტროფული შემცირება, ზოგჯერ სრული გამყიფებაც კი.

აი როგორ აფასებდა პროფესორი ჩ. ლუშჩიკი ამ შედეგს ყოფილი სსრკ-ის მეცნიერებათა აკადემიის მყარი სხეულების რადიაციული ფიზიკის სამეცნიერო საბჭოს სხდომაზე (1986 წლის 7 იანვარი): «По своей бесспорной новизне, общетеоретической и прикладной значимости, по своей неожиданности с точки зрения существовавшего уровня знаний, по своей перспективности для дальнейшего развития радиационной физики твердых тел, суть которого четко и правильно сформулирована в предлагаемой формуле открытия, вполне заслуживает быть признаным научным открытием». ეს მიდგომა თამამად შეიძლება ვაღიაროთ ახალი მასალების მიღების მეთოდადაც.

CO_2-ლაზერების ოპტიკურ სისტემებში იონური კრისტალებია გამოყენებული (მაგალითად, NaCl-ის ლინზები). ისინი ხშირად ვერ უძლებენ მძლავრ ლაზერულ გამოსხივებას, რაც სერიოზულ დაბრკოლებას უქმნის მათ ნორმალურ მუშაობას. გამოითქვა მოსაზრება (ნობელის პრემიის ლაურეატი ნ. პროხოროვი), რომ ამ პრობლემის გადასაწყვეტად გამოყენებული ყოფილიყო გარე ველების კომბინირებული ზემოქმედების მეთოდი. მართლაც, ნაჩვენები იყო (ე. ანდრონიკაშვილი, ი. პაპერნო, მ. გალუსტაშვილი), რომ მასალის წინასწარი რადიაციულ-მექანიკური დამუშავება (კომბინირებული ზემოქმედება!) რამდენჯერმე ზრდის კრისტალების ოპტიკურ სიმტკიცეს ანუ მათ მდგრადობას მძლავრი ლაზერული გამოსხივებისადმი (იხ. **ნახაზი 2**) [25].

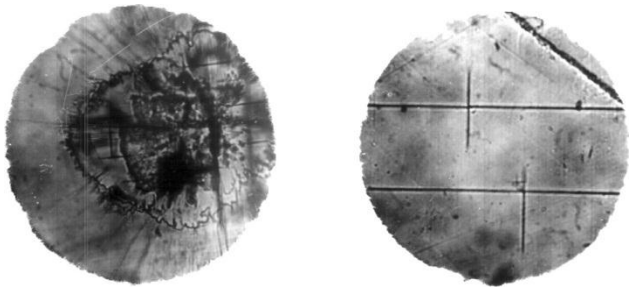

(ა) (ბ)

ნახაზი 1. (ა) საკონტროლო ნიმუში I ინტენსივობის ლაზერული სხივის ზემოქმედების შემდეგ. (ბ) გამა-პლასტიფიცირებული – $3I$ ინტენსივობის ლაზერული სხივის ზემოქმედების შემდეგ.

პლასტიფიკაციის ეფექტმა დასაბამი მისცა ახალ მიმართულებას მყარი სხეულების რადიაციული ფიზიკის დარგში – გარე ველების რადიაციასთან შეუღლებული ზემოქმედების ფიზიკა (რადიაცია პლუს მექანიკური ძაბვა, რადიაცია პლუს ელექტრული ველი, რადიაცია პლუს დარტყმითი ტალღა და ა.შ.). სწორედ ამ მიმართულებამ შვა ოთახის ტემპერატურაზე არამდგრადი ლაზერული ცენტრების სტაბილიზების ორიგინალური მეთოდი (ვ. კვაჭაძე, მ. აბრამიშვილი): ნომინალურად სუფთა LiF-ის მონოკრისტალებზე ბირთვული გამოსხივების მცირე დოზებისა და მცირე მექანიკური ძაბვების ერთდროული ზემოქმედება იწვევს F_2^+ იონის სტაბილური კონფიგურაციების შექმნას [16, 17]. გასაკვირია არაა, რომ ამ შედეგმაც ჰპოვა გამოხმაურება სსრკ-ის მეცნიერებათა აკადემიის თეორიული და ექსპერიმენტული ფიზიკის ინსტიტუტში.

ჩვეულებრივ ამ უნიკალური ლაზერული თვისებების მქონე ცენტრებზე სტაბილური გენერაციის მიღება მოითხოვს აქტიური ელემენტის – შეღებილი

კრისტალის გაცივებას კრიოგენულ ტემპერატურებამდე, რაც ართულებს თვით ლაზერსა და მასთან მუშაობის პირობებს. მართალია, F_2^+-ის თერმიული მდგრადობის გაზრდა მიიღწევა ლაზერულ კრისტალში ლითონის ორვალენტოვანი და / ან ჰიდროქსილის იონების წინასწარი შეყვანით (დღეს, როგორც წესი, ამ მეთოდს მისდევენ პრაქტიკაში), მაგრამ ამ გზით პრობლემა სრულად ვერ გადაიჭრება. მინარევის დიდი რაოდენობა ვნებს აქტიური ელემენტის ძირითად გენერაციულ თვისებებს და ამცირებს მის ოპტიკურ სიმტკიცეს. ოთახის ტემპერატურაზე თერმულად მდგრადი ლაზერული ცენტრების შექმნის აქ წარმოდგენილი მეთოდი კი არ მოითხოვს კრისტალის წინასწარ ლეგირებას კათიონური თუ ანიონური მინარევებით; იგი საშუალებას იძლევა სრულად იქნას გამოყენებული ნომინალურად სუფთა კრისტალში არსებული ჟანგბადის იონების რესურსი სტაბილური კონფიგურაციების ($F_2^+O^{2-}$) შესაქმნელად. ამასთან ეს ახალი მეთოდი კი არ ამცირებს, არამედ ზრდის ოპტიკურ სიმტკიცეს [26, 27].

ბოლო ხანებში კრისტალებზე გარე ველების კომბიმირებული ზემოქმედება განხორციელდა რადიაციისა და მაგნიტური ველის გამოყენებით (მ. გალუსტაშვილი, დ. დრიაევი) [28]. აღმოჩნდა, რომ რენტგენის სხივების მცირე დოზებისა და სუსტი მაგნიტური ველის ერთდროული მოქმედების შედეგად მცირდება კრისტალის რადიაციული განმტკიცების ხარისხი. ამგვარად, გასული საუკუნის დასასრულს კრისტალოგრაფიის ინსტიტუტში (ქ. მოსკოვი) აღმოჩენილი მაგნიტო-პლასტიკური ეფექტი ხორციელდება მაიონებელი რადიაციით დასხივებულ კრისტალებშიც.

პლასტიფიკაციის ეფექტი და მისი თანმდევი მოვლენები სრულად არის აღწერილი წიგნში [29], რომლის მეოთხე თავი შეიცავს სათანადო მიმოხილვას: V. Kvatchadze, M. Galustashvili. Mechanical and optical properties of ionic crystals exposed to the combined action of various external fields (Review).

გასული საუკუნის მეორე ნახევარში სულ უფრო მეტ პრაქტიკულ მნიშვნელობას იძენენ იონური კრისტალები. ამან გაზარდა აქ მოყვანილი შედეგების მნიშვნელობაც. მივუთითებთ ზოგიერთ მათგანს:

ლაზერული მასალების ფიზიკა. აღმოჩენილია ოთახის ტემპერატურაზე ჩვეულებრივად არამდგრადი ლაზერული ცენტრების სტაბილიზაციის მოვლენა ნომინალურად სუფთა ლითიუმის ფტორიდის მონოკრისტალებში [17, 26, 27].

დოზიმეტრული მასალების ფიზიკა. ნაჩვენებია, რომ მაგნიუმის ჟანგის მონოკრისტალები წარმოადგენენ პერსპექტიულ მასალას თერმოლუმინენსცენტური დოზიმეტრის (თლდ) მეთოდით სწრაფი ნეიტრონების ნაკადების სელექციური დეტექტირებისათვის შერეულ რადიაციულ ველში [30, 31].

ჰოლოგრაფიული მასალების ფიზიკა. სამგანზომილებიანი მარეგისტრირებელი გარემოს ოპტიკური თვისებების ოპტიმიზების მიზნით შესწავლილია ჟანგბადის ანიონური მინარევების შემცველი ადიტიურად შეღებილი კრისტალები. დადგენილია, რომ ასეთი კრისტალების წინასწარი მაიონებელი დასხივება იწვევს ჰოლოგრაფიული ოპტიკური ინფორმაციის ჩაწერის ეფექტურობის გაზრდას [32 – 34].

სწორედ მეორე ეტაპზე მიღებულ შედეგებთან დაკავშირებულ განაცხადებზე გაიცა ყოფილი სსრკ-ის პატენტები მათი პრაქტიკული მნიშვნელობის გამო.

უპრიანია აღვნიშნოთ ერთი პრობლემაც. გასული საუკუნის 80-იან წლებში ყოფილ საბჭოთა კავშირში მწყობრში უნდა ჩამდგარიყო მორიგი ბირთვული რეაქტორი, რომლის აქტიური ზონის პირველ კედლად ნავარაუდევი იყო მაღალი რადიაციული სიმტკიცის მქონე ოქსიდების გამოყენება (MgO, Al_2O_3 და სხვ.). შეიქმნა მეცნიერთა კოლაბორაცია "დიელექტრიკი" საქართველოს, ბალტიისპირეთის რესპუბლიკებისა და

რუსეთის მონაწილეობით. საქართველოს აქტიურობას ამ კოლაბორაციაში სწორედ ე. ანდრონიკაშვილის ფიზიკის ინსტიტუტის იონური კრისტალების მკვლევართა ჯგუფი განაპირობებდა. რადიაციულ ველში მომუშავე ამ მასალებისთვის ხომ ის პარამეტრები იყო პრიორიტეტული, რომლებით მხოლოდ ამათ რომ შეეძლოთ გამოეკვლიათ (მექანიკური თვისებები, სითბოგამტარობა [18 – 20]).

დაახლოებით 50 წლიანი ინტენსიური კვლევისა და თავსგადამტყდარი ქარტეხილების შემდეგ იონური კრისტალების – ე.წ. რეალური კრისტალების – შემსწავლელ ჯგუფს ე. ანდრონიკაშვილის ფიზიკის ინსტიტუტში შემორჩნენ: მ. აბრამიშვილი, ი. ახვლედიანი, ზ. ახვლედიანი, მ. გალუსტაშვილი, დ. დრიაევი, ვ. კვაჭაძე, მ. ნადარეიშვილი, თ. ყალაბეგიშვილი და მათთან ასოცირებული გ. დეკანოზიშვილი და გ. აბრამიშვილი. "რეალური კრისტალების" ჯგუფში გაერთიანებული არიან, აგრეთვე, ფ. აკოპოვი, ნ. არაბაჯიანი, ვ. თავხელიძე – თანამშრომლები დაბალტემპერატურული რადიაციული მასალათმცოდნეობის განყოფილებიდან (ამ განყოფილების ფართომასშტაბიანი კვლევები ცალკე აღნიშვნის ღირსია და თავის მეისტორიეს ელოდება!). სწორედ "რეალური კრისტალებია" დღეს მემკვიდრე იმ სახელგანთქმული განყოფილებებისა. არც რადიაციულ მოვლენათა კვლევა უარყვიათ ამ მკვლევარებს. ამ მიზნით ბოლო ათწლეულში გამოყენებული იყო დუბნის, ტაშკენტის, სევასტოპოლისა და კიევის რეაქტორები. ამგვარად, კვლევების ევოლუციის სპირალი არ წყდება. ამ სპირალის ორი ეტაპი აქ უკვე ნაჩვენები იყო: კრისტალების რადიაციით შეძენილი თვისებების კვლევა და კრისტალების თვისებების გამიზნული მართვა. ბუნებრივია დამდგარიყო ახალი, მესამე, ეტაპი, რომელსაც პირობით შეიძლება ეწოდოს ახალი მასალების შექმნის ეტაპი. ამჟამად "რეალური კრისტალებისა" და ტექნოლოგ-მკვლევართა ერთი ჯგუფის (ი. ბაირამაშვილის ჯგუფი) საერთო ძალისხმევით მუშავდება რადიაციულად მაღალი სიმტკიცის კონსტრუქციული კერამიკა (კომპოზიციური მასალა) მეოთხე თაობის რეაქტორებისთვის. დამუშავებაში იგულისხმება შექმნა და წინასწარი და პოსტრადიაციული კვლევა და გამოცდა ნორმალურ და ექსტრემალურ პირობებში. პილოტური ინფორმაცია ამის შესახებ მოცემულია შრომაში [35].

მითითებები

1. M. M. Nadareishvili, K. A. Kvavadze, G. G. Basilia, Sh. A. Dvali, Z. K. Khorguashvili. J. Low Temp. Phys., 2003, 130, 5/6, 529.
2. N. Momono, T. Matuzaki, T. Nagata, M. Oda, V. Ido. J. Low Temp. Phys., 1999, 117, 353.
3. E. L. Andronikashvili. In: Proc. Symp. Program. Utiliz. Res. Reactors. 1961, London – New York: Acad. Press, 321.
4. Э. Л. Андроникашвили, Н. Г. Политов, М. Ш. Гетия. В сб.: Действие ядерных излучений на материалы. 1962, Москва: Изд. АН СССР, 277.
5. J. Silcox, P. B. Hirsch. Phil. Mag., 1959, 4, 1356.
6. Э. Л. Андроникашвили, Н. Г. Политов, М. Ш. Гетия, Л. Ф. Ворожейкина. Изв. АН СССР (Сер. Физ.), 1965, 29, 366.
7. Н. Г. Политов. Изв. АН СССР (Сер. Физ.), 1967, 31, 1926.
8. Э. Л. Андроникашвили, Р. Д. Дохнер. ФТТ, 1981, 23, 298.
9. М. В. Галусташвили. ФТТ, 1970, 12, 1213.
10. Д. Г. Дриаев, В. М. Мелик–Шахназаров. ФТТ, 1966, 8, 3280.

11. З. Г. Ахвледиани, Н. Г. Политов. Опт. и спектроск., 1968, 25, 163.
12. И. Г. Ахвледиани, Т. Л. Калабегишвили. ФТТ, 1983, 25, 3505.
13. Z. G. Akhvlediani, I. G. Akhvlediani, T. L. Kalabegishvili. Phys. Status Solidi B, 1983, 119, 503.
14. Н. Г. Политов, Л. Ф. Ворожейкина. ФТТ, 1970, 12, 343.
15. V. I. Altukhov, V. G. Kvachadze. Phys. Status Solidi, 1978, 85, 769.
16. V. G. Kvachadze, M. G. Abramishvili, V. I. Altukhov. J. Low Temp. Phys., 1985, 58, 143.
17. М. Г. Абрамишвили, В. И. Алтухов, В. Г. Квачадяе. ФТТ, 1984, 26, 1895.
18. M. G. Abramishvili, V. I. Altukhov, T. L. Kalabegishvili, V. G. Kvachadze. Phys. Status Solidi B, 1981, 104, 49.
19. В. Г. Квачадзе, М. Г. Абрамишвили, Т. Л. Калабегишвили, В. И. Алтухов. Вопр. ат. науки и тех. (Сер.: Физ. радиац. поврежд. и радиац. материаловед.), 1981, 1(15), 62.
20. M. G. Abramishvili, V. I. Altukhov, T. L. Kalabegishvili, V. G. Kvachadze. Phys. Status Solidi B, 1984, 121, 95.
21. Р. Пайерлс. В сб.: Теоретическая физика XX века. 1962, Москва: ИЛ.
22. E. L. Andronikashvili, M. V. Galustashvili, R. D. Dokhner. In: Proc. Int. Conf. Def. Insul. Cryst. 1981, Berlin – Heidelberg – New York, 439.
23. Э. Л. Андроникашвили, Н. Г. Политов, И. М. Паперно, А. К. Размадзе. Пис. в ЖЭТФ, 1971, 13, 436.
24. И. А. Наскидашвили, И. А. Гиндин, Э. С. Лапиашвили, И. М. Неклюдов. Отчет ХФТИ АН УССР и ИФ АН ГССР № 922, 1968.
25. Э. Л. Андроникашвили, И. М. Паперно, М. В. Галусташвили, Э. М. Бархударов, М. И. Тактакишвили. ФТТ, 1979, 21, 2739.
26. M. Abramishvili, G. Abramishvili, M. Galustashvili, T. Kalabegishvili, V. Kvatchadze. J. Luminesc., 2013, 140, 126.
27. М. Г. Абрамишвили, З. Г. Ахвледиани, Т. Л. Калабегишвили, В. Г. Квачадзе, З. К. Саралидзе. ФТТ, 1998, 40, 2044.
28. M. G. Galustashvili, M. G. Abramishvili, D. G. Driaev, V. G. Kvachadze. Phys. Solid State, 2011, 53, 1340.
29. Eds. E. Belotserkovsky, Z. Ostaltsov. Ionizing Radiation: Applications, Sources and Biological Effects. 2012, New York: Nova Sci. Publ. Inc.
30. V. Kvatchadze, G. Dekanozishvili, T. Kalabegisvili, V. Gritsyna, V. Tavkhelidze. J. Mater. Sci. Eng. A, 2011, 1, 872.
31. V. Kvachadze, G. Dekanozishvili, T. Kalabegishvili, V. Vylet, A. Kurasbediani, M. Galustashvili, Z. Akhvlediani, N. Keratishvili, D. Zardiashvili. Radiat. Eff. Def. Solids, 2007, 162, 17.
32. К. А. Гарибашвили, В. Г. Квачадзе, В. В. Мумладзе, Т. К. Нахуцришвили, З. Г. Пичхая. ЖПС, 1990, 52, 1023.
33. М. Г. Абрамишвили, К. А. Гарибашвили, В. Г. Квачадзе, В. А. Котария, Э. Е. Тимофеева. Опт. и спектроск., 1991, 70, 411.
34. К. А. Гарибашвили, В. Г. Квачадяе, Х. С. Кевлишвили, Р. Г. Тушурашвили, З. Г. Пичхая, А. Э. Яшвили. ЖПС, 1991, 55, 979.
35. И. А. Баирамашвили, М. В. Галусташвили, Д. Ш. Джобава, В. Г. Квачадзе, З. З. Мествиришвили. Nano Studies, 2013, 8, 305.

NEW PHENOMENA IN SCIENCE
How they were explained

F. Habashi

Laval University
Québec City, Canada
Fathi.Habashi@arul.ulaval.ca

Accepted Jenuary 22, 2014

Abstract

While Röntgen correctly explained the newly discovered rays and Thomson was able to correctly identify the electron, other scientists failed to explain their discoveries. Fermi's eka-rhenium and Hahn's fission reaction are examples of confusing situations. On the other hand, Frédéric Joliot and Irène Curie were unable to explain the results of their experiments.

Introduction

When a scientist faces a discovery it is natural the he or she tries to explain it. Sometimes the explanation proves to be right and sometimes it is wrong. History of science is full of such stories. The oldest story is that of alchemists. There was nothing in the knowledge of that time from which one could conclude that it was impossible to obtain gold from lead, to obtain lead from litharge or mercury from cinnabar. Copper was already obtained when a piece of iron was immersed in a solution of blue vitriol (copper sulfate) (**Figure 1**) and copper can also be turned yellow like gold during smelting when mixed with a certain earth such as calamine and orpiment.

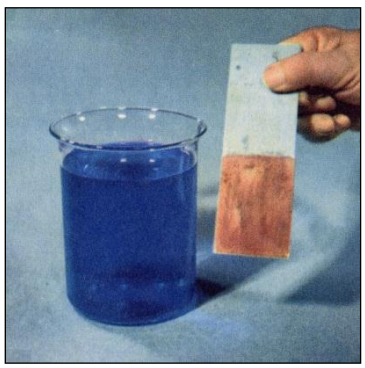

Figure 1. Transmutation of iron into copper as viewed by alchemists.

The concept of transmutation is deep-rooted in human thought. In the Old Testament the Egyptian magicians changed iron rods into serpents. In the New Testament, Jesus while attending a wedding feast changed water into wine. In Homer's Odyssey, Minerva with a rod turned the aged Ulysses suddenly into a youth. Even as late as the eighteenth century miners believed that lead gradually became silver and that bismuth was an intermediate stage in the process. The alchemists concluded that this process of transmutation was possible and why not convert a base metal directly into gold?

In modern terms, the transmutation of iron into copper is an electrochemical reaction: iron gives up electrons while copper in solution picks up these electrons to become metallic copper. Lead ores always contain silver and when lead is recovered then heated in air at high temperature silver present in the lead is obtained. When copper is heated in presence of a zinc ore, brass is obtained which is an alloy of copper and zinc. It was thus possible to explain the observations of alchemists. In modern times, great discoveries were made which changed our lives.

Discovery of X-rays

X-rays were discovered accidentally by Wilhelm Konrad Röntgen (**Figure 2**) professor of physics at the University of Würzburg in Germany on Friday November 8, 1895 through their ability to induce fluorescence in certain salts of heavy metals, even after passing through several millimetres thickness of optically opaque material. Röntgen immediately dropped his investigations of electrical discharges in gases, in which he was engaged at the time of his discovery, and proceeded to study the new radiations. His first observations established many of the fundamental properties of X-rays, and the work of numerous other investigators who immediately began to study the phenomenon quickly confirmed his results and extended them in many directions.

Figure 2. Wilhelm Konrad Röntgen (1845 – 1923).

Röntgen quickly found that obstacles placed between the tube and the fluorescent screen cast shadows. This fact convinced him that he was dealing with some kind of rays.

Because of their unknown nature, he named them X-rays. He found that the rays penetrate all substances to a greater or less degree. In general, dense substances are more opaque to the rays than light substances. Röntgen was the winner of the first Nobel Prize in physics in 1901.

A Crookes tube which emits X-rays began to be known as an X-ray tube. When the hand is interposed between an X-ray and a fluorescent screen, the rays penetrate the fleshy parts of the hand more easily than the bones, so that the bones stand out as shadows on the screen. The idea that the bones of a living hand could be photographed amazed the public. The newspapers of the period carried headlines of this new marvel. The Birmingham artist Robert Alan Thom (1915 – 1979) painted a picture in 1966 showing Roentgen at his first public demonstration of the newly discovered X-rays in the evening of January 23, 1896. The lecture took place at the Physics Department Auditorium of the University of Würzburg in Germany where Röntgen was the rector. The painting shows Albert von Kölliker, professor of anatomy at the University putting his hand on a photographic plate to make an X-ray picture (**Figure 3**).

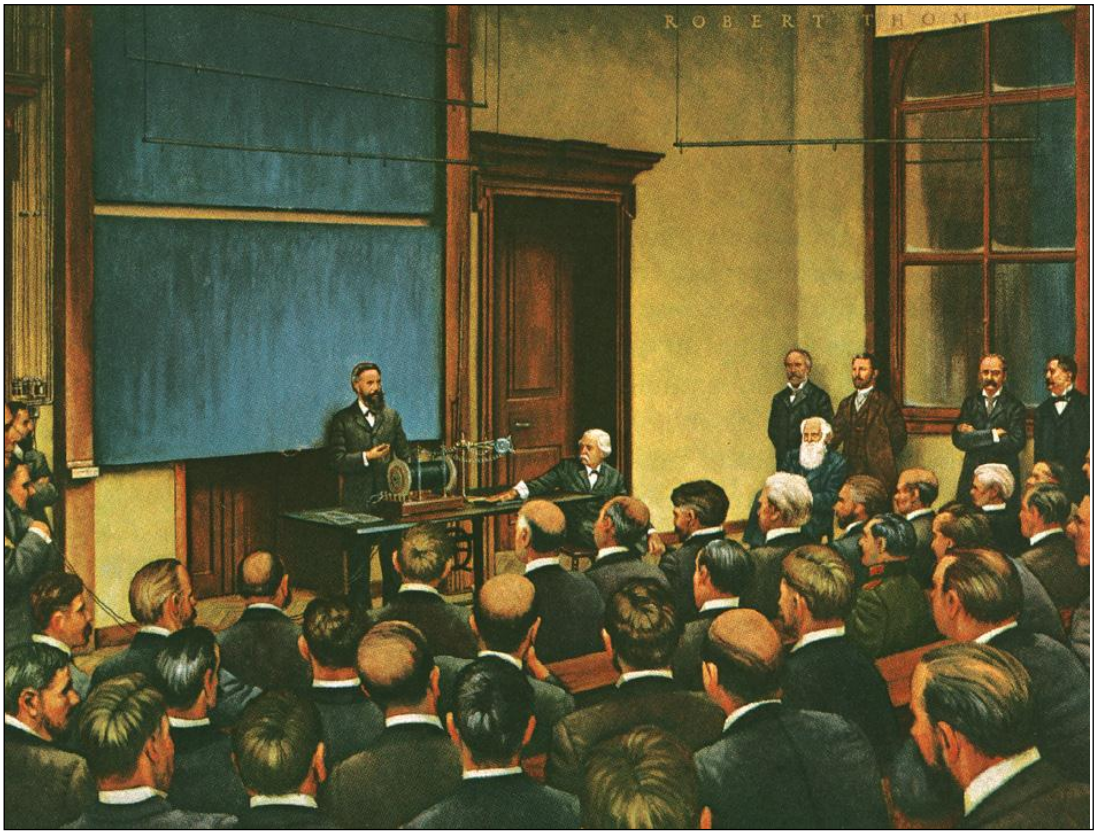

Figure 3. Röntgen's announcement of the discovery of a New Type of Radiation from *Great Moments in Medicine* by Parke, Davis & Company, Northwood Institute Press, Detroit 1966.

This new kind of unknown and invisible ray passed through glass and through paper. In further experiments the rays passed through sheet aluminum, through tinfoil, through rubber, through most materials. A packet of photographic film, wrapped carefully in black paper, was found to be exposed. These new rays could expose carefully-concealed photographic plates. In retrospect it seems certain that X-rays had been produced in many laboratories for several years, produced by the high voltages that were often used in connection with gaseous discharge tubes; Röntgen was merely the first experimenter to notice them.

Discovery of the electron

On April 30, 1897, professor of physics at Cambridge Universoty Joseph John Thomson (**Figure 4**) announced during a lecture at the Royal Institution of Great Britain in London, that the rays he had observed streaming from the cathode in a discharge tube consisted of negatively charged particles which he called "corpuscles". He correctly concluded that these corpuscles are matter in a finer state of subdivision than the ordinary atom. Of course this discovery revolutionized science and technology, leading to advances in communications, transportation, medicine, and other benefits that we take for granted today. He was awarded the Nobel Prize for physics in 1906.

Figure 4. Joseph John Thomson (1856 – 1940).

It was improvements in vacuum technology that enabled Thomson to examine the electrons in his tube. If the pressure of the gas in the tube is too high, the electrons scatter off the gas molecules. In that case, it is not possible to produce a fine beam and measure its deflection accurately.

Discovery of radioactivity

When Röntgen's first experiments with X-rays were reported in France in January 1896, it occurred to Antoine Henri Becquerel (1852 – 1908) (**Figure 5**) that penetrating radiations might be connected with luminescent materials, since X-rays were produced where the glass of a cathode-ray tube showed its strongest fluorescent glow. Becquerel began a series of tests of minerals known to show phosphorescence after exposure to light. Samples were placed in contact with a photographic plate wrapped in black paper, and the whole arrangement was placed in sunlight. Among the materials tested the only one that gave positive results was a compound of uranium, and the surprising fact that this compound produced the effect even when not previously exposed to light. This convinced the experimenter that it could emit some kind of penetrating radiation quite independent of its ability to show phosphorescence.

Fluorescence and phosphorescence are processes in which certain substances absorb energy, for example from visible or ultraviolet light, or from cathode rays or X-rays. This energy is again emitted as light of a characteristic colour. The distinction between the two processes lies only in the delay or lack of delay between the absorption and re-radiation of the energy. Now we know that fluorescence and phosphorescence are not the processes which

produce X-rays, and that they are also not at all related to the kind of rays Becquerel discovered. Without abandoning his hypothesis, Becquerel succeeded in showing that neither the ability to phosphoresce nor exposure to light was needed for obtaining these rays, but only the presence of uranium. Thus the discovery of this new property of uranium mineral is perhaps an excellent example of how wrong assumptions sometimes lead to results of value.

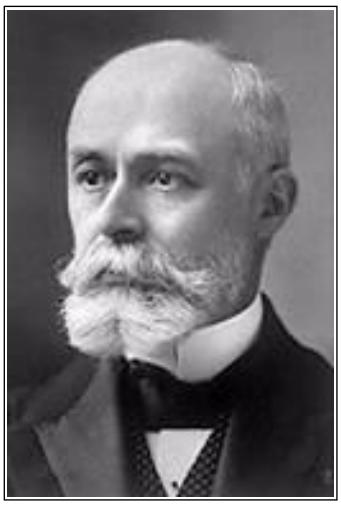

Figure 5. Antoine Henri Becquerel (1852 – 1908).

An extensive investigation of the radiation of uranium minerals and salts was begun by Marie Curie (1867 – 1934) (**Figure 6**) using pitchblende, a natural ore rich in compounds of uranium. This material showed an activity, measured by its ability to produce ionization, far greater than was to be expected on the basis of the amount of uranium it contained, and Mme Curie suspected that this might be due to a new and much more highly active substance present in the ore. Pierre and Marie Curie then undertook a long series of repeated crystallizations of salts derived from pitchblende in order to concentrate the active ingredient. Finally, from a ton of the ore, they obtained a small quantity of a new active element, which they named *polonium*, and, later, a minute amount (less than 0.02 g) of a still more active element, *radium*. Further experiments by the Curies and by others soon led to the discovery of many other radioactive substances now known to be chemical elements occupying the last places in the Periodic Table. Except for their radioactivity, uranium, thorium, polonium, and radium seemed perfectly ordinary elements with a normal, permanent existence.

Figure 6. Marie Curie (1867 – 1934).

Discovery of the neutron

Between 1930 and 1932, some physicists including Frédéric Joliot and Irène Curie noted that when certain light elements such as beryllium were exposed to alpha particles, some kind of radiation was formed, which showed its presence by ejecting protons from paraffin. They were unable to interpret their results. It was James Chadwick (1891 – 1974) (**Figure 7**) in 1932 who repeated these experiments and explained the phenomenon by supposing that alpha particles were knocking neutral particles out of the nuclei of the beryllium atom and that these neutral particles were in turn knocking protons out of the paraffin. In this way the *neutron* was discovered. He was awarded Nobel Prize for physics in 1935.

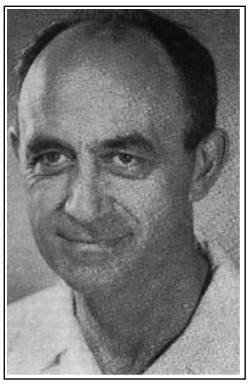

Figure 7. James Chadwick (1891–1974). **Figure 8.** Enrico Fermi (1901–1954).

Discovery of eka-rhenium

In 1934, Enrico Fermi in Rome (**Figure 8**) discovered that neutrons may, be captured by atoms and that the frequency of capture increases when they are slowed down by passing them through a hydrogen-rich material such as paraffin or water. He was thus able to produce atoms of higher atomic weights than those bombarded. For example, on bombarding cobalt with neutrons he was able to produce nickel

$$^{59}_{27}\mathrm{Co} + {}^{1}_{0}\mathrm{n} \rightarrow {}^{60}_{27}\mathrm{Co} \rightarrow {}^{60}_{28}\mathrm{Ni} + \mathrm{e}^{-}.$$

																H	He
Li	Be											B	C	N	O	F	Ne
Na	Mg	Al											Si	P	S	Cl	Ar
K	Ca	Sc	Ti	V	Cr	Mn	Fe	Co	Ni	Cu	Zn	Ga	Ge	As	Se	Br	Kr
Rb	Sr	Y	Zr	Nb	Mo	Tc	Ru	Rh	Pd	Ag	Cd	In	Sn	Sb	Te	I	Xe
Cs	Ba	†	Hf	Ta	W	Re	Os	Ir	Pt	Au	Hg	Tl	Pb	Bi	Po	At	Rn
Fr	Ra	Ac	Th	Pa	U	93											

†	La	Ce	Pr	Nd	Pm	Sm	Eu	Gd	Tb	Dy	Ho	Er	Tm	Yb	Lu

Figure 9. The Periodic Table in the 1930s at the time of the confusion between trans-uranium elements and fission. Element 93 was referred to as eka-rhenium.

When, however, Fermi and his co-workers bombarded uranium with neutrons, they obtained more than one radioactive product. Following the same line of thought as in their previous experiments they suggested that one of these products was formed by neutron capture, i.e., that it was a trans-uranium element or element number 93. Fermi put the new element under rhenium in the Periodic Table and called it eka-rhenium (**Figure 9**). Rhenium had been discovered a few years earlier in 1925, by Ida Tacke, Walter Noddack, and Otto Berg in Berlin.

Figure 10. Ida Noddack (born Tacke) (1896 – 1978).

The publication of Fermi's paper on eka-rhenium in 1934 naturally attracted the attention of one of the discoverers of rhenium, Ida Tacke, who in 1926 had married Walter Noddack (1893 – 1962) and became Ida Noddack (**Figure 10**).

After reading Fermi's paper she published in the same year a comment criticising his conclusions. In this comment, entitled "The Periodic System of the Elements and its Gaps," she showed that Fermi's experimental evidence was incomplete and his conclusions were unjustified. She interpreted his results by saying that "When heavy nuclei are bombarded by neutrons, it would be reasonable to conceive that they break down into numerous large fragments which are isotopes of known elements but are not neighbours of the bombarded element (in the Periodic Table)." [1]

Her argument was as follows: when atoms are bombarded by protons or alpha particles, the nuclear reactions that take place involve the emission of an electron, a proton, or a helium nucleus and the mass of the bombarded atom suffers little change. When, however, neutrons are used, new types of nuclear reaction should take place that are completely different from those previously known. Incidentally, Fermi received the Nobel Prize in 1938 for his work on slow neutrons.

[1] Es wäre denkbar, daß bei der Beschießung schwerer Kerne mit Neutronen diese Kerne in mehrere größere Bruchstücke zerfallen, die zwar Isotope bekannter Elemente, aber nicht Nachbarn der bestrahlten Elemente sind. (English translation by the writer.)

Discovery of uranium fission

Fermi's experiments were repeated by Otto Hahn (1879 – 1968) (**Figure 11**) and his co-workers in Berlin. They agreed with his conclusions and published a series of twenty papers on the complex radiochemical separations of the so-called trans-uranium elements. The results, however, became so conflicting that after four years of intensive research the concept of trans-uranium elements became doubtful. This doubt arose when experiments by Hahn's co-worker, Fritz Strassmann (1902 – 1980) (**Figure 12**), showed that $BaCO_3$, which was added as a carrier in the radiochemical separation of the products of bombardment, could not be separated from these products by dissolution in HBr and fractional crystallization of the bromides.

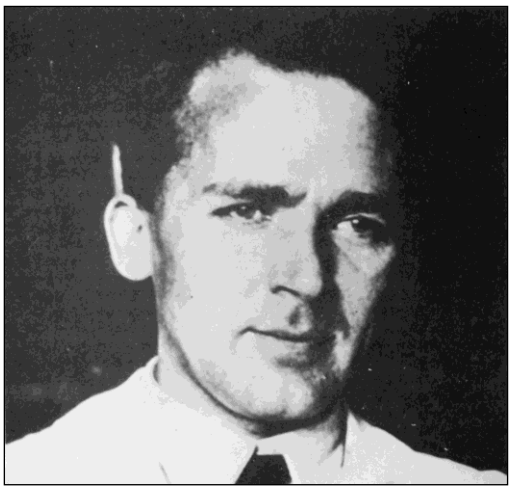

Figure 11. Otto Hahn (1879 – 1968). **Figure 12.** Fritz Strassmann (1902 – 1980).

This observation eliminated the possibility that radium was present in the products and it became evident that barium itself must be one of the products. This conclusion could not be reconciled with the physics of the day because barium had an atomic weight of only 137 while that of uranium was 238. With the discovery of fission, the gap between chemistry and physics was closed. In their paper dated January 6, 1939, Hahn and Strassmann wrote in *Die Naturwissenschaften*, "As chemists we must actually say that the new particles do not behave like radium but in fact like barium; as nuclear physicists we cannot make this conclusion which is in conflict with all experience in nuclear physics." [2] Hahn then started speculating about the mechanism of barium formation. Hahn communicated these astonishing results to his former co-worker, Lise Meitner (1878 – 1968) (**Figure 13**), in Stockholm. Meitner and her nephew Otto Frisch (1904 – 1979) (**Figure 14**) were able to explain the experiments as fission of the uranium atom.

[2] Als Chemiker müssen wir tatsächlich sagen, daß die neuen Körper sich nicht wie Radium verhalten, sondern eher wie Barium; als Kern-Physiker können wir uns nicht dazu entschließen, diesen aller Erfahrung der Kern physikwiderspechenden Schritt zu tun. (English translation by the writer.)

Figure 13. Lise Meitner (1878 – 1968). **Figure 14.** Otto Frisch (1904 – 1979).

Otto Hahn (in 1966) in his autobiography wrote a single phrase referring to Noddack's idea: "Her suggestion was so out-of-line with the then-accepted ideas about the atomic nucleus that it was never seriously discussed". Dieter Hahn, in his biography of his grandfather, wrote in 1979 that Lise Meitner rejected Noddack's hypothesis describing it as a "free fantasy" – and there was no support for this hypothesis. Further, Meitner argued that there was nothing theoretically or experimentally wrong with the trans-uranium explanation.

After reading Hahn's article in *Die Naturwissenschaften*, Ida Noddack wrote a short article in the same journal in March 1939, in which she reminded Hahn of her suggestion five years earlier that the uranium atom might have undergone splitting, and ended by telling him regretfully that he never cited her paper on this matter although she had once explained her views to him personally. The editor of the journal apparently asked Hahn to comment, but he refused. As a result, the editor added a note to the article that read as follows:

Editor's remark: Otto Hahn and Fritz Strassmann informed us that they have neither the time nor the interest to answer the preceding note. They think that they would rather renounce commenting, as the possibility of breaking down a heavy atom into smaller fragments – an idea already expressed by many others – cannot be concluded without experimental evidence. They leave the judgment of the correctness of the views of Frau Ida Noddack and the way she expressed them to the peers.

Epilogue

Discovering a new phenomenon in nature usually creates confusion in scientific circles for a number of years. While Röntgen was able to correctly describe the phenomenon he discovered and called it X-rays in a very short time, Becquerel published a dozen papers, nearly each one contradicting the other, when he discovered the new phenomenon of radioactivity. A similar situation was faced by Otto Hahn when he discovered uranium fission. In her statement, Ida Noddack conceived, before anyone else, the idea of nuclear fission. Her argument was as follows: when atoms are bombarded by protons or alpha particles, the nuclear reactions that take place involve the emission of an electron, a proton, or a helium nucleus and the mass of the bombarded atom suffers little change. When, however, neutrons are used, new types of nuclear reaction should take place that are completely different from those previously known.

Suggested reading

1. F. Habashi. From Alchemy to Atomic Bombs. 2002, Québec City: Métallurgie Extractive Québec. – Distributed by Laval University Bookstore: www.zone.ul.ca
2. F. Habashi. Ida Noddack (1896 – 1978). Personal Recollections on the Occasion of 80th Anniversary of the Discovery of Rhenium. 2005, Québec City: Métallurgie Extractive Québec. – Distributed by Laval University Bookstore: www.zone.ul.ca

ბორის, ბორიდებისა და მონათესავე ნაერთების მე-18 საერთაშორისო სიმპოზიუმი (ბბსს 2014)

ბორის, ბორიდებისა და მონათესავე მასალების მე-18 საერთაშორისო სიმპოზიუმმა (ბბსს 2014 – ISBB 2014), რომელიც 2014 წლის 31 აგვისტოდან 5 სექტემბრამდე მიმდინარეობდა ჰონოლულუში, ჰავაი, აშშ, განიხილა და შეაჯამა ბორისა და ბორშემცველი მასალების მიღების მეთოდების დამუშავებაში, მათი ფიზიკური თვისებების გამოკვლევასა და ტექნოლოგიურ გამოყენებებში დღეს მიღწეული პროგრესი. ეს უაღრესად მნიშვნელოვანია, რადგანაც უკანასკნელ ხანებში ძალზე სწრაფად ფართოვდება ბორის ნაერთებისა და კომპოზიტების, მათ შორის ამ მასალების ნანოსტრუქტურული ფორმების, გამოყენებათა სფერო. ესენია: მრეწველობა, სოფლის მეურნეობა, ენერგეტიკა, მედიცინა, შეიარაღება, გარემოს დაცვა, საყოფაცხოვრებო ტექნიკა და სხვა.

ბბსს 2014-ის ორგანიზატორები და სპონსორები.

ბორის, ბორიდებისა და მონათესავე მასალების საერთაშორისო სიმპოზიუმები (ბბსს) რეგულარულად ტარდება 1959 წლიდან მოყოლებული. ბბსს 2014-ის ორგანიზატორი იყო ამერიკის შეერთებული შტატების ისეთი ცნობილი სამეცნიერო ცენტრი, როგორიცაა ჰავაის უნივერსიტეტი – ოკეანისა და დედამიწის მეცნიერებისა და ტექნოლოგიის სკოლის (ოდმტს), ჰავაის უნივერსიტეტის ფონდისა და ჰავაის უნივერსიტეტის კვლევითი კორპორაციის (ჰუკკ) სახით; ხოლო სპონსორები იყვნენ ამერიკის კერამიკოსთა საზოგადოება (ACerS), კორპორაცია ბორაქსი (U.S. Borax Inc., Rio Tinto Minerals), ეტიმაინი (Etimine, USA, Inc.), ბორენი (Boren, თურქეთის ბორის კვლევის ეროვნული ინსტიტუტი), ტექნოდიამანტი (Technodiamant, ნიდერლანდები), ნეცში (Netzsch Group, გერმანია) და ბრუკერი (Bruker Corporation).

ბბსს 2014-ის პრობლემატიკა აქტუალურია კონკრეტულად საქართველოსათვისაც. საყურადღებოა, რომ ყოფილ საბჭოთა კავშირში ახლანდელი ფ. თავაძის მეტალურგიისა და მასალათმცოდნეობის ინსტიტუტი ასრულებდა ბორის, ბორიდებისა და მონათესავე ნაერთების კვლევების ერთ-ერთი მაკოორდინებელი სამეცნიერო ცენტრის ფუნქციას. ბბსს 2-ჯერ, 1972 და 1984 წლებში, გაიმართა საქართველოში. ეს ტრადიცია შენარჩუნებული და განვითარებულია და საფუძვლად უდევს ქართული კვლევითი ჯგუფების დღევანდელ ინტენსიურ თანამშრომლობას ბორისა და ბორშემცველი მასალების მოწინავე სამეცნიერო ცენტრებთან საზღვარგარეთ. ბორის პრობლემატიკა აქტუალურია საქართველოში ტექნოლოგიური პროგრესისათვისაც. ამის კარგი მაგალითია წყალბადის უსაფრთხო და ტევადი ნანორეზერვუარები ბორის ნიტრიდის ფუძეზე, განკუთვნილი ეკოლოგიური ენერგეტიკისათვის.

2014 წლის ჰავაის სიმპოზიუმში მონაწილეობდა ორი ქართველი მეცნიერი – ლევან ჩხარტიშვილი (საქართველოს ტექნიკური უნივერსიტეტის საინჟინრო ფიზიკის დეპარტამენტის პროფესორი, ფ. თავაძის მეტალურგიისა და მასალათმცოდნეობის ინსტიტუტის ბორისა და ფხვნილოვანი კომპოზიტური მასალების ლაბორატორიის მეცნიერი თანამშრომელი) და ივანე მურუსიძე (ილიას სახელმწიფო უნივერსიტეტის პროფესორი, ამავე უნივერსიტეტის გამოყენებითი ფიზიკის ინსტიტუტის დირექტორი). საერთო ჯამში ქართული კვლევით ჯგუფების მიერ სიმპოზიუმზე წარმოდგენილ იქნა 2 ზეპირი და 8 პოსტერული მოხსენება საკმაოდ მრავალფეროვან თემატიკაზე:

- ლ. ჩხარტიშვილი. ბორის ნიტრიდებში ატომური მუხტების ნახევრადემპირული განსაზღვრა.
- ი. მურუსიძე, ლ. ჩხარტიშვილი. ბორის ბრტყელი ფურცლის ელექტრონული ზონური სტრუქტურის თაობაზე.
- ლ. ჩხარტიშვილი, ნ. მამისაშვილი, ნ. მაისურაძე. ერთპარამეტრიანი მოდელი ნანომილაკური ბორის მრავალკედლიანი გეომეტრიისათვის.
- თ. ფაღავა, ლ. ჩხარტიშვილი. ბორის როლი სილიციუმში მეორადი რადიაციული დეფექტების წარმოქმნაში.
- თ. ა. ბაციკაძე, დ. ლ. გაბუნია, ვ. მ. გაბუნია, თ. გ. გიგიტაშვილი, ო. ა. ცაგარეიშვილი, ლ. ს. ჩხარტიშვილი. ბორისა და ბორის კარბიდის მიღება რკალში – ახლებური მიდგომები.
- მ. ე. ანთაძე, დ. ლ. გაბუნია, ო. ა. ცაგარეიშვილი, ლ. ს. ჩხარტიშვილი. β-რომბოედრული ბორის კრისტალების თავისუფალი ზრდის თავისებურებანი.
- ო. ცაგარეიშვილი, ა. გაჩეჩილაძე, მ. დარჩიაშვილი, ბ. მარგიევი, ლ. რუხაძე, ლ. ჩხარტიშვილი. ხახუნის პროცესები ჰექსაგონალური ბორის ნიტრიდით მოდიფიცირებულ ლითონურ კომპოზიტურ მასალებში.

- გ. დარსაველიძე, ო. ცაგარეიშვილი, მ. დარჩიაშვილი, ლ. ჩხარტიშვილი, ი. ყურაშვილი, ა. სიჭინავა, ი. ტაბატაძე. რეალური ზედაპირის გავლენა პოლიკრისტალური β-რომბოედრული ბორის ფიზიკურ-მექანიკურ თვისებებზე.
- მ. ანთაძე, ა. მიქელაძე, ა. გაჩეჩილაძე, რ. ჭედია, ბ. მარგიევი, ლ. ჩხარტიშვილი, ო. ცაგარეიშვილი. ლითონ–კერამიკული კომპოზიტის მიღება B_4C–TiB_2-ის ფუძეზე.
- ლ. სარტინსკა, ე. ვოინიჩი, თ. ერენი, ე. ალტაი, ლ. ჩხარტიშვილი, ი. მურუსიძე, ო. ცაგარეიშვილი, დ. გაბუნია. ტანტალის მალეგირებელ ატომებთან დაკავშირებული ლოკალიზებული რხევები β-რომბოედრულ ბორში.

პროგრამის და თეზისების კრებულის გარეკანი.

ბბსს 2014-ის მოხსენებათა თეზისები დაიბეჭდა ცალკე კრებულის სახით. რაც შეეხება სრულ ტექსტებს, ისინი სათანადო რეცენზირების გავლის შემთხვევაში სტატიების სახით გამოქვეყნდება ჟურნალში Solid State Sciences.

ამ საერთაშორისო სამეცნიერო ფორუმის მასშტაბურობის შესახებ წარმოდგენა შეიძლება შეგვიქმნას მოკლე სტატისტიკამ: მოხსენებები წარმოდგენილი იყო მსოფლიოს 18 ქვეყნის (ამერიკის შეერთებული შტატები, ავსტრალია, ავსტრია, ბრაზილია, გერმანია, თურქეთი, იაპონია, პოლონეთი, რუსეთი, საფრანგეთი, საქართველო, სლოვაკეთი, უკრაინა, ყაზახეთი, შვედეთი, შვეიცარია, ჩეხეთი და

ჩინეთი) მოწინავე უნივერსიტეტებისა და კვლევითი ინსტიტუტებიდან. სიმპოზიუმზე პლენარული სხდომების გარდა, მუშაობა მიმდინარეობდა 8 სექციაში:

- ბეტა-ბორი, ბორის კარბიდი
- სტრუქტურული და ფიზიკური თვისებები
- ზემტკიცე მასალები
- კვლევები მაღალ წნევებზე
- თერმოელექტრული მასალები
- ნანომასალები
- ჰექსაბორიდები, დოდეკაბორიდები, ფიზიკური თვისებები
- ბორშემცველი მასალები

გაიმართა პოსტერული სესიებიც. სულ 119 მოხსენება იყო წარმოდგენილი (მათ შორის – 5 პლენარული, 33 მოწვეული, 29 ზეპირი და 52 პოსტერული).

ლევან ჩხარტიშვილი (საქართველო) აკეთებს მოხსენებას.

ივანე მურუსიძე (საქართველო) პასუხობს მოხსენების შემდგომ კითხვებს.

მონაწილეები დაბინავებული იყვნენ წყნარი ოკეანის სანაპიროზე მდებარე სასტუმროში “პრინც ჰოტელ ვაიკიკი”; იქვე, სასტუმროს საკონფერენციო დარბაზში, იმართებოდა სიმპოზიუმის სხდომები.

ხედი ცისარტყელით “პრინც ჰოტელ ვაკიკის” ფანჯრებიდან.

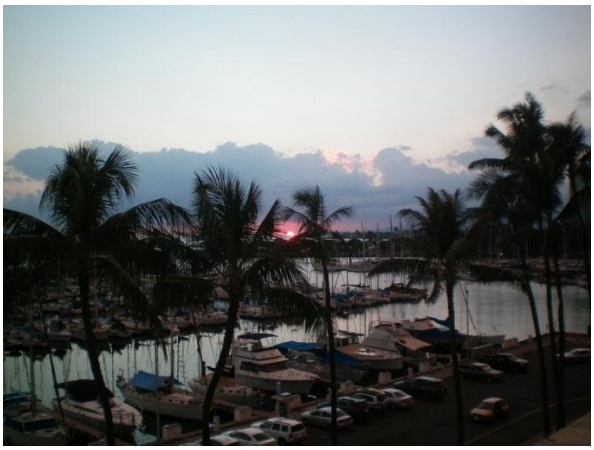

მზის ჩასვლა წყნარ ოკეანეში.

ჰონოლულუს ერთ-ერთ ქუჩაზე.

ხიდი არხზე ჰონოლულუში.

კუნძულ ოაჰუს სამხრეთ-აღმოსავლეთი სანაპირო პარკში.

ჰანაუმას ყურე.

ლევან ჩხარტიშვილი (საქართველო) ჰონოლულუს ერთ-ერთ ქუჩაზე.

ჰავაიური გვრგვინებით შემკული სიმპოზიუმის მონაწილეები – ივანე მურუსიძე (საქართველო), ონურალფ იუჯელი (თურქეთი), როზა აბდულქარიმოვა (ყაზახეთი) და ლევან ჩხარტიშვილი (საქართველო) – სასტუმროს ტერასაზე მეგობრული ბანკეტის დაწყებამდე.

ივანე მურუსიძე (საქართველო) და ტაკეო მორი (იაპონია) სანაპირო პარკში.

სიმპოზიუმის ორგანიზატორებმა მონაწილეებს საინტერესო სოციალური პროგრამა შესთავაზეს. იგი მოიცავდა ექსკურსიას კუნძულ ოაჰუს, სადაც მდებარეობს

ჰავაის არქიპელაგის (იგივე შტატის) დედაქალაქი ჰონოლულუ, სამხრეთ-აღმოსავლეთ სანაპიროზე მდებარე პარკში და პოლინეზიური ფოლკლორის საღამოს, აგრეთვე, მონაწილეთა მეგობრულ ბანკეტს.





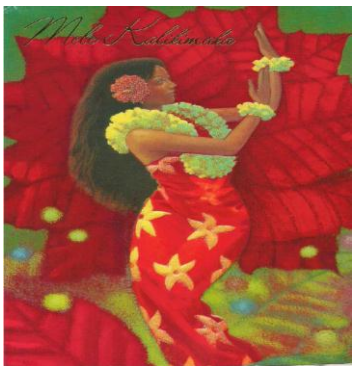

ჰავაიური სახვითი ხელოვნების ნიმუშები.

პოლინეზიური ფოლკლორის საღამოზე.

სიმპოზიუმის დღეებში, კერძოდ, 2014 წლის 2 სექტემბერის გაიმართა ბორის, ბორიდებისა და მონათესავე მასალების საერთაშორისო სიმპოზიუმების საერთაშორისო სამეცნიერო კომიტეტის სხდომა. საქართველოდან კომიტეტის სხდომაში მონაწილეობდა პროფ. ლ. ჩხარტიშვილი, როგორც აღნიშნული კომიტეტის მუდმივი წევრი. მიღებულ იქნა დადგენილებები კომიტეტის შემადგენლობის ცვლილებების, მიმდინარე სიმპოზიუმის მასალების პუბლიკაციისა და მომავალი სიმპოზიუმის ორგანიზების თაობაზე.

გადაწყდა, რომ ბორის, ბორიდებისა და მონათესავე მასალების მე-19 საერთაშორისო სიმპოზიუმი (ბბსს 2017) გაიმართება 2017 წლის სექტემბერში გერმანიის ქალაქ ფრაიბურგში პროფ. ჰარალდ ჰილებრეხტის თავმჯდომარეობით.

ივანე მურუსიძე

2014 წლის 10 სექტემბერი

ISSN 1987-8826